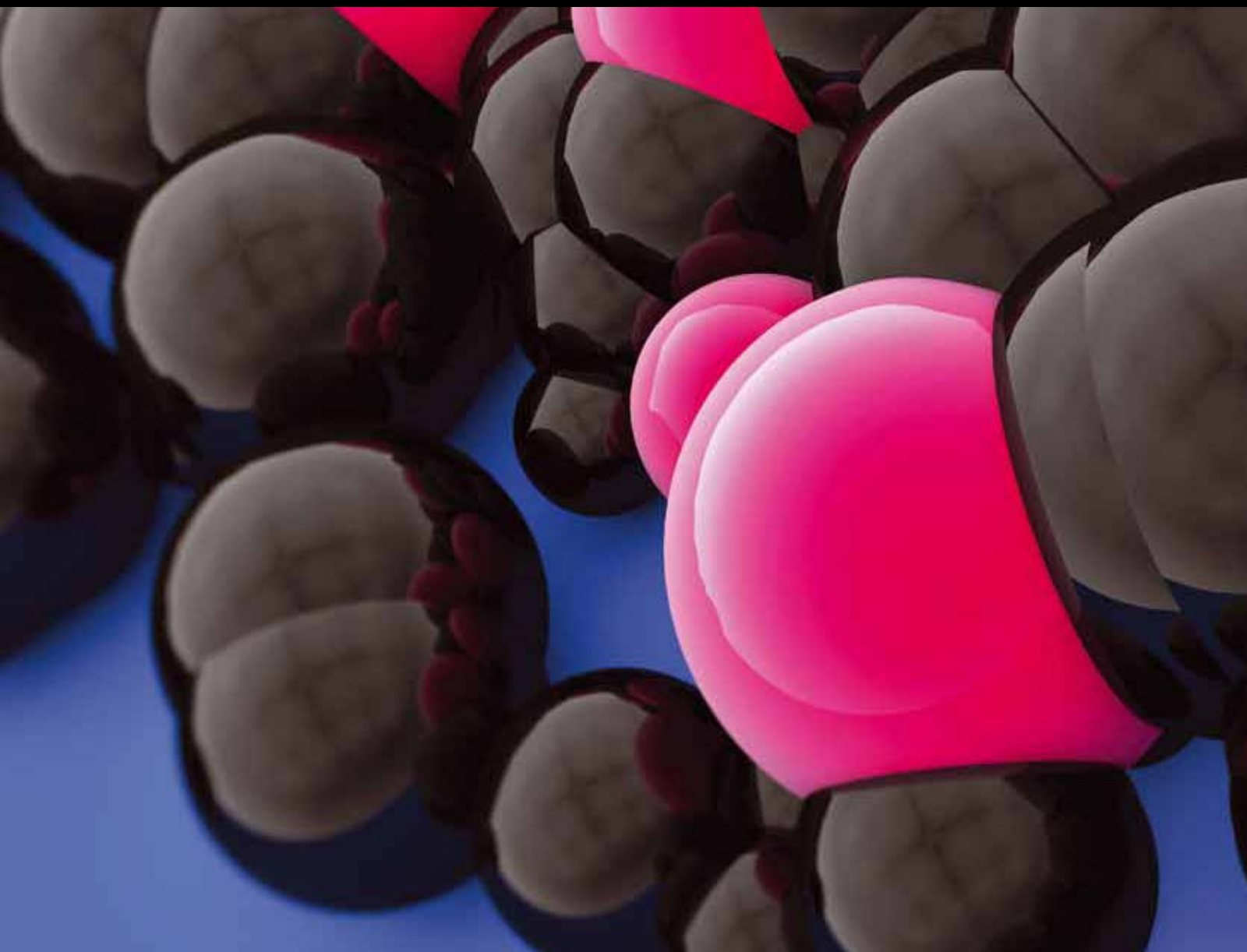


NANO/MICROSTRUCTURED MATERIALS: Rapid, Low-Cost, AND ECO-FRIENDLY SYNTHESIS METHODS

GUEST EDITORS: AMIR KAJBAFVALA, MINGHANG LI, HAMED BAHMANPOUR,
MOHAMMAD H. MANESHIAN, AND ALEXANDER KAUFFMANN





Nano/Microstructured Materials: Rapid, Low-Cost, and Eco-Friendly Synthesis Methods

**Nano/Microstructured Materials: Rapid,
Low-Cost, and Eco-Friendly Synthesis Methods**

Guest Editors: Amir Kajbafvala, Minghang Li,
Hamed Bahmanpour, Mohammad H. Maneshian,
and Alexander Kauffmann



Copyright © 2013 Hindawi Publishing Corporation. All rights reserved.

This is a special issue published in "Journal of Nanoparticles." All articles are open access articles distributed under the Creative Commons Attribution License, which permits unrestricted use, distribution, and reproduction in any medium, provided the original work is properly cited.

Editorial Board

Gunjan Agarwal, USA
Ipsita Banerjee, USA
Xujin Bao, UK
Bridgette Budhlall, USA
Nitin Chopra, USA
Anne Davidson, France
Ovidiu Ersen, France
Georg Garnweitner, Germany
Vincent Gomes, Australia
Fabien Grasset, France
John Zhanhu Guo, USA
Youssef Habibi, Belgium
Jean-François Hochepped, France
Frank Hubenthal, Germany

Go Kawamura, Japan
Joseph Koo, USA
Karen Martirosyan, USA
Atsushi Ohtaka, Japan
Agnes Ostafin, USA
Kihong Park, Korea
Jerome Plain, France
Alexander Pyatenko, Japan
You Qiang, USA
Vijaya Rangari, USA
Swadeshmukul Santra, USA
Raphael Schneider, France
Nikolaos Semaltianos, Greece
Tapas Sen, UK

Young-Seok Shon, USA
Shu Taira, Japan
Katsuaki Tanabe, Japan
Isabelle Texier, France
Rodica Turcu, Romania
Francesc Vies, Spain
Hsing-Lin Wang, USA
Dongsheng Wen, UK
Otto Wilson, USA
Yang Xu, USA
Nikolaos Zafeiropoulos, Greece
Xiangwu Zhang, USA
Chuan Jian Zhong, USA

Contents

Nano/Microstructured Materials: Rapid, Low-Cost, and Eco-Friendly Synthesis Methods,

Amir Kajbafvala, Minghang Li, Hamed Bahmanpour, Mohammad H. Maneshian,
and Alexander Kauffmann

Volume 2013, Article ID 530170, 3 pages

Green Synthesis of Nanocrystalline $\text{Cu}_2\text{ZnSnS}_4$ Powder Using Hydrothermal Route, Shri kant Verma,
Vikash Agrawal, Kiran Jain, Renu Pasricha, and Suresh Chand

Volume 2013, Article ID 685836, 7 pages

Antibacterial Activity of Silver Nanoparticles Synthesized by Bark Extract of *Syzygium cumini*,

Ram Prasad and Vyshnava Satyanarayana Swamy

Volume 2013, Article ID 431218, 6 pages

Sol-Gel Synthesis of $\text{TiO}_2/\text{SiO}_2$ and ZnO/SiO_2 Composite Films and Evaluation of Their Photocatalytic Activity towards Methyl Green, V. L. Chandraboss, B. Karthikeyan, J. Kamalakkannan, S. Prabha,
and S. Senthilvelan

Volume 2013, Article ID 507161, 7 pages

Ecofriendly and Facile One-Pot Multicomponent Synthesis of Thiopyrimidines under Microwave Irradiation, Biswa Mohan Sahoo, B. V. V. Ravi Kumar, Jnyanaranjan Panda, and S. C. Dinda

Volume 2013, Article ID 780786, 6 pages

Electrochemical Method for Ag-PEG Nanoparticles Synthesis, M. Virginia Roldan, Nora Pellegri,
and Oscar de Sanctis

Volume 2013, Article ID 524150, 7 pages

Synthesis of Gold Nanoparticles Using Whole Cells of *Geotrichum candidum*, Amit Kumar Mittal,
Abhishek Kaler, Aparna Vasant Mulay, and Uttam Chand Banerjee

Volume 2013, Article ID 150414, 6 pages

CuO-CeO_2 Nanocomposite: An Efficient Recyclable Catalyst for the Synthesis of Aryl-14H-dibenzo[a-j]xanthenes, Jalal Albadi, Abdolhossein Razeghi, Hossein Abbaszadeh,
and Azam Mansournezhad

Volume 2013, Article ID 546194, 5 pages

Rapid, Low-Cost, and Ecofriendly Approach for Iron Nanoparticle Synthesis Using *Aspergillus oryzae* TFR9, Jagadish Chandra Tarafdar and Ramesh Raliya

Volume 2013, Article ID 141274, 4 pages

Naturally Self-Assembled Nanosystems and Their Templated Structures for Photonic Applications,

K. Pradeesh, Nageswara Rao Kotla, Shahab Ahmad, Vindesh K. Dwivedi, and G. Vijaya Prakash

Volume 2013, Article ID 531871, 13 pages

Microwave-Assisted Synthesis of Mixed Metal-Oxide Nanoparticles, Akraati Verma, Reena Dwivedi,
R. Prasad, and K. S. Bartwal

Volume 2013, Article ID 737831, 11 pages

Selective Hydrogenation of p-Chloronitrobenzene on Nanosized PdNiB Catalysts, Yu-Wen Chen and Der-Shing Lee
Volume 2013, Article ID 132180, 10 pages

Tuning the Pore Size in Ionic Nanoparticle Networks, Marie-Alexandra Neouze Gauthey, Marco Litschauer, Michael Puchberger, Martin Kronstein, and Herwig Peterlik
Volume 2013, Article ID 682945, 9 pages

Photocatalytic Properties of Microwave-Synthesized TiO₂ and ZnO Nanoparticles Using Malachite Green Dye, A. K. Singh and Umesh T. Nakate
Volume 2013, Article ID 310809, 7 pages

Rapid Green Synthetic Protocol for Novel Trimetallic Nanoparticles, B. Karthikeyan and B. Loganathan
Volume 2013, Article ID 168916, 8 pages

Synthesis of ZnO Nanostructures by Microwave Irradiation Using Albumen as a Template, T. Prakash, R. Jayaprakash, G. Neri, and Sanjay Kumar
Volume 2013, Article ID 274894, 8 pages

Microwave Assisted Growth of ZnO Nanorods and Nanopolydops Nanostructure Thin Films for Gas and Explosives Sensing, A. K. Singh
Volume 2013, Article ID 783691, 12 pages

Green Chemistry Approach for Efficient Synthesis of Schiff Bases of Isatin Derivatives and Evaluation of Their Antibacterial Activities, Jnyanaranjan Panda, V. Jagannath Patro, Biswa Mohan Sahoo, and Jitendriya Mishra
Volume 2013, Article ID 549502, 5 pages

Studying the Effects of Adding Silica Sand Nanoparticles on Epoxy Based Composites, Tahir Ahmad, Othman Mamat, and Rafiq Ahmad
Volume 2013, Article ID 603069, 5 pages

Editorial

Nano/Microstructured Materials: Rapid, Low-Cost, and Eco-Friendly Synthesis Methods

Amir Kajbafvala,¹ Minghang Li,² Hamed Bahmanpour,³ Mohammad H. Maneshian,² and Alexander Kauffmann⁴

¹ Department of Materials Science and Engineering, North Carolina State University, 911 Partners Way, Engineering Building I, Raleigh, NC 27695-7907, USA

² Department of Materials Science and Engineering, University of North Texas, Denton, TX 76203, USA

³ Department of Chemical Engineering and Materials Science, University of California, Davis, CA 95616, USA

⁴ Leibniz Institute for Solid State and Materials Research Dresden, P.O. Box 27 01 16, 01171 Dresden, Germany

Correspondence should be addressed to Amir Kajbafvala; akajbaf@ncsu.edu

Received 9 July 2013; Accepted 9 July 2013

Copyright © 2013 Amir Kajbafvala et al. This is an open access article distributed under the Creative Commons Attribution License, which permits unrestricted use, distribution, and reproduction in any medium, provided the original work is properly cited.

Chemists are required to generate a diverse array of organic and inorganic molecules using eco-friendly conditions, including low-cost and short-reaction times. A primary driver of synthetic chemistry is, therefore, the development of efficient and environmentally benign synthetic protocols, as the pressure to produce the myriad of substances required by society in an eco-friendly fashion has continued to increase. Up to now, many works have been published on synthesis and characterization of various multidimensional micro/nanostructured materials via diverse synthesis methods. However, complex conditions and long synthesis time were required for most of these technologies.

Microwave-assisted processing methods, as good examples, have been developed for a variety of applications in organic and inorganic synthesis and transformations. There are many examples of the successful application of MW-assisted green chemistry for synthesis of micro/nanostructured materials in the literature. This special issue addresses rapid methods for synthesis of organic and inorganic micro/nanomaterials to maximize the efficient use of safer raw materials and to reduce waste for fabrication of various micro/nanostructured materials. This special issue contains nineteen papers including seventeen research and two review papers.

In “*Studying the effects of adding silica sand nanoparticles on epoxy based composites*,” T. Ahmad et al. produced

Epoxy-SiO₂ nanocomposites using Tronoh silica sand nanoparticles as reinforcement. They reported that density of the epoxy-SiO₂ nanocomposites increases from 1.157 g/cm³ to 1.244 g/cm³. The mechanical properties of the fabricated nanocomposites decrease with the addition of silica sand nanoparticles due to improper mixing of the nanoparticles. SEM micrographs show white and agglomerate zones on fracture surfaces which indicate that silica sand nanoparticles are not homogeneously dispersed in epoxy.

In their paper, J. Panda et al. studied a “*Green chemistry approach for efficient synthesis of Schiff bases of Isatin derivatives and evaluation of their antibacterial activities*.” They synthesized Schiff base of Isatin derivatives by conventional and microwave irradiation method. With microwave synthesis, the yield of product increases from 60% up to 85% as compared to conventional method. By microwave irradiation the reactions are completed within 5–10 min, which reduced the time, waste, and formation of byproduct. This microwave-assisted synthesis is reported as a simple and eco-friendly route. From their results of antibacterial studies, they concluded that compounds exhibited significant antibacterial activities against both Gram-positive and gram-negative organisms.

In his paper, A. K. Singh presented “*Microwave assisted growth of ZnO nanorods and nanopolypods nanostructure thin films for gas and explosives sensing*.” It was shown that use

of triethanolamine (TEA) as capping agent has resulted in the additional growth of ZnO NPPs. The structural analysis shows hexagonal wurtzite structure of ZnO with planes highly oriented along (002) direction. The sensing study of ZnO NRs and ZnO NRs/NPPs samples shows that the sensor response (S) increases with temperature for both liquefied petroleum gas (LPG) and oxygen, while, with the increase in gas concentration from 0.2 to 0.4 vol%, the sensor response increases gradually and attains saturation for LPG, and, for oxygen, the response is found to be linear with the increase in gas concentration. The sensor sensing and the recovery time analysis show that the recovery time reduces with the increase in operation temperature for both gas and explosives. Additionally, the recovery time achieved for LPG at 0.4 vol% concentration is much lesser than that previously reported for ZnO thin film with much higher LPG concentration.

In their paper, "Synthesis of ZnO nanostructures by microwave irradiation using albumen as a template," T. Prakash et al. synthesized ZnO nanostructures via a microwave irradiation method in the presence of albumen as a biotemplate. The composition and morphology of the nanostructures are affected by the presence of albumen as a template. The optical band gap of the polycrystalline ZnO nanoparticles increases from 3.22 to 3.25 eV for the sample synthesized in the presence of albumen because of the defects' decrease. The good quality of ZnO nanostructures produced was also demonstrated by PL studies.

In "Rapid green synthetic protocol for novel trimetallic nanoparticles," B. Karthikeyan and B. Loganathan presented the preparation of nanosized trimetallic nanocomposites and trimetallic nanotubes from an aqueous solution of corresponding metallic precursors. They reported a simple microwave irradiated synthesis of Au-Pt-Ag trimetallic nanocomposites and Au-Pd-Pt trimetallic nanotubes. EDX analysis confirmed that the percentage of Pt is maximum on the surface of trimetallic nanoparticles and nanotubes.

In their paper, "Photocatalytic properties of microwave-synthesized TiO_2 and ZnO nanoparticles using malachite green dye," A. K. Singh and U. T. Nakate synthesized TiO_2 and ZnO nanoparticles using a green, efficient, and cost-effective microwave method. The photocatalytic activity of these nanoparticles was studied for malachite green (MG) dye under UV light. The photocatalytic tests showed that TiO_2 and ZnO nanoparticles have 49.35% and 23.31% photodegradation efficiency, respectively, for MG dye under UV light. TiO_2 nanoparticles show more than two-order photodegradation property for MG dye as compared to ZnO.

In "Tuning the pore size in ionic nanoparticle networks" M. -A. N. Gauthey et al. described a new ionic nanoparticle networks (INNS) material based on zirconia nanoparticles and compared the porous characteristics of different INNs, with various metal oxide nanoparticles. In these materials, the liking imidazolium moieties are maintained in the network and thus remained accessible to adsorbed molecules. The INN based on zirconia nanoparticles linked by ionic liquid-like imidazolium bridging units. It was shown that the porous

characteristics of the INN depend on the size and shape of the nanoparticles. INNs based on large spherical nanoparticles, like SiO_2 , are macroporous, while INNs based on small spherical nanoparticles, like TiO_2 , are microporous.

In their paper, Y. -W. Chen and D. S. Lee investigated "Selective hydrogenation of *p*-chloronitrobenzene on nanosized PdNiB catalysts." They prepared a series of PdNiB nanoalloy catalysts with various Pd contents by chemical reduction method with NaBH_4 as the reducing agent. The magnetization of PdNiB remarkably increased with doping Pd into NiB. High activity and selectivity on PdNiB in the hydrogenation of *p*-CNB could be attributed to both ensemble effect and electronic effect.

In their paper, "Microwave-assisted synthesis of mixed metal-oxide nanoparticles," A. Verma et al. synthesized ZrO_2 and ZrTiO_4 nanoparticles by microwave-assisted citrate sol-gel method. Nanoparticles of V_2O_5 supported on ZrO_2 were also synthesized by microwave-assisted solution combustion method. The low-angle powder XRD measurements confirm the mesoporous nature of ZrV_2O_7 and formation of single phase material up to 10 wt% of vanadium incorporation. The HRTEM data confirms the formation of single phase t- ZrO_2 . Raman spectra further support the crystalline phase as well as the specific bands to show the modes of vibration in Zr-O system, whereas the specific bands indicate the modes of vibration in Zr-Ti-O and ZrV_2O_7 systems. The crystallite sizes were found to be in the ranges of ~5–10 nm, ~2–5 nm, and ~20–50 nm for ZrO_2 , ZrTiO_4 , and ZrV_2O_7 , respectively.

In their review article, "Naturally self-assembled nanosystems and their templated structures for photonic applications," K. Pradeesh et al. discussed fabrication, structural, and optical exciton features of naturally self-assembled low-dimensional IO-hybrid nanosystems. While the fabrication of these self-assembled systems is usually from solution chemistry techniques, a novel device-compatible thin film fabrication from very inexpensive method, that is, intercalation, was reviewed. Finally, the designing and fabrication of optoelectronic compatible photonic architectures from these IO-hybrids, especially from template-assisted method, have been clearly discussed.

In "Rapid, low-cost, and ecofriendly approach for iron nanoparticle synthesis using *Aspergillus oryzae* TFR9," J. C. Tarafdar and R. Raliya demonstrated a rapid, low-cost, and eco-friendly synthesis method for fabricating iron nanoparticles using the fungi *Aspergillus oryzae* TFR9.

In their paper, "CuO-CeO₂ nanocomposite: an efficient recyclable catalyst for the synthesis of aryl-14H-dibenzo[*a-j*]xanthenes," J. Albadi et al. developed a new, efficient, and green procedure for the synthesis of biologically important xanthene derivatives catalyzed by recyclable CuO-CeO₂ nanostructured catalyst, under solvent-free conditions. This catalyst can promote the yields and reaction times over eight runs without noticeable loss in its efficiency.

In their paper, A. K. Mittal et al. studied "Synthesis of gold nanoparticles using whole cells of *Geotrichum candidum*." Various reaction parameters like cell age, temperature, pH, cell mass, and metal ion concentration were optimized to

increase the yield and to improve the dispersity of nanoparticles. The gold nanoparticle throughout the cell mass suggests that Au^{+3} ions entered the cells through a transport system. The presence of different metabolic enzymes inside the cells or cytoplasm probably reduced Au^{+3} to Au^0 and capped it by protective peptide/proteins.

In their article, “*Electrochemical method for Ag-PEG nanoparticles synthesis*,” M. V. Roldán et al. presented an electrochemical method to prepare Ag nanoparticles using polyethylene glycol (PEG) as stabilizer. The PEG chain length does not show effects on the shape of the nanoparticles obtained, which are spherical for all the cases. Nevertheless, with the longer polymer chain length, it is possible to control the particle size through the PEG concentration.

In their paper, B. M. Sahoo et al. studied an “*Ecofriendly and facile one-pot multicomponent synthesis of thiopyrimidines under microwave irradiation*.” With the help of microwave synthesis, the yield of product increased from 55% up to 85% as compared to conventional synthesis. In addition, the reaction time is reduced from 4–8 hrs to 5–10 min.

In their paper, V. L. Chandraboss et al. studied “*Sol-gel synthesis of $\text{TiO}_2/\text{SiO}_2$ and ZnO/SiO_2 composite films and evaluation of their photocatalytic activity towards methyl green*.” In this work, $\text{TiO}_2/\text{SiO}_2$ and ZnO/SiO_2 composite films were prepared by the sol-gel method. These $\text{TiO}_2/\text{SiO}_2$ and ZnO/SiO_2 films were then used for the photodegradation of methyl green (MG) under UV-light irradiation.

In “*Antibacterial activity of silver nanoparticles synthesized by bark extract of *Syzygium cumini**,” R. Prasad and V. S. swamy used the silver nanoparticles synthesized from the bark extract of *S. cumini* and its antibacterial effect on the bacteria, namely, *Escherichia coli*, *Staphylococcus aureus*, *Pseudomonas aeruginosa*, *Azotobacter chroococcum*, and *Bacillus licheniformis*. In the present study, silver nanoparticles are synthesized at room temperature within a less span of time. The size of the nanoparticles ranges from 20 to 60 nm with spherical shape. These nanoparticles showed a broad spectrum antimicrobial activity against both Gram-positive and Gram-negative bacteria. Investigation on the antibacterial activity of synthesized silver nanoparticles using *S. cumini* extract against *Staphylococcus aureus* and *Bacillus licheniformis* reveals high potential as antimicrobial agent in pharmaceutical, food, and cosmetic industries.

In their paper, “*Green synthesis of nanocrystalline $\text{Cu}_2\text{ZnSnS}_4$ powder using hydrothermal route*,” S. K. Verma et al. presented a simple and relatively safe approach of hydrothermal synthesis of the quaternary semiconductor CZTS nanoparticles. Spherical nanoparticles with diameters of about 4–5 nm are obtained without using any expensive vacuum facilities or high temperature annealing temperature.

thanks are extended to all reviewers for enhancing the quality of these papers.

Amir Kajbafvala
Minghang Li
Hamed Bahmanpour
Mohammad H. Maneshian
Alexander Kauffmann

Acknowledgments

We would like to express our kind appreciation to all authors in this special issue for their contribution. Furthermore,

Research Article

Green Synthesis of Nanocrystalline $\text{Cu}_2\text{ZnSnS}_4$ Powder Using Hydrothermal Route

Shri kant Verma,¹ Vikash Agrawal,¹ Kiran Jain,¹ Renu Pasricha,² and Suresh Chand¹

¹ Organic and Hybrid Solar Cell Group, National Physical Laboratory (CSIR), New Delhi 110 012, India

² Material & Chemical Microscopy Group, National Physical Laboratory (CSIR), New Delhi 110 012, India

Correspondence should be addressed to Kiran Jain; kiran@mail.nplindia.org

Received 12 April 2013; Accepted 7 May 2013

Academic Editor: Amir Kajbafvala

Copyright © 2013 Shri kant Verma et al. This is an open access article distributed under the Creative Commons Attribution License, which permits unrestricted use, distribution, and reproduction in any medium, provided the original work is properly cited.

Nanocrystalline $\text{Cu}_2\text{ZnSnS}_4$ (CZTS) powder was synthesized by a hydrothermal process, using thiourea as sulfur precursor. The powder was qualitatively analyzed using X-ray to identify the phase, and the size of the particles was determined using transmission electron microscopy (TEM). Raman peak at 337.5 cm^{-1} confirms the formation of pure CZTS particles. The powder was also synthesized solvothermally using ethylenediamine as solvent. The hydrothermally synthesized powder indicated the presence of the kesterite phase $\text{Cu}_2\text{ZnSnS}_4$ and particle size of about 4–5 nm. This environmentally green synthesis by hydrothermal route can produce gram scale synthesis of material with a chemical yield in excess of ~90%. UV Vis absorption spectra measurements indicated the band gap of as-synthesized CZTS nanoparticles to be 1.7 eV, which is near the optimum value for photovoltaic solar cell, showing its possible use in photovoltaics.

1. Introduction

Thin film solar cells based on chalcopyrite type semiconductors like CuInSe_2 , CuInGaSe_2 (CIGS), and so forth have shown high efficiency and applicability for large scale applications [1]. CIGS based solar cells exhibit improved stability under long-term excitation, and their best efficiency available nowadays exceeds 20% [2]; however, gallium and indium used for preparation of the active layer are rare earth elements and are expensive also. Hence, $\text{Cu}_2\text{ZnSn(SSe)}_4$ was found of more interest, because of less toxicity, earth abundance, nearly optimum direct band gap (E_g) of about 1.05–1.50 eV, and a high absorption coefficient [3, 4]. Compared with the vacuum approaches, the nonvacuum approaches are the more desired techniques to achieve low production costs, because of the advantages offered by these methods, such as simplicity, easy to scale up, and high material utilization [4, 5]. Diverse deposition routes of $\text{Cu}_2\text{ZnSnS}_4$ (CZTS) thin films such as sputtering, spray pyrolysis, sol-gel, and electro-deposition have been reported [6, 7]. Much attention has been focused recently on fabrication of low cost and highly efficient solar cells. In this respect, the synthesis of nanocrystalline powders through wet chemical routes is gaining importance, since spin

casting or printing nanocrystalline powders enable roll to roll processing for large scale manufacturing. Solar cells based on $\text{Cu}_2\text{ZnSnSe}_4$ (CZTS) have achieved power conversion efficiencies as high as 11.1% using a hydrazine based approach [8]. However, hydrazine is highly toxic and very unstable, and its use requires extreme caution during handling. Recent advances in the synthesis of colloidal semiconductor nanocrystals (NCs) have paved the way for the use of a large variety of different techniques for the preparation of nanoparticle inks [9, 10]. Decreasing the particle size to the quantum confinement regime allows the band gap to be tuned as a function of the crystallite size, which facilitates the realization of multijunctions. Another advantage of using NCs is well controlled stoichiometry, which is one of the limiting steps of other deposition methods. To adapt these NCs for industrial purposes, in solar cell applications, the development of synthesis methods enabling the precise control of size, shape, and composition is of crucial importance. In the last few years, the synthesis of colloidal CZTS NCs appeared, and the use of CZTS inks for solar cell applications has also been demonstrated [9–14]. The choice of a user friendly method of large scale nanocrystalline synthesis process is a prerequisite to successively achieve the mission of cost effectiveness. There

are not many reports on the synthesis of nanocrystalline CZTS powders. Thin film solar cells based on colloidal route have achieved a power conversion efficiency of 7.3% and 8.4% [9, 10].

Hydrothermal/solvothermal process is an attractive route for large scale synthesis of nanocrystalline powders. Hydrothermal reactions have been widely used to synthesize nanocrystalline materials such as TiO_2 , ZnO , CdS , ZnS , and ZnSe [11–18]. Ternary semiconductor quantum dots CuInS_2 , CuInSe_2 have also been prepared by this method [19, 20]. Madarász et al. [21] prepared CZTS using thermal decomposition of thiourea complexes of Cu (I), Zn (II), and Sn (II) chlorides. Hydrothermal/solvothermal processing route was used to synthesize CZTS and related materials [22–29]. Wang et al. [22] synthesized CZTS by hydrothermal process. Cao and Shen [23] synthesized CZTS by solvothermal route, wherein ethylenediamine (EDA) was used as a solvent. Jiang et al. [24] reported the synthesis of orthorhombic CZTS using a hydrothermal method using EDA. In this approach, a mixed solvent EDA and water of 1:1 ratio and thiocarbamide were used as sulfur source. The presence of EDA and the annealing temperature were reported by Jiang et al. [24] to play an important role in the process of CZTS phase transitions between the tetragonal and orthorhombic structures. Large scale single crystalline CZTS nanosheets of thickness as thin as 20 nm were produced by a solvothermal approach depending on the EDA concentration [26].

In the present work, we have synthesized CZTS nanopowder by hydrothermal method, using thiourea as sulfur agent. This method is milder, simpler, more practical, and more ecofriendly than the solvothermal method, which uses EDA as solvent. The results demonstrate that hydrothermal route produces single phase nanocrystalline kesterite phase of CZTS. These investigations indicated that the formation of a crystal phase is closely related to the reaction conditions and the sulfur source, the solvent may affect the size and phase properties. The physical properties of the CZTS nanocrystalline particles, such as structure, morphology, and optical properties, were studied. The as-synthesized CZTS nanoparticles prepared in water showed a kesterite phase, with nanocrystallite size of 4–5 nm. The use of water as a solvent offers a more green or environmentally benign process, removing the requirement of organic solvents or hazardous substances. From the viewpoint of green chemistry, the hydrothermal approach is a good candidate since the reaction can proceed at a mild temperature in water in a sealed environment. Taking organic compound thiourea as a source of sulfur, the toxicity is lowered as compared with H_2S or Na_2S . Furthermore, thiourea decomposes at a temperature of about 80°C and releases S_2^- slowly, causing the reaction to proceed slowly and control easily.

2. Experimental

2.1. Synthesis of Nanocrystalline $\text{Cu}_2\text{ZnSnS}_4$ Powder. CZTS nanocrystalline powder was synthesized by solvothermal as well as hydrothermal route. In the solvothermal process, appropriate amounts of analytical grade CuCl_2 ,

$(\text{C}_2\text{H}_3\text{O}_2)_2\text{Zn}$, SnCl_4 , and S were added into a stainless steel autoclave with a teflon liner, which was filled with ethylenediamine up to 50% of the total volume (1000 mL). The autoclave was sealed and maintained at 180°C for 16 h and then allowed to cool to room temperature naturally. The precipitates were filtered off and washed with absolute ethanol. Finally, the product was collected for characterization.

In a hydrothermal process, appropriate amounts of analytical grade CuCl_2 , $(\text{C}_2\text{H}_3\text{O}_2)_2\text{Zn}$, SnCl_4 and NH_2CSNH_2 (thiourea) were added into a stainless steel autoclave with a teflon liner, which was filled with double distilled water up to 50% of the total volume (1000 mL). The concentration of thiourea was kept 20% higher than stoichiometric ratio for the complete sulfurization of the compound. The autoclave was sealed and maintained at 180°C for 16 h and then allowed to cool to room temperature naturally. The precipitate was filtered off and washed with double distilled water.

2.2. Characterization. Structural characteristics of powders were determined by X-ray diffraction in 2θ range from 10° to 80° using Bruker Analytical X-ray diffractometer equipped with graphite-monochromatized $\text{Cu K}\alpha$ radiation ($\lambda = 1.5418 \text{ \AA}$) and transmission electron microscope using a JEOL 2010F TEM operating at an accelerating voltage of 100 kV. For TEM measurements, carbon coated copper grids were prepared by dispersing 0.1 g powder in 10 ml deionized (DI) water by ultrasonic treatment for about 250 sec. One drop of this solution was placed over grid and left to dry. The particle size and morphology were investigated by UV Vis absorption spectra which were taken on a UV Vis spectrophotometer (Shimadzu UV-1601), in which chloroform was used as a reference solvent. Raman measurements were performed using Renishaw inVia Raman spectrometer, operating at 514.5 nm Ar ion laser.

3. Results and Discussion

Figure 1 shows the XRD pattern of the as-synthesized CZTS nanocrystalline particles. The diffraction pattern of the hydrothermally synthesized CZTS powder showed peaks at $2\theta = 28.66, 33.1, 47.77, 56.70, 69.59,$ and 76.94° . All of these peaks can be indexed to the kesterite phase of CZTS (JCPDS 26-0575). The major XRD diffraction peaks can be attributed to the (112), (200), (220), and (312) planes, respectively. Similar peaks were present in the powder synthesized by solvothermal process.

Besides these results, some extra peaks at 2θ of $26.822, 30.811,$ and 51.891° , indicated by solvothermally prepared CZTS powder, can be attributed to the diffraction peaks of (100), (102), and (103) planes of wurtzite structure of ZnS (JCPDS36-1450). No direct information could be found to confirm the existence of SnS or SnS_2 . An earlier report on solvothermal synthesis had shown similar impurity phase that was removed on annealing [23]. The powder prepared by hydrothermal route do not show presence of ZnS impurity phase. According to the Debye-Scherrer formula $d = 0.9\lambda/(\beta \cdot \cos \theta)$, where β is the line width at an angle 2θ and λ is X-ray wave length. The diameter d of both hydrothermal

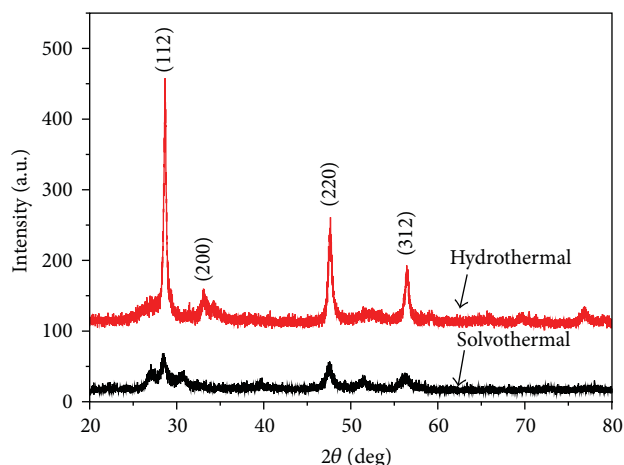


FIGURE 1: XRD pattern of as-synthesized CZTS powders.

and solvothermal synthesis routes of CZTS gives average nanoparticle size within 4–5 nm range.

As the XRD pattern of the CZTS particles is very similar to those of ZnS and Cu_2SnS_4 , the Raman spectra of the material was used to characterize the final material. Figures 2(a) and 2(b) show the Raman scattering data for hydrothermally and solvothermally synthesized nanoparticles. Raman peaks for Cu_2S , ZnS, and SnS_2 are expected at 472 cm^{-1} , 351 cm^{-1} , and 315 cm^{-1} , respectively [30, 31]. In the present samples, the line widths are quite broad. The broadening of Raman peaks has been observed previously for nanocrystals of other materials and attributed to phonon confinement within the nanocrystals. This, together with the low intensity of the Raman peaks, made it very difficult to clearly identify the presence of impurity phases, especially in hydrothermally synthesized nanoparticles. For the material synthesized by hydrothermal route, Figure 2(a) showed a wide peak present at 335 cm^{-1} , and no other peak in the $100\text{--}500\text{ cm}^{-1}$ region was observed. On the other hand, the sample synthesized by solvothermal route showed three peaks present at 236 , 343 , and 472 cm^{-1} . The peaks present at 343 , and 472 cm^{-1} may belong to the CZTS and Cu_2S phases, respectively. The presence of peaks other than that of CZTS further confirmed the presence of impurity phases in solvothermally synthesized material. Similar results were observed earlier by Cao and Shen, even though the impurity phases disappear after annealing [23]. On the other hand, in hydrothermal synthesis at 180°C , even the as-synthesized CZTS material is almost in pure phase, with negligible impurity phases.

Figures 3(a)–3(d) show the TEM image of hydrothermally synthesized CZTS nanoparticles. Figures 3(a) and 3(b) showed the presence of several small sized monodispersed CZTS nanoparticles of size 4 to 5 nm. Figure 3(b) shows the presence of sharper lattice fringes in the images of corresponding nanoparticles (encircled) that shows the high crystallinity of these nanoparticles. The selected area electron diffraction pattern of CZTS nanocrystals shown in Figure 3(c) confirms the single crystalline nature of nanoparticles. Also, the pattern matches well with JCPDS data card

number 26-0575 as indicated by the diffraction rings corresponding to the (200) and (220) planes of the kesterite structure of CZTS nanoparticles. Figure 3(d) shows the enlarged view of nanoparticle encircled in Figure 3(b) and the lattice fringes in the high resolution TEM image are separated by 0.31 nm which matches the spacing distance of the (112) plane of $\text{Cu}_2\text{ZnSnS}_4$ nanocrystals.

Figures 4(a) and 4(d) show the transmission electron microscopic (TEM) image of CZTS nanoparticles synthesized by solvothermal method. Figures 4(a) and 4(c) show the CZTS nanoparticles of spherical shape having average size 5–6 nm. Figure 4(b) showed the agglomerated cluster of CZTS nanoparticles of size $\sim 100\text{ nm}$, which consists of several small CZTS nanoparticles. Inset of Figure 4(a) displays the HRTEM image of CZTS nanoparticles that shows the lattice fringe distance of 0.31 nm belonging to the (112) plane of the kesterite structure. Figure 4(d) shows the SAED ring pattern of polycrystalline CZTS nanoparticles.

The absorption spectra were measured in chloroform and the as-prepared nanocrystals were ultrasonically dispersed for several minutes in chloroform. Final solution was then transferred to the cuvette to measure the absorption spectra, and pure chloroform was used as reference. Figure 5(a) shows absorption spectra of CZTS nanoparticles, synthesized by hydrothermal and solvothermal methods. The band gaps were obtained by plotting $(Ah\nu)^2$ as a function of $h\nu$. Hydrothermally synthesized powder shows an optical band gap of 1.7 eV , while the solvothermally synthesized powder showed a band gap of 1.5 eV . This value corresponds well with the literature values and is near the optimum value for photovoltaic solar conversion in a single-band-gap device. The energy band structure of CZTS has already been calculated, and the measured band gap of kesterite CZTS is within $1.4\text{--}1.5\text{ eV}$ [20, 21], and since the crystallite size of CZTS powder for hydrothermally synthesized powder is near 4–5 nm, some band gap enhancement is expected due to quantum confinement.

The chemical composition of nanocrystals was determined using XRF technique. The composition obtained for solvothermal route showed the presence of molar concentration of different components as ($\text{Cu} = 2$, $\text{Zn} = 0.7$, $\text{Sn} = 1.07$, and $\text{S} = 3.57$) with lesser Zn; however, for hydrothermal route, the composition is slightly deficient in Cu as compared to Zn and Sn ($\text{Cu} = 2$, $\text{Zn} = 1.23$, $\text{Sn} = 1.45$, and $\text{S} = 4.11$). These compositions were calculated on average area of sample since large area of the thin film of CZTS was scanned. These relative chemical compositions were obtained for a film of $1\text{ inch} \times 1\text{ inch}$ dimension, and thus, a large number of particles have been simultaneously analyzed. Therefore, they represent an average value.

The synthesis of large scale nanopowders by green technology is gaining importance nowadays. In this respect, the present hydrothermal synthesis of CZTS powder is important since water is a nonpolluting and nontoxic medium to synthesize nanopowders. Also, in hydrothermal process, reaction takes place in a closed reactor; thus, no fumes/gases are released in the atmosphere. The hydrothermally synthesized CZTS nanoparticles exhibited a good solubility in the isopropanol and showed a black color due to their strong

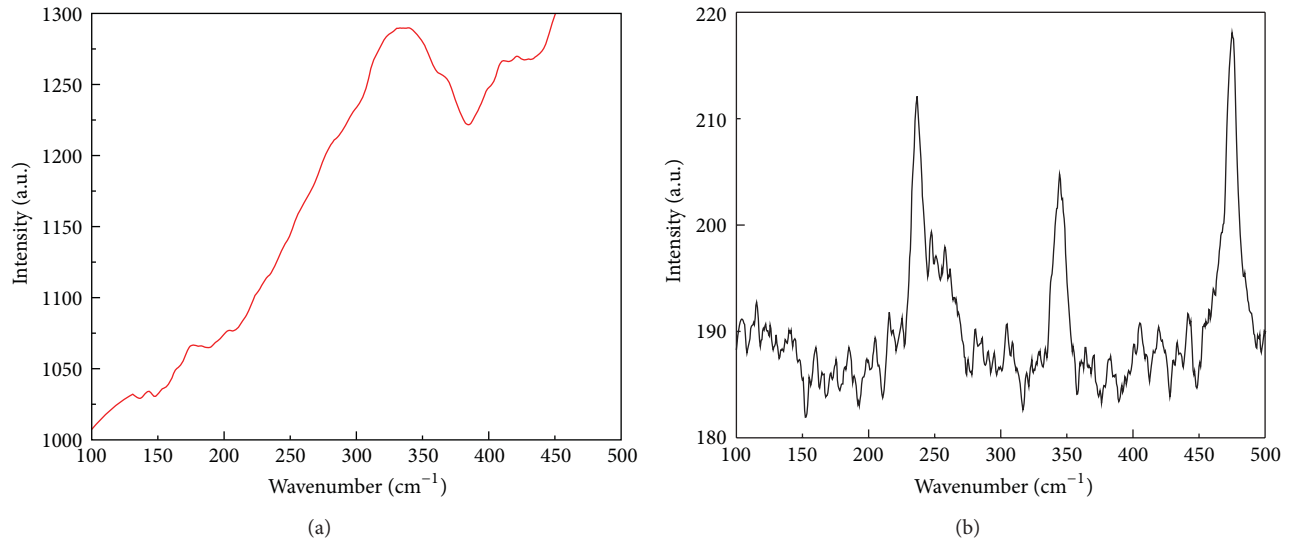


FIGURE 2: Raman spectra for CZTS nanoparticles synthesized by (a) hydrothermal and (b) solvothermal route.

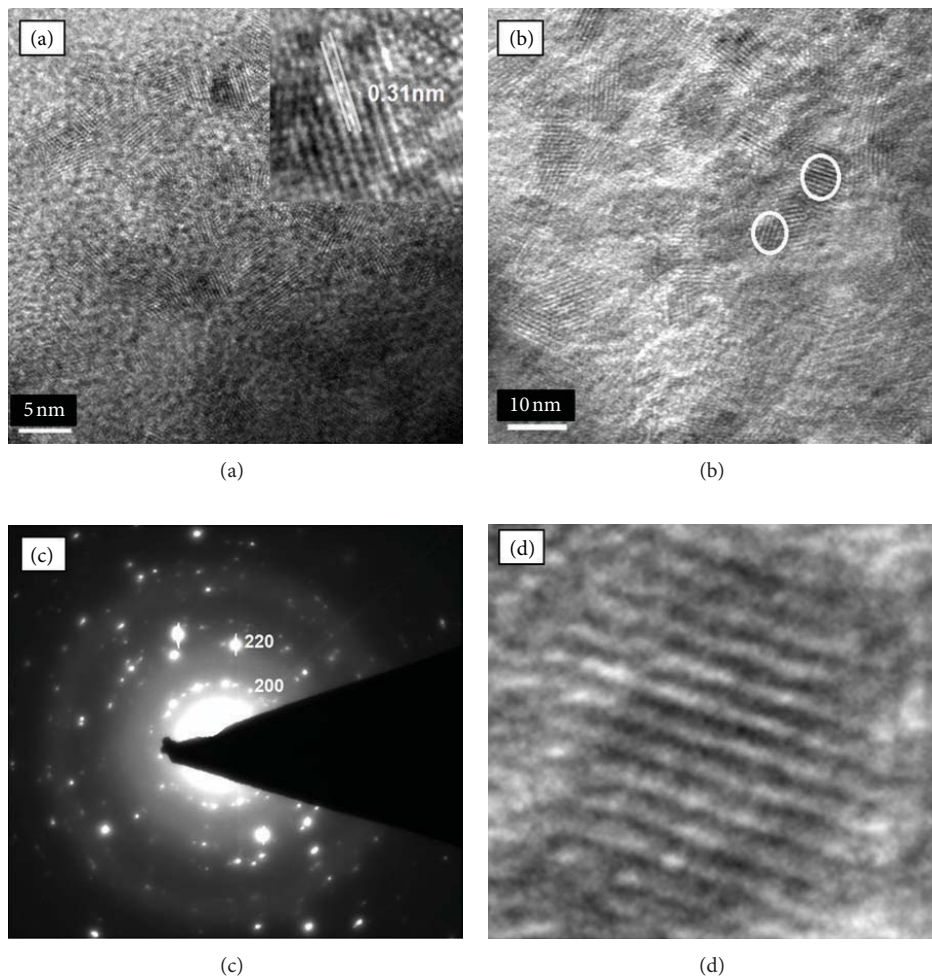


FIGURE 3: TEM images of hydrothermally synthesized CZTS powder: (a) average particle size (inset lattice fringes), (b) average particle size, (c) electron diffraction pattern, and (d) lattice fringes in single particle.

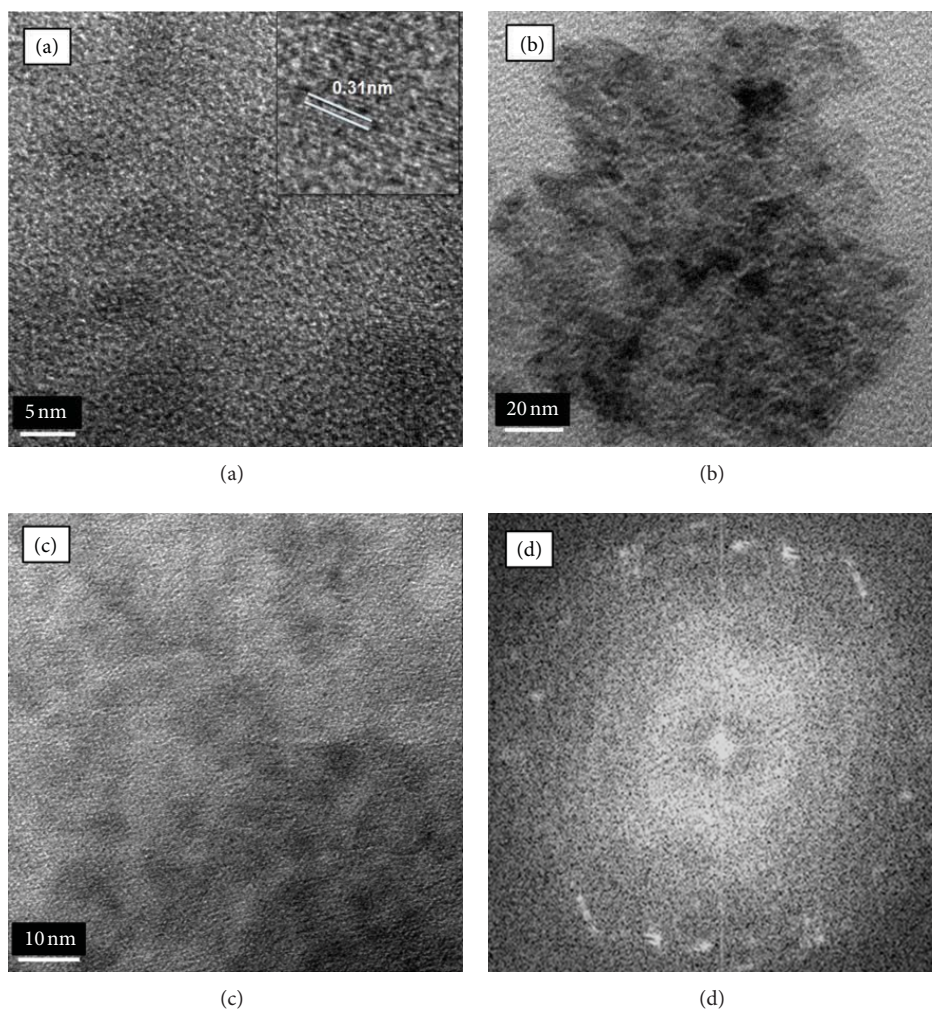


FIGURE 4: TEM images of solvothermally synthesized CZTS powder: (a) average particle size (inset lattice fringes), (b) cluster of nanoparticles, (c) distributed nanoparticles, and (d) electron diffraction pattern.

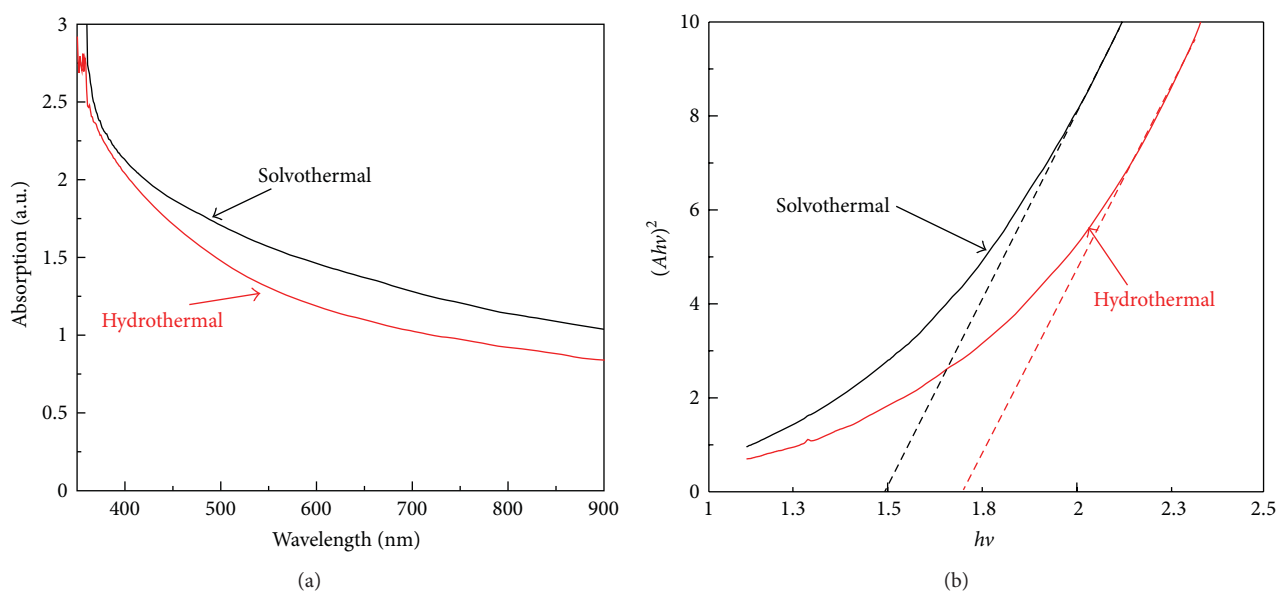
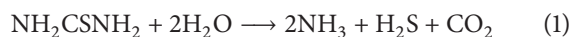


FIGURE 5: (a) Absorbance spectra of as-synthesized CZTS nanoparticles, and (b) $(Ah\nu)^2$ versus $h\nu$ curve.

absorbance for visible light. The particle size of these nanomaterials is approximately 4–5 nm, and some effect of quantum confinement was observed for these CZTS nanocrystals, due to which an enhanced band gap of 1.7 eV was observed as compared to the bulk band gap of 1.45–1.5 eV reported for CZTS material. The solvothermally synthesized powder did not show any quantum confinement effect.

To propose the growth mechanism, we will first consider the reactions happening to yield CZTS powder. With the increase in temperature and stirring, metal ions are complexed with thiourea. (Thiourea in solution forms metal-thiourea complexes.) On hydrothermal heating, thiourea decomposes to give hydrogen sulfide (H_2S) as follows:



H_2S , produced in this way, reacts with different metal ions, to form CZTS compound. Thiourea plays two important roles in the formation of sulfides. First, it acts as a complexing reagent by forming metal-thiourea ligands, and second it acts as the source of sulfur after the breaking of C=S double bond by the strong nucleophilic substitution of the oxygen atoms in H_2O molecules [31]. The metal-thiourea ligands serves as a reservoir of metal ions and regulate the nucleation rate by the slow release of ions into solution. When the reactants were heated, the released S_2^{2-} combined with the metal ions and precipitation of sulfides occurred due to the stronger coordination capability between metal ions and S_2^{2-} . Because of the excess of thiourea, the metal atoms on the surface of the CZTS nanocrystallites formed could coordinate with excess thiourea and thus greatly restrict the growth of CZTS nanocrystallites. Due to this, hydrothermally synthesized CZTS is of smaller size as compared to solvothermally synthesized CZTS. Thus, both, the formation of metal-thiourea ligands and the gradual release of S_2^{2-} , can control the nucleation and aggregation of CZTS nanocrystallites, leading to the large-scale harvesting of monodispersed nanocrystalline particles.

4. Conclusions

A simple and relatively safe approach of hydrothermal synthesis of the quaternary semiconductor $\text{Cu}_2\text{ZnSnS}_4$ (CZTS) nanoparticles was used. Nearly spherical nanoparticles of approximately 4–5 nm diameter were obtained without using any expensive vacuum facilities or high temperature annealing. The elemental analysis of the synthesized CZTS particles, performed by XRF, agreed well with the theoretical value of 2 : 1 : 1 : 4. The highly crystalline nature of the CZTS nanoparticles was confirmed by the X-ray diffraction and high-resolution TEM analysis. The appearance of the strongest Raman peak at 337.5 cm^{-1} in the Raman spectrum leaves no doubt about the formation of pure CZTS nanoparticles. An intercomparative study with solvothermal synthesis revealed that the hydrothermal process is far better in terms of being cheaper, easier, and environmentally green process. As-synthesized nanoparticles using solvothermal route produced mixed phase nanoparticles, which convert to pure CZTS only after annealing. The UV-Vis absorption spectrum

exhibited broad absorption in the visible region. The band gap was estimated to be 1.7 eV which shows the quantum confinement effect in such small sized nanoparticles. The observation of such small sized nanoparticles using such a simple, greener, and inexpensive method is quite advantageous in the respect that hydrothermal synthesis route is well known for its large scale synthesis. There is no need for any capping agent to control the size, which is difficult and cumbersome to remove afterwards for most of the applications example for charge transfer among particles to take place.

Conflict of Interests

The authors declare that they have no conflict of interests.

Acknowledgments

The authors are thankful to (Technologies and Products for Solar Energy Utilization through Networks) (TAPSUN) program (NWP-54 Project) from CSIR for financial support. One of the authors (Shri kant Verma) is obliged to Professor R. C. Budhani (DNPL), for the kind permission for his project. The authors are obliged for the valuable discussion and suggestions given by Dr. Asit Patra. They are also thankful to Dr. N. Vijayan for XRD measurements, Mr. K. N. Sood, and SEM and TEM investigations.

References

- [1] T. Wada, S. Nakamura, and T. Maeda, "Ternary and multinary Cu-chalcogenide photovoltaic materials from CuInSe_2 to $\text{Cu}_2\text{ZnSnS}_4$ and other compounds," *Progress in Photovoltaics*, vol. 20, no. 5, pp. 520–525, 2012.
- [2] P. Jackson, D. Hariskos, E. Lotter et al., "New world record efficiency for $\text{Cu}(\text{In,Ga})\text{Se}_2$ thin-film solar cells beyond 20%," *Progress in Photovoltaics*, vol. 19, no. 7, pp. 894–897, 2011.
- [3] H. Katagiri, K. Jimbo, W. S. Maw et al., "Development of CZTS-based thin film solar cells," *Thin Solid Films*, vol. 517, no. 7, pp. 2455–2460, 2009.
- [4] E. H. Sargent, "Infrared photovoltaics made by solution processing," *Nature Photonics*, vol. 3, no. 6, pp. 325–331, 2009.
- [5] K. Tanaka, M. Oonuki, N. Moritake, and H. Uchiki, " $\text{Cu}_2\text{ZnSnS}_4$ thin film solar cells prepared by non-vacuum processing," *Solar Energy Materials and Solar Cells*, vol. 93, no. 5, pp. 583–587, 2009.
- [6] H. Wang, "Progress in thin film solar cells based on $\text{Cu}_2\text{ZnSnS}_4$," *International Journal of Photoenergy*, vol. 2011, Article ID 801292, 10 pages, 2011.
- [7] K. Ramaswamy, M. A. Malik, and P. O. Brien, "Routes to copper zinc tin sulfide $\text{Cu}_2\text{ZnSnS}_4$ a potential material for solar cells," *Chemical Communications*, vol. 48, pp. 5703–5714, 2012.
- [8] T. K. Todorov, J. Tang, S. Bag et al., "Beyond 11% efficiency: characteristics of state of the art $\text{Cu}_2\text{ZnSn}(\text{S}, \text{Se})_4$ solar cells," *Advanced Energy Materials*, vol. 3, no. 1, pp. 34–38.
- [9] Q. Guo, G. M. Ford, W.-C. Yang et al., "Fabrication of 7.2% efficient CZTSSe solar cells using CZTS nanocrystals," *Journal of the American Chemical Society*, vol. 132, no. 49, pp. 17384–17386, 2010.

- [10] B. Shin, O. Gunawan, Y. Zhu, N. A. Bojarczuk, S. J. Chey, and S. Guha, "Thin film solar cell with 8.4% power conversion efficiency using an earth-abundant $\text{Cu}_2\text{ZnSnS}_4$ absorber," *Progress in Photovoltaics*, vol. 21, no. 1, pp. 72–76, 2013.
- [11] S. E. Habas, H. A. S. Platt, M. F. A. M. Van Hest, and D. S. Ginley, "Low-cost inorganic solar cells: from ink to printed device," *Chemical Reviews*, vol. 110, no. 11, pp. 6571–6594, 2010.
- [12] A. Khare, A. W. Wills, L. M. Ammerman, D. J. Norris, and E. S. Aydil, "Size control and quantum confinement in $\text{Cu}_2\text{ZnSnS}_4$ nanocrystals," *Chemical Communications*, vol. 47, no. 42, pp. 11721–11723, 2011.
- [13] C. Steinhagen, M. G. Panthani, V. Akhavan, B. Goodfellow, B. Koo, and B. A. Korgel, "Synthesis of $\text{Cu}_2\text{ZnSnS}_4$ nanocrystals for use in low-cost photovoltaics," *Journal of the American Chemical Society*, vol. 131, no. 35, pp. 12554–12555, 2009.
- [14] Q. J. Guo, H. W. Hillhouse, and R. Agrawal, "Synthesis of $\text{Cu}_2\text{ZnSnS}_4$ nanocrystal ink and its use for solar cells," *Journal of the American Chemical Society*, vol. 131, no. 33, pp. 11672–11673, 2009.
- [15] M. Rajamathi and R. Seshadri, "Oxide and chalcogenide nanoparticles from hydrothermal/solvothermal reactions," *Current Opinion in Solid State and Materials Science*, vol. 6, no. 4, pp. 337–345, 2002.
- [16] H. Zhang, X. Ma, Y. Ji, J. Xu, and D. Yang, "Single crystalline CdS nanorods fabricated by a novel hydrothermal method," *Chemical Physics Letters*, vol. 377, no. 5–6, pp. 654–657, 2003.
- [17] L. Wang, J. Dai, X. Liu, Z. Zhu, X. Huang, and P. Wu, "Morphology-controlling synthesis of ZnS through a hydrothermal/solvothermal method," *Ceramics International*, vol. 38, no. 3, pp. 1873–1878, 2012.
- [18] H. Gong, H. Huang, M. Wang, and K. Liu, "Characterization and growth mechanism of ZnSe microspheres prepared by hydrothermal synthesis," *Ceramics International*, vol. 33, no. 7, pp. 1381–1384, 2007.
- [19] Q. Lu, J. Hu, K. Tang, Y. Qian, G. Zhou, and X. Liu, "Synthesis of nanocrystalline CuMS_2 ($M = \text{In}$ or Ga) through a solvothermal process," *Inorganic Chemistry*, vol. 39, no. 7, pp. 1606–1607, 2000.
- [20] J. Chang, J. E. Han, and D.-Y. Jung, "Solvothermal synthesis of copper indium diselenide in toluene," *Bulletin of the Korean Chemical Society*, vol. 32, no. 2, pp. 434–438, 2011.
- [21] J. Madarász, P. Bombicz, M. Okuya, and S. Kaneko, "Thermal decomposition of thiourea complexes of Cu(I), Zn(II), and Sn(II) chlorides as precursors for the spray pyrolysis deposition of sulfide thin films," *Solid State Ionics*, vol. 141–142, pp. 439–446, 2001.
- [22] C. Wang, C. Cheng, Y. Cao, W. Fang, L. Zhao, and X. Xu, "Synthesis of $\text{Cu}_2\text{ZnSnS}_4$ nanocrystallines by a hydrothermal route," *Japanese Journal of Applied Physics*, vol. 50, no. 6, Article ID 065003, 2011.
- [23] M. Cao and Y. Shen, "A mild solvothermal route to kesterite quaternary $\text{Cu}_2\text{ZnSnS}_4$ nanoparticles," *Journal of Crystal Growth*, vol. 318, no. 1, pp. 1117–1120, 2011.
- [24] H. Jiang, P. Dai, Z. Feng, W. Fan, and J. Zhan, "Phase selective synthesis of metastable orthorhombic $\text{Cu}_2\text{ZnSnS}_4$," *Journal of Materials Chemistry*, vol. 22, no. 15, pp. 7502–7506, 2012.
- [25] Y.-F. Du, W.-H. Zhou, Y.-L. Zhou et al., "Solvothermal synthesis and characterization of quaternary $\text{Cu}_2\text{ZnSnSe}_4$ particles," *Materials Science in Semiconductor Processing*, vol. 5, pp. 214–217, 2012.
- [26] L. Shi and Q. Li, "Thickness tunable $\text{Cu}_2\text{ZnSnSe}_4$ nanosheets," *CrystEngComm*, vol. 13, no. 21, pp. 6507–6510, 2011.
- [27] Y.-L. Zhou, W.-H. Zhou, Y.-F. Du, M. Li, and S.-X. Wu, "Sphere-like kesterite $\text{Cu}_2\text{ZnSnS}_4$ nanoparticles synthesized by a facile solvothermal method," *Materials Letters*, vol. 65, no. 11, pp. 1535–1537, 2011.
- [28] O. Zaberca, A. Gillorin, B. Durand, and J. Y. Chane-Ching, "A general route to the synthesis of surfactant-free, solvent-dispersible ternary and quaternary chalcogenide nanocrystals," *Journal of Materials Chemistry*, vol. 21, no. 18, pp. 6483–6486, 2011.
- [29] Y.-L. Zhou, W.-H. Zhou, M. Li, Y.-F. Du, and S.-X. Wu, "Hierarchical $\text{Cu}_2\text{ZnSnS}_4$ particles for a low-cost solar cell: morphology control and growth mechanism," *Journal of Physical Chemistry C*, vol. 115, no. 40, pp. 19632–19639, 2011.
- [30] Y. Wang and H. Gong, "Low temperature synthesized quaternary chalcogenide $\text{Cu}_2\text{ZnSnS}_4$ from nano-crystallite binary sulfides," *Journal of the Electrochemical Society*, vol. 158, no. 8, pp. H800–H803, 2011.
- [31] M. Grossberg, J. Krustok, J. Raudoja, K. Timmo, M. Altosaar, and T. Raadik, "Photoluminescence and Raman study of $\text{Cu}_2\text{ZnSn}(\text{Se}_x\text{S}_{1-x})_4$ monograins for photovoltaic applications," *Thin Solid Films*, vol. 519, no. 21, pp. 7403–7406, 2011.

Research Article

Antibacterial Activity of Silver Nanoparticles Synthesized by Bark Extract of *Syzygium cumini*

Ram Prasad and Vyshnava Satyanarayana Swamy

Amity Institute of Microbial Technology, Amity University Uttar Pradesh, Sector 125, Noida 201303, India

Correspondence should be addressed to Ram Prasad; rprasad@amity.edu

Received 31 January 2013; Revised 15 March 2013; Accepted 3 April 2013

Academic Editor: Amir Kajbafvala

Copyright © 2013 R. Prasad and V. S. Swamy. This is an open access article distributed under the Creative Commons Attribution License, which permits unrestricted use, distribution, and reproduction in any medium, provided the original work is properly cited.

The unique property of the silver nanoparticles having the antimicrobial activity draws the major attention towards the present nanotechnology. The environmentally nontoxic, ecofriendly, and cost-effective method that has been developed for the synthesis of silver nanoparticles using plant extracts creates the major research interest in the field of nanobiotechnology. The synthesized silver nanoparticles have been characterized by the UV-visible spectroscopy, atomic force microscopy (AFM), and scanning electron microscopy (SEM). Further, the antibacterial activity of silver nanoparticles was evaluated by well diffusion method, and it was found that the biogenic silver nanoparticles have antibacterial activity against *Escherichia coli* (ATCC 25922), *Staphylococcus aureus* (ATCC 29213), *Pseudomonas aeruginosa* (ATCC 27853), *Azotobacter chroococcum* WR 9, and *Bacillus licheniformis* (MTCC 9555).

1. Introduction

The broad spectrum of nanotechnology is important in the major fields of biology, chemistry, physics, and material sciences. Nanotechnology deals with the study of materials at the nanometers [1, 2]. The day to day development of nanotechnology creates a major interest in the development and fabrications of different dimensioned nanoparticles [3]. The nanomaterials can be synthesized by different methods including chemical, physical, irradiation, and biological methods. The development of new chemical or physical methods has resulted in environmental contaminations, since the chemical procedures involved in the synthesis of nanomaterials generate a large amount of hazardous byproducts [4]. Thus, there is a need for “green nanotechnology” that includes a clean, safe, ecofriendly, and environmentally nontoxic method of nanoparticle synthesis, and in this method there is no need to use high pressure, energy, temperature, and toxic chemicals [5, 6]. The biological methods include synthesis of nanomaterials from the extracts of plant, bacterial, fungal species, and so forth. The synthesis of nanoparticles from the plant extracts is considered to be a process [7]. The preparation and maintenance of fungal and bacterial cultures are

time consuming and require aseptic conditions and large manual skills to maintain the cultures [8].

Plant extracts include bark, root, leaves, fruit, flowers, rhizoids, and latex and are used to synthesize the nanoparticles. These nanoparticles show different dimensions including the size, shape, and dispersion which have more efficacy than those synthesized from the chemical and physical procedures. Therefore, the use of green plants for similar nanoparticle biosynthesis methodologies is an exciting possibility which has compatibility for pharmaceutical and other biomedical applications, as they do not use toxic chemicals for the synthesis of nanoparticles [9, 10].

Nanoparticles had a wide variety of application in the major fields of medicine, electronics, therapeutics, and diagnostic agents. Silver nanoparticles have wide application in biomedical science like treatment of burned patients, antimicrobial activity and used the targeted drug delivery, and so forth [11]. Nowadays the nanoparticles are coated on the medical appliances, food covering sheets, and cans for storing the beverages and food [12–14]. However, there are many problems and toxicity of using metal oxide nanoparticles on the human health. Use of plants for the synthesis of nanoparticles does not require high energy, temperatures, and it is easily

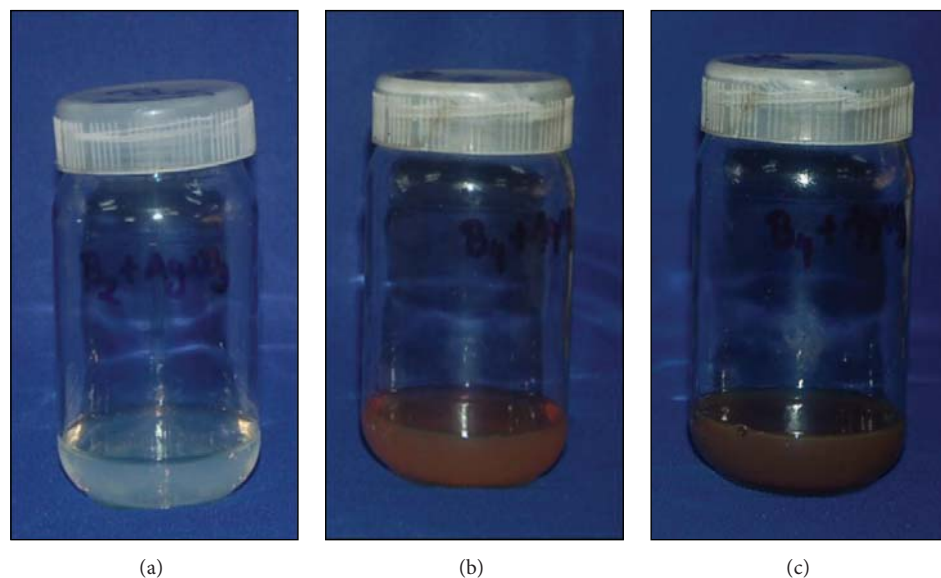


FIGURE 1: *Syzygium cumini* bark extract sample. Change in the color of the solution from brown to dark brown. (a) Silver nitrate solution, (b) reaction mixture, and (c) change in the color of the solution.

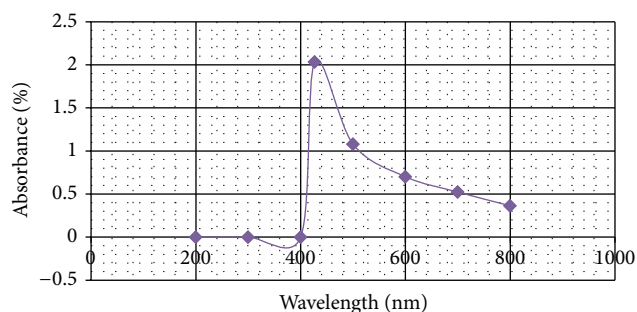


FIGURE 2: UV-visible spectrum of silver nanoparticles.

scaled up for large scale synthesis, and it is cost effective too [15–17].

Syzygium cumini is a medicinal plant available in the tropical forests and is used for treatment of diabetes. The leaves and bark are used for controlling blood pressure and gingivitis [14]. The plant contains a variety of phytochemical compounds such as phenols, tannins, alkaloids, glycosides, amino acids, and flavones, and these molecules are expected to self-assemble and cap the metal nanoparticles formed in their presence and thereby induce some shape control during metal ion reduction [18]. In this study we used the silver nanoparticles synthesized from the bark extract of *S. cumini* and its antibacterial effect on the bacteria, namely, *Escherichia coli* (ATCC 25922), *Staphylococcus aureus* (ATCC 29213), *Pseudomonas aeruginosa* (ATCC 27853), *Azotobacter chroococcum* WR 9, and *Bacillus licheniformis* (MTCC 9555).

2. Materials and Methods

2.1. Chemicals. All analytical reagents and media components were purchased from HiMedia (Mumbai, India) and Sigma Chemicals (St. Louis, MO, USA).

2.2. Preparation of Plant Extract. The fresh bark of *Syzygium cumini* was collected and kept in hot air oven for drying at 60°C for six hours. The dried bark was chopped into fine pieces with the help of mixer grinder. It was collected, weighed for 2.5 g, and then mixed in 100 mL of double distilled water. This mixture was boiled at 60°C in the water bath for one hour. The solution was cooled at room temperature and filtered by Whatman filter paper No. 1. The filtrate was collected and stored at 4°C for further experiment.

2.3. Synthesis of Silver Nanoparticles. Silver nanoparticles (AgNO_3) were synthesized by reducing the freshly prepared 1 mM silver nitrate and stored under dark conditions with the bark extract. The reaction mixture was prepared in ratio of 9:1 (V/V) of freshly prepared silver nitrate solution and bark extract, respectively. The initial color of the solution was observed.

2.4. UV-Visible Spectroscopy. The silver nanoparticles show the plasmon resonance at 400 to 450 nm in the UV-Visible spectrum. The UV-Visible spectrum of synthesized silver nanoparticles was analysed by spectrophotometer (LAB INDIA UV 300+).

2.5. Atomic Force Microscopy. Atomic force microscopy is an advanced characterization technique to identify the size,

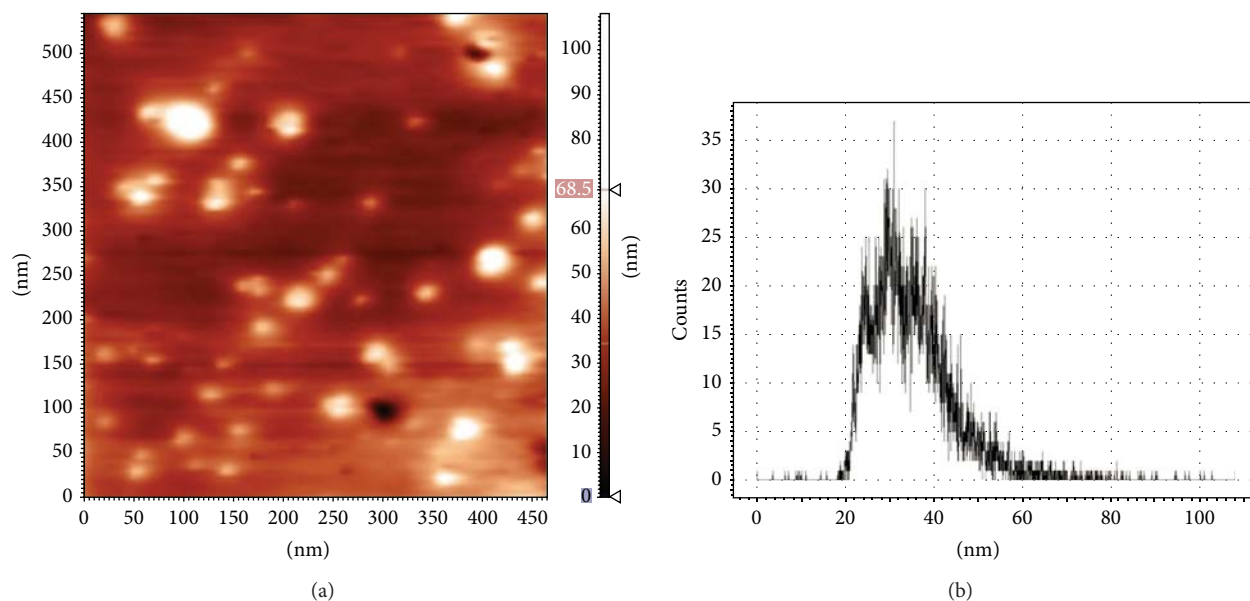


FIGURE 3: Atomic force microscopy. (a) Image of synthesized silver nanoparticles and (b) its histogram.

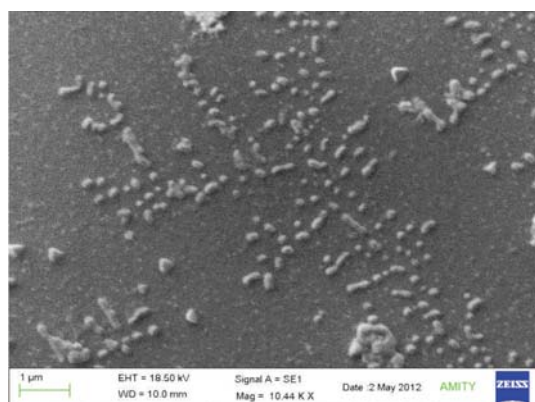


FIGURE 4: SEM images of silver nanoparticles synthesized by *S. cumini* bark extract.

shape, and dispersion of the silver nanoparticles. In order to characterize the silver nanoparticles, the sample was prepared by sonication at room temperature for about 15 minutes in the ultrasonicator. Then the sample solution was dried as a thin layer on mica-based glass slide which was used to view under the AFM Model NT-MDA Solver.

2.6. Scanning Electron Microscopy. SEM analysis of the silver nanoparticles provides the information regarding the dimensions including the surface, shape, and size. The sample was prepared by sonicating the sample solution for 15 minutes at room temperature. A small drop of sonicated sample was dried on a glass slide, and it was coated by gold and observed under ZEISS EVO HD SEM.

2.7. Antibacterial Property. The antibacterial property of the silver nanoparticles was determined by using the bacterial

species including the pathogenic bacteria such as *Escherichia coli* (ATCC 25922), *Staphylococcus aureus* (ATCC 29213), *Pseudomonas aeruginosa* (ATCC 27853), *Azotobacter chroococcum* WR 9, and *Bacillus licheniformis* (MTCC 9555), by the well diffusion method [14]. The different concentrations used were at low concentrations (2, 5, 10, and 15 μL) and at higher concentrations (25, 50, 75, and 100 μL) for the identification of antimicrobial activity of the above bacterial species. All the plates were incubated at 37°C for 24 hours, and the zone of inhibition of bacteria was measured.

3. Results and Discussion

The green synthesis of silver nanoparticles using *S. cumini* bark extract was successfully carried out, as the change in the color of the solution from yellowish brown to dark brown color exhibits the reduction of the silver nitrate in aqueous solution due to excitation of surface plasmon vibrations in silver nanoparticles [19]. During this reaction process the pH of the solution changes from 5.93 to 5.72, which implies that the reaction occurs under acidic condition. This complete reaction occurs in seven hours. The brown to dark brown color change of the reaction mixture indicated the formation of silver nanoparticles (Figure 1).

The formation of silver nanoparticles was confirmed through measurement of UV-Visible spectrum of the reaction mixture. The UV-Visible spectrophotometric analysis of colloidal reaction mixture of silver nanoparticles synthesized using *S. cumini* bark showed sharp peak at 427 nm in the spectrum, and broadening of peak indicated that the particles are polydispersed [20] (Figure 2). The efficiency of this method was tested for stability also. The reaction mixture was stored for 45 days, and no precipitation in the solution was observed. It was also checked through UV-Vis absorption on regular interval.

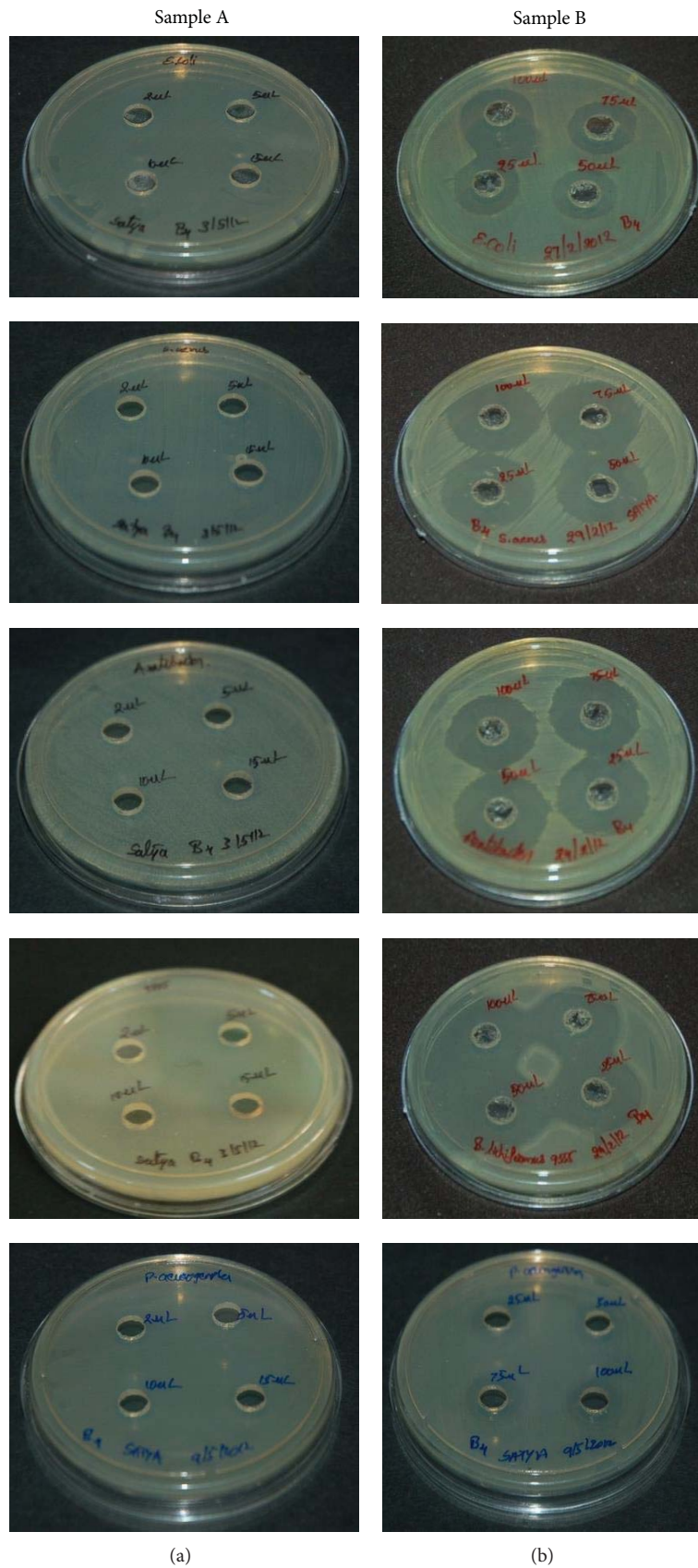


FIGURE 5: Antibacterial effects varying the concentrations of silver nanoparticles samples, (a) lower concentrations (2, 5, 10, and 15 μL) and (b) Higher concentrations (25, 50, 75, and 100 μL).

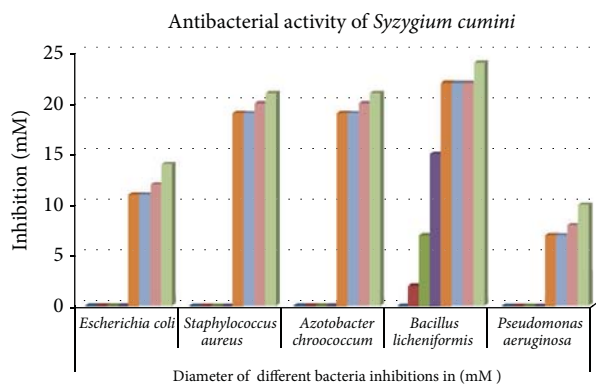


FIGURE 6: Antibacterial activity of *Syzygium cumini*, with different concentrations ranging from 2, 5, 10, 15, 25, 50, 75, and 100 μL .

The atomic force microscopy (AFM) results display the surface morphology of the monodispersed silver nanoparticles using *S. cumini* bark extract. The particle size of the silver nanoparticles that ranges from 20 to 60 nm was observed. The topographical image of silver nanoparticles indicated that they are agglomerated and formed distinct nanoparticles (Figures 3(a) and 3(b)). The bright spots on the micrograph indicated that the nanoparticles are spherical in shape.

The biosynthesized silver nanoparticles were characterized by scanning electron microscopy for their morphology and size. The SEM micrograph reveals that the synthesized silver nanoparticles have spherical morphology with size range from 20 to 60 nm and also indicated that the particles are well separated showing no agglomeration (Figure 4).

The different species of bacteria show zone of inhibition in the well diffusion method of antimicrobial activity. The different patterns of the zone of inhibitions are observed in Figure 5. Synthesized silver nanoparticles showed antibacterial activity against both Gram positive and negative bacteria (Figure 6). The highest zone of inhibition was observed for *Bacillus licheniformis* even at lower concentration. The exact mechanism of the inhibition of the bacteria is still unknown, but some hypothetical mechanisms show that the inhibition is due to ionic binding of the silver nanoparticles on the surface of the bacteria which creates a great intensity of the proton motive force, and the one hypothesis from the research states that the silver nanoparticles invade the bacterial cell and bind to the vital enzymes containing thiol groups [12, 21, 22]. Also, the findings of Sereemaspan et al. (2008) [23] suggested the inhibition of oxidation-based biological process by penetration of metallic nanosized particles across the microsomal membrane [23, 24]. The molecular basis for the biosynthesis of these silver crystals speculated that the organic matrix contains silver binding properties that provide amino acid moieties that serve as the nucleation sites [25, 26].

4. Conclusions

The biological synthesis of the silver nanoparticles is rapid, ecofriendly, cost-effective, and simple method of synthesis. In the present study-silver nanoparticles are synthesized at room

temperature within a less span of time. The synthesized silver nanoparticles were characterized by UV-visible spectrometer, AFM, and SEM analysis. The size of the nanoparticles ranges from 20 to 60 nm with spherical shape. AFM and SEM reveal that the synthesized silver nanoparticles are well dispersed showing no agglomeration. These nanoparticles showed a broad spectrum antimicrobial activity against both Gram positive and Gram negative bacteria. Investigation on the antibacterial activity of synthesized silver nanoparticles using *cumini* extract against *Staphylococcus aureus* and *Bacillus licheniformis* reveals high potential as antimicrobial agent in pharmaceutical, food, and cosmetic industries.

Conflict of Interests

The authors declare that they have no conflict of interests.

Acknowledgments

The authors are thankful to Drs. Gaurav Raikhy and Ravi Mani Tripathi, Amity University, India, for critically reading the paper and analyzing the data.

References

- [1] E. K. Elumalai, T. N. V. K. V. Prasad, J. Hemachandran, T. S. Vijiyan, T. Thirumalai, and E. David, "Extracellular synthesis of silver nanoparticles using leaves of *Euphorbia hirta* and their antibacterial activities," *Journal of Pharmaceutical Sciences and Research*, vol. 2, no. 9, pp. 549–554, 2010.
- [2] A. V. Singh, R. Patil, M. B. Kasture, W. N. Gade, and B. L. V. Prasad, "Synthesis of Ag-Pt alloy nanoparticles in aqueous bovine serum albumin foam and their cytocompatibility against human gingival fibroblasts," *Colloids and Surfaces B*, vol. 69, no. 2, pp. 239–245, 2009.
- [3] C. Marambio-Jones and E. M. V. Hoek, "A review of the antibacterial effects of silver nanomaterials and potential implications for human health and the environment," *Journal of Nanoparticle Research*, vol. 12, no. 5, pp. 1531–1551, 2010.
- [4] M. Zhang, M. Liu, H. Prest, and S. Fischer, "Nanoparticles secreted from ivy rootlets for surface climbing," *Nano Letters*, vol. 8, no. 5, pp. 1277–1280, 2008.
- [5] S. Jeong, S. Yeo, and S. Yi, "Antibacterial characterization of silver nanoparticles against *E. coli* ATCC-15224," *Journal of Material Science*, vol. 40, article 5407, 2005.
- [6] N. Savithramma, R. M. Linga, K. Rukmini, and D. P. Suvarnalatha, "Antimicrobial activity of silver nanoparticles synthesized by using medicinal plants," *International Journal of ChemTech Research*, vol. 3, no. 3, pp. 1394–1402, 2011.
- [7] A. Saxena, R. M. Tripathi, and R. P. Singh, "Biological synthesis of silver nanoparticles by using onion *Allium cepa* extract and their antibacterial activity," *Digest Journal of Nanomaterials and Biostructures*, vol. 5, no. 2, pp. 427–432, 2010.
- [8] S. Schultz, D. R. Smith, J. J. Mock, and D. A. Schultz, "Single-target molecule detection with nonbleaching multicolor optical immunolabels," *Proceedings of the National Academy of Sciences of the United States of America*, vol. 97, no. 3, pp. 996–1001, 2000.
- [9] K. Vijayaraghavan and S. P. K. Nalini, "Biotemplates in the green synthesis of silver nanoparticles," *Biotechnology Journal*, vol. 5, no. 10, pp. 1098–1110, 2010.

- [10] R. M. Crooks, M. Zhao, L. Sun, V. Chechik, and L. K. Yeung, "Dendrimer-encapsulated metal nanoparticles: synthesis, characterization and application to catalysis," *American Chemical Society*, vol. 34, no. 3, pp. 181–190, 2001.
- [11] A. Singh, D. Jain, M. K. Upadhyay, N. Khandelwal, and H. N. Verma, "Green synthesis of silver nanoparticles using *Argemone mexicana* leaf extract and evaluation of their antimicrobial activities," *Digest Journal of Nanomaterials and Biostructures*, vol. 5, no. 2, pp. 483–489, 2010.
- [12] V. K. Sharma, R. A. Yngard, and Y. Lin, "Silver nanoparticles: green synthesis and their antimicrobial activities," *Advances in Colloid and Interface Science*, vol. 145, no. 1-2, pp. 83–96, 2009.
- [13] K. S. Prasad, D. Pathak, A. Patel et al., "Biogenic synthesis of silver nanoparticles using *Nicotiana tobaccum* leaf extract and study of their antibacterial effect," *African Journal of Biotechnology*, vol. 10, no. 41, pp. 8122–8130, 2011.
- [14] P. Ram, V. S. Swamy, P. K. Suranjit, and V. Ajit, "Biogenic synthesis of silver nanoparticles from the leaf extract of *Syzygium cumini* (L.)," *International Journal of Pharma and Bio Sciences*, vol. 3, no. 4, pp. 745–752, 2012.
- [15] S. Ghosh, S. Patil, M. Ahire et al., "Synthesis of silver nanoparticles using *Dioscorea bulbifera* tuber extract and evaluation of its synergistic potential in combination with antimicrobial agents," *International Journal of Nanomedicine*, vol. 7, pp. 483–496, 2012.
- [16] P. S. Vankar and D. Shukla, "Biosynthesis of silver nanoparticles using lemon leaves extract and its applications for antimicrobial finish on fabric," *Applied Nanoscience*, vol. 2, pp. 163–168, 2012.
- [17] K. S. Mukunthan, E. K. Elumalai, T. N. Patel, and V. R. Murthy, "*Catharanthus roseus*: a natural source for the synthesis of silver nanoparticles," *Asian Pacific Journal of Tropical Biomedicine*, pp. 270–274, 2011.
- [18] N. Ahmad, S. Sharma, M. K. Alam et al., "Rapid synthesis of silver nanoparticles using dried medicinal plant of basil," *Colloids and Surfaces B*, vol. 81, no. 1, pp. 81–86, 2010.
- [19] S. S. Shankar, A. Rai, B. Ankamwar, A. Singh, A. Ahmad, and M. Sastry, "Biological synthesis of triangular gold nanoprisms," *Nature Materials*, vol. 3, no. 7, pp. 482–488, 2004.
- [20] V. S. Swamy and P. Ram, "Green synthesis of silver nanoparticles from the leaf extract of *Santalum album* and its antimicrobial activity," *Journal of Optoelectronic and Biomedical Materials*, vol. 4, no. 3, pp. 53–59, 2012.
- [21] C. Ramteke, T. Chakrabarti, B. K. Sarangi, and R. A. Pandey, "Synthesis of silver nanoparticles from the aqueous extract of leaves of *Ocimum sanctums* for enhanced antibacterial activity," *Journal of Chemistry*, vol. 2013, Article ID 278925, 7 pages, 2013.
- [22] S. Kavita, J. Santhanalakshmi, and B. Viswanathan, "Green synthesis of silver nanoparticles using *Polyalthia longifolia* leaf extract along with D-Sorbitol: Study of Antibacterial Activity," *Journal of Nanotechnology*, vol. 2011, Article ID 152970, 5 pages, 2011.
- [23] A. Sereemasapun, P. Hongpiticharoen, R. Rojanathanes, P. Maneewattanapinyo, S. Ekgasit, and W. Warisnoicharoen, "Inhibition of human cytochrome P450 enzymes by metallic nanoparticles: a preliminary to nanogenomics," *International Journal of Pharmacology*, vol. 4, no. 6, pp. 492–495, 2008.
- [24] R. M. Linga and N. Savithamma, "Antimicrobial activity of silver nanoparticles synthesized by using stem extract of *Svensonia hyderabadensis* (Walp.) mold-a rare medicinal plant," *Research in Biotechnology*, vol. 3, no. 3, pp. 41–47, 2012.
- [25] N. Prabhu, T. R. Divya, and G. Yamuna, "Synthesis of silver phyto nanoparticles and their antibacterial efficacy," *Digest Journal of Nanomaterials and Biostructures*, vol. 5, no. 1, pp. 185–189, 2010.
- [26] N. Savithamma, M. Linga Rao, K. Rukmini, and P. Suvarnalatha Devi, "Antimicrobial activity of silver nanoparticles synthesized by using medicinal plants," *International Journal of ChemTech Research*, vol. 3, no. 3, pp. 1394–1402, 2011.

Research Article

Sol-Gel Synthesis of $\text{TiO}_2/\text{SiO}_2$ and ZnO/SiO_2 Composite Films and Evaluation of Their Photocatalytic Activity towards Methyl Green

V. L. Chandraboss, B. Karthikeyan, J. Kamalakkannan, S. Prabha, and S. Senthilvelan

Department of Chemistry, Annamalai University, Annamalai Nagar, Tamil Nadu 608 002, India

Correspondence should be addressed to S. Senthilvelan; dr_senthilvel@yahoo.co.in

Received 31 January 2013; Accepted 2 March 2013

Academic Editor: Amir Kajbafvala

Copyright © 2013 V. L. Chandraboss et al. This is an open access article distributed under the Creative Commons Attribution License, which permits unrestricted use, distribution, and reproduction in any medium, provided the original work is properly cited.

The $\text{TiO}_2/\text{SiO}_2$ and ZnO/SiO_2 composite films were prepared by sol-gel dip coating method. The surface morphology and crystal structure of thin films were characterized by means of scanning electron microscopy (SEM) with elementary dispersive X-ray analysis (EDX) and X-ray diffractometer (XRD). Optical properties of films have been investigated using ultraviolet and visible spectroscopy (UV-visible spectroscopy). The photocatalytic activity was established by testing the degradation and decolorization of methyl green (MG) from aqueous solution with artificial UV-light.

1. Introduction

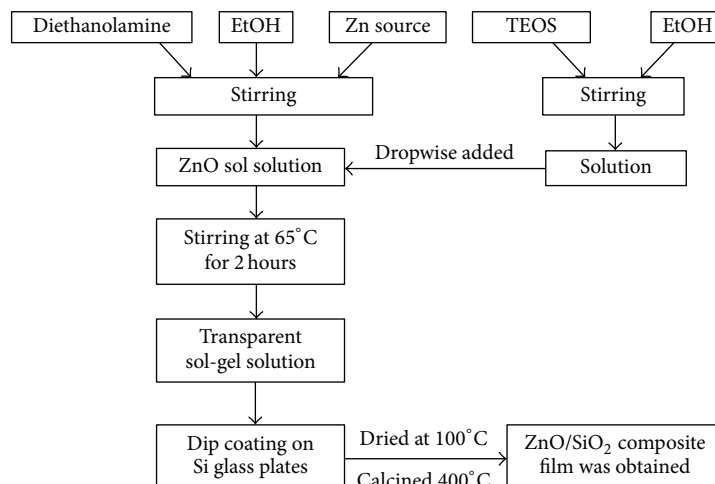
Nanomaterials may provide solutions to scientific and ecological challenges in the areas of catalysis, medicine, solar energy conversion, and water treatment [1, 2]. This increasing demand must be accompanied by “green” synthesis methods. In the global efforts to decrease generated hazardous waste, “green” chemistry and chemical processes are progressively integrating with contemporary developments in science and industry. Implementation of these sustainable processes should adopt the 12 fundamental principles of green chemistry [3]. These principles are gear to guide in minimizing the use of dangerous products and maximizing the efficiency of chemical processes. Hence, any synthetic route or chemical process should address these principles by using environmentally benign solvents and nontoxic chemicals [4].

From a biological and physiological point of view, the removal of poisonous chemicals from waste water is currently one of the most important subjects in pollution control. MG is a basic triphenylmethane-type dicationic dye, usually used for staining solutions in medicine and biology [5] and as a photochromophore to sensitize gelatinous films [6]. Triphenylmethane dyes are used widely in the textile industry

for dyeing of nylon, wool, cotton, and silk as well as for coloring of waxes, varnish, oil, plastics, and fats.

The application of illuminated semiconductors has been effectively working for the decomposition of variety of organic contaminants in water [7]. The major organic compounds that constitute the industrial wastewater include dyes, phenols, chlorophenols, aliphatic alcohols, aromatics, polymers, and carboxylic acids. Among these, toluene, salicylic acid, and 4-chlorophenol have been identified as a water pollutant arising from numerous sources including paper milling, textile, and cosmetic industries [8], causing bad odor to the water. Hence, the destruction of organic compounds is of considerable interest. Over the years, a large number of semiconductors have been utilized as photocatalysts. The most commonly studied photocatalysts are TiO_2 and ZnO [9, 10].

TiO_2 films have been broadly studied in photocatalytic degradation of the dyes, because of their low solubility in wastewater, high oxidation efficiency, ecofriendly properties, and avoiding the need for posttreatment separation in a system. Moreover, the coatings propose a benefit of a strong particle-substrate coupling that allows long-term performance. A variety of methods are obtainable for the preparation of nanostructured TiO_2 -based photocatalytic films,



SCHEME 1: Preparation route of ZnO/SiO₂ composite film.

such as vacuum arc plasma evaporation [11], electrochemical method [12–14], classical and modified sol-gel methods [15–18], and chemical vapor deposition (CVD) [19, 20].

ZnO has a competitive photocatalytic activity (PA) greater in some cases than TiO₂, for example, in the discoloration of Reactive Blue19, a textile anthraquinone dye, in aqueous suspension [21], and in the oxidation of protocatechuic acid [22]. Furthermore, ZnO thin films have been found to decompose aqueous solutions of reactive dyes [23, 24], as well as phenol and chlorophenol [25], and other environmental pollutants [26, 27].

ZnO is available at low cost, which gives it an important advantage. However, the solar UV-light reaching the surface of the earth and available to excited TiO₂ is relatively small (around 4%), and artificial UV-light sources are somewhat expensive. The biggest advantage of ZnO is that it absorbs over a larger fraction of the solar spectrum than TiO₂ [28, 29]. The biggest advantage of ZnO in comparison with TiO₂ is that it absorbs over a larger fraction of UV spectrum and the corresponding threshold of ZnO is 425 nm [30]. For this reason, ZnO is the most suitable photocatalyst for photocatalytic degradation of dyes under UV-light irradiation.

Recently, some researchers synthesized TiO₂, ZnO thin films, and composite materials for photocatalytic activity of some industrial pollutants and dyes [31–34]. In this context our research group has successfully prepared TiO₂/SiO₂ and ZnO/SiO₂ composite films by sol-gel method. Then, the photocatalytic activity of these composites towards is studied.

2. Materials and Methods

2.1. Materials. Zinc acetate dihydrate [Zn(CH₃COO)₂·2H₂O], titanium tetraisopropoxide [Ti(iso-OC₃H₇)₄], tetraethyl orthosilicate [TEOS], methyl green, diethanolamine, and ethanol were purchased and used as such. The aqueous solutions were prepared by using double distilled water. All glassware was cleaned with chromic acid followed by thorough washing with distilled water. Chemical structure of MG is shown in Figure 1.

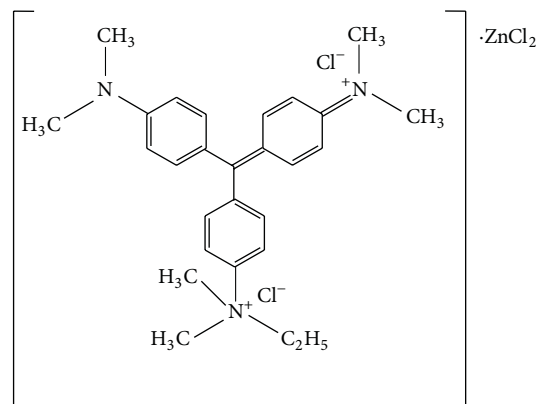


FIGURE 1: Chemical structure of methyl green.

2.2. Preparation of TiO₂/SiO₂ and ZnO/SiO₂ Composite Films.

Initially diethanolamine in ethanol was stirred well and then zinc acetate dihydrate was added to the previous solution (solution I). Tetraethyl orthosilicate dissolved in ethanol is taken as another (solution II). The solution II is added to the solution I and stirred (600 rpm) at 65°C for 2 hour. The dip coating was achieved when cleaned glass plates were gradually immersed into the solution. The films were dried at 100°C for 4 hours to evaporate the solvent and to remove the organic residuals. Finally the films were calcinated at 400°C to get uniform ZnO/SiO₂ composite film (Scheme 1). The above procedure was also carried out for TiO₂-doped SiO₂ film.

2.3. Analytical Methods. Scanning electron microscopy (SEM) with elementary dispersive X-ray analysis (EDX) experiments was carried out on an FEI Quanta FEG 200 instrument with EDX analyzer facility at 25°C. X-ray diffraction (XRD) spectra were recorded on the X'PERT PRO model X-ray diffractometer from Pan Analytical instruments operated at a voltage of 40 kV and a current of 30 mA with Cu K α radiation. UV-visible absorbance spectra were measured over a range of 200–800 nm with a Shimadzu

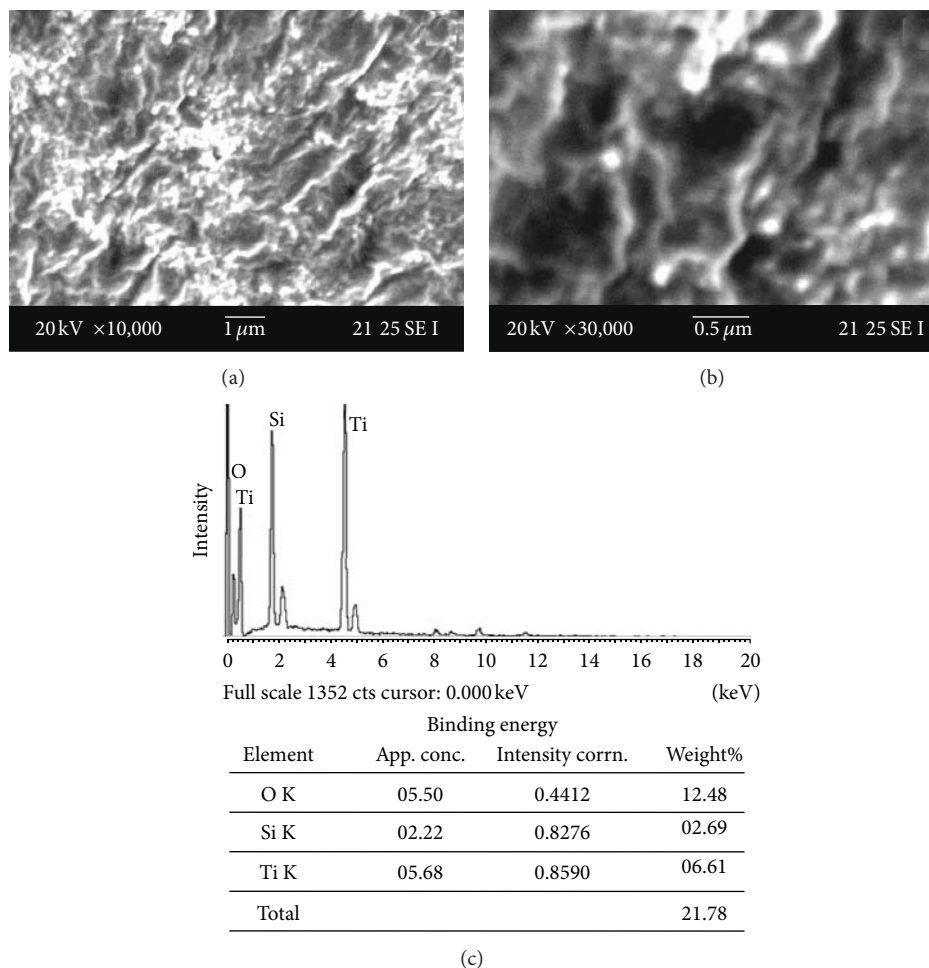


FIGURE 2: SEM images of $\text{TiO}_2/\text{SiO}_2$ composite film with scale bars of (a) $1\ \mu\text{m}$, (b) $0.5\ \mu\text{m}$, and (c) EDX spectrum of $\text{TiO}_2/\text{SiO}_2$ composite film.

UV-1650PC recording spectrometer using a quartz cell with 10 mm of optical path length.

2.4. Photocatalytic Activity. Photocatalytic studies were carried out in a multilamp photoreactor (HML MP88, supplied by Heber Scientific, India) fitted with eight 8 W mercury UV lamps of wavelength 365 nm. The volume of the reaction solution was maintained as 30 mL. Air was bubbled through the reaction solution for effective stirring. The degradation of MG was followed spectrophotometrically. The solution was diluted to keep the absorbance within the Beer-Lambert law limit.

3. Results and Discussion

3.1. Characterization of $\text{TiO}_2/\text{SiO}_2$ and ZnO/SiO_2 Composite Films

3.1.1. SEM with EDX Analysis. The morphology of the $\text{TiO}_2/\text{SiO}_2$ and ZnO/SiO_2 composite films was determined by scanning electron microscopy. Figure 2 shows SEM micrograph of $\text{TiO}_2/\text{SiO}_2$ film annealed at 400°C (scale bars of 1 and $0.5\ \mu\text{m}$)

(Figures 2(a) and 2(b)). EDX analysis confirmed the presence of Ti, Si, and O (Figure 2(c)). Figure 3 shows SEM micrograph of ZnO/SiO_2 film annealed at 400°C (scale bars of 1 and $0.5\ \mu\text{m}$) (Figures 3(a) and 3(b)). EDX analysis confirmed the presence of Zn, Si, and O (Figure 3(c)). Uniform morphology of the prepared composite materials has been confirmed from the previous observation.

3.1.2. XRD Analysis. Figure 4(a) shows XRD of TiO_2 -doped SiO_2 composite film. The peaks at 23.5° , 27.0° , 38.0° , 42.4° , and 48.8° are the diffractions of the TiO_2 (1 0 1), SiO_2 (1 0 1), TiO_2 (1 1 2), SiO_2 (2 0 0), and TiO_2 (2 0 0). The diffractogram consists of broad diffraction peaks of TiO_2 anatase phase (JCPDS file no. 84-1286). Figure 4(b) shows XRD of ZnO -doped SiO_2 composite film. The peaks at 26.5° , 31.7° , 33.3° , 36.0° , 49.4° , and 68.9° are the diffractions of the SiO_2 (1 0 1), ZnO (1 0 0), ZnO (0 0 2), ZnO (1 0 1), SiO_2 (1 1 2), and ZnO (2 0 1). The diffractogram consists of broad diffraction peaks of ZnO (JCPDS file no. 36-1451).

3.1.3. Optical Transmittance Analysis. Optical transmittance spectra of $\text{TiO}_2/\text{SiO}_2$ and ZnO/SiO_2 composite films

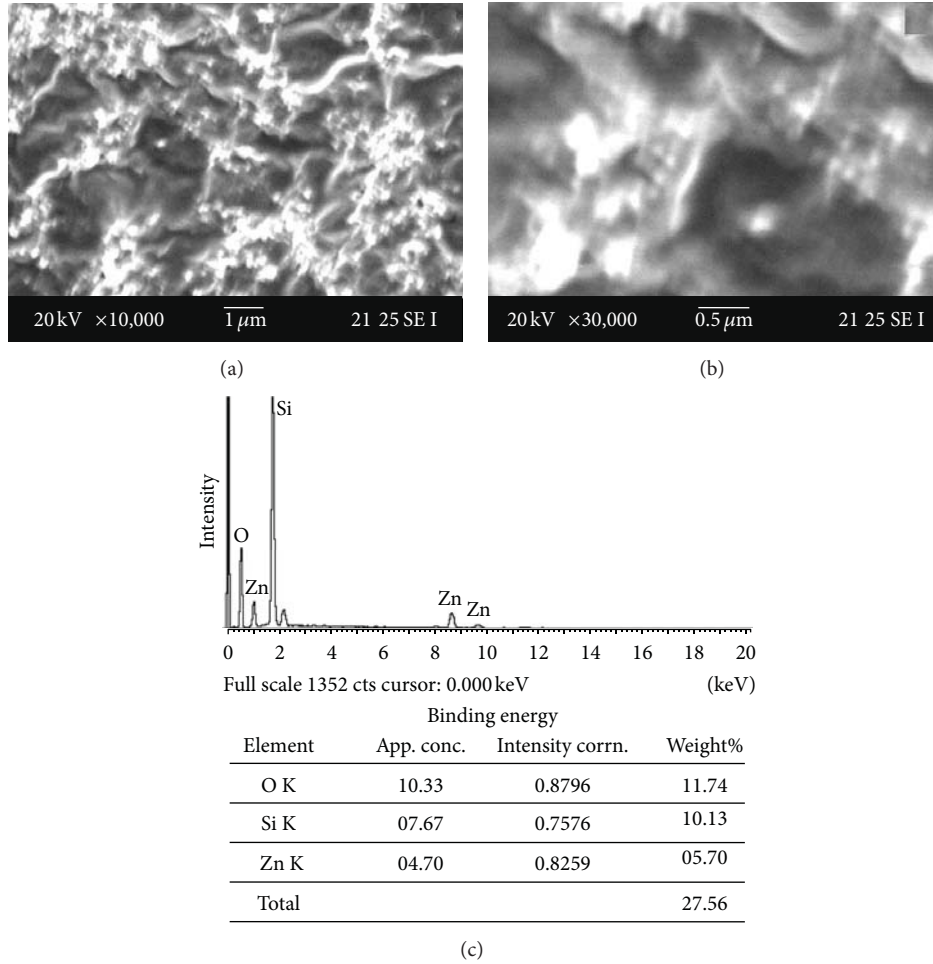


FIGURE 3: SEM images of ZnO/SiO₂ composite film with scale bars of (a) 1 μm, (b) 0.5 μm, and (c) EDX spectrum of ZnO/SiO₂ composite film.

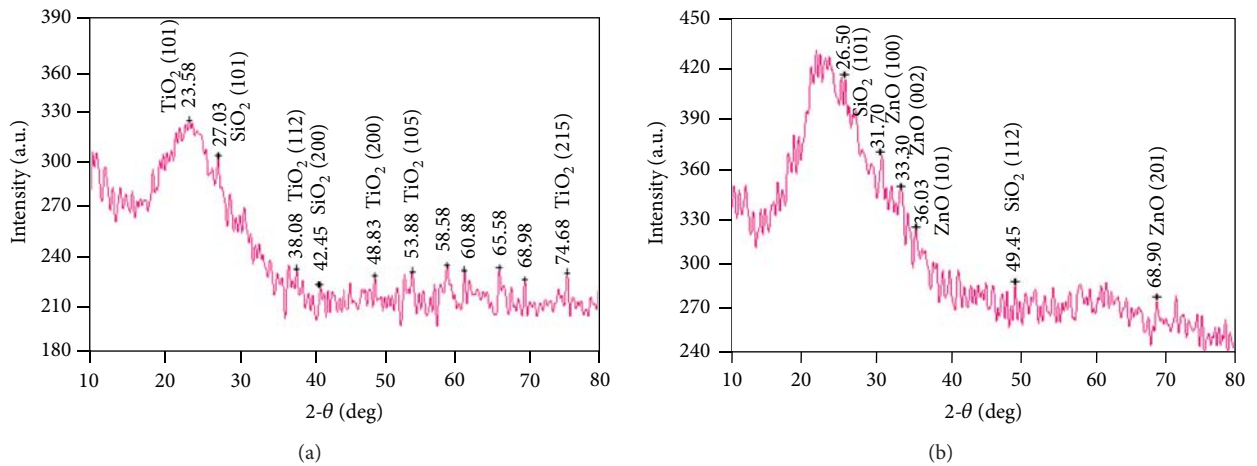


FIGURE 4: XRD amorphous data of (a) TiO₂/SiO₂ composite film and (b) ZnO/SiO₂ composite film.

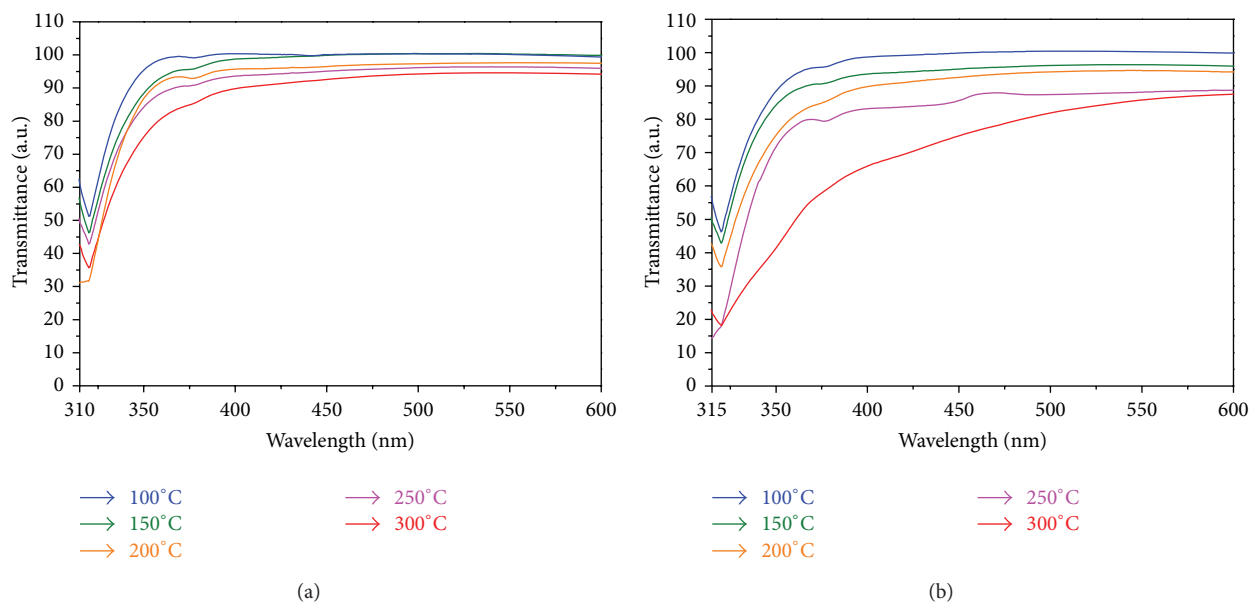


FIGURE 5: Optical transmittance spectra of (a) $\text{TiO}_2/\text{SiO}_2$ composite film and (b) ZnO/SiO_2 composite film.

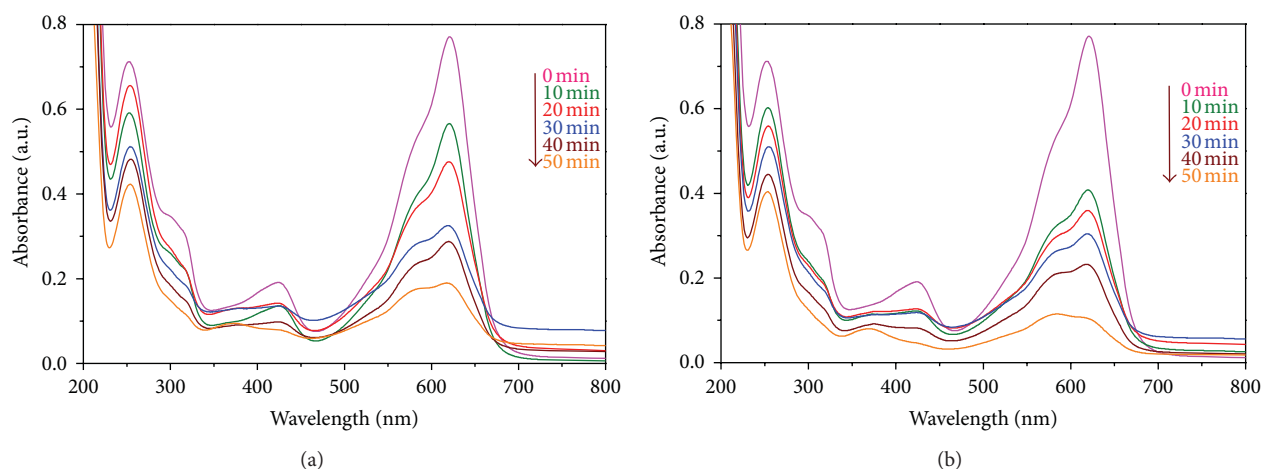


FIGURE 6: UV-visible absorption spectra of methyl green at 10-minute interval: (a) $\text{TiO}_2/\text{SiO}_2$ composite film and (b) ZnO/SiO_2 composite film.

annealed at different temperatures (100°C , 150°C , 200°C , 250°C , and 300°C) are shown in Figure 5. When the films were heated at different temperatures, the transmittance of the films becomes lower as the temperature increases. Transmittance of the ZnO/SiO_2 film was slightly lower than the $\text{TiO}_2/\text{SiO}_2$ with increasing temperature (Figures 5(a) and 5(b)).

3.2. Photodegradation and Decolorization of MG

3.2.1. Photodegradation of Methyl Green with Artificial UV Light. The photodegradation of MG in aqueous medium in the presence of atmospheric air on $\text{TiO}_2/\text{SiO}_2$ and ZnO/SiO_2 composite films was studied using multilamp photoreactor

with mercury UV lamps of wavelength 365 nm . The reference wavelength of MG reaction solution is 630 nm . Initially the dye solution is dark green in color; after the photodegradation and decolorization the color of the solution becomes pale green. The reaction time affords the photodegradation and decolorization of MG.

3.2.2. Photocatalytic Activity of $\text{TiO}_2/\text{SiO}_2$ and ZnO/SiO_2 Composite Films. The absorption spectrum of MG in the presence of $\text{TiO}_2/\text{SiO}_2$ and ZnO/SiO_2 is shown in Figures 6(a) and 6(b), respectively. The absorption spectrum shows the decrease in intensity with respect to time. The rapid decrease in the intensity of ZnO/SiO_2 is noted in the photocatalysis compared with $\text{TiO}_2/\text{SiO}_2$. The enhanced

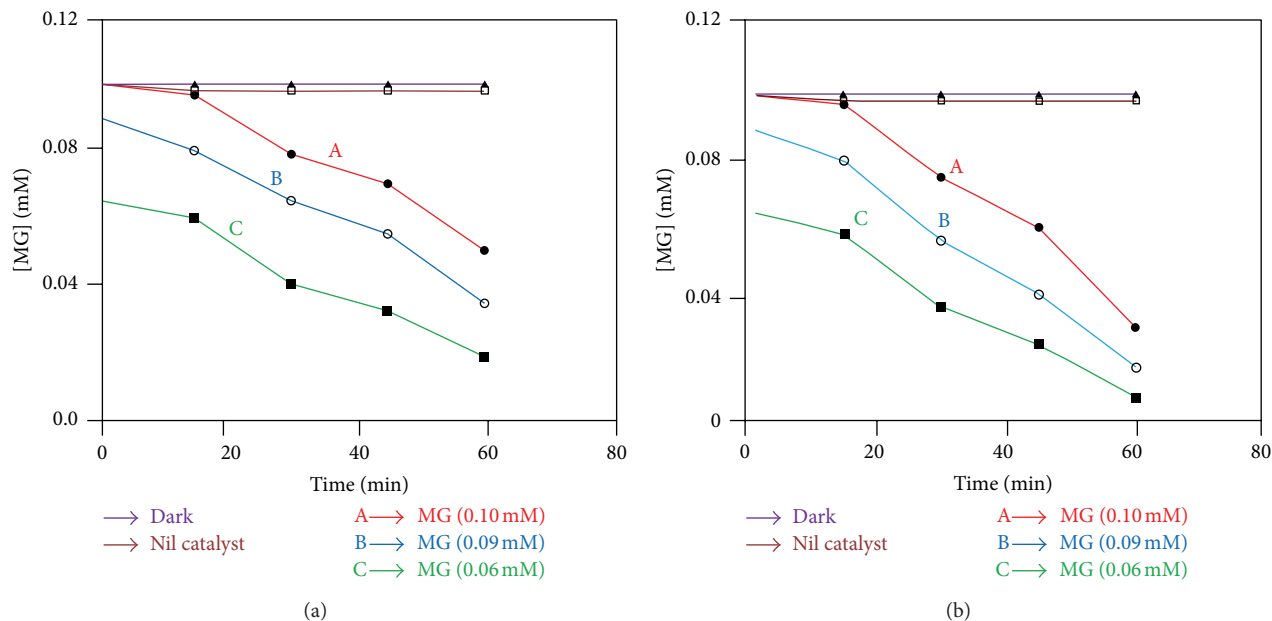


FIGURE 7: Photodegradation at different concentration of methyl green: (a) TiO₂/SiO₂ composite film and (b) ZnO/SiO₂ composite film.

photocatalytic activity shown by ZnO/SiO₂ is compared with TiO₂/SiO₂ composites.

3.2.3. Effect of Dye Concentration. The progress of the photodegradation of MG represents increases with light intensity in the presence of TiO₂/SiO₂ and ZnO/SiO₂ composite films. Different concentrations of MG were prepared and used for the photodegradation process. At lower concentration, the degradation and decolorization of MG are high but at higher concentration, the photocatalytic activity is low (Figure 7). The photodegradation of TiO₂/SiO₂ and ZnO/SiO₂ is shown in Figures 7(a) and 7(b), respectively. From these figures, it is concluded that the degradation efficiency of ZnO/SiO₂ composite film is higher than TiO₂/SiO₂ composites only at lower concentration of MG.

4. Conclusions

TiO₂/SiO₂ and ZnO/SiO₂ composite films were prepared by the sol-gel method. The prepared films were characterized by SEM with EDX, XRD, and optical transmittance studies. TiO₂/SiO₂ and ZnO/SiO₂ films were used for the photodegradation of MG under UV-light irradiation. The photodegradation of MG on TiO₂/SiO₂ and ZnO/SiO₂ composite films in aqueous medium has been studied as a function of dye concentration. ZnO/SiO₂ composite film exhibited reasonable activity under UV-light and had much better activity when compared to that of TiO₂/SiO₂ composite films.

Acknowledgment

S. Senthilvelan is highly thankful to UGC, New Delhi, for granting a major research project (F. no. 39-771/2010(SR)).

References

- [1] J. A. Dahl, B. L. S. Maddux, and J. E. Hutchison, "Toward greener nanosynthesis," *Chemical Reviews*, vol. 107, no. 6, pp. 2228–2269, 2007.
- [2] J. E. Hutchison, "Greener nanoscience: a proactive approach to advancing applications and reducing implications of nanotechnology," *ACS Nano*, vol. 2, no. 3, pp. 395–402, 2008.
- [3] J. M. DeSimone, "Practical approaches to green solvents," *Science*, vol. 297, no. 5582, pp. 799–803, 2002.
- [4] P. Raveendran, J. Fu, and S. L. Wallen, "Completely "Green" synthesis and stabilization of metal nanoparticles," *Journal of the American Chemical Society*, vol. 125, no. 46, pp. 13940–13941, 2003.
- [5] F. J. Green, *The Sigma-Aldrich Handbook of Stains, Dyes, and Indicators*, Aldrich Chemical, Milwaukee, Wis, USA, 1990.
- [6] T. Geethakrishnan and P. K. Palanisamy, "Degenerate four-wave mixing experiments in Methyl green dye-doped gelatin film," *Optik*, vol. 117, no. 6, pp. 282–286, 2006.
- [7] M. A. Behnajady, N. Modirshahla, and R. Hamzavi, "Kinetic study on photocatalytic degradation of C.I. Acid Yellow 23 by ZnO photocatalyst," *Journal of Hazardous Materials*, vol. 133, no. 1–3, pp. 226–232, 2006.
- [8] A. Mills, C. E. Holland, R. H. Davies, and D. Worsely, "Photo mineralization of salicylic acid: a kinetic study," *Journal of Photochemistry and Photobiology A*, vol. 83, pp. 257–263, 1994.
- [9] S. K. Kansal, M. Singh, and D. Sud, "Studies on photodegradation of two commercial dyes in aqueous phase using different photocatalysts," *Journal of Hazardous Materials*, vol. 141, no. 3, pp. 581–590, 2007.
- [10] Y. Wei, Y. Huang, J. Wu et al., "Synthesis of hierarchically structured ZnO spheres by facile methods and their photocatalytic deNO_x properties," *Journal of Hazardous Materials*, vol. 248, pp. 202–210, V.
- [11] T. Miyata, S. Tsukada, and T. Minami, "Preparation of anatase TiO₂ thin films by vacuum arc plasma evaporation," *Thin Solid Films*, vol. 496, no. 1, pp. 136–140, 2006.

- [12] S. Wang, X. Wu, W. Qin, and Z. Jiang, "TiO₂ films prepared by micro-plasma oxidation method for dye-sensitized solar cell," *Electrochimica Acta*, vol. 53, no. 4, pp. 1883–1889, 2007.
- [13] X. H. Wu, Z. H. Jiang, L. H. Liu, X. D. Li, and X. G. Hu, "TiO₂ ceramic films prepared by micro-plasma oxidation method for photodegradation of rhodamine B," *Materials Chemistry and Physics*, vol. 80, no. 1, pp. 39–43, 2003.
- [14] S. Karuppachamy, N. Suzuki, S. Ito, and T. Endo, "Enhanced efficiency of dye sensitized solar cells by UV-O3 treatment of TiO₂ layer," *Current Applied Physics*, vol. 9, pp. 243–248, 2009.
- [15] D. L. Liao, C. A. Badour, and B. Q. Liao, "Preparation of nanosized TiO₂/ZnO composite catalyst and its photocatalytic activity for degradation of methyl orange," *Journal of Photochemistry and Photobiology A*, vol. 194, no. 1, pp. 11–19, 2008.
- [16] X. Zhang and Q. Liu, "Preparation and characterization of titania photocatalyst co-doped with boron, nickel, and cerium," *Materials Letters*, vol. 62, no. 17-18, pp. 2589–2592, 2008.
- [17] L. Andronic and A. Duta, "The influence of TiO₂ powder and film on the photodegradation of methyl orange," *Materials Chemistry and Physics*, vol. 112, no. 3, pp. 1078–1082, 2008.
- [18] I. Stambolova, V. Blaskov, I. N. Kuznetsova, N. Kostova, and S. Vassilev, "Effect of the thermal treatment on the morphology and optical properties of nanosized TiO₂ films," *Journal of Optoelectronics and Advanced Materials*, vol. 13, pp. 381–386, 2011.
- [19] B. H. Kim, J. Y. Lee, Y. H. Choa, M. Higuchi, and N. Mizutani, "The effect of target density and its morphology on TiO₂ thin films," *Materials Science and Engineering B*, vol. 107, pp. 289–294, 2004.
- [20] T. K. Ghorai, D. Dhak, S. K. Biswas, S. Dalai, and P. Pramanik, "Photocatalytic oxidation of organic dyes by nano-sized metal molybdate incorporated titanium dioxide (M_xMo_xTi_{1-x}O₆) (M = Ni, Cu, Zn) photocatalysts," *Journal of Molecular Catalysis A*, vol. 273, no. 1-2, pp. 224–229, 2007.
- [21] I. Poullos, D. Makri, and X. Prohaska, "Photocatalytic treatment of olive milling wastewater: oxidation of protocatechuic acid," *GLOBAL NEST*, vol. 1, pp. 55–62, 1999.
- [22] S. Sakthivel, B. Neppolian, M. V. Shankar, B. Arabindoo, M. Palanichamy, and V. Murugesan, "Solar photocatalytic degradation of azo dye: comparison of photocatalytic efficiency of ZnO and TiO₂," *Solar Energy Materials and Solar Cells*, vol. 77, no. 1, pp. 65–82, 2003.
- [23] C. A. K. Gouvêa, F. Wypych, S. G. Moraes, N. Durán, N. Nagata, and P. Peralta-Zamora, "Semiconductor-assisted photocatalytic degradation of reactive dyes in aqueous solution," *Chemosphere*, vol. 40, no. 4, pp. 433–440, 2000.
- [24] C. Lizama, J. Freer, J. Baeza, and H. D. Mansilla, "Optimized photodegradation of reactive blue 19 on TiO₂ and ZnO suspensions," *Catalysis Today*, vol. 76, no. 2–4, pp. 235–246, 2002.
- [25] S. Lathasree, A. N. Rao, B. Sivasankar, V. Sadasivam, and K. Rengaraj, "Heterogeneous photocatalytic mineralisation of phenols in aqueous solutions," *Journal of Molecular Catalysis A*, vol. 223, no. 1-2, pp. 101–105, 2004.
- [26] L. B. Khalil, W. E. Mourad, and M. W. Rophael, "Photocatalytic reduction of environmental pollutant Cr(VI) over some semiconductors under UV/visible light illumination," *Applied Catalysis B*, vol. 17, no. 3, pp. 267–273, 1998.
- [27] Y. Huang, Y. Wei, J. Wu et al., "Low temperature synthesis and photocatalytic properties of highly oriented ZnO/TiO₂-xNy coupled photocatalysts," *Applied Catalysis B*, vol. 123, pp. 9–17, 2012.
- [28] S. Sakthivel, B. Neppolian, M. Palanichamy, B. Arabindoo, and V. Murugesan, "Photocatalytic degradation of leather dye, Acid green 16 using ZnO in the slurry and thin film forms," *Indian Journal of Chemical Technology*, vol. 6, no. 3, pp. 161–165, 1999.
- [29] I. Poullos and I. Tsachpinis, "Photodegradation of the textile dye Reactive Black 5 in the presence of semiconducting oxides," *Journal of Chemical Technology and Biotechnology*, vol. 74, pp. 349–357, 1999.
- [30] S. S. Shinde, P. S. Shinde, C. H. Bhosale, and K. Y. Rajpure, "Zinc oxide mediated heterogeneous photocatalytic degradation of organic species under solar radiation," *Journal of Photochemistry and Photobiology B*, vol. 104, no. 3, pp. 425–433, 2011.
- [31] I. Stambolova, M. Shipochka, V. Blaskov, A. Loukanovb, and S. Vassilevc, "Sprayed nanostructured TiO₂ films for efficient photocatalytic degradation of textile azo dye," *Journal of Photochemistry and Photobiology B*, vol. 117, pp. 19–26, 2012.
- [32] G. Torres Delgado, C. I. Zúñiga Romero, S. A. Mayén Hernández, R. Castanedo Pérez, and O. Zelaya Angel, "Optical and structural properties of the sol-gel-prepared ZnO thin films and their effect on the photocatalytic activity," *Solar Energy Materials and Solar Cells*, vol. 93, no. 1, pp. 55–59, 2009.
- [33] X. Zhang and H. Zheng, "Synthesis of TiO₂-doped SiO₂ composite films and its applications," *Bulletin of Materials Science*, vol. 32, pp. 787–790, 2008.
- [34] A. Mahyar, M. A. Behnajady, and N. Modirshahla, "Enhanced photocatalytic degradation of C.I. Basic violet 2 using TiO₂-SiO₂ composite nanoparticles," *Photochemistry and Photobiology*, vol. 87, no. 4, pp. 795–801, 2011.

Research Article

Ecofriendly and Facile One-Pot Multicomponent Synthesis of Thiopyrimidines under Microwave Irradiation

Biswa Mohan Sahoo,¹ B. V. V. Ravi Kumar,¹ Jnyanaranjan Panda,¹ and S. C. Dinda²

¹ Department of Medicinal Chemistry, Roland Institute of Pharmaceutical Sciences, Khodasingi, Berhampur 760 010, India

² School of Pharmaceutical Education & Research, Berhampur University, Berhampur 760 007, Odisha, India

Correspondence should be addressed to Biswa Mohan Sahoo; biswamohan81@gmail.com

Received 31 December 2012; Revised 20 February 2013; Accepted 25 February 2013

Academic Editor: Alexander Kauffmann

Copyright © 2013 Biswa Mohan Sahoo et al. This is an open access article distributed under the Creative Commons Attribution License, which permits unrestricted use, distribution, and reproduction in any medium, provided the original work is properly cited.

A rapid, improved, and ecofriendly synthesis of thiopyrimidines is carried out via one-pot multicomponent reaction of ethylcyanoacetate, substituted benzaldehydes, and thiourea in presence of ethanolic K_2CO_3 using microwave irradiation heating method. Excellent yields, shorter reaction time, and easy workup are the major advantageous features of this green protocol. So the application of multicomponent reactions involves the combination of multiple starting materials with different functional groups leading to the highly efficient and environmentally friendly construction of multifunctional drug molecules. The structures of the newly synthesized products were assigned on the basis of IR and ¹HNMR spectral data.

1. Introduction

One-pot multicomponent organic reactions (MCORs) have emerged as an efficient tool for benign synthesis by virtue of their convergence, productivity, facile execution, and generation of highly diverse and complex products from easily available starting materials in a single operation. MCORs are now being tuned for synthesizing various heterocyclic compounds due to their diverse biological activities [1]. The environmental acceptability of the process is improved if the multicomponent strategy is applied under microwave irradiation (MWI) technology [2]. For an organic synthesis, a major adverse effect on the environment is the consumption of energy for heating. To overcome this problem, it is highly desirable to develop suitable methods of heating that use microwave irradiation. So, the synthetic methodologies nowadays should be designed in such a way to use and generate substances that possess little or no toxicity to human health and the environment. Microwave heating provides a valuable tool to perform reactions faster with enhanced product yields with high purity by reducing unwanted formation of byproducts [3]. From an environmental and economic perspective, it is becoming obvious that the traditional

methods of performing chemical synthesis are unsustainable and have to be changed. Multicomponent coupling reactions provide a solution since they are more efficient, cost effective, and less wasteful than traditional methods. The achievement of making multiple bonds in a one-pot multicomponent coupling reaction promotes a sustainable synthetic approach to develop new drug molecule in a drug discovery process.

Microwave (MW) irradiation facilitates better thermal management of chemical reactions. The rapid MW heat transfer allows reactions to be carried out very much faster compared to conventional heating methods often resulting in increased product yield [4, 5]. Furthermore, the products of temperature sensitive reactions from kinetic or thermodynamic pathways can be selectively tuned and isolated. The fundamental mechanism of microwave irradiated synthesis involves agitation of polar molecules or ions that oscillate under the effect of an oscillating electric or magnetic field. In the presence of an oscillating field, particles try to orient themselves or be in phase with the field. Only materials that absorb microwave radiation are relevant to microwave synthesis [6, 7].

These materials can be categorized according to the three main mechanisms of heating such as dipolar polarization,

conduction, and interfacial polarization. In the electromagnetic spectrum, the microwave radiation region is located between infrared radiation and radiowaves. Microwaves have wavelengths of $1\text{ mm} \pm 1\text{ m}$, which corresponds to the frequencies between 0.3 and 300 GHz [8, 9]. Microwave radiation is introduced into the reaction system remotely without direct physical contact with reaction materials, which can lead to a rapid increase in temperature throughout the sample causing less byproducts formation or decomposition of products. Microwave heating is able to heat the target compounds without heating the entire furnace or oil bath, which saves time and energy. In contrast, conventional heating of organic reactions such as oil baths, sand baths, or heating mantles is rather slow and creates an inward temperature gradient, which may result in localized overheating and reagent decomposition when heated for prolonged periods. In conventional heating method, the wall of reactor is heated by convection or conduction. The microwave-assisted organic synthesis has been classified into various categories such as microwave-assisted reactions using solvents, microwave-assisted reactions under solvent-free conditions, microwave-assisted reactions using solid-liquid phase, and microwave-assisted reactions on mineral supports in dry media [10, 11].

Since the multicomponent reactions often create the complete and complex molecular products in a single synthetic step, it is more accepted to describe this modern synthetic procedure as microwave multicomponent synthesis (MMS) [12, 13]. The experimental benefits of generating complex structures from the simple starting materials without engaging protection-deprotection protocols and lengthy product purification procedures improve the synthetic approach for medicinal chemist wishing to contribute products to a more scientifically innovative society [14]. The previous facts prompted us to synthesize thiopyrimidines via one-pot multicomponent reaction of ethylcyanoacetate, substituted benzaldehydes, and thiourea in presence of ethanolic K_2CO_3 using microwave irradiation heating method [15–18]. Generally the one-pot multicomponent synthesis of thiopyrimidines follows the principle of Biginelli reaction protocol [19, 20].

2. Experimental Method

2.1. Materials. The melting points were taken in open capillaries and are uncorrected. The purity of the compounds was checked by TLC on precoated silica gel-aluminum plates and visualized by exposure to UV light (254 nm) or iodine vapor. The IR spectra of the compounds were recorded on FT-IR Spectrophotometer, IR Affinity-1 (SHIMADZU), using potassium bromide (KBr) powder and the values are expressed in cm^{-1} . $^1\text{H-NMR}$ spectra of selected compounds were recorded on multinuclear FT-NMR Spectrometer, Advance-II (Bruker) (at 400 MHz), using tetramethylsilane [$\text{Si}(\text{CH}_3)_4$] as an internal standard. The microwave irradiated synthesis was performed in scientific microwave oven (Catalyst System, Model No-CATA 2R). All the reactions were carried out at power level-2, which corresponds to 210 W.

2.2. Chemistry. Multicomponent reactions (MCRs) constitute a highly valuable synthetic tool for the construction of polyfunctionalized heterocyclic compounds. Thus, a series of thiopyrimidine derivatives was synthesized based on multicomponent reaction (MCR) which involves one-pot organic reactions [21, 22]. This reaction involves two mechanisms such as Knoevenagel condensation and Michael addition. First various substituted benzaldehydes ($\text{RC}_6\text{H}_4\text{CHO}$) react with ethylcyanoacetate ($\text{NCCH}_2\text{COOC}_2\text{H}_5$) in presence of ethanolic K_2CO_3 to produce an intermediate by Knoevenagel condensation reaction. Then the intermediate reacts with thiourea [$\text{SC}(\text{NH}_2)_2$] via Michael addition to produce thiopyrimidines as depicted in Scheme 1.

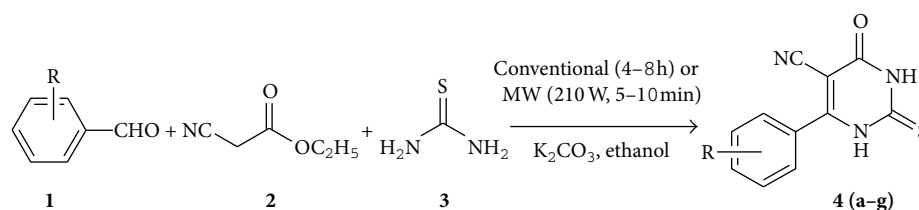
2.3. Synthesis of Thiopyrimidines

2.3.1. Conventional Method. A mixture of appropriate substituted benzaldehydes ($\text{RC}_6\text{H}_4\text{CHO}$) (0.03 mole), ethylcyanoacetate ($\text{NCCH}_2\text{COOC}_2\text{H}_5$) (0.03 mole, 3.39 g), and thiourea [$\text{SC}(\text{NH}_2)_2$] (0.03 mole, 2.28 g) in ethanol ($\text{C}_2\text{H}_5\text{OH}$) (25 mL) containing potassium carbonate (K_2CO_3) (0.03 mole, 4.15 g) was taken and refluxed for 4–8 h on a water bath. The completion of reaction was monitored by TLC. The potassium salt of compound **4(a–g)**, which precipitated during the reaction, was poured into cold water and acidified with glacial acetic acid (CH_3COOH). The precipitate was filtered out, dried, and recrystallized from ethanol ($\text{C}_2\text{H}_5\text{OH}$).

2.3.2. Microwave-assisted Method. Required quantity of reactants and catalysts as mentioned previously was taken and refluxed under microwave irradiation for 5–10 min at power level-2 (210 W). The completion of reaction was monitored by TLC. The potassium salt of compound **4(a–g)**, which precipitated during the reaction, was poured into cold water and acidified with glacial acetic acid (CH_3COOH). The precipitate was filtered out, dried, and recrystallized from ethanol.

3. Results and Discussion

In the present study, thiopyrimidine derivatives were synthesized by both conventional and microwave techniques. As compared to conventional method, microwave synthesis provides higher yield in lesser reaction time. From the results as summarized in Table 1, it can be observed that in case of conventional method of heating, the reactants are slowly activated by a conventional external heating source (water bath). Heat is driven into the reacting substances, passing first through the walls of the vessel in order to reach the solvent and the reactants. So, this is a slow method for transferring heat energy into the reaction medium. Hence, for the synthesis of the titled compounds of present work, which takes 4–8 h to complete the reaction. While considering microwave synthesis, microwaves couple directly with the reacting molecules of reaction mixture, leading to a rapid rise in the temperature. Since this process is not limited by the thermal conductivity of the vessel, the



SCHEME 1: Synthetic route of the titled compounds 4(a-g).



FIGURE 1: Photographs displaying microwave irradiated synthesis of titled compounds.

result is an instantaneous localized superheating of reacting substances that will respond to either dipole rotation or ionic conduction. Since the ability of a molecule to couple with the microwave radiation is a function of its molecular polarisability (i.e., a function of its dipole moment), only polar molecules interact with microwave energy. As a part of ongoing research of developing environmentally benign synthesis of thiopyrimidine derivatives, we explored a green multicomponent reaction (MCR) protocol using ethanol as solvent. Three component reactions such as the Biginelli reaction with ethylcyanoacetate, substituted benzaldehydes, and thiourea are well-known microwave-induced reactions (MW). Here an attempt was also made to carry out the synthesis of thiopyrimidine by microwave at power level-1 (140 W) but this energy was not sufficient to complete the reaction for getting final product. For the investigation of the optimized reaction condition, it was observed that the synthesis of target compounds by microwave required 5–10 min at power level-2 which corresponds to the energy of 210 W. The photograph of microwave irradiated synthesis of titled compounds was given in Figure 1. During synthesis, thin layer chromatographic (TLC) study was carried out to monitor the completion of reaction using chloroform : ethyl acetate (60 : 40) as the mobile phase. The retention factor (R_f) of the synthesized compounds was in the range of 0.32–0.51. The melting points of the synthesized compounds were also checked and the results were given in Table 2. All the synthesized compounds are solid, white, crystalline,

or amorphous. The photographs of some of the synthesized compounds were given in Figure 2. Most of the compounds are freely soluble in CH_3OH , $\text{C}_2\text{H}_5\text{OH}$, CH_2Cl_2 , $(\text{CH}_3)_2\text{SO}$, $(\text{CH}_3)_2\text{NC(O)H}$. The compounds were analyzed by IR and $^1\text{H-NMR}$ spectra. All the compounds showed an IR absorption band at a region $3410\text{--}3525\text{ cm}^{-1}$ which corresponds to the asymmetric stretching of 2^0-NH group. They also showed the IR absorption band in the regions of $3150\text{--}3030\text{ cm}^{-1}$, $2235\text{--}2198\text{ cm}^{-1}$, $1795\text{--}1693\text{ cm}^{-1}$, $1640\text{--}1590\text{ cm}^{-1}$, $1450\text{--}1530\text{ cm}^{-1}$, and $1380\text{--}1270\text{ cm}^{-1}$ for different groups like (Ar-H Str.), (CN Str.), (C=O Str.), (C=C Str.), (Sec. N-H def.), and (C-N str.) vibration, respectively. The halogenated derivatives showed the IR absorption bands in the regions $900\text{--}1100\text{ cm}^{-1}$, $755\text{--}780\text{ cm}^{-1}$, and $495\text{--}585\text{ cm}^{-1}$ corresponds to (C-F str.), and (C-Cl str.), (C-Br str.) vibrations respectively. The IR absorption band in the region $1230\text{--}1255\text{ cm}^{-1}$ which corresponds to the C=S str. vibration. The $^1\text{H-NMR}$ spectra showed two singlets in the range $\delta\ 8.00\text{--}8.30\text{ ppm}$ due to -NH proton. They also showed the signals at $\delta\ 7.46\text{--}7.91\text{ ppm}$ due to aromatic proton (Ar-H).

4. Conclusion

A new series of thiopyrimidine derivatives was synthesized successfully by both conventional and microwave irradiated methods to compare the reaction time and yield of the compounds. With the help of microwave synthesis, the yield of product increased from 55% up to 85% as compared to



FIGURE 2: Photographs displaying some of the synthesized compounds by microwave irradiation method.

conventional synthesis. And also the reaction time is reduced from 4–8 h to 5–10 min. Microwave synthesis reduced the formation of waste and byproduct. This is particularly relevant for high energy heterocyclic reactions. The predominant use of protic solvents leads to quicker, greener, and therefore more environmentally friendly reaction. The application of MW irradiation technology in MMS significantly enhanced the synthetic yield of thiopyrimidine obtained by consecutive Knoevenagel and Michael addition reactions performed on a

mixture of substituted benzaldehydes, ethylcyanoacetate, and thiourea. MCRs have been proved as simple and convenient ways to produce a plethora of physiologically active thiopyrimidines. The strategy of MCR has been developed to enable the rapid construction of diverse structures from starting materials in a single operation. Multicomponent reactions are economically and environmentally very advantageous because multistep syntheses produce considerable amounts of waste mainly due to complex isolation procedures often

TABLE 1: Comparative data on reaction time, heating energy, and yield of compounds 4(a-g) by conventional and microwave assisted synthesis.

Compound code	Conventional synthesis			Microwave synthesis		
	Time (h)	Energy (temp. °C)	Yield (%)	Time (min.)	Energy (power. watt)	Yield (%)
4a	4	98–100	66	5	210	85
4b	6	98–100	65	10	210	85
4c	5	98–100	62	7	210	82
4d	8	98–100	60	9	210	79
4e	6	98–100	61	6	210	82
4f	7	98–100	55	8	210	78
4g	6	98–100	59	7	210	80

TABLE 2: Melting point and TLC report of synthesized compounds 4(a-g).

4 (a-g)

Comp. code	R	M.F	M.W.	mp (°C)	R _f
4a	H	C ₁₁ H ₇ N ₃ OS	229.25	285–287	0.36
4b	-4F	C ₁₁ H ₆ FN ₃ OS	247.24	195–197	0.37
4c	-2Cl	C ₁₁ H ₆ ClN ₃ OS	263.70	185–187	0.51
4d	-3Cl	C ₁₁ H ₆ ClN ₃ OS	263.70	275–276	0.37
4e	-4Cl	C ₁₁ H ₆ ClN ₃ OS	263.70	205–207	0.32
4f	-3Br	C ₁₁ H ₆ BrN ₃ OS	308.15	250–252	0.35
4g	-4Br	C ₁₁ H ₆ BrN ₃ OS	308.15	242–244	0.40

involving expensive, toxic, and hazardous solvents after each step. Thus, MCRs are suited for synthesis of compound libraries and are considered as an important tool during the developmental process of new drugs.

Acknowledgments

The authors are very much thankful to Roland Institute of Pharmaceutical Sciences, Berhampur, and School of Pharmaceutical Education & Research, Berhampur University, Odisha, for providing necessary facilities to carry out the research work. The authors are also thankful to SAIF, Panjab University Chandigarh, for spectral analysis of synthesized compounds.

References

- [1] M. C. Bagley and M. C. Lubinu, "Microwave-assisted multicomponent reactions for the synthesis of heterocycles," *Journal of Heterocyclic Chemistry*, vol. 1, pp. 31–58, 2006.
- [2] S. Ravichandran and E. Karthikeyan, "Microwave synthesis—a potential tool for green chemistry," *International Journal of ChemTech Research*, vol. 3, no. 1, pp. 466–470, 2011.
- [3] M. Charde, A. Shukla, V. Bukhariya, J. Mehta, and R. Chakole, "A review on: a significance of microwave assist technique in green chemistry," *International Journal of Phytopharmacy*, vol. 2, no. 2, pp. 39–50, 2012.
- [4] B. S. Sekhon, "Microwave-assisted pharmaceutical synthesis: an overview," *International Journal of PharmTech Research*, vol. 2, no. 1, pp. 827–833, 2010.
- [5] M. A. Surati, S. Jauhari, and K. R. Desai, "A brief review: microwave assisted organic reaction," *Archives of Applied Science Research*, vol. 4, no. 1, pp. 645–661, 2012.
- [6] P. Lidström, J. Tierney, B. Wathey, and J. Westman, "Microwave assisted organic synthesis—a review," *Tetrahedron*, vol. 57, no. 45, pp. 9225–9283, 2001.
- [7] A. Loupy, *Microwaves in Organic Synthesis*, Wiley-VCH, Weinheim, Germany, 2006.
- [8] C. O. Kappe, "Controlled microwave heating in modern organic synthesis," *Angewandte Chemie International Edition*, vol. 43, no. 46, pp. 6250–6284, 2004.
- [9] F. R. Alexandre, L. Domon, S. Frère, A. Testard, V. Thiéry, and T. Besson, "Microwaves in drug discovery and multi-step synthesis," *Molecular Diversity*, vol. 7, no. 2–4, pp. 273–280, 2003.
- [10] S. Caddick and R. Fitzmaurice, "Microwave enhanced synthesis," *Tetrahedron*, vol. 65, no. 17, pp. 3325–3355, 2009.

- [11] A. Madhvi, S. J. Surati, and K. R. Desai, "A brief review: microwave assisted organic reaction," *Archives of Applied Science Research*, vol. 4, no. 1, pp. 645–661, 2012.
- [12] H. M. Hugel, "Microwave multicomponent synthesis," *Molecules*, vol. 14, no. 12, pp. 4936–4972, 2009.
- [13] J. L. Krstenansky and L. Cotterill, "Recent advances in microwave-assisted organic syntheses," *Current Opinion in Drug Discovery and Development*, vol. 3, no. 4, pp. 454–461, 2000.
- [14] M. Borisagar, K. Joshi, H. Ram, K. Vyas, and K. Nimavat, "A one-pot microwave irradiation synthesis of 1,2,4-triazolo[1,5-A]pyrimidines," *Acta Chimica & Pharmaceutica Indica*, vol. 2, no. 2, pp. 101–105, 2012.
- [15] A. Kruithof, E. Ruijter, and V. A. Orru, "Microwave-assisted multicomponent synthesis of heterocycles," *Current Organic Chemistry*, vol. 15, no. 2, pp. 204–236, 2011.
- [16] S. J. Vaghasia and V. H. Shah, "Microwave assisted synthesis and antimicrobial activity of some novel pyrimidine derivatives," *Journal of the Serbian Chemical Society*, vol. 72, no. 2, pp. 109–117, 2007.
- [17] J. M. Gajera and S. N. Tondlekar, "A novel and one-pot synthesis of 6-arylpyrimidin-4-ol," *Research Letters in Organic Chemistry*, pp. 1–3, 2008.
- [18] N. Agarwal, P. Srivastava, S. K. Raghuwanshi et al., "Chloropyrimidines as a new class of antimicrobial agents," *Bioorganic and Medicinal Chemistry*, vol. 10, no. 4, pp. 869–874, 2002.
- [19] K. Singh, K. Singh, B. Wan, S. Franzblau, K. Chibale, and J. Balzarini, "Facile transformation of Biginelli pyrimidin-2(1H)-ones to pyrimidines. In vitro evaluation as inhibitors of *Mycobacterium tuberculosis* and modulators of cytostatic activity," *European Journal of Medicinal Chemistry*, vol. 46, no. 6, pp. 2290–2294, 2011.
- [20] C. O. Kappe, "A reexamination of the mechanism of the Biginelli dihydropyrimidine synthesis. Support for an N-acyliminium ion intermediate," *Journal of Organic Chemistry*, vol. 62, no. 21, pp. 7201–7204, 1997.
- [21] M. Kidwai, K. Singhal, and S. Kukreja, "One-pot green synthesis for pyrimido[4,5-d]pyrimidine derivatives," *Zeitschrift fur Naturforschung*, vol. 62, no. 5, pp. 732–736, 2007.
- [22] A. H. Kategaonkar, S. A. Sadaphal, K. F. Shelke, B. B. Shingate, and M. S. Shingare, "Microwave assisted synthesis of pyrimido[4,5-d]pyrimidine derivatives in dry media," *Ukrainica Bioorganica Acta*, vol. 1, pp. 3–7, 2009.

Research Article

Electrochemical Method for Ag-PEG Nanoparticles Synthesis

M. Virginia Roldán, Nora Pellegrini, and Oscar de Sanctis

Laboratorio de Materiales Cerámicos, FCElyA, IFIR, Universidad Nacional de Rosario (UNR), Avenida Pellegrini 250, S2000BTP Rosario, Argentina

Correspondence should be addressed to M. Virginia Roldán; vroldan@fceia.unr.edu.ar

Received 29 January 2013; Accepted 15 March 2013

Academic Editor: Mohammad H. Maneshian

Copyright © 2013 M. Virginia Roldán et al. This is an open access article distributed under the Creative Commons Attribution License, which permits unrestricted use, distribution, and reproduction in any medium, provided the original work is properly cited.

In this work we present an electrochemical method to successfully prepare silver nanoparticles using only polyethylene glycol as stabilizer and without any other reactive. Here we study the use of the polymeric stabilizer to allow the introduction of a potential tool to reinforce the control of the size and shape of the nanoparticles throughout the synthesis process. The evolution of the reactions was followed by UV-Vis spectroscopy. The electrode processes were characterized by cyclic voltammetric measurements and the final product was studied by Atomic Force Microscopy, Transmission Electron Microscopy, and X-Ray Diffraction. The influences of the current density, polymer length, and concentration media were analyzed.

1. Introduction

Noble metal nanoparticles have been intensely investigated due to their amazing properties such as optical, catalytic, and electric ones that can be controlled depending on the particles size, the size distribution, and shape [1]. Metallic silver particles in particular are technologically important because they show unique properties normally related to noble metals (excellent conductivity [2], chemical stability, nonlinear optical behavior [3, 4], etc.) besides other specific ones (catalytic activity [5], antibacterial action [6]). These characteristics make them suitable for a variety of potential applications on several devices [7–9].

Several methods have been reported for Ag nanoparticles synthesis, including Ag ions chemical reduction in aqueous solutions with or without stabilizing agents [10–13], thermal decomposition in organic solvents [14, 15], biochemical reduction [16, 17], chemical and photo reduction in reverse micelles [18–20], “nanosphere lithography” (NSL) [21], electrochemical reduction [22–27], irradiation reduction [28], microwave assisted [29–31] and chemical reduction in nonaqueous solvents with surface modifiers [32, 33]. Each method has typical advantages and disadvantages.

Particularly, the electrochemical techniques are quite interesting because they allow obtaining particles with a high purity using fast and simple procedures and controlling the

particle size easily by adjusting the current density [22, 23]. Through these techniques particles have been obtained with determined size and shape [24, 25] of several compositions [26, 27, 34–36]. Also, this method is eco-friendly because it avoids the use of reducer agents that usually are toxic.

Different stabilizers have been used in electrochemical techniques, which include organic monomers as electrostatic stabilizers [26] and polymeric compounds as steric stabilizers [37]. Ionic organic compounds can act as stabilizers and support electrolytes simultaneously avoiding the use of additional chemicals [26]. However, some authors showed that steric stabilizers allow obtaining more stable nanoparticles than electrostatic stabilizers [38]. Also, chemical reduction techniques assisted by polymers allow controlling the shape and size of nanoparticles by changing the polymer chain length [39, 40]. On the other hand, some authors showed that polyethylene glycol-stabilized silver nanoparticles are highly stable and sufficiently permeable to allow the diffusion of small molecules [41]. Thus, they are useful to several applications as Surface-enhanced Raman Scattering techniques and others. Then, we propose the use of the polymeric stabilizer polyethylene glycol to obtain stable nanoparticles and we study their ability to control the nanoparticles morphology.

In this work we present an electrochemical method to prepare silver nanoparticles using polyethylene glycol as stabilizer. We study the effect of the stabilizer concentration,

polymer chain length, and current density over the particle size and shape. These are common strategies for the control of the particle morphology, but they have dissimilar behavior at different systems, mainly the stabilizer concentration. Also, the use of a polymeric stabilizer allows the introduction of a potential tool to reinforce the control of the size and shape of the nanoparticles by using different polymer chains lengths and so we study this strategy too.

2. Experimental Section

2.1. Electrochemical Synthesis of Silver Nanoparticles. Silver nanoparticles were prepared by electrochemical reduction within a simple two-electrode type cell. The volume of the electrolysis cell was 50 ml. A platinum sheet (0.5×7 cm) was employed as cathode and a platinum rod (0.1×7 cm) as anode, the two being 3 cm apart. The cell was maintained into an ultrasonic bath. Silver nitrate (AgNO_3 , Merck) was used as silver ion precursor and polyethylene glycol (PEG, Aldrich) with different chains lengths $M_w = 400$ (PEG-400), 600 (PEG-600), 1450 (PEG-1450), 2000 (PEG-2000), and 6000 (PEG-6000) which was employed as stabilizing agent.

In a typical synthesis, the reaction medium was prepared to obtain an aqueous solution of silver nitrate 2.5 mM with 0.5 to 2% w/v of PEG. The solution was mixed and purged with N_2 during 20 minutes. Then, the electrolysis was carried out under ultrasonication at constant current and N_2 atmosphere during 30 minutes. The current chosen (7 mA, 10 mA, or 13 mA) was given by adjusting the applied potential.

2.2. Characterization of Silver Nanoparticles. In order to study the optical behavior of silver colloid, ultraviolet-visible (UV-Vis) absorption spectra of different samples were recorded by a Jasco V-530 UV-Vis spectrophotometer using as reference a corresponding blank sample.

The shapes and sizes of the nanoparticles were determined by Atomic Force Microscopy (AFM) and Transmission Electron Microscopy (TEM). AFM images were taken using NanoTec ELECTRONICA equipment in tapping mode configuration with a Si_3N_4 tip in air at room temperature. In order to prepare the sample for the AFM study, the particles were redissolved in ethanol and drop-cast onto a freshly peeled HOPG substrate. TEM images were taken with Philips EM 301 equipment. Samples were prepared by placing a drop over a TEM grid and leaving it to evaporate the solvent. To study the crystalline structure of the nanoparticles, X-ray Diffraction patterns were recorded by grazing incidence with a 2° incidence angle with an X'Pert Phillips PW 1700 diffractometer using CuK radiation (1.5405 \AA) and a graphite monochromator (the step size was of $2\theta = 0.2^\circ$; 10 s/step) for samples prepared over SiO_2 by drop-cast.

The cyclic voltammetric measurements (CV) were performed with an EG&G potentiostat/galvanostat in a conventional three-electrode cell at room temperature. A platinum rod embedded in epoxy resin was used as a working electrode and only its cross section was allowed to contact the electrolytes; a platinum microelectrode and a saturated

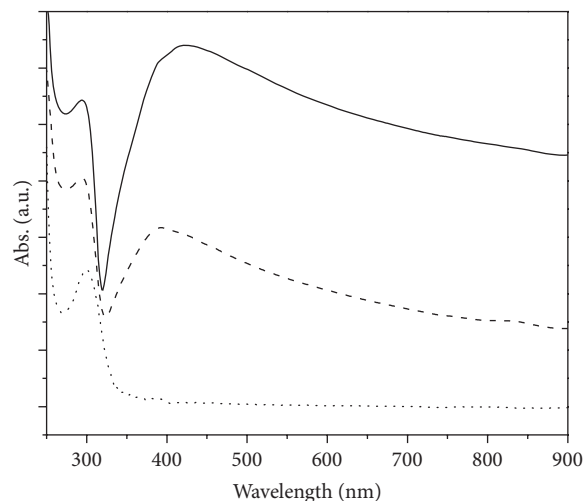


FIGURE 1: Absorption spectra of silver nanoparticles prepared using PEG-2000 at a concentration of 1% w/v with a current equal to 10 mA. Initial spectrum (dotted line) and spectra after 15 (dashed line) and 30 minutes of reaction (solid line).

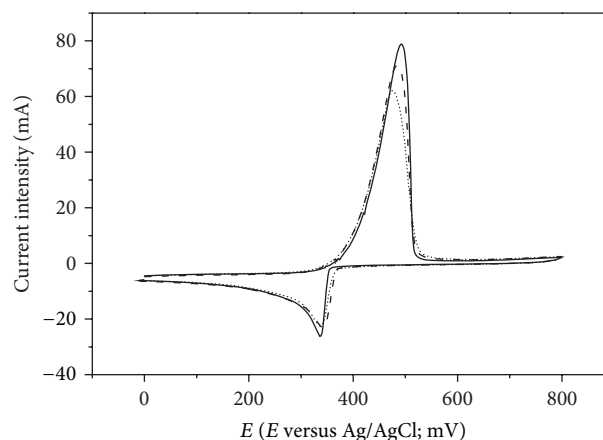


FIGURE 2: Cyclic voltammograms of 2.5 mM AgNO_3 aqueous solutions with 1% w/v (dashed line), 2% w/v (dotted line), and without PEG-2000 (solid line).

Ag/AgCl electrode were used as the auxiliary electrode and the reference electrode, respectively.

3. Results and Discussion

3.1. Characterization of the Reaction Progress. The reaction mixture was characterized in different stages of the reaction progress by UV-Vis spectroscopy. Figure 1 shows the evolution of the optical properties for silver nanoparticles prepared by electrochemical reduction using PEG-2000 as stabilizer at a concentration of 1% w/v and applying a current equal to 10 mA. At the initial time, the absorption spectrum exhibits a single shoulder at a wavelength near to 300 nm, which was attributed to ions NO_3^- in aqueous solution [42] with a lower contribution of Ag^+ [43]. After 15 minutes of reaction, a broad band appeared at 392 nm and its intensity increased until an

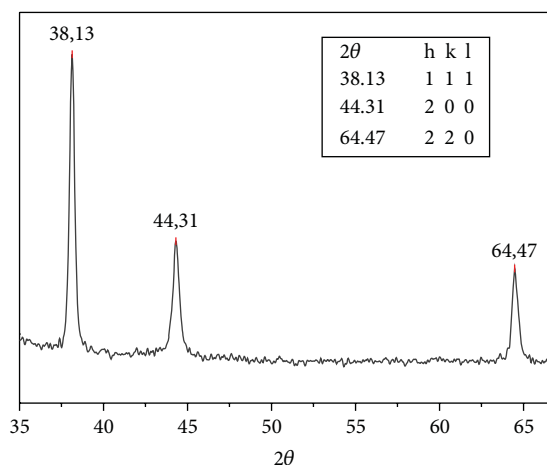


FIGURE 3: X-Ray Diffraction pattern of silver nanoparticles. The principal position peaks are shown in the figure.

absorption maximum centered at 425 nm which was obtained after 30 minutes of reaction. This latter absorption band corresponds to the surface plasmon resonance of spherical silver nanoparticles [44]. An absorption minimum appears at 320 nm, which corresponds to a minimum in the imaginary part of the refractive index for bulk silver [45]. In a control experiment a similar solution was placed in the ultrasonic bath with nitrogen atmosphere, but no one current was applied. After 50 minutes no spectral change was observed (not shown here); then reducing action by PEG-2000 was ruled out in these conditions.

In the electrochemical synthesis of silver nanoparticles, there is a competition between two different cathode surface processes: the silver particle formation and the silver deposition on cathode [46]. The key to electrochemical synthesis of silver nanoparticles in aqueous medium is to avoid formation of silver plating and to force reduced particles to leave the cathode surface. In order to test the PEG influence over these processes, CV experiments were carried out [37]. Figure 2 shows the CV in silver nitrate solutions with different amounts of PEG. All CV experiments present one reduction peak near 337.4 mV and one oxidation peak near 492.0 mV approximately. The reduction peak is attributed to silver ions reduction and their electrodeposition on the platinum surface; the oxidation peak is related to oxidation of the silver electrodeposition on the electrode [42]. CV show that the reduction peak intensity is the same for all the cases. The oxidation peak intensity decreases when the PEG amount increases and this is attributed to the PEG influence over the electrode processes. In the PEG-free solution the reduced silver was almost completely deposited on the surface of working electrode and then, when the scan was swept in the oxidation sense, almost all the reduced silver was oxidized. On the other hand, in the PEG containing solution, the silver ions reduced were divided: a part was deposited on the electrode surface whereas another part was reduced to nanoparticles and stabilized by PEG. Thus, when the scan was swept in the oxidation sense, only the deposited silver was oxidized again. So, CV results show that PEG

effectively enhances the nanoparticles formation and reduces the electrodeposition on the electrode surface.

3.2. Characterization of Silver Nanoparticles. The nanoparticles were characterized by XRD, AFM microscopy, and UV-Vis spectroscopy. In Figure 3 the XRD pattern of nanoparticles, is shown where three distinct diffraction peaks were observed at 2θ values of 38.13° , 44.31° , and 64.47° , corresponding to the (111), (200), and (220) crystalline planes of cubic Ag, respectively. The broad nature of the XRD peaks is attributed to the nanosize of the particles [47].

In order to determine the size and shape of the particles, AFM images were registered. Figure 4 shows a typical AFM image. The particles are uniformly spherical in shape with an average diameter of 30.36 nm. The average diameter was determined by statistical analysis from histograms of several AFM images of the nanoparticles. This average diameter is near to the value obtained from the XRD spectrum. An average nanoparticle size of 45.85 nm was calculated from the breadth of (111) diffraction line at its half-intensity (Figure 3), with an instrumental broadening of 0.25° , using the Scherrer equation [48]. If we compare the mean sizes of the Ag nanoparticles estimated by microscopic technique and XRD, it seems that the Scherrer calculus overestimated the radius. This fact is due to the fact that the sample is polydisperse and the XRD is particularly sensitive to the largest particles or crystallites [49]; then, this result seems to be reasonable.

TEM images (Figure 5) show mainly spherical particles between 10 and 30 nm of size and a few nanospheres bigger, with diameter of 200 nm approximately. These last ones would be responsible for the dispersion effect that is observed as a mild decline of the signal towards longer wavelengths in the UV-Vis extinction spectra.

Furthermore, the morphological characteristics of the particles during different experiments stages were followed by the study of the UV-Vis spectra taking into account the knowing relations between the number and position of the absorption bands and the size and shape of the particles [50]. In silver nanospheres with diameter shorter than 100 nm only one peak in the UV-Vis spectra is observed between 400 and 500 nm [51].

In metallic nanoparticles, the size dependence of the surface plasmon absorption is not easily explained as in the case of semiconductor nanoparticles, where a blue shift or a red shift of the absorption onset undoubtedly results from decreasing size or increasing size, respectively.

The peak position of surface resonance is not well suited for discussion of size effect within the intrinsic size region in metallic nanoparticles [52]. However, the size dependence of the optical spectra of large nanoparticles ($2R > 25$ nm) is an extrinsic particle-size effect governed only by dimension of the particle with respect to the wavelength of the light, and therefore a red shift of the peak position of surface resonance undoubtedly results from increasing size [43]. This relationship is used to obtain qualitative information about relative media size between different samples.

3.3. Influence of Synthesis Conditions. In order to determine the influence of the current density, PEG concentration and

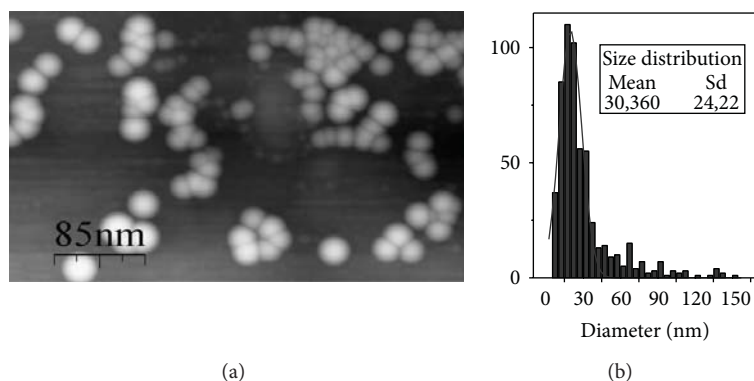


FIGURE 4: AFM image of PEG protected silver nanoparticles (a) and the corresponding size distribution analysis (b).

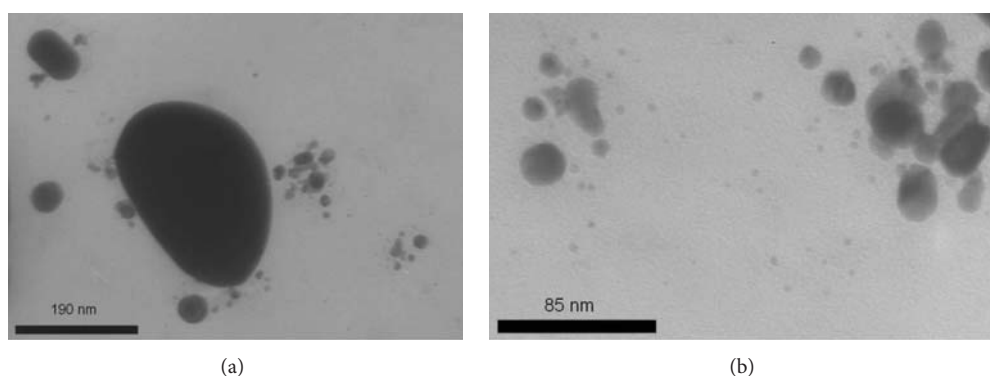


FIGURE 5: TEM images of PEG protected silver nanoparticles.

polymer chain length on the size and shape of the Ag nanoparticles several experiments were performed to study one by one each parameter of the experimental conditions. After each experiment, a UV-Vis spectrum was taken to analyze the number and position of the absorption bands and then to infer the nanoparticles shape and relative size.

3.3.1. Current Density. Reetz and Helbig determined that the particle size of Pd clusters obtained by electrochemical reduction can be controlled by variation of the current density [53]. In order to determine if the current density has some effect on silver particle size, the synthesis was repeated using currents of 7, 10, and 13 mA, respectively, whereas the other conditions were the same for these samples: 2.5 mM AgNO₃ and 1% w/v PEG-2000. Figure 6 shows the UV-Vis spectra of the obtained colloids. A blue shift in the plasmon peak can be observed as the current is increased, from 454 nm for the sample prepared at 7 mA to 405 nm for the sample prepared at 13 mA. This infers that for our samples the use of higher current density during the synthesis produces small particles. This behavior is similar to other reports by several authors for different systems with other metallic ions or stabilizers [45, 53].

3.3.2. PEG Concentration. The influence of PEG-2000 concentration on the silver particle size was studied through UV-Vis spectroscopy. The synthesis was repeated using PEG-2000 concentration of 0.5, 1, 1.5, and 2% w/v. Figure 7 shows the

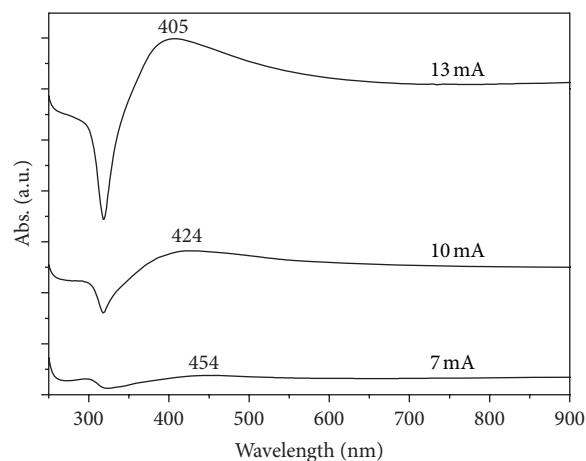


FIGURE 6: UV-Vis spectra of Ag nanoparticles obtained by using different current density during the synthesis process. From the bottom to the top: 7 mA, 10 mA and 13 mA. In the figure, the plasmon position is indicated for each spectrum.

UV-Vis spectra for the colloids obtained with different PEG-2000 amounts.

A displacement of the maximum of absorption was observed towards the blue with the increase of the concentration of PEG-2000 in the range between 0.5 and 2% w/v. Then, increasing the PEG concentration in the reaction medium,

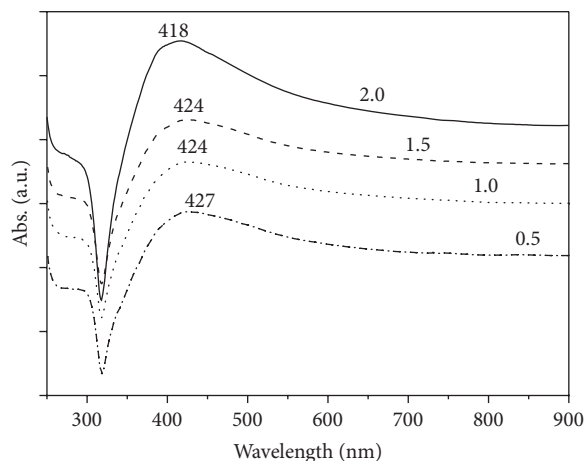


FIGURE 7: UV-Vis spectra of Ag nanoparticles obtained by using different polymer concentrations of PEG-2000 during the synthesis process. From the bottom to the top: 0.5, 1.0, 1.5, and 2.0% w/v. In the figure, the plasmon position is indicated for each spectrum.

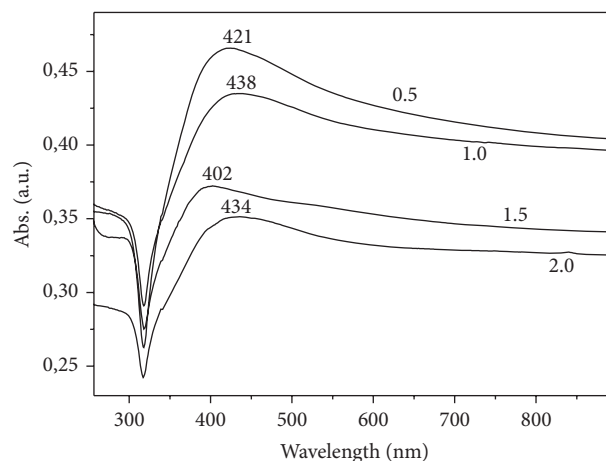


FIGURE 9: UV-Vis spectra of Ag nanoparticles obtained by using different polymer concentration of PEG-600 during the synthesis. From the bottom to the top: 0.5, 1.0, 1.5, and 2.0% w/v. In the figure, the plasmon position is indicated for each spectrum.

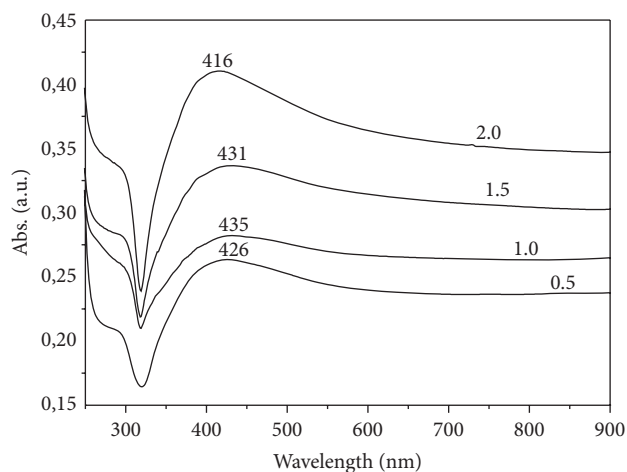


FIGURE 8: UV-Vis spectra of Ag nanoparticles obtained by using different polymer concentration of PEG-6000 during the synthesis process. From the bottom to the top: 0.5, 1.0, 1.5, and 2.0% w/v. In the figure, the plasmon position is indicated for each spectrum.

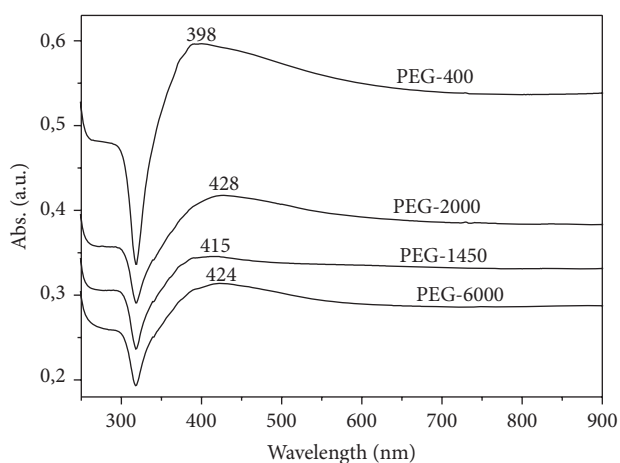


FIGURE 10: UV-Vis spectra of Ag nanoparticles obtained by using different polymer length during the synthesis process. From the bottom to the top: PEG-6000, PEG-1450, PEG-2000, and PEG-400. In the figure, the plasmon position is indicated for each spectrum.

the particle size obtained decreases. Then, it is concluded that it is possible to reinforce the control over the particle size by adjusting the PEG-2000 concentration. This behavior was similar when the same experiment was repeated using PEG-6000 in the range between 1 and 2% w/v (Figure 8). Meanwhile with PEG-600 an unsystematic behavior of the position of the maximum of absorption in function of the wavelength was found (Figure 9), and the same to PEG-400 (not shown here). Then, it is concluded that it is possible to control the particle size by adjusting the PEG-2000 and PEG-6000 concentration between 1 and 2% w/v.

3.3.3. PEG Chain Length. In some cases, when polymeric stabilizers are used, just by changing the chain length of the stabilizer, variations in the form of particles can be produced

[39]. The effect of PEG chain length on the particle size was also investigated by UV-Vis spectroscopy. Polymers with several molecular weights were used: $M_w = 400, 1450, 2000,$ and 6000 . Nevertheless, in all our experiments only one maximum of absorption between 400 and 430 nm appears to be assigned to the spherical appearance of nanoparticles (Figure 10). Then, it is concluded that the M_w did not influence the form of particles and nanospheres are obtained for all the cases.

With all the studies shown during these investigations we obtained stable nanoparticles using PEG as stabilizer and we found the correct experimental parameters that control the morphology. These nanoparticles have the possibility to be used for several purposes, such as bactericide, because they could be manipulated as a powder.

4. Conclusions

Spherical silver nanoparticles were synthesized by an electrochemical method with PEG as stabilizer. This method is a rapid and eco-friendly technique to obtain silver nanoparticles. PEG is an efficient stabilizer that favours the particle formation over silver deposition on the cathode. The influence of synthesis conditions was studied. The current density is an adequate parameter to control particle size. The PEG chain length does not show effects on the shape of the nanoparticles obtained, which are spherical for all the cases. Nevertheless, with the longer polymer chain length it is possible to control the particle size through the PEG concentration. Thus, the use of polymeric stabilizer of long chain adds an additional tool to control the particle size with respect to other electrochemistry techniques.

Acknowledgments

The authors thank UNR and CONICET for their institutional and financial support. This work was performed principally with the aid of Grant PICT 20466 from Agencia Nacional de Promoción Científica y Tecnológica, Argentina. The authors thank Dr. Claudia Palopoli (Ph.D.) for the CV measurements and discussion.

References

- [1] D. Feldheim and C. Foss, *Metal Nanoparticles: Synthesis, Characterization and Applications*, Marcel Dekker, New York, NY, USA, 2002.
- [2] J. Lue, "A review of characterization and physical property studies of metallic nanoparticles," *Journal of Physics and Chemistry of Solids*, vol. 62, pp. 1599–1612, 2001.
- [3] N. Faraji, W. Mahomood Mat Yunus, A. Kharazmi, E. Saion, M. Shahmiri, and N. Tamchek, "Synthesis, characterization and nonlinear optical properties of silver/PVA nanocomposites," *Journal of the European Optical Society*, vol. 7, p. 12040, 2012.
- [4] T. He, C. Wang, X. Pan, and Y. Wang, "Nonlinear optical response of Au and Ag nanoparticles doped polyvinylpyrrolidone thin films," *Physics Letters A*, vol. 373, pp. 592–595, 2009.
- [5] R. Vadakkekara, M. Chakraborty, and P. Parikh, "Catalytic performance of silica-supported silver nanoparticles for liquid-phase oxidation of ethylbenzene," *Industrial and Engineering Chemistry Research*, vol. 51, no. 16, pp. 5691–5698, 2012.
- [6] M. Radzig, V. Nadtochenko, O. Koksharova, J. Kiwi, V. Lipasva, and I. Khmel, "Antibacterial effects of silver nanoparticles on gram-negative bacteria: influence on the growth and biofilms formation, mechanisms of action," *Colloids and Surfaces B*, vol. 102, pp. 300–306, 2013.
- [7] M. V. Roldán, A. Frattini, O. de Sanctis, H. Troiani, and N. Pellegrini, "Characterization and applications of Ag nanoparticles in waveguides," *Applied Surface Science*, vol. 254, no. 1, pp. 281–285, 2007.
- [8] Q. Wu, H. Cao, Q. Luan et al., "Biomolecule-assisted synthesis of water-soluble silver nanoparticles and their biomedical applications," *Inorganic Chemistry*, vol. 47, no. 13, pp. 5882–5888, 2008.
- [9] S. Prabhu and E. Poulouse, "Silver nanoparticles: mechanism of antimicrobial action, synthesis, medical applications, and toxicity effects," *International Nano Letters*, vol. 2, p. 32, 2012.
- [10] L. M. Liz Marzan and I. Lado-Tourino, "Reduction and stabilization of silver nanoparticles in ethanol by nonionic surfactants," *Langmuir*, vol. 12, pp. 3585–3589, 1996.
- [11] M. Guzmán, J. Dille, and S. Godet, "Synthesis of silver nanoparticles by chemical reduction method and their antibacterial activity," *International Journal of Chemical and Biological Engineering*, vol. 2, pp. 104–111, 2009.
- [12] G. N. Glavee, K. J. Klabunde, C. M. Sorensen, and G. C. Hadjipanayis, "Borohydride reduction of cobalt ions in water. Chemistry leading to nanoscale metal, boride, or borate particles," *Langmuir*, vol. 9, no. 1, pp. 162–169, 1993.
- [13] N. Leopold and B. Lendl, "A new method for fast preparation of highly surface-enhanced raman scattering (SERS) active silver colloids at room temperature by reduction of silver nitrate with hydroxylamine hydrochloride," *The Journal of Physical Chemistry B*, vol. 107, no. 24, pp. 5723–5727, 2003.
- [14] P. Jeevanandam, C. Srikanth, and S. Dixit, "Synthesis of monodisperse silver nanoparticles and their self-assembly through simple thermal decomposition approach," *Materials Chemistry and Physics*, vol. 122, no. 2-3, pp. 402–407, 2010.
- [15] K. Akhbari, A. Morsali, and P. Retailleau, "Silver nanoparticles from the thermal decomposition of a two-dimensional nano-coordination polymer," *Polyhedron*, vol. 29, no. 18, pp. 3304–3309, 2010.
- [16] T. Edison and M. Sethuraman, "Instant green synthesis of silver nanoparticles using *Terminalia chebula* fruit extract and evaluation of their catalytic activity on reduction of methylene blue," *Process Biochemistry*, vol. 47, pp. 1351–1357, 2012.
- [17] V. Kotakadi, Y. Rao, S. Gaddam, T. Prasad, A. Reddy, and D. Sai Gopal, "Simple and rapid biosynthesis of stable silver nanoparticles using dried leaves of *Catharanthus roseus*. Linn. G. Donn and its anti microbial activity," *Colloids and Surfaces B*, vol. 105, pp. 194–198, 2013.
- [18] K. Shameli, M. Ahmad, E. Al-Mulla et al., "Green biosynthesis of silver nanoparticles using *Callicarpa maingayi* stem bark extraction," *Molecules*, vol. 17, no. 7, pp. 8506–8517, 2012.
- [19] R. Trbojevič, N. Pellegrini, A. Frattini, O. de Sanctis, P. J. Morais, and R. M. Almeida, "Preparation and isolation of gold nanoparticles coated with a stabilizer and sol-gel compatible agent," *Journal of Materials Research*, vol. 17, no. 8, pp. 1973–1980, 2002.
- [20] D. Zhang, X. Liu, X. Wang, X. Yang, and L. Lu, "Optical properties of monodispersed silver nanoparticles produced via reverse micelle microemulsion," *Physica B*, vol. 406, no. 8, pp. 1389–1394, 2011.
- [21] K. H. Baek, J. H. Kim, K. B. Lee, H. S. Ahnn, and C. S. Yoon, "Surface plasmon resonance tuning of silver nanoparticle array produced by nanosphere lithography through ion etching and thermal annealing," *Journal of Nanoscience and Nanotechnology*, vol. 10, no. 5, pp. 3118–3122, 2010.
- [22] M. L. Rodríguez-Sánchez, M. J. Rodríguez, M. C. Blanco, J. Rivas, and M. A. López-Quintela, "Kinetics and mechanism of the formation of Ag nanoparticles by electrochemical techniques: a plasmon and cluster time-resolved spectroscopic study," *The Journal of Physical Chemistry B*, vol. 109, pp. 1183–1191, 2005.
- [23] M. M. Wadkar, V. R. Chaudhari, and S. K. Haram, "Synthesis and characterization of stable organosols of silver nanoparticles by electrochemical dissolution of silver in DMSO," *Journal of Physical Chemistry B*, vol. 110, no. 42, pp. 20889–20894, 2006.

- [24] J. Zhu, X. Liao, X. Zhao, and H. Chen, "Preparation of silver nanorods by electrochemical methods," *Materials Letters*, vol. 49, no. 2, pp. 91–95, 2001.
- [25] M. Mazur, "Electrochemically prepared silver nanoflakes and nanowires," *Electrochemistry Communications*, vol. 6, no. 4, pp. 400–403, 2004.
- [26] Y. Yu, S. Chang, C. Lee, and C. Wang, "Gold nanorods: electrochemical synthesis and optical properties," *The Journal of Physical Chemistry B*, vol. 101, no. 34, pp. 6661–6664, 1997.
- [27] M. Zhou, S. Chen, S. Zhao, and H. Ma, "RETRACTED: one-step synthesis of Au-Ag alloy nanoparticles by a convenient electrochemical method," *Physica E*, vol. 33, pp. 28–34, 2006.
- [28] M. Bordenave, A. Scarpettini, M. Roldán, N. Pellegrini, and A. Bragas, "Plasmon-induced photochemical synthesis of silver triangular prisms and pentagonal bipyramids by illumination with light emitting diodes," *Materials Chemistry and Physics*, vol. 139, no. 1, pp. 100–106, 2013.
- [29] H. Peng, A. Yang, and J. Xiong, "Green, microwave-assisted synthesis of silver nanoparticles using bamboo hemicelluloses and glucose in an aqueous medium," *Carbohydrate Polymers*, vol. 91, pp. 348–355, 2013.
- [30] A. Pal, S. Shah, and S. Devi, "Microwave-assisted synthesis of silver nanoparticles using ethanol as a reducing agent," *Materials Chemistry and Physics*, vol. 114, pp. 530–532, 2009.
- [31] H. Yin, T. Yamamoto, Y. Wada, and S. Yanagida, "Large-scale and size-controlled synthesis of silver nanoparticles under microwave irradiation," *Materials Chemistry and Physics*, vol. 83, no. 1, pp. 66–70, 2004.
- [32] A. Frattini, N. Pellegrini, D. Nicastro, and O. de Sanctis, "Effect of amine groups in the synthesis of Ag nanoparticles using aminosilanes," *Materials Chemistry and Physics*, vol. 94, no. 1, pp. 148–152, 2005.
- [33] L. Huang, Y. Zhai, S. Dong, and J. Wang, "Efficient preparation of silver nanoplates assisted by non-polar solvents," *Journal of Colloid and Interface Science*, vol. 331, no. 2, pp. 384–388, 2009.
- [34] A. Rodríguez-López, A. Paredes-Arroyo, J. Mojica-Gomez et al., "Electrochemical synthesis of magnetite and maghemite nanoparticles using dissymmetric potential pulses," *Journal of Nanoparticle Research*, vol. 14, p. 993, 2012.
- [35] C. Y. Cheng, S. Thiagarajan, and S. M. Chen, "Electrochemical fabrication of AuRh nanoparticles and their electroanalytical applications," *International Journal of Electrochemical Science*, vol. 6, no. 5, pp. 1331–1341, 2011.
- [36] D. F. Yancey, E. V. Carino, and R. M. Crooks, "Electrochemical synthesis and electrocatalytic properties of Au@Pt dendrimer-encapsulated nanoparticles," *Journal of the American Chemical Society*, vol. 132, no. 32, pp. 10988–10989, 2010.
- [37] B. Yin, H. Ma, S. Wang, and S. Chen, "Electrochemical synthesis of silver nanoparticles under protection of poly(*N*-vinylpyrrolidone)," *The Journal of Physical Chemistry B*, vol. 107, no. 34, pp. 8898–8904, 2003.
- [38] M. Tejmaya, I. Römer, R. Merrifield, and J. Lead, "Stability of citrate, PVP, and PEG coated silver nanoparticles in ecotoxicology media," *Environmental Science and Technology*, vol. 46, no. 13, pp. 7011–7017, 2012.
- [39] C. Luo, Y. Zhang, X. Zeng, Y. Zeng, and Y. Wang, "The role of poly(ethylene glycol) in the formation of silver nanoparticles," *Journal of Colloid and Interface Science*, vol. 288, no. 2, pp. 444–448, 2005.
- [40] R. G. Shimmin, A. B. Schoch, and P. V. Braun, "Polymer size and concentration effects on the size of gold nanoparticles capped by polymeric thiols," *Langmuir*, vol. 20, no. 13, pp. 5613–5620, 2004.
- [41] A. Shkilnyy, M. Soucé, P. Dubois, F. Warmont, M. L. Saboungi, and I. Chourpa, "Poly(ethylene glycol)-stabilized silver nanoparticles for bioanalytical applications of SERS spectroscopy," *Analyst*, vol. 134, no. 9, pp. 1868–1872, 2009.
- [42] D. Sutton, *Electronic Spectra of Transition Metal Complexes*, McGraw-Hill, London, UK, 1968.
- [43] H. Wang, X. Qiao, J. Chen, X. Wang, and S. Ding, "Mechanisms of PVP in the preparation of silver nanoparticles," *Materials Chemistry and Physics*, vol. 94, pp. 449–453, 2005.
- [44] U. Kreibitz and M. Vollmer, *Optical Properties of Metal Clusters*, Springer, Berlin, Germany, 1995.
- [45] X. K. Meng, S. C. Tang, and S. Vongehr, "A review on diverse silver nanostructures," *Journal of Materials Science & Technology*, vol. 26, pp. 487–522, 2010.
- [46] L. Rodríguez-Sánchez, M. C. Blanco, and M. A. López-Quintela, "Electrochemical synthesis of silver nanoparticles," *The Journal of Physical Chemistry B*, vol. 104, pp. 9683–9688, 2000.
- [47] R. He, X. Qian, J. Yin, and Z. Zhu, "Preparation of polychrome silver nanoparticles in different solvents," *Journal of Materials Chemistry*, vol. 12, pp. 3783–3786, 2002.
- [48] R. Jenkins and R. L. Snyder, *Introduction to X-Ray Powder Diffractometry*, John Wiley & Sons, New York, NY, USA, 1996.
- [49] S. Calvin, S. X. Luo, C. Caragianis-Broadbridge et al., "Comparison of extended x-ray absorption fine structure and Scherrer analysis of x-ray diffraction as methods for determining mean sizes of polydisperse nanoparticles," *Applied Physics Letters*, vol. 87, Article ID 233102, 3 pages, 2005.
- [50] K. Kelly, E. Coronado, L. Zhao, and G. Schatz, "The optical properties of metal nanoparticles: the influence of size, shape, and dielectric environment," *The Journal of Physical Chemistry B*, vol. 107, pp. 668–677, 2003.
- [51] D. Evanoff and G. Chumanov, "Size-controlled synthesis of nanoparticles. 2. Measurement of extinction, scattering, and absorption cross sections," *The Journal of Physical Chemistry B*, vol. 108, no. 37, pp. 13957–13962, 2004.
- [52] S. Link and M. A. El-Sayed, "Spectral properties and relaxation dynamics of surface plasmon electronic oscillations in gold and silver nanodots and nanorods," *The Journal of Physical Chemistry B*, vol. 103, pp. 8410–8426, 1999.
- [53] M. Reetz and W. Helbig, "Size-selective synthesis of nanostructured transition metal clusters," *Journal of the American Chemical Society*, vol. 116, no. 16, pp. 7401–7402, 1994.

Research Article

Synthesis of Gold Nanoparticles Using Whole Cells of *Geotrichum candidum*

Amit Kumar Mittal, Abhishek Kaler, Aparna Vasant Mulay, and Uttam Chand Banerjee

Department of Pharmaceutical Technology, National Institute of Pharmaceutical Education and Research, Sector-67,
SAS Nagar, Punjab 160062, India

Correspondence should be addressed to Uttam Chand Banerjee; ucbanerjee@niper.ac.in

Received 31 January 2013; Accepted 12 March 2013

Academic Editor: Hamed Bahmanpour

Copyright © 2013 Amit Kumar Mittal et al. This is an open access article distributed under the Creative Commons Attribution License, which permits unrestricted use, distribution, and reproduction in any medium, provided the original work is properly cited.

The synthesis of nanoparticles with desired size and shape is an important area of research in nanotechnology. Use of biological system is an alternative approach to chemical and physical procedures for the synthesis of metal nanoparticles. An efficient environment-friendly approach for the biosynthesis of rapid and stable Gold nanoparticles (AuNPs) using whole cells of *Geotrichum candidum* is discussed in this paper. The enzymes/proteins present in the microorganism might be responsible for the reduction of metal salts to nanoparticles. Various reaction parameters such as culture age, temperature, pH, metal salt, and cell mass concentrations were optimized. The AuNPs were characterized by UV-visible spectroscopy, dynamic light scattering (DLS), energy dispersive spectroscopy (EDS), scanning electron microscope (SEM), and Fourier transform infrared spectroscopy (FTIR). Nanoparticles were isolated by sonicating the whole cells after treatment with Tween 80. The whole cell mediated process showed the simplistic, feasible, easy to scale up, and low-cost approach for the synthesis of AuNPs.

1. Introduction

Metal nanoparticles have been an extensive area of research because of their unique chemical, physical, and optical properties [1]. These make them potential candidates in the field of catalysis, labeling, biosensing, drug delivery, antimicrobial, and so forth [2, 3]. AuNPs have wider ranges of applications in the biomedical field for biosensor development, drug delivery, imaging, photo diagnostics, and so forth [4]. Development of reliable processes for the synthesis of metal nanomaterials with excellent dispersity and stability with minimum harmful effects is the need of the day [5]. Traditional chemical and physical methods reported in the literature involve the use of hazardous chemicals and extreme reaction conditions [6–8]. The current research is directed towards the development of eco-friendly protocols for the synthesis of nanomaterials/nanostructures of desirable sizes and shapes [9, 10]. Considering applications of AuNPs in the fields of biology and medicine, environment, and technology, there is a growing need for the development of cost-effective method for the synthesis of new nanoparticles

[11]. The biological methods fulfil all the requirements of a process to be green [12]. Synthesis of nanoparticles utilizing biological system such as bacteria, fungi, and several plant extracts have been widely reported in the literature [6, 13–15]. Microorganisms are able to produce metal nanomaterials either intra- or extracellularly. Intracellular synthesis of metal nanoparticles (*Pseudomonas stutzeri*, *Escherichia coli*, *Vibrio cholerae*, *Pseudomonas aeruginosa*, *Salmonella typhimurium*, and *Staphylococcus aureus*) has been investigated by many workers [16, 17]. The formation of extracellular silver nanoparticles by photoautotrophic cyanobacteria, *Plectononema boryanum*, has been described in [18]. The intracellular synthesis of AuNPs by microbial reduction of Au³⁺ using *Shewanella* algae has been investigated by Konishi et al. in 2006 and Konishi et al. in 2007 [19, 20]. The synthesis of AuNPs of different sizes and shapes has been reported in both aqueous and nonpolar organic solvents [21, 22]. Some well-known examples of plant mediated synthesis of gold nanotriangles using aloe-vera extract and tamarind leaf extract are also available in literature [23, 24]. In this paper, we report the intracellular synthesis of AuNPs using

yeast, *Geotrichum candidum*, its downstream processing and characterization.

2. Materials and Methods

2.1. Chemicals. Gold (III) chloride trihydrate salt (99.99%) was purchased from Sigma-Aldrich (Steinheim, Germany). Different salts, buffer, and media components were purchased from Qualigens Chemicals (Mumbai, India), Hi Media (Mumbai, India), and Central Drug House (P) (New Delhi, India).

2.2. Microorganism and Culture Conditions. *Geotrichum candidum* NCIM 980 was procured from National Collection of Industrial Microorganisms, National Chemical Laboratory, Pune, India. The organism was grown in YPD medium (yeast extract 3 g/L, peptone 3 g/L and dextrose 10 g/L, pH 6.5) at 30°C in an incubator shaker (200 rpm).

2.3. Synthesis of Gold Nanoparticle and Its Downstream Processing. The cells were grown in specified medium for 24 h at 30°C in shaker incubator (200 rpm). The fermentation broth was centrifuged at 7,000 ×g for 15 min; cells were washed thoroughly and resuspended in deionised water. Suspension of wet cell mass (10%) in deionised water was prepared. Tetrachloroauric acid trihydrate ($\text{AuCl}_4 \cdot 3\text{H}_2\text{O}$) was added to the cell suspension (10%) to final concentration of 1 mM. The reaction was carried out at 30°C, 200 rpm for 72 h and observed for visual colour change. For the isolation of nanoparticles from the whole cells, various disruption methods were used. Cell disruption was performed using ultrasonication after treatment with surfactant (Tween 80). The supernatant was collected after centrifugation at 10,000 ×g for 15 min and lyophilized to concentrate the AuNPs.

2.4. Characterization of Nanoparticles. An essential part in the synthesis of nanoparticles is its characterization. The synthesised AuNPs were characterized by UV-visible spectrometry, dynamic light scattering (DLS), scanning electron microscopy (SEM), Fourier transform infrared spectroscopy (FTIR), and energy dispersive spectroscopy (EDS). Observation of strong broad surface plasmon peaks at visible regions (510–525 nm) has been well documented for AuNPs, with sizes ranging widely from 10 to 100 nm. The reduction of pure Au^{+3} ions to Au^0 was monitored by measuring through UV-Vis spectroscopy by taking the samples of reaction mixture (gold nanoparticle solution). Dynamic light scattering (DLS or Zeta-sizer) was used to measure the size, size distribution, and potential (charge) of nanoparticles dispersed in a liquid. Scanning electron microscopic (SEM) analysis was done using the instrument (S-3400, Hitachi) operated at an excitation voltage of 25 kV. The nanoparticles or whole cell suspensions were mounted onto steel stage using double-sided adhesive tape on a glass cover slip by just dropping a very small amount of the sample on the cover slip, and the film was allowed to dry and coated with gold using ion sputter (E-1010, Hitachi). The SEM was used for the

determination of size and morphology of the nanoparticles. The functional groups and capping of the synthesized AuNPs were confirmed by FTIR spectroscopy. Elemental analysis and chemical composition of NPs were determined using energy dispersive spectroscopy.

2.5. Optimization of Various Reaction Parameters

2.5.1. Culture Age and Its Concentration. Cell age has pronounced effect on the synthesis of nanoparticles. In order to determine the optimum culture cell age for nanoparticle production, the cells were harvested at different phases of growth. After harvesting, the cells were thoroughly washed, resuspended in deionised water, and tetrachloroauric acid trihydrate ($\text{AuCl}_4 \cdot 3\text{H}_2\text{O}$) was added to make final concentration of 1 mM, and reaction mixture was incubated at 30°C (200 rpm). After 48 h, cells were harvested by centrifugation at 7,000 ×g for 15 min. The effect of cell mass concentration was studied by incubating different concentrations of cells (25–250 mg/mL) with gold salt at 35°C (200 rpm) for 72 h. From time to time, the samples were taken from the reaction mixture, and nanoparticles were characterized according to the set procedures.

2.5.2. Reaction Temperature. Tetrachloroauric acid trihydrate ($\text{AuCl}_4 \cdot 3\text{H}_2\text{O}$) was added in 1 mM concentration to the resuspended whole cells, and the flasks were incubated at a range of temperature of 15 to 40°C (200 rpm). Samples were collected at a regular interval of time and characterized accordingly.

2.5.3. Reaction pH. To the cell suspension, tetrachloroauric acid trihydrate ($\text{AuCl}_4 \cdot 3\text{H}_2\text{O}$) was added to achieve a final concentration of 1 mM, and the flasks were incubated at 35°C (200 rpm). A range of pH (3–13) of the reaction mixture was chosen. Samples were collected at a regular interval of time and characterized accordingly.

2.5.4. Metal Salts. To the whole cell suspension, different concentrations (1 to 10 mM) of $\text{AuCl}_4 \cdot 3\text{H}_2\text{O}$ were added, and the flasks were incubated at 35°C (200 rpm). Samples were collected at a regular interval of time and characterized accordingly.

3. Results and Discussion

The shape, size, and size distribution of metal nanoparticles produced by the reduction of gold ion (Au^{3+}) by *Geotrichum candidum* in solution depend on various reaction conditions such as temperature, cell age, cell mass pH, and concentration of metal salt. After downstream processing, the nanoparticles were characterized by various techniques.

3.1. Characterization of AuNPs

3.1.1. Visual Observation. It has been reported [25] in the literature that the formation of AuNPs is detected by observing

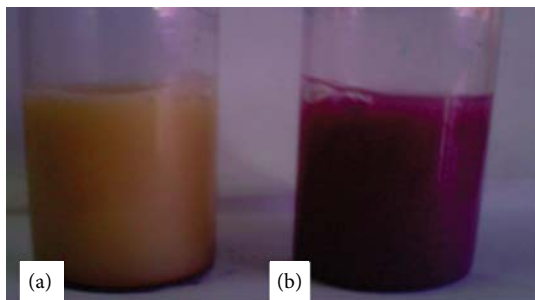


FIGURE 1: Visual observations of AuNPs produced by whole cell *Geotrichum candidum*.

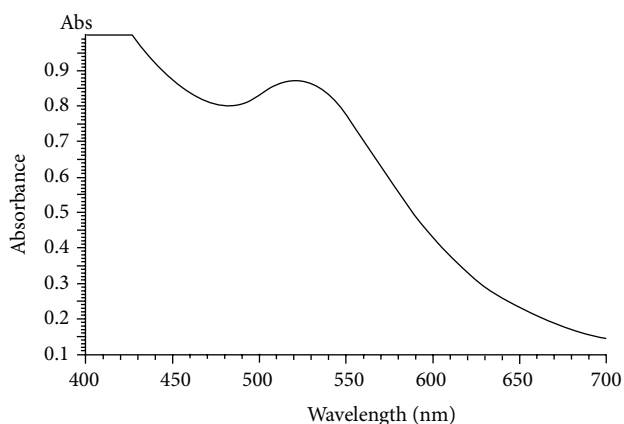


FIGURE 2: UV-Vis spectra of AuNPs produced by whole cell *Geotrichum candidum*.

the colour change of reaction mixture. In this case, also the formation of nanoparticle was preliminarily identified by observing the colour change of the reaction mixture (Figure 1). The cell mass of *G. candidum* turned light yellow (Figure 1(a)) to purple colour (Figure 1(b)) indicating the synthesis of AuNPs. The synthesis might be either intracellular or on the cell surface.

3.1.2. UV-Vis Spectral Analysis. As previously reported by other workers [26] on the colloidal solution of gold nanoparticle when subjected to UV-Vis spectrometry, a strong peak was absorbed at 520–530 nm (Figure 2).

3.1.3. Control of Size and Shape of AuNPs. To achieve the better size and shape of AuNPs synthesised by the cells of *Geotrichum candidum*, parameters such as cell age, pH, temperature, metal ion, and cell mass concentration were optimized. Metabolic activities of cell vary with the cell age. The cellmass harvested at 48 h of growth produced highest amount of AuNPs (Figure 3(a)). This may be due to expression of higher amount of reductant at that the time of harvest (48 h growth) resulting in higher reduction. With the increase in temperature, reaction rate increased up to a certain value and then it started decreasing. Temperature

of 35°C was found to be optimum for nanoparticle synthesis, beyond which the absorption at 520 nm decreased (Figure 3(b)). This may be due to instability of reductive compounds (protein/peptide) at higher temperatures. Gericke and Pinches [27] also found similar effect for the Au-nanoparticle synthesis. Nanoparticle synthesis is a crystallisation phenomenon that depends upon solubility of salt in the media. pH affects the solubility and thus can affect the nanoparticle formation. The optimum pH for synthesis of gold nanoparticle was found to be 7 where the maximum absorption was observed (Figure 3(c)). Both above and below pH 7, aggregation took place. Higher concentration of auric chloride was found to be toxic to the microbial cell. Lower concentration of auric chloride (1 mM) was very efficiently reduced by the cells of *G. candidum* (Figure 3(d)). Cellmass concentration also showed prominent effect on the nanoparticle formation. Keeping all the other parameters constant, the cellmass concentration was varied from 25 to 250 mg/mL, and 50 mg/mL was found to give maximum yield of AuNPs (Figure 3(e)).

3.1.4. Zetasizer. The synthesized nanoparticles have average particle size of about 76.58 nm and PDI of 0.231 (Figure 4(a)) which indicates monodispersity, and Zeta potential of -17.5 mV (Figure 4(b)) shows that the synthesized AuNPs are capped by -vely charged groups and are moderately stable.

3.1.5. Scanning Electron Microscopy (SEM) Analysis. A representative SEM image of the synthesized AuNPs is shown in Figure 5. This SEM image shows that the synthesized nanoparticles lay on the surface of *Geotrichum candidum* (Figure 5(a)). The average nanoparticle size lies in the range of 65–70 nm. Figure 5(b) shows the harvested AuNPs isolated from the cellmass of *G. candidum*.

3.1.6. Energy Dispersive Spectroscopy (EDS). An area profile EDS spectra of AuNPs (Figure 6) synthesized by whole cells of *G. candidum* after purification showed the presence of strong signals of the gold atoms.

3.1.7. FTIR Spectroscopy. FTIR spectroscopy analysis was done to reveal the involvement of possible biomolecules affecting the reduction and subsequent capping of the metal nanoparticles [28] synthesized by *G. candidum*. The proteins can bind to nanoparticles through its various functional groups [29]. The FTIR spectra revealed the presence of different functional groups such as amide and $-\text{COOH}$ linkages on amino acid residues in protein and synthesized AuNPs. The bands were observed at 1299 cm^{-1} , 3433.14 cm^{-1} , 2923.27 cm^{-1} , and 1735.66 cm^{-1} (Figure 7), acknowledged as amide III band, $-\text{OH}$ stretching, C–H stretching, and C–O stretching of carboxylic acid, respectively [30]. The band at 1647 cm^{-1} represents C=O stretching of amide bond. The band at 1351.71 cm^{-1} represents C–N stretching which is commonly present in proteins, indicating the presence of protein as ligand for AuNPs, which increases the stability

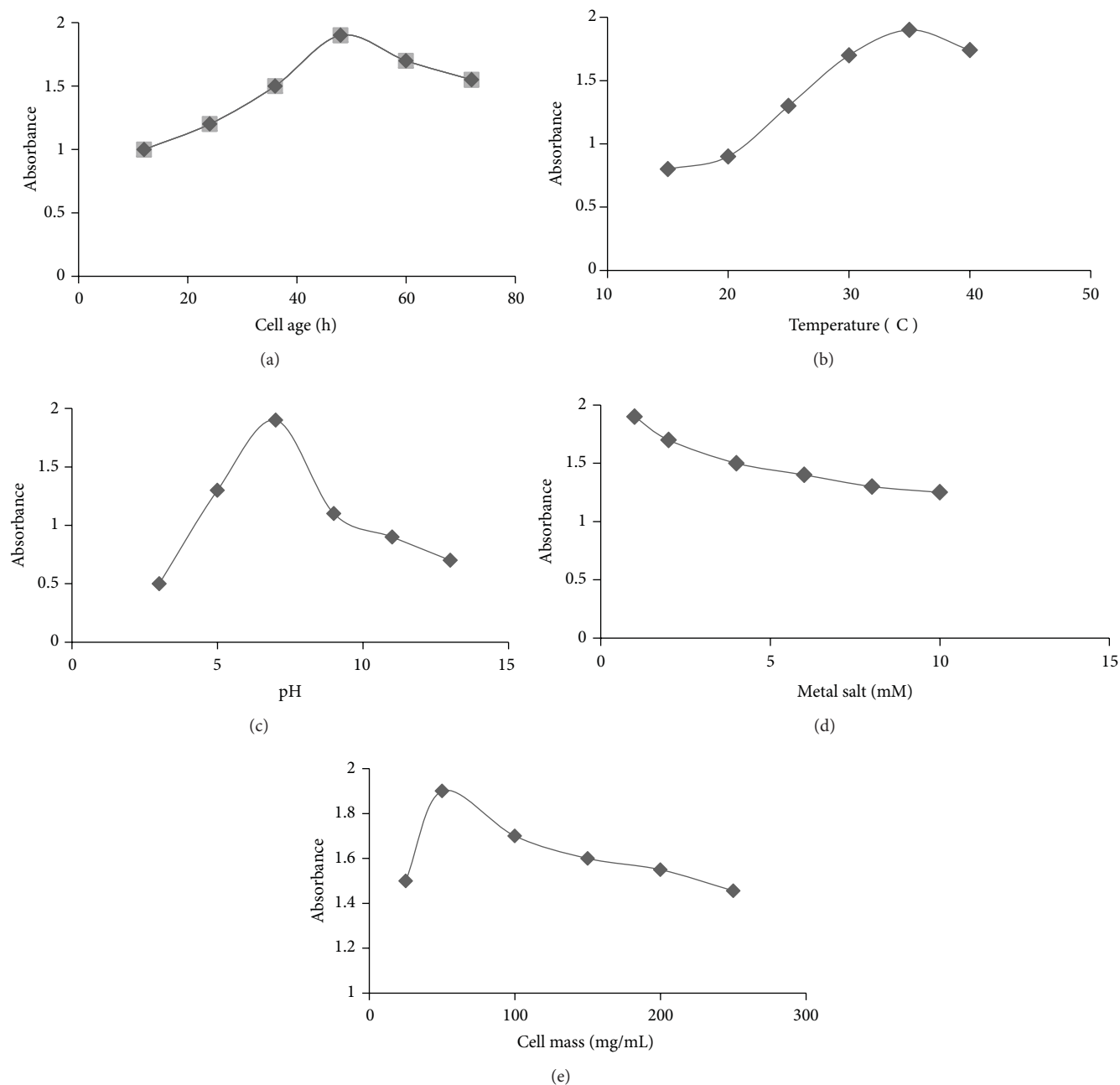


FIGURE 3: Optimization of various physicochemical parameters for AuNPs synthesis by whole cells of *Geotrichum candidum*.

of synthesized nanoparticles [31]. All peaks of FTIR spectra showed the presence of protein attachment to the AuNPs.

4. Conclusion

Geotrichum candidum was reported for the first time to synthesize AuNPs. Various reaction parameters like cell age, temperature, pH, cell mass, and metal ion concentration, were optimized to increase the yield and to improve the dispersity of nanoparticles. Proteins are responsible for the reduction of metal salts as well as its stabilization by capping. The gold nanoparticle throughout the cellmass suggests that

Au^{+3} ions entered the cells through a transport system. The presence of different metabolic enzymes inside the cells or cytoplasm probably reduced Au^{+3} to Au^0 and capped it by protective peptide/proteins. The microorganism mediated synthesis of metal nanoparticles can be a viable alternative to physical and chemical methods and can be easily scaled up.

Conflict of Interests

All the authors have no conflict of interests relevant to this paper.

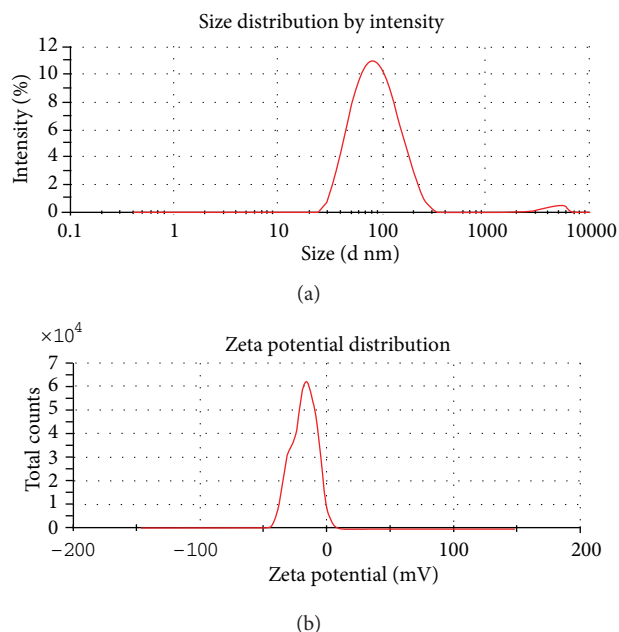
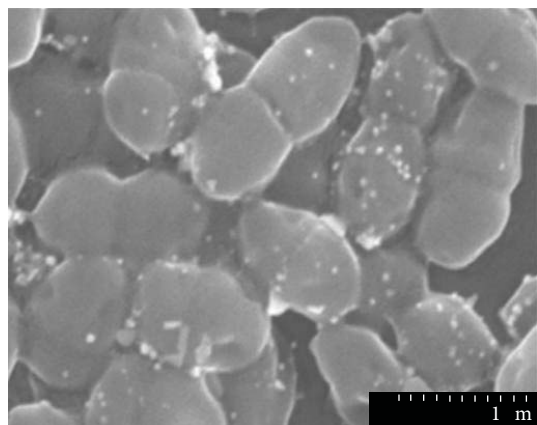
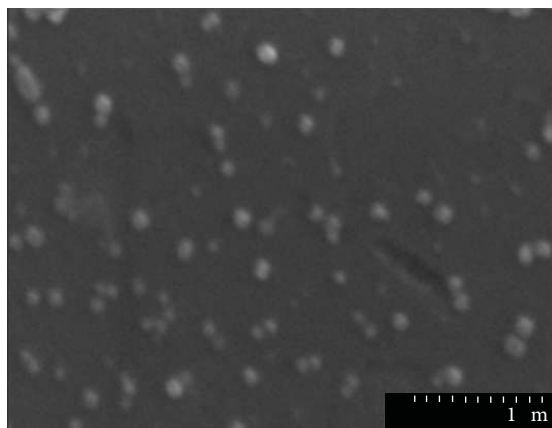


FIGURE 4: (a) Zetasizer distribution and (b) Zeta potential of AuNPs synthesized by whole cell of *Geotrichum candidum*.



(a)



(b)

FIGURE 5: SEM images of AuNPs synthesized by *Geotrichum candidum* (a) in the whole cell and (b) after downstream processing.

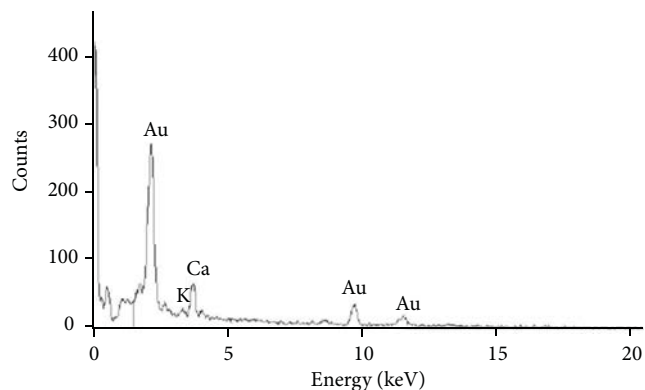


FIGURE 6: EDS spectra of AuNPs synthesized by whole cells *G. candidum*.

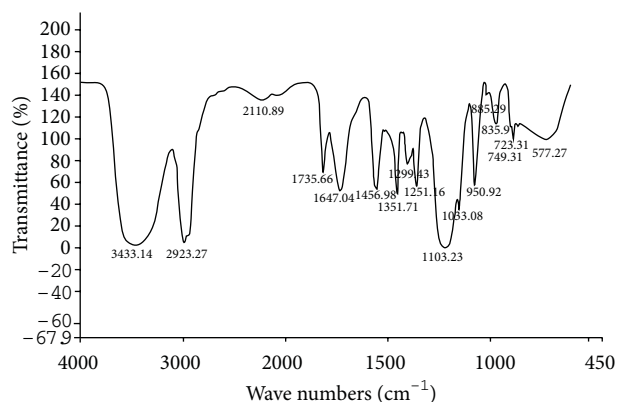


FIGURE 7: FTIR spectra of AuNPs synthesized by whole cell *Geotrichum candidum* NCIM 980 after harvesting.

Acknowledgments

One of the authors (A. K. Mittal) gratefully acknowledges financial support from the CSIR, and both A. Kaler and A. V. Muly gratefully acknowledge the financial support from DBT, New Delhi, India.

References

- [1] P. K. Jain, X. Huang, I. H. El-Sayed, and M. A. El-Sayed, "Noble metals on the nanoscale: optical and photothermal properties and some applications in imaging, sensing, biology, and medicine," *Accounts of Chemical Research*, vol. 41, no. 12, pp. 1578–1586, 2008.
- [2] F. S. Rosarin and S. Mirunalini, "Nobel metallic nanoparticles with novel biomedical properties," *Journal of Bioanalysis & Biomedicine*, vol. 3, pp. 085–091, 2011.
- [3] M. Solomon and G. G. M. D'Souza, "Recent progress in the therapeutic applications of nanotechnology," *Current Opinion in Pediatrics*, vol. 23, no. 2, pp. 215–220, 2011.
- [4] E. Boisselier and D. Astruc, "Gold nanoparticles in nanomedicine: preparations, imaging, diagnostics, therapies and toxicity," *Chemical Society Reviews*, vol. 38, no. 6, pp. 1759–1782, 2009.

- [5] J. A. Dahl, B. L. S. Maddux, and J. E. Hutchison, "Toward greener nanosynthesis," *Chemical Reviews*, vol. 107, no. 6, pp. 2228–2269, 2007.
- [6] K. N. Thakkar, S. S. Mhatre, and R. Y. Parikh, "Biological synthesis of metallic nanoparticles," *Nanomedicine*, vol. 6, no. 2, pp. 257–262, 2010.
- [7] R. Sanghi and P. Verma, "15 Microbes as green and eco-friendly nanofactories," in *Green Chemistry for Environmental Sustainability*, S. K. Sharma, Ed., p. 315, CRC Press, 2010.
- [8] H. Korbekandi, S. Iravani, and S. Abbasi, "Production of nanoparticles using organisms Production of nanoparticles using organisms," *Critical Reviews in Biotechnology*, vol. 29, no. 4, pp. 279–306, 2009.
- [9] A. Ahmad, P. Mukherjee, S. Senapati et al., "Extracellular biosynthesis of silver nanoparticles using the fungus *Fusarium oxysporum*," *Colloids and Surfaces B*, vol. 28, no. 4, pp. 313–318, 2003.
- [10] A. K. Gade, P. Bonde, A. P. Ingle, P. D. Marcato, N. Durán, and M. K. Rai, "Exploitation of *Aspergillus niger* for synthesis of silver nanoparticles," *Journal of Biobased Materials and Bioenergy*, vol. 2, no. 3, pp. 243–247, 2008.
- [11] L. Dykman and K. Nikolai, "AuNPs in biomedical applications: recent advances and perspectives," *Chemical Society Reviews*, vol. 41, no. 6, pp. 2256–2282, 2012.
- [12] S. Marimuthu, A. A. Rahuman, G. Rajakumar et al., "Evaluation of green synthesized silver nanoparticles against parasites," *Parasitology Research*, vol. 108, no. 6, pp. 1541–1549, 2011.
- [13] A. K. Mittal, Y. Chisti, and U. C. Banerjee, "Synthesis of metallic nanoparticles using plant extracts," *Biotechnology Advances*, vol. 31, no. 2, pp. 346–356, 2013.
- [14] A. K. Mittal, A. Kaler, and U. C. Banerjee, "Free radical scavenging and antioxidant activity of silver nanoparticles synthesized from flower extract of *Rhododendron dauricum*," *Nano Biomedicine and Engineering*, vol. 4, no. 3, pp. 118–124, 2012.
- [15] K. B. Narayanan and N. Sakthivel, "Biological synthesis of metal nanoparticles by microbes," *Advances in Colloid and Interface Science*, vol. 156, no. 1–2, pp. 1–13, 2010.
- [16] Z. Sadowski, "Biosynthesis and application of silver and AuNPs," *Wroclaw University of Technology*, p. 257, 2009.
- [17] A. Kaler, R. Nankar, M. S. Bhattacharyya, and U. C. Banerjee, "Extracellular biosynthesis of silver nanoparticles using aqueous extract of *Candida viswanathii*," *Journal of Bionanoscience*, vol. 5, no. 1, pp. 53–58, 2011.
- [18] M. F. Lengke, M. E. Fleet, and G. Southam, "Biosynthesis of silver nanoparticles by filamentous cyanobacteria from a silver(I) nitrate complex," *Langmuir*, vol. 23, no. 5, pp. 2694–2699, 2007.
- [19] Y. Konishi, T. Tsukiyama, K. Ohno, N. Saitoh, T. Nomura, and S. Nagamine, "Intracellular recovery of gold by microbial reduction of AuCl_4^- ions using the anaerobic bacterium *Shewanella algae*," *Hydrometallurgy*, vol. 81, no. 1, pp. 24–29, 2006.
- [20] Y. Konishi, K. Ohno, N. Saitoh et al., "Bioreductive deposition of platinum nanoparticles on the bacterium *Shewanella algae*," *Journal of Biotechnology*, vol. 128, no. 3, pp. 648–653, 2007.
- [21] P. R. Selvakannan, S. Mandal, R. Pasricha, S. D. Adyanthaya, and M. Sastry, "One-step synthesis of hydrophobized gold nanoparticles of controllable size by the reduction of aqueous chloroaurate ions by hexadecylaniline at the liquid-liquid interface," *Chemical Communications*, no. 13, pp. 1334–1335, 2002.
- [22] T. K. Sau and C. J. Murphy, "Room temperature, high-yield synthesis of multiple shapes of gold nanoparticles in aqueous solution," *Journal of the American Chemical Society*, vol. 126, no. 28, pp. 8648–8649, 2004.
- [23] S. P. Chandran, M. Chaudhary, R. Pasricha, A. Ahmad, and M. Sastry, "Synthesis of gold nanotriangles and silver nanoparticles using *Aloe vera* plant extract," *Biotechnology Progress*, vol. 22, no. 2, pp. 577–583, 2006.
- [24] B. Ankamwar, M. Chaudhary, and M. Sastry, "Gold nanotriangles biologically synthesized using tamarind leaf extract and potential application in vapor sensing," *Synthesis and Reactivity in Inorganic, Metal-Organic and Nano-Metal Chemistry*, vol. 35, no. 1, pp. 19–26, 2005.
- [25] P. Mukherjee, S. Senapati, D. Mandal et al., "Extracellular synthesis of AuNPs by the fungus *Fusarium oxysporum*," *ChemBioChem*, vol. 3, no. 5, pp. 461–463, 2002.
- [26] S. S. Shankar, A. Rai, A. Ahmad, and M. Sastry, "Rapid synthesis of Au, Ag, and bimetallic Au core-Ag shell nanoparticles using *Neem (Azadirachta indica)* leaf broth," *Journal of Colloid and Interface Science*, vol. 275, no. 2, pp. 496–502, 2004.
- [27] M. Gericke and A. Pinches, "Biological synthesis of metal nanoparticles," *Hydrometallurgy*, vol. 83, no. 1–4, pp. 132–140, 2006.
- [28] S. S. Shankar, A. Ahmad, and M. Sastry, "Geranium leaf assisted biosynthesis of silver nanoparticles," *Biotechnology Progress*, vol. 19, no. 6, pp. 1627–1631, 2003.
- [29] C. M. Niemeyer, "Nanoparticles, proteins, and nucleic acids: biotechnology meets materials science," *Angewandte Chemie International Edition*, vol. 40, no. 22, pp. 4129–4158, 2001.
- [30] B. D. Chithrani, A. A. Ghazani, and W. C. W. Chan, "Determining the size and shape dependence of gold nanoparticle uptake into mammalian cells," *Nano Letters*, vol. 6, no. 4, pp. 662–668, 2006.
- [31] N. Vigneshwaran, N. M. Ashtaputre, P. V. Varadarajan, R. P. Nachane, K. M. Paralikar, and R. H. Balasubramanya, "Biological synthesis of silver nanoparticles using the fungus *Aspergillus flavus*," *Materials Letters*, vol. 61, no. 6, pp. 1413–1418, 2007.

Research Article

CuO-CeO₂ Nanocomposite: An Efficient Recyclable Catalyst for the Synthesis of Aryl-14*H*-dibenzo[a-j]xanthenes

Jalal Albadi,¹ Abdolhossein Razeghi,² Hossein Abbaszadeh,³ and Azam Mansournezhad³

¹ College of Science, Behbahan Khatam Alanbia University of Technology, Behbahan 736254, Iran

² Catalysis and Reaction Engineering, Tehran University, Tehran, Iran

³ Department of Chemistry, Gachsaran Branch, Islamic Azad University, Gachsaran, Iran

Correspondence should be addressed to Jalal Albadi; jalal.albadi@gmail.com

Received 7 January 2013; Revised 16 February 2013; Accepted 20 February 2013

Academic Editor: Hamed Bahmanpour

Copyright © 2013 Jalal Albadi et al. This is an open access article distributed under the Creative Commons Attribution License, which permits unrestricted use, distribution, and reproduction in any medium, provided the original work is properly cited.

CuO-CeO₂ nanocomposite is reported as a highly efficient recyclable catalyst that is applied for the synthesis of Aryl-14*H*-dibenzo[a-j]xanthenes under solvent-free conditions. The catalyst was synthesized by coprecipitation method and characterized by X-ray powder diffraction (XRD), BET specific surface area, field emission scanning electron microscopy (FESEM), and energy dispersive spectroscopy (EDS) analysis. The copper nanoparticles are dispersed as fine and amorphous phases on the surface of ceria and made nanoclusters with average size of about 33 nm. This catalyst can be recovered by simple filtration and recycled up to 8 consecutive runs without any losing of its efficiency. This procedure provides several advantages such as simple workup, mild reaction conditions, short reaction times, and high yields of the products.

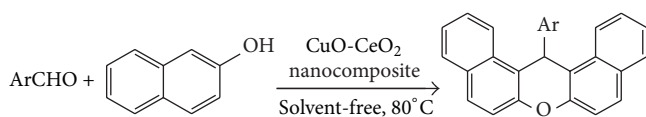
1. Introduction

In recent years, nanocatalysis has emerged as a sustainable and competitive alternative to conventional catalyst since the nanoparticles possess a high-surface-to-volume ratio, which enhances their activity and selectivity, while, at the same time, maintaining the intrinsic features of a heterogeneous catalyst [1]. In particular, nanocrystalline oxides have proved to be useful to chemists in the laboratory and industry due to the good activation of adsorbed compounds and reaction rate enhancement, selectivity, easier workup and recyclability of the supports, and the eco-friendly green reaction conditions [2–6]. Also, the practical applications of nanocomposite metal oxides as the catalysts in organic synthesis have been increased due to their high catalytic activity because of the high surface area [7, 8]. The recyclability of the catalyst is the added advantage in the case of these catalysts. The catalytic activity of CuO-CeO₂ nanocomposite is well known for the oxidation of CO in H₂-rich streams [9]. Xanthene derivatives are important class of compounds that received significant attention from many pharmaceutical and organic chemists because of the broad spectrum of their biological and pharmaceutical properties such as antibacterial [10],

anti-inflammatory [11], and antiviral properties [12]. Furthermore, these compounds are used as dyes and fluorescent material for visualization of biomolecules and in laser technologies due to their useful spectroscopic properties [13, 14]. Aryl-14*H*-dibenzo[a-j]xanthenes are among the most important classes in the family of xanthenes due to their distinctive structures and great potential for the further transformations [15]. Various methods have been reported for the synthesis of Aryl-14*H*-dibenzo[a-j]xanthenes; among these methods, the one-pot condensation of β -naphthol with aldehydes is the most common procedure. Therefore, various catalysts have been developed for the improvement of this reaction [16–25]. In the continuation of our research program to develop the efficient, and green catalysts in organic synthesis [26–29], herein, we wish to report a green, efficient and recyclable catalyst for the synthesis of Aryl-14*H*-dibenzo[a-j]xanthenes under solvent-free conditions (Scheme 1).

2. Experimental

All products were identified by the comparison of their spectral and physical data with authentic samples. Chemicals (2-naphthol, aromatic aldehydes, cerium, and copper nitrates)



SCHEME 1: Synthesis of Aryl-14H-dibenzo[a-j]xanthenes catalyzed by CuO-CeO₂ nanocomposite oxide.

were purchased from Merck Chemical company in Germany. Yields refer to isolated pure products.

2.1. Catalyst Preparation. CuO-CeO₂ nanocomposite was prepared by coprecipitation method using aqueous solution of cerium and copper nitrates and drop-wise adding KOH as precipitant agent under vigorous mixing, while temperature and pH were fixed at unique values. Then, acquired sample was filtered, washed, and calcined to obtain final catalyst for using as synthesis of Aryl-14H-dibenzo[a-j]xanthenes.

2.2. General Procedure for Synthesis of Aryl-14H-dibenzo[a-j]xanthenes. A mixture of 2-naphthol (2 mmol), aldehyde (1 mmol), and CuO-CeO₂ nanocomposite (0.05 g) was added to a round-bottomed flask. The reaction mixture was placed in an oil bath at 80°C and magnetically stirred for the appropriate times according to Table 1. After completion of the reaction (monitored by TLC), the mixture reaction was cooled to room temperature, next acetone (10 mL) was added, and the mixture stirred for 5 min. Then, the catalyst was recovered by filtration to be reused subsequently. The filtrate was evaporated to dryness, and the solid residue recrystallized from hot ethanol to give pure products in high yields. The experimental procedure with this catalyst is very simple and the catalyst can be removed easily by filtration. The solid products were easily recrystallized from hot ethanol and were obtained in good to high yields during the short reaction times. Very low amount of the catalyst is needed. Moreover, our procedure is environmentally friendly as it does not use any toxic auxiliary or solvent.

2.3. Catalyst Characterization. The catalyst structure characterization was performed by X-ray powder diffraction (XRD), using a Bruker AXS D8 advanced diffractometer equipment with CuK α radiation ($\lambda = 1.5406 \text{ \AA}$). The Debye-Scherrer equation is used to determine average crystallite size of nanoparticles. Field emission scanning electron microscopy (FESEM) and energy dispersive spectroscopy (EDS) carried out by a Hitachi S4160 instrument to see the morphology, the evaluation of cluster size, and the metal composition of the catalyst. BET specific surface area was estimated from the N₂ adsorption/desorption isotherms, measured at 77°K using a Quantachrome CHEMBET-3000 instrument.

3. Results and Discussions

XRD pattern of fresh CuO-CeO₂ nanocomposite calcined at 450°C is illustrated (Figure 1). The main reflection placed at 2θ range of 15–80° indicates a cubic fluorite structure

TABLE 1: Synthesis of Aryl-14H-dibenzo[a-j]xanthenes catalyzed by CuO-CeO₂ nanocomposite.

Entry	Aldehyde	Time (min)	Yield (%) ^a	M. P. (°C)
1	PhCHO	15	93	185–186
2	2-NO ₂ C ₆ H ₄ CHO	12	91	213–215
3	3-NO ₂ C ₆ H ₄ CHO	15	90	210–211
4	4-NO ₂ C ₆ H ₄ CHO	8	90	310–312
5	2-ClC ₆ H ₄ CHO	12	90	213–215
6	4-ClC ₆ H ₄ CHO	10	91	289–290
7	2,4-Cl ₂ C ₆ H ₃ CHO	12	90	251–252
8	2,6-Cl ₂ C ₆ H ₃ CHO	15	89	267–269
9	4-FC ₆ H ₄ CHO	10	90	237–238
10	2-MeC ₆ H ₄ CHO	18	89	258–260
11	3-MeC ₆ H ₄ CHO	12	90	199–201
12	4-MeC ₆ H ₄ CHO	20	90	228–229
13	4-MeOC ₆ H ₄ CHO	30	89	202–204
14	4-BrC ₆ H ₄ CHO	15	91	296–298
15	4-OHC ₆ H ₄ CHO	45	88	139–141

^a Isolated yield. ^b Products were characterized by the comparison of their spectroscopic data (NMR and IR) and melting points with those reported in the literature [17, 18].

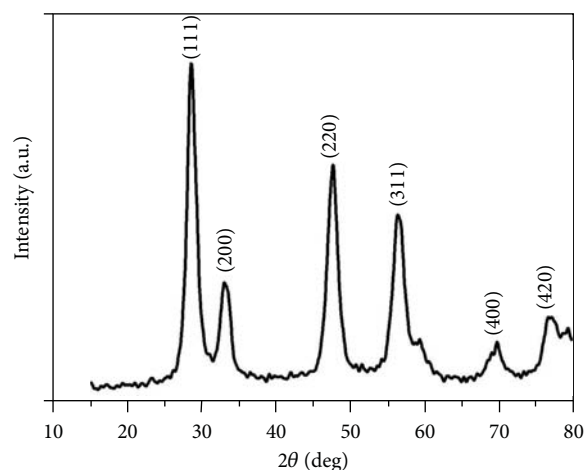
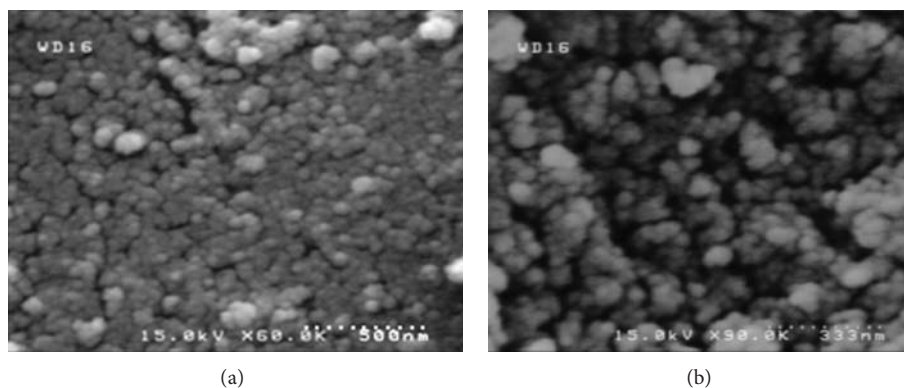
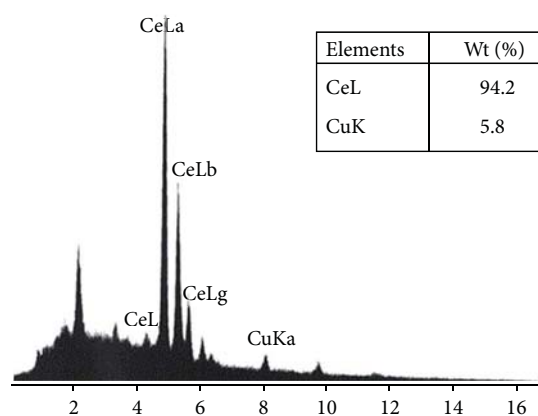


FIGURE 1: XRD pattern of the CuO-CeO₂ nanocomposite catalyst.

with highest intensity at (1, 1, 1) plane that belongs to the XRD standard JCPDS card number of 43-1002. According to the pattern of pure CeO₂ (not shown in the figure), only the diffraction peaks of ceria crystallites are detected, and there is no peaks related to copper oxide nanoparticles. It is supposed that fine dispersion and/or amorphous structure of CuO with low content on the surface of ceria clusters is responsible for absence of copper oxide peaks at the XRD pattern [9, 30, 31]. However, there is some difference between values of unit cell parameters for pure CeO₂ and CuO-CeO₂ due to lattice shrinkage in surface ceria structure. The calculation showed 5.45 and 5.42°Å for CeO₂ and CuO-CeO₂, respectively. The observed shrinkage may be consequence of partial incorporation of CuO into the CeO₂ lattice structure that has been reported for coprecipitation synthesis [30, 31]. The calculated average crystal size of the ceria in the

FIGURE 2: FESEM image of the CuO-CeO₂ nanocomposite catalyst.FIGURE 3: EDS analysis of the CuO-CeO₂ nanocomposite catalyst.

catalyst based on dominant peak at 2θ of 28.5° using Debye-Scherrer equation was 7.5 nm. BET specific surface area result was $131 \text{ m}^2/\text{g}$ that confirms estimated value for average nanoparticle size of the catalyst by XRD test.

Figures 2(a) and 2(b) present FESEM micrograph of the catalyst at two different magnifications to study the morphology and the evaluation of nanoclusters size of catalyst. It seems that 7 nm particles calculated based on the BET surface area are agglomerated to approximately 33 nm sized clusters and made bigger nanostructure CuO-CeO₂ catalyst.

EDS analysis (Figure 3) showed the presence of 5.8 and 94.2 wt.% for Cu and Ce elements in the catalyst, respectively.

Optimization of the reaction conditions showed that the best results in the presence of 0.05 g of CuO-CeO₂ nanostructured catalyst at 80°C were obtained under solvent-free conditions, when the relative ratio of the aldehyde and 2-naphthol was 2:1, respectively. Using these optimized conditions, the reaction of various aromatic aldehydes, containing electron-donating and electron-withdrawing groups, was explored (Table 1). Aliphatic aldehydes remain intact under the same reaction conditions. Therefore, the method can be useful for the chemoselective synthesis of Aryl-14H-dibenzo[a-j]xanthenes from aromatic aldehydes in the presence of aliphatic ones.

TABLE 2: Recyclability of CuO-CeO₂ nanocomposite.

Run	1	2	3	4	5	6	7	8
Time (min)	15	15	15	18	18	20	20	25
Yield (%) ^a	93	93	92	92	92	90	88	88

^a Isolated yield.

The activity of the recycle catalyst was also examined under the optimized conditions, and the desired product was obtained in high yields after 1–8 runs (Table 2). To investigate these property for our introduced catalyst, the reaction of benzaldehyde with 2-naphthol was selected as the model (Table 2). After each reaction, we washed and dried the catalyst with acetone and reused for the next run. This process was repeated for 8 runs, and no appreciable yield decrease was observed.

4. Conclusions

We have developed a new, efficient, and green procedure for the synthesis of biologically important xanthene derivatives catalyzed by recyclable CuO-CeO₂ nanostructured catalyst, under solvent-free conditions. This catalyst can promote the yields and reaction times over 8 runs without noticeable loss in its efficiency. Moreover, high yields of products, short reaction times, ease of workup, and clean operation are the most important advantages of this method which makes the procedure beneficial compared to conventional methods.

Acknowledgment

The authors are thankful to the Behbahan Khatam Al-Anbia, University of Technology, for the partial support of this work.

References

- [1] D. Astruc, *Nanoparticles and Catalysis*, Wiley-VCH, Weinheim, Germany, 2008.
- [2] H. Sharghi and M. Hosseini, "Solvent-free and one-step Beckmann rearrangement of ketones and aldehydes by zinc oxide," *Synthesis*, no. 8, pp. 1057–1059, 2002.

- [3] M. H. Sarvari and H. Sharghi, "Reactions on a solid surface. A simple, economical and efficient Friedel-Crafts acylation reaction over zinc oxide (ZnO) as a new catalyst," *Journal of Organic Chemistry*, vol. 69, no. 20, pp. 6953–6956, 2004.
- [4] S. F. Yin, B. Q. Xu, S. J. Wang, C. F. Ng, and C. T. Au, "Magnesia-Carbon nanotubes (MgO-CNTs) nanocomposite: novel support of Ru Catalyst for the generation of CO_x-free Hydrogen from Ammonia," *Catalysis Letters*, vol. 96, pp. 113–116, 2004.
- [5] M. T. Drexler and M. D. Amiridis, "Kinetic investigation of the heterogeneous synthesis of flavanone over MgO," *Catalysis Letters*, vol. 79, no. 1–4, pp. 175–181, 2002.
- [6] R. S. Varma, "Solvent-free organic syntheses: using supported reagents and microwave irradiation," *Green Chemistry*, vol. 1, no. 1, pp. 43–55, 1999.
- [7] S. Samantaray, D. K. Pradhan, G. Hota, and B. G. Mishra, "Catalytic application of CeO₂-CaO nanocomposite oxide synthesized using amorphous citrate process toward the aqueous phase one pot synthesis of 2-amino-2-chromenes," *Chemical Engineering Journal*, vol. 193, pp. 1–9, 2012.
- [8] S. Li, W. Zhang, M. H. So, C. M. Che, R. Wang, and R. Chen, "One-pot solvothermal synthesis of Pd/F_eSO₄ nanocomposite and its magnetically recyclable and efficient catalysis for Suzuki reactions," *Journal of Molecular Catalysis A*, vol. 359, pp. 81–87, 2012.
- [9] A. Razeghi, A. Khodadadi, H. Ziaei-Azad, and Y. Mortazavi, "Activity enhancement of Cu-doped ceria by reductive regeneration of CuO-CeO₂ catalyst for preferential oxidation of CO in H₂-rich streams," *Chemical Engineering Journal*, vol. 164, no. 1, pp. 214–220, 2010.
- [10] S. Chatterjee, M. Iqbal, J. C. Kauer et al., "Xanthene derived potent nonpeptidic inhibitors of recombinant human calpain I," *Bioorganic and Medicinal Chemistry Letters*, vol. 6, no. 13, pp. 1619–1622, 1996.
- [11] J. P. Poupelin, G. Saint Ruf, O. Foussard Blanpin, G. Narcisse, G. Uchida-Ernouf, and R. Lacroix, "Synthesis and antiinflammatory properties of bis (2 hydroxy 1 naphthyl) methane derivatives," *European Journal of Medicinal Chemistry*, vol. 13, no. 1, pp. 67–71, 1978.
- [12] O. Sirkecioglu, N. Tulinli, and A. Akar, "Synthesis of 14-Aryl-14H-dibenzo[a-j]xanthenes," *Journal of Chemical Research*, pp. 502–506, 1995.
- [13] R. M. Ion, A. Planner, K. Wiktorowicz, and D. Frackowiak, "The incorporation of various porphyrins into blood cells measured via flow cytometry, absorption and emission spectroscopy," *Acta Biochimica Polonica*, vol. 45, no. 3, pp. 833–845, 1998.
- [14] R. J. Sarma and J. B. Baruah, "One step synthesis of dibenzoxanthenes," *Dyes and Pigments*, vol. 64, no. 1, pp. 91–92, 2005.
- [15] K. Chibale, M. Visser, D. Van Schalkwyk, P. J. Smith, A. Saravanamuthu, and A. H. Fairlamb, "Exploring the potential of xanthene derivatives as trypanothione reductase inhibitors and chloroquine potentiating agents," *Tetrahedron*, vol. 59, no. 13, pp. 2289–2296, 2003.
- [16] L. Wu, J. Zhang, L. Fang, C. Yang, and F. Yan, "Silica chloride catalyzed synthesis of 14-aryl-14H-dibenzo[a,i]xanthene-8,13-diones," *Dyes and Pigments*, vol. 86, no. 1, pp. 93–96, 2010.
- [17] S. Allameh, A. Davoodnia, and A. Khojastehnezhad, "An efficient and eco-friendly synthesis of 14-Aryl-14H-dibenzo[a-j]xanthenes using H₄[SiW₁₂O₄₀] as a heterogeneous and reusable catalyst under solvent-free conditions," *Chinese Chemical Letters*, vol. 23, pp. 17–20, 2012.
- [18] I. Mohammadpoor-Baltork, M. Moghadam, V. Mirkhani, S. Tangestaninejad, and H. R. Tavakoli, "Highly efficient and green synthesis of 14-aryl(alkyl)-14H-dibenzo[a,j] xanthene and 1,8-dioxooctahydroxanthene derivatives catalyzed by reusable zirconyl triflate [ZrO(OTf)₂] under solvent-free conditions," *Chinese Chemical Letters*, vol. 22, no. 1, pp. 9–12, 2011.
- [19] A. R. Hajipour, Y. Ghayeb, N. Sheikhan, and A. E. Ruoho, "Brønsted acidic ionic liquid as an efficient and reusable catalyst for synthesis of 14-aryl-or 14-Aryl-14H-dibenzo[a-j]xanthenes under solvent-free conditions," *Synlett*, no. 5, pp. 741–744, 2010.
- [20] S. Ko and C. F. Yao, "Heterogeneous catalyst: amberlyst-15 catalyzes the synthesis of 14-substituted-14H-dibenzo[a,j] xanthenes under solvent-free conditions," *Tetrahedron Letters*, vol. 47, no. 50, pp. 8827–8829, 2006.
- [21] T. S. Rivera, A. Sosa, G. P. Romanelli, M. N. Blanco, and L. R. Pizzio, "Tungstophosphoric acid/zirconia composites prepared by the sol-gel method: an efficient and recyclable green catalyst for the one-pot synthesis of 14-Aryl-14H-dibenzo[a-j]xanthenes," *Applied Catalysis A*, vol. 443, pp. 207–213, 2012.
- [22] M. Dabiri, M. Baghbanzadeh, M. Shakouri Nikcheh, and E. Arzroomchilar, "Eco-friendly and efficient one-pot synthesis of alkyl- or Aryl-14H-dibenzo[a-j]xanthenes in water," *Bioorganic and Medicinal Chemistry Letters*, vol. 18, no. 1, pp. 436–438, 2008.
- [23] G. B. Dharma Rao, M. P. Kaushik, and A. K. Halve, "An efficient synthesis of naphtha[1, 2-e]oxazinone and 14-substituted-14H-dibenzo [a, j] xanthene derivatives promoted by zinc oxide nanoparticle under thermal and solvent-free conditions," *Tetrahedron Letters*, vol. 53, pp. 2741–2744, 2012.
- [24] F. Shirini and N. Ghaffari Khaligh, "Succinimide-N-sulfonic acid: an efficient catalyst for the synthesis of xanthene derivatives under solvent-free conditions," *Dyes and Pigments*, vol. 95, pp. 789–794, 2012.
- [25] R. Kumar, G. C. Nandi, R. K. Verma, and M. S. Singh, "A facile approach for the synthesis of 14-aryl- or alkyl-14H-dibenzo[a,j]xanthenes under solvent-free condition," *Tetrahedron Letters*, vol. 51, no. 2, pp. 442–445, 2010.
- [26] J. Albadi, M. Keshavarz, F. Shirini, and M. Vafaie-nezhad, "Copper iodide nanoparticles on poly(4-vinyl pyridine): a new and efficient catalyst for multicomponent click synthesis of 1,4-disubstituted-1,2,3-triazoles in water," *Catalysis Communications*, vol. 27, pp. 17–20, 2012.
- [27] J. Albadi, N. Iravani, F. Shirini, and F. Dehghan, "A green recyclable poly(4-vinylpyridine)-supported copper iodide nanoparticle catalyst for the chemoselective synthesis of pentaerythritol diacetals from aromatic aldehydes," *Journal of Chemical Research*, vol. 36, no. 10, pp. 610–611, 2012.
- [28] J. Albadi, N. Iravani, and M. Khoshakhlagh, "A new, green and recyclable poly(4-vinylpyridine)-supported copper iodide nanoparticles catalyst for the synthesis of aryl -14H-dibenzo[a-o]xanthenes," *Iranian Journal of Catalysis*, vol. 2, pp. 85–89, 2012.
- [29] J. Albadi, M. Keshavarz, M. Abedini, and M. Vafaie-nezhad, "Copper iodide nanoparticles on poly(4-vinyl pyridine) as new and green catalyst for multicomponent click synthesis of 1, 4-disubstituted-1, 2, 3-triazoles in water," *Chinese Chemical Letters*, vol. 23, pp. 797–800, 2012.
- [30] P. Ratnasamy, D. Srinivas, C. V. V. Satyanarayana et al., "Influence of the support on the preferential oxidation of CO in hydrogen-rich steam reformates over the CuO-CeO₂-ZrO₂ system," *Journal of Catalysis*, vol. 221, pp. 455–465, 2004.

- [31] Z. Liu, R. Zhou, and X. Zheng, "Preferential oxidation of CO in excess hydrogen over a nanostructured CuO-CeO₂ catalyst with high surface areas," *Catalysis Communications*, vol. 9, pp. 2183–2186, 2008.

Research Article

Rapid, Low-Cost, and Ecofriendly Approach for Iron Nanoparticle Synthesis Using *Aspergillus oryzae* TFR9

Jagadish Chandra Tarafdar and Ramesh Raliya

Central Arid Zone Research Institute, Jodhpur 342003, India

Correspondence should be addressed to Jagadish Chandra Tarafdar; jctarafdar@yahoo.in

Received 31 January 2013; Accepted 28 February 2013

Academic Editor: Mohammad H. Maneshian

Copyright © 2013 J. C. Tarafdar and R. Raliya. This is an open access article distributed under the Creative Commons Attribution License, which permits unrestricted use, distribution, and reproduction in any medium, provided the original work is properly cited.

Development of reliable and ecofriendly green approach for synthesis of metallic nanoparticles biologically is an important step in the field of application of nanoscience and nanotechnology. The present paper reports the green approach for iron nanoparticle synthesis using *Aspergillus oryzae* TFR9 using FeCl_3 as a precursor metal salt. Valid characterization techniques employed for biosynthesized iron nanoparticles including dynamic light scattering (DLS), transmission electron microscopy (TEM), and high resolution-transmission electron microscopy (HR-TEM) for morphological study. X-ray energy dispersive spectroscopy (EDS) spectrum confirmed the presence of elemental iron signal in high percentage. Apart from ecofriendliness and easy availability, low-cost biomass production will be more advantageous when compared to other chemical methods. Biosynthesis of iron nanoparticles using fungus has greater commercial viability that it may be used in agriculture, biomedical and engineering sector.

1. Introduction

Nanotechnology is the manipulation or self-assembly of individual atoms, molecules, or molecular clusters into structures to create material and devices with new and vastly different properties. “Nano” suffix usually refers to a size scale between 1 nanometer (nm) and 100 nm at least at one dimension [1]. Owing to its inimitable properties, nanotechnology provides the basic tools and subsequently the technology for gathering information and designing innovative devices to probe questions related to biological importance of nutritional availability, and the application of this knowledge in diverse sector including physics, chemistry, biology, and engineering [2].

Conventional methods such as sol-gel, aerosol, template assisted, sonochemical, laser exposer, wet-chemical synthesis, thermal decomposition, plasma synthesis, and hydrothermal synthesis often required several processing steps, controlled pH, temperature, pressure, much expensive equipment, and toxic chemicals. Furthermore, such techniques also generate several byproducts which are toxic to ecosystems. So, there is a need to develop a low-cost, ecofriendly method for agriculturally important nanoparticles [3, 4].

Therefore, microbial systems are now being increasingly explored as safer alternatives for production of nanoparticles [5, 6]. Shahi and Patra [7] produced nanoparticles of usnic acid with an ascomycetes fungus. Lee et al. [8] produced superparamagnetic nanoparticles by *Shewanella* sp. Yadav et al. [9] produced selenium containing nanostructures using *Pseudomonas aeruginosa* while Sadowski and Maliszewska [10] produced nanoparticles of silver using *Pseudomonas stutzeri*. Senapati et al. [11] produced bimetallic alloy of Au-Ag using microorganisms.

Synthesis of nanoparticles using fungi (eukaryotic organism) has several advantages over prokaryotic mediated approach regarding reproducibility of nanosized materials, and these also include ease to multiplication, grow, handling, and rest of downstream process for this top-down approach of nanobiosynthesis through nanofactories [3].

During the recent years, there has been a great deal of interest in iron nanoparticles due to technological applications such as high-density magnetic recording media, biosensors, ferrofluids, magnetic resonance imaging, nutrients and biomedicine [12]. Iron is the metal used at the active site of many important redox enzymes dealing with cellular

respiration and oxidation reduction in plants and animals. Iron also acts as cofactor and structural component for various enzymes.

In the present investigation attempt was made for rapid, low cost and ecofriendly iron nanoparticles synthesis using the fungi *Aspergillus oryzae* TFR9. This study includes morphological and elemental characterization of the biosynthesized iron nanoparticles.

2. Experimental

2.1. Isolation of Fungi. The fungus, *Aspergillus oryzae* TFR9 (NCBI GenBank accession no. JQ675292), was isolated from agricultural research farm (26°18'N 73°01'E) of Central Arid Zone Research Institute, Jodhpur, India. The pure culture of fungi was isolated by plating the primary inoculum on Martin's-rose Bengal agar medium (HiMedia, India, pH 7.2) after serial dilutions of collective soil sample. Antibiotic chloramphenicol (Sigma-Aldrich, St. Louis, MI, USA) was added at a concentration of $10 \mu\text{g mL}^{-1}$ after autoclaving to prevent bacterial contamination. Inoculated plates were incubated at 28°C for 72 h in biological oxygen demand (BOD) incubator. Individual fungal colonies were picked and further purified by subculturing on potato dextrose agar (PDA) media (HiMedia, India). Preliminary identification of fungal isolates was performed on the basis of morphological characteristics, results not shown here.

2.2. Molecular Identification of Used Fungus. The molecular level identification in which partial sequencing of 18S and 28S rRNA and complete sequence of internal transcribed sequence 1 (ITS-1), internal transcribed sequence 2 (ITS-2), and 5.8S rRNA gene (complex of 18S-ITS1-5.8S-ITS2-28S-) was made using universal primer ITS1 (5'-TCCGT-AGGTGAACCTGCG-3') and ITS 4 (5'-TCCTCCGCTTA-TTGATATGC-3'). The genomic DNA was isolated by cetyltrimethylammonium bromide (CTAB) extraction method suggested by Sambrook et al. [13]. The rRNA (ribonucleic acid) sequence was submitted to the GenBank of National Centre for Biotechnological Information (NCBI).

2.3. Biosynthesis of Iron Nanoparticles. The fungi, *Aspergillus oryzae* TFR9 (NCBI GenBank accession no. JQ675292), was grown up in 150 mL Erlenmeyer flask containing 50 mL potato dextrose broth medium. After adjusting, the pH of the medium to 5.8, the culture was grown with continuous shaking on a rotary shaker (150 rpm) at 28°C for 72 h. After complete incubation, fungal mycelia were separated from the culture broth by filtration process using Whatman filter paper no. 1 (Whatman, England) under biosafety cabinet (iMSet, Surana Scientific, India) followed by washed thrice with sterile double distilled water. The harvested fungal mycelia were resuspended in 50 mL sterile Milli-Q-water in 150 mL Erlenmeyer flask and again kept on a rotary shaker (150 rpm) at 28°C for 12 h. After incubation, the cell-free filtrate was obtained by separating the fungal biomass using 0.45μ size membrane filter (Whatman, England). Using cell-free filtrate,

salt solution of FeCl_3 (Sigma, USA) was prepared with final concentration of 10^{-3} M in Erlenmeyer flasks, which was found to be optimum precursor salt concentration for the synthesis of iron nanoparticles. The entire mixture was kept on rotary shaker at 28°C at 150 rpm. The reaction was allowed to carry out for a period of 12 h. The biotransformed product was collected periodically for characterization of particle size on the basis of dynamic light scattering method.

Isolation of Fungi

Fungus was isolated (Martin's rose Bengal agar medium, pH 7.2, 28°C for 72 h)

↓

Further subculturing on potato dextrose agar media

↓

Molecular identification

↓

Biosynthesis of iron nanoparticles

Biosynthesis of Iron Nanoparticles

Fungus was grown up in 150 mL Erlenmeyer flask containing 50 mL potato dextrose broth medium (pH 5.8, 28°C for 72 h at 150 rpm on shaker)

↓

Mycelia separated from the culture broth by filtration using Whatman filter paper no. 1

↓

Harvested fungal mycelia resuspended in 50 mL sterile Milli-Q water in 150 mL Erlenmeyer flask and kept on a shaker (150 rpm) at 28°C for 12 h.

↓

Cell-free filtrate obtained by separating the fungal biomass using 0.45μ size membrane filter

↓

Salt solution of FeCl_3 prepared using cell-free filtrate (10^{-3} M)

↓

Entire mixture kept on shaker (150 rpm) at 28°C for 12 h.

↓

Iron nanoparticle synthesized

2.4. Characterization of Iron Nanoparticles

2.4.1. DLS Analysis. The particle size of iron nanoparticles was monitored using dynamic light scattering (DLS) measurements which determines particle size by measuring the rate of fluctuations in the laser light intensity scattered by particles as they diffuses through solvent. Particle size analyzer (Beckman DelsaNano C, USA) was used for size measurement and confirmation of nanoparticles size distribution.

2.4.2. TEM and HR-TEM Analysis. For the confirmation of biosynthesized iron nanoparticle size and shape, transmission electron microscope (TEM) measurements were carried out using drop coating method in which a drop of solution containing nanoparticles was placed on the carbon coated copper grids and kept under vacuum desiccation for overnight before loading them onto a specimen holder. TEM and high-resolution transmission electron microscope (HR-TEM) micrographs of the sample were taken using the JEM-2100F TEM instrument. The instrument was operated at an accelerating voltage of 200 kV.

2.4.3. EDS Analysis. X-ray energy dispersive spectroscopy (EDS) was used for elemental composition analysis, and samples were prepared on a carbon coated copper grids and kept under vacuum desiccation for three hours before loading them onto a specimen holder. Elemental analysis on single particles was carried out using Thermo-Noran EDS attachment equipped with TEM (JEM-2100F). It was performed for determination of the elemental composition and purity of the sample by atom percentage of metal.

3. Results and Discussion

3.1. Identification of Fungi. Identification of fungi *Aspergillus oryzae* TFR9 (NCBI GenBank accession no. JQ675292) was made on the basis of molecular characterization of fungal isolate which was performed by partial sequencing of 18S and 28S rRNA and complete sequence of internal transcribed sequence 1 (ITS-1), internal transcribed sequence 2 (ITS-2), and 5.8S rRNA gene (complex of -18S-ITS1-5.8S-ITS2-28S) and has been submitted in the NCBI GenBank (Accession no. JQ675292). The sequence was compared using Basic Local Alignment Search Tool (BLAST) of NCBI and submitted sequence is available on a public domain <http://www.ncbi.nlm.nih.gov>.

3.2. Biosynthesis of Iron Nanoparticles. The biosynthesis of iron nanoparticles was carried out by exposure of a precursor salt aqueous FeCl_3 solution of 10^{-3} M concentration to fungal cell-free filtrate obtained by incubating the fungus *Aspergillus oryzae* TFR9 in an aqueous solution. The reaction was carried out for 12 h at 28°C .

3.3. Characterization of Iron Nanoparticles. Particle size of biosynthesized iron nanoparticles was analyzed using particle size analyzer (Figure 1). Histogram clearly shows particle size in ranges between 10 nm and 24.6 nm. The polydispersity index (PDI) was 0.258 which shows high monodisperse nature of the particles. PDI reflects the uniformity in synthesized nanoparticles and measured by DLS. The size and uniformity in the biosynthesized iron nanoparticles were further validated by TEM study.

TEM measurements were used to study the morphological confirmation of iron nanoparticles. A TEM micrograph (Figure 2) showed well distribution of spherical iron nanoparticles. Furthermore it can be seen in the HR-TEM

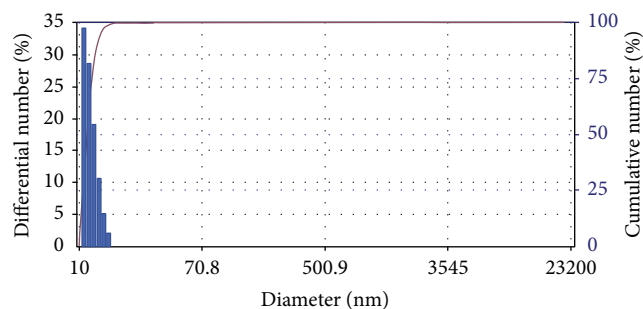


FIGURE 1: DLS histogram of iron nanoparticles for particle size analysis.

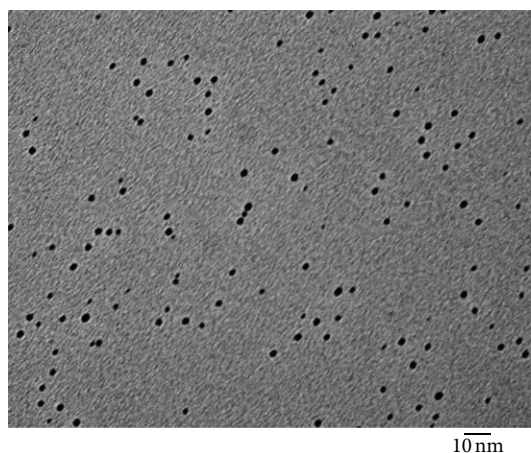


FIGURE 2: TEM micrograph of biologically synthesized iron nanoparticles.

micrograph (Figure 3), which supports also the crystalline nature of biosynthesized iron nanoparticle.

EDS analysis of the particles revealed a strong signal for iron nanoparticles at 6.4 keV, characteristic of iron metal. The EDS spectrum of drop coated biosynthesized iron nanoparticles was shown in Figure 4. Quantitative measuring results obtained from EDS analysis reflect that 84% atom particles were of iron metal which confirms the purity of iron metal in the biotransformed product. The other peaks of chlorine (12.4% atom) and oxygen (3.6% atom) are owing to used precursor salt for biosynthesis of iron nanoparticles.

Microorganisms are well known to defend themselves from metal stress either by segregating the ions intracellular or by secreting them into the external medium [14]. This defensive behavior can be exploited for the biosynthesis of advanced functional iron nanomaterials which has definite edge over chemical synthesis methods. Hazardous organic solvents and surfactants which are often employed in chemical synthesis can be avoided through biosynthesis. Further bio-based synthesis of iron nanoparticles can be reproducible and the resulting nanoparticles were further stabilized by the proteins and reducing agents secreted by the fungus [15]. Extracellular secretion of enzymes offers the advantage to obtain pure, monodisperse nanoparticles, which are free

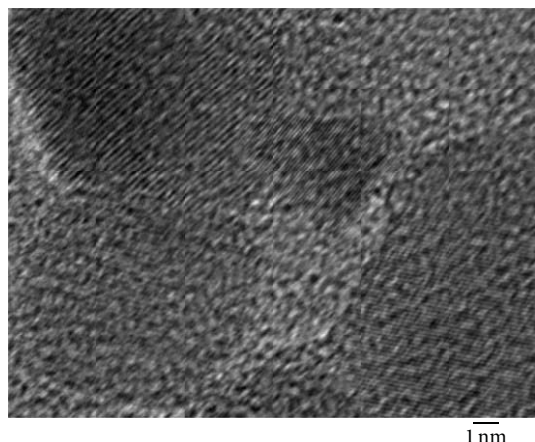


FIGURE 3: HR-TEM micrograph of single iron nanoparticles.

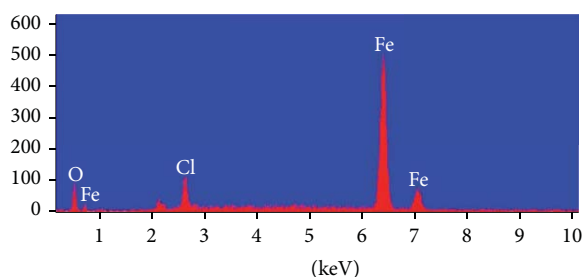


FIGURE 4: EDS spectrum of biosynthesized iron nanoparticles.

from cellular components, associated with organisms and easy downstream processing.

4. Conclusions

In conclusion, the present research of economically efficient, ecofriendly green approach was made to synthesize iron nanoparticles using the fungi *Aspergillus oryzae* TFR9. These useful features of the biosynthesized iron nanoparticles may benefit in agriculture, biomedical, and engineering sector.

Conflict of Interests

The authors declare that they have no conflict of interests.

Acknowledgment

The authors are grateful to ICAR for funding the NAIP project under which the present work has been carried out.

References

- [1] J. C. Tarafdar and R. Raliya, *Nanotechnology*, Scientific Publishers, Jodhpur, India, 2012.
- [2] N. Jain, A. Bhargava, S. Majumdar, J. C. Tarafdar, and J. Panwar, "Extracellular biosynthesis and characterization of silver nanoparticles using *Aspergillus flavus* NJP08: a mechanism perspective," *Nanoscale*, vol. 3, no. 2, pp. 635–641, 2011.
- [3] N. Jain, A. Bhargava, J. C. Tarafdar, S. K. Singh, and J. Panwar, "A biomimetic approach towards synthesis of zinc oxide nanoparticles," *Applied Microbiology and Biotechnology*, vol. 97, no. 2, pp. 859–869, 2013.
- [4] J. C. Tarafdar, A. Agrawal, R. Raliya, P. Kumar, U. Burman, and R. K. Kaul, "ZnO Nano-particles induced synthesis of polysaccharides and phosphatases by *Aspergillus* fungi," *Journal of Advance Science, Engineering and Medicine*, vol. 4, pp. 324–328, 2012.
- [5] R. Raliya and J. C. Tarafdar, "Novel approach for silver nanoparticle synthesis using *Aspergillus terreus* CZR-1: mechanism perspective," *Journal of Bionanoscience*, vol. 6, pp. 12–16, 2012.
- [6] R. K. Kaul, P. Kumar, U. Burman et al., "Magnesium and iron nanoparticles production using microorganism and varying salts," *Materials Science-Poland*, vol. 30, no. 3, pp. 254–258, 2012.
- [7] S. K. Shahi and M. Patra, "Microbially synthesized bioactive nanoparticles and their formulation active against human pathogenic fungi," *Reviews on Advanced Materials Science*, vol. 5, no. 5, pp. 501–509, 2003.
- [8] J. H. Lee, Y. Roh, and H. G. Hur, "Microbial production and characterization of superparamagnetic magnetite nanoparticles by *Shewanella* sp. HN-41," *Journal of Microbiology and Biotechnology*, vol. 18, no. 9, pp. 1572–1577, 2008.
- [9] V. Yadav, N. Sharma, R. Prakash, K. K. Raina, L. M. Bharadwaj, and N. T. Prakash, "Generation of selenium containing nanostructures by soil bacterium, *Pseudomonas aeruginosa*," *Biotechnology*, vol. 7, no. 2, pp. 299–304, 2008.
- [10] Z. Sadowski and I. H. Maliszewska, "Synthesis of silver nanoparticles using microorganisms," *Materials Science-Poland*, vol. 26, pp. 419–442, 2008.
- [11] S. Senapati, A. Ahmad, M. I. Khan, M. Sastry, and R. Kumar, "Extracellular biosynthesis of bimetallic Au-Ag alloy nanoparticles," *Small*, vol. 1, no. 5, pp. 517–520, 2005.
- [12] I. Koh, X. Wang, B. Varughese, L. Isaacs, S. H. Ehrman, and D. S. English, "Magnetic iron oxide nanoparticles for biorecognition: evaluation of surface coverage and activity," *Journal of Physical Chemistry B*, vol. 110, no. 4, pp. 1553–1558, 2006.
- [13] J. Sambrook, E. F. Fritsch, and T. Maniatis, *Molecular Cloning: A Laboratory Manual*, Cold Spring Harbour Laboratory Press, New York, NY, USA, 1989.
- [14] K. B. Narayanan and N. Sakthivel, "Biological synthesis of metal nanoparticles by microbes," *Advances in Colloid and Interface Science*, vol. 156, pp. 1–13, 2010.
- [15] S. Anil Kumar and M. I. Khan, "Heterofunctional nanomaterials: fabrication, properties and applications in nanobiotechnology," *Journal of Nanoscience and Nanotechnology*, vol. 10, no. 7, pp. 4124–4134, 2010.

Review Article

Naturally Self-Assembled Nanosystems and Their Templated Structures for Photonic Applications

**K. Pradeesh, Nageswara Rao Kotla, Shahab Ahmad,
Vindesh K. Dwivedi, and G. Vijaya Prakash**

Nanophotonics Lab, Department of Physics, Indian Institute of Technology Delhi, Hauz Khas, New Delhi 110016, India

Correspondence should be addressed to G. Vijaya Prakash; prakash@physics.iitd.ac.in

Received 25 January 2013; Accepted 24 February 2013

Academic Editor: Amir Kajbafvala

Copyright © 2013 K. Pradeesh et al. This is an open access article distributed under the Creative Commons Attribution License, which permits unrestricted use, distribution, and reproduction in any medium, provided the original work is properly cited.

Self-assembly has the advantage of fabricating structures of complex functionalities, from molecular levels to as big as macroscopic levels. Natural self-assembly involves self-aggregation of one or more materials (organic and/or inorganic) into desired structures while templated self-assembly involves interstitial space filling of diverse nature entities into self-assembled ordered/disordered templates (both from molecular to macro levels). These artificial and engineered new-generation materials offer many advantages over their individual counterparts. This paper reviews and explores the advantages of such naturally self-assembled hybrid molecular level systems and template-assisted macro-/microstructures targeting simple and low-cost device-oriented fabrication techniques, structural flexibility, and a wide range of photonic applications.

1. Introduction

Fabrication of nano/mesa photonic architectures from *top-down* technology involve precise growth techniques like molecular beam epitaxy (MBE), chemical vapor deposition (CVD) and also involve patterning techniques such as photolithography, particle beam lithography, scanning probe lithography, and nanoimprint lithography. While the above mentioned processes are laborious, time-consuming, and costly, the “*bottom-up*” technology based on *self-assembly* approach is the simplest, cost effective technique. Self-assembly is one of the most important “*molecular engineering*” strategies used in fabricating complex functional structures, from micro to the molecular levels, utilising the advantage of self-interaction of molecules. *Molecular self-assembly* is a strategy for nanofabrication that involves designer molecules and supramolecular entities so that molecules naturally aggregate into specific desired structures [1, 2]. This method reduces many difficult steps in nanofabrication, those involving atomic-level modifications of the structures. Moreover, molecular self-assembly tends to produce structures that are relatively defect-free and self-healing, because the target structures are selective with

thermodynamically stable assembly between the possible configurations. Several self-assembly methods have been developed in the recent past, such as phase-separation of copolymers, formation of pores in alumina, liquid crystals, zerogels, and polymer spheres templating [3–5]. At molecular levels, one of the examples of self-assembly is the *intercalation strategy* wherein the organic entities are space-filled within naturally self-assembled crystalline inorganic semiconductor hosts, with an opportunity to produce a very special and tailor-made semiconductor, known as *inorganic-organic hybrids* [6–8]. In a macro level, mono dispersed mesa sized spherical colloids are self-assembled to form three-dimensionally periodic lattices and are famously known as synthetic opals (3D photonic crystals) [9–17]. Another relatively easy and cost-effective methodology to produce nano to wavelength-scaled photonic structures with long-range order is through self-organized systems, which can be used to create periodic patterns, followed by material filling into the interstitial spaces through techniques like electrochemical deposition. This approach is called templated self-assembly. Overall, for large-scale production, the self-assembly and template assisted self-assembly techniques are better alternatives to *top-down* technology.

2. Naturally Self-Assembled Nanosystems

Though inorganic semiconductors are still a material of choice for high-performance semiconductor devices, in recent years organic semiconductors have attracted considerable interest for applications as active materials in low-cost semiconductor devices. For example, displays based on organic light-emitting diodes have already made their way into commercial products, and semiconductor devices like organic FETs have been demonstrated and are being rapidly improved [18–22]. Analogous to low-dimensional inorganic semiconductors are low-dimensional organic nanolayers, which are basically a self-assembly of organic molecules (e.g., *J*-aggregates) [23–25]. Significant advantages of these self-organized molecular nanostructures (*J*-aggregates) are the ultra-sharp absorption line widths with giant oscillator strengths, especially room-temperature performance. *J*-aggregates exhibit a very narrow and red-shifted electronic absorption band (*J* band) and strong fluorescence with a small Stokes shift. These characteristic optical properties, which are the origins of their expected functions, are explained by the interaction between the transition dipole moments [26, 27]. However, while organic semiconductors have obvious advantages, due to simple fabrication and high performance, the main draw-backs are a slow-optical response, lack of thermal/mechanical durability, and most importantly limited life span.

3. Naturally Self-Assembled Inorganic-Organic (IO) Hybrid Systems and Applications

Inorganic-organic (IO) hybrid nanostructures have recently emerged as highly-promising systems for applications as optoelectronic devices, opening up a new dimension to nanotechnology, as unique replacement to their inorganic and organic counterparts. These hybrid systems have great advantage to combine distinct properties of inorganic and organic components within a single-molecular material. The art of combining dissimilar components to yield improved materials is not actually new: ancient building construction material, adobe [28], was made from a mixture of clay (inorganic) and straw (organic). Another classical example is “*blue Maya color*” developed in around 900 A.D., is an IO-hybrid composite. In fact the *Maya blue* is an inorganic-organic hybrid composed of *palygorskite* clay and organic indigo dye $C_{16}H_{10}N_2O_2$ [29, 30]. The most characteristic beauty is its unusual stability; even after centuries of exposure to heat, humidity, and extreme atmospheric conditions, the color hardly faded.

Among various IO-hybrids, one of the most interesting and well-studied materials is a *perovskite* type hybrid [31]. These self-organized materials are derived from the general structure form of AMX_3 where A is an organic moiety, M is a divalent metal (such as Pb^{2+} , Sn^{2+} , Ge^{2+} , Cu^{2+} , Ni^{2+} , Mn^{2+} , Fe^{2+} , Co^{2+} , and Eu^{2+}), and X is a halide (such as I, Br, and Cl). This simple 3D structure AMX_3 consists of corner-sharing MX_6 octahedra extended in three dimensions, where the “A” cations are located in the larger

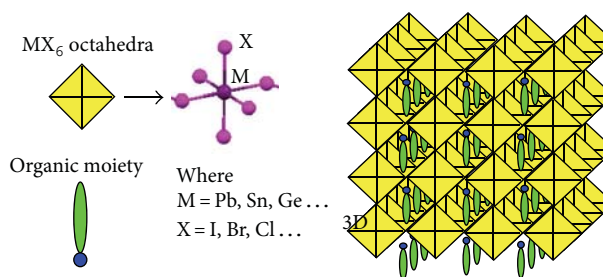


FIGURE 1: Schematic of MX_6 octahedra and the organic moiety of the basic AMX_3 perovskite unit cell and three-dimensional network formed by AMX_3 perovskite unit cells.

12-fold coordinated voids between the octahedra (Figure 1). These self-assembling inorganic-organic perovskites adopt an alternating framework of semiconducting inorganic sheets and organic layers. The increasing interest is because of the ability to derive low-dimensional crystals, which show unique crystal structure and physical and optical properties, from parent 3D networks of AMX_3 from simple and effective natural self-assembly [32–43]. These materials involve different types of interactions allowing the assembly of complex and highly-ordered structures with various bonding schemes. The chemical bonding involved in these IO-hybrid assembled systems are generally described as

- (i) covalent/ionic bonding within the inorganic network which favors the formation of sheets of corner-sharing metal halide octahedra,
- (ii) hydrogen/ionic bonding between the organic cations and the halogens in the inorganic sheets,
- (iii) various weak interactions like *Van der Waals* interactions between the organic R-groups.

Many structural, electrical, thermochromic, and magnetic studies were carried out from almost a decade, to explore the advantages of IO-hybrids over organic and inorganic counterparts [44–46]. These hybrids have an advantage of structural flexibility to choose suitable organic spacers (usually monofunctional or difunctional amines). The crystallographic orientation and the thickness of the perovskite sheets can be tailored as per the choice of appropriate organic cations. In other words, inorganic units can be self-organized into low-dimensional crystals of zero-(0D), one-(1D) and two-(2D) dimensional networks (Figure 2). In 0D networks, MX_6 octahedra are isolated and are surrounded with the organic spacers. In 1D networks, metal halides (MX_6 octahedra) are extended as a chain along one direction with corner/edge/face shared to form 1D hybrid. Similarly, inorganic network can be extended as layered sheets with corner shared MX_6 octahedra to form 2D networks. In 2D, inorganic and organic layers are stacked alternatively with orientation along a specific crystal direction.

During synthesis, the organic moieties, apart from controlling the dimensionality, can also alter the crystallographic orientation of the parent network. For example, based on the organic moiety interaction with metal halide network,

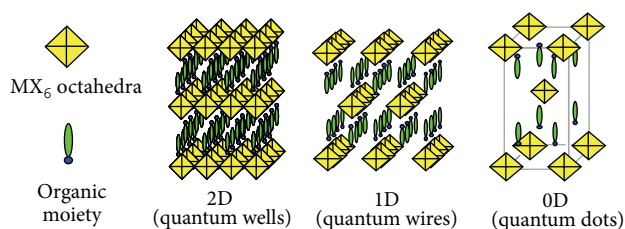


FIGURE 2: Schematic of 2D, 1D, and 0D IO-hybrid derived from parent AMX_3 type 3D IO-hybrid.

the resultant network can deviate from $\langle 100 \rangle$ oriented 2D network [47] to 1D dimensional $\langle 110 \rangle$ oriented hybrid structures also [48, 49]. Under special circumstances, based on organic moiety conformation, the metal halides may self-assemble into either edge sharing or face sharing of metal halide octahedra, forming various low dimensional inorganic halide networks of different orientations. Based on such different networks, these hybrids show marked variation in their structural and optical features [50–59].

Several studies were carried out in the recent past to prove the potential ability of IO-hybrids in photonic applications: electro-absorption and electroluminescence [60–64], photoconductive devices, [65, 66], optical nonlinear devices [67, 68], stark effect [69] magneto-absorption, and spontaneous magnetization [70, 71]. Apart from linear optical studies, high-optical excitation effects such as ultrafast dynamics of excitons [50, 72], observation of higher-order excitons (biexciton and triexciton) [51, 52, 73–75], and even an attempt of biexciton lasing [76] were also reported. Photonic devices such as thin film transistors (TFTs), inorganic-organic field-effect transistors (IOFETs), inorganic-organic light emitting diodes (IOLEDs), and scintillators were also been successfully demonstrated [77–79].

4. Naturally Self-Assembled Two-Dimensional IO-Hybrid Systems

Among the several low-dimensional hybrids mentioned before, 2D hybrids are of special interest. The 2D ($\langle 100 \rangle$ oriented) hybrids are analogous to natural *multiple quantum wells* (MQWs), where inorganic and organic sheets (of molecular level sizes) are alternatively stacked. This is of special attraction because such natural MQWs are easily achieved from solution-processing techniques, without any involvement of laborious instrumentation like molecular beam epitaxy deposition. Various possible layered schemes of these MQWs are shown in Figure 3. Depending on respective inorganic and organic bandgaps, these MQWs can be classified [80] into Type I, II, or III (Figure 3).

In Type I, the conduction band of the inorganic layer is generally below that of the organic layer, and the valence band is above that of the organic layer (Figure 3). Therefore, inorganic sheets act as “quantum wells” for both electrons and holes leading to Type I heterostructure. Similarly, if larger bandgap inorganic sheets are integrated with more complex, conjugated organic cations (with bandgap less than

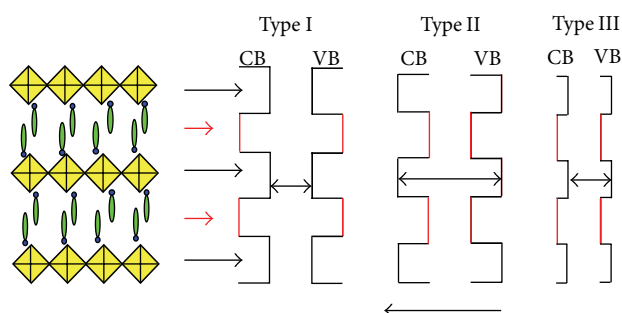


FIGURE 3: 2D IO-hybrid structure and several possible energy level schemes.

inorganic layer), the well and barrier layer roles can be reversed [77] forming Type II heterostructure (Figure 3). In special cases, by appropriate modifications of the chemistry of the organic and inorganic layers, the bandgaps for the organic and inorganic layers can also be offset, leading to Type III heterostructure, in which the wells for the electrons and holes are in different layers. The present study deals with the IO-hybrid system of $R-PbI_4$ (where R is organic), having Type I structure, where the inorganic (PbI network ~ 3 eV) bandgap is much less than the organic bandgap (4 to 6 eV), therefore, the electron-hole confinement is solely within inorganic network.

The most influencing factors in 2D IO-hybrids are (1) the choice of organic moiety, (2) how the organic moiety intercalates into the inorganic network (*vice versa*), thereby altering the structural rearrangement and the consequent energy band structure, (3) quantum confinement due to quantum-limit widths of the individual organic and inorganics, and (4) the dielectric contrast between the organic and inorganic sheets. Technically the last two are dependent on first two factors.

5. Structure and Fabrication Strategies of Naturally Self-Assembled IO-Hybrid Systems

5.1. Structure of Naturally Self-Assembled IO-Hybrids. Generic way of visualization of these IO-hybrids is intercalation of organic guest moieties into a parent crystalline host. Recent efforts in the crystal engineering resulted into the reduction of structures into 0, 1, 2, or 3- low-dimensional hybrid networks [32, 33, 77, 83–87]. The dimensionality of these IO-hybrids, based on the bridging of organic moiety between the MX one-dimensional planes, is critically dependent on (1) the choice of hydrogen bonding scheme between protonated amine terminal group(s) of organic moiety and the MX network and (2) the driving force, size, and shape of the organic molecule [80]. The simplest MX_4^{2-} network consists of corner-sharing metal halide octahedra oriented along $\langle 100 \rangle$ plane and, based on how the organic is

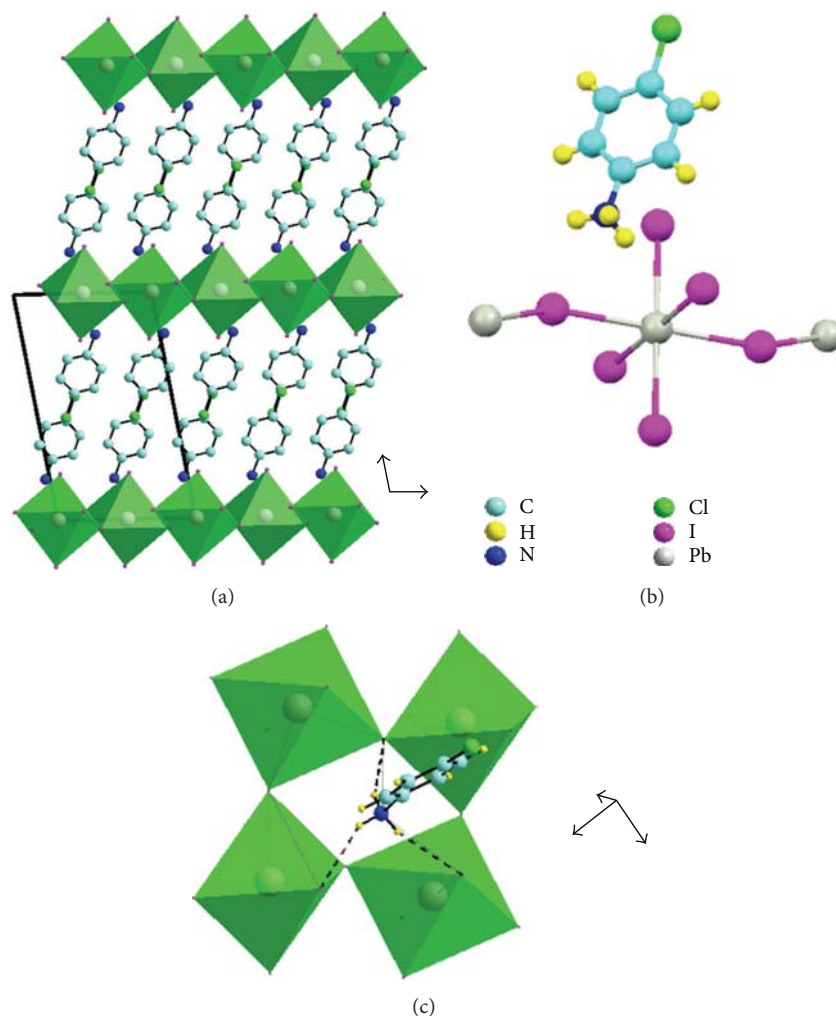


FIGURE 4: (a) Packing structure, (b) asymmetric unit, and (c) NH-I terminal halide configuration (equilateral triangle configuration) of CAPI [81].

intercalated into the parental network, intercalated structures of 0D, 1D, 2D, and 3D can be expected [32, 33, 48, 86, 88, 89].

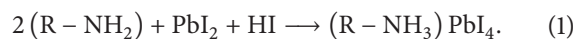
In the two-dimensional R-MX₄ type hybrids, (MX₄)²⁻ octahedral network sheets are stacked up along ⟨100⟩ direction with alternate layers of organic moieties. The crystallographic information for one of the IO-hybrid (4-ClC₆H₄NH₃)₂PbI₄ (CAPI) has been presented in Figure 4. CAPI IO-hybrid crystallizes in the monoclinic space group P2₁/c in which the asymmetric unit consists of half a (PbI₄)²⁻ anion and one (Cl-C₆H₄NH₃)⁺ cation. These structures comprises of well-ordered organic and inorganic layers, arranged alternately stacked along the *a*-direction with layers infinitely extended in the *bc* plane.

5.2. General View of Synthesis, Fabrication, and Implications.

Many device applications demand simple and effective fabrication protocols specially the techniques to make highly uniform device-quality thin films. IO-hybrids are generally fabricated from conventional solution processing methods, and single crystals are harvested by slow evaporation

technique [90–94]. Though several synthesis recipes are available, a simpler, generalized, high product yield, and commercially viable process is as follows. Stoichiometric quantities of organic moiety and inorganic (PbI₂) were mixed with concentrated aqueous HI at 60°C. The resultant solution was allowed to rest at 60°C for an hour and then cooled slowly to room temperature without stirring. The precipitate, thus, obtained was filtered off and dried.

The general synthesis is as follows:



Single crystals of the respective compounds were harvested from slow evaporation process by dissolving the compound in a sparingly soluble solvent. However, the synthesis procedure slightly varies from its generic route depending on the nature of organic moiety.

From the application perspective, thin film processing demands to achieve easy and controlled thickness/morphology over large areas and most importantly highly oriented IO-hybrids. The applications of IO-hybrids will be

immense only if the fabrication parameters are precisely controlled. For the same reason, one has to develop methods of fabrication that can be carefully predicted and controlled for a predetermined technological application. Usual way of fabricating these thin films is from spin-coating of IO-hybrid solutions onto a desired substrate. Although other techniques like single- and double-source thermal vapor deposition, Langmuir Blodgett (LB) method, layer by layer deposition, spray pyrolysis, and low-temperature melting process had been employed to obtain films, it is always difficult to find empirical conditions and processes to obtain well-ordered thin films of these IO-hybrids [95–100]. Especially the applicability of thermal vapor deposition technique is limited due to stability and contamination issues and to balance organic and inorganic evaporation rates simultaneously. Recently, Rikukawa group [95] had developed layer-by-layer self-assembly method to fabricate ultra-thin films of bifunctional amino end-group based IO-hybrid. This method is based on alternate dipping of hydrophilic substrates in organic iodide and lead halides solutions followed by repeated washing to remove unreacted residuals, and this procedure was repeated several times to obtain required self-assembly films, up to 12 layers.

We have recently explored one of the much simpler, but efficient technique, so-called intercalation process to fabricate highly-ordered IO-hybrids over centimeter size lateral dimensions. In fact, the word *intercalation* in general refers to insertion of guest into self-assembled 2D/3D solids. Gieseking [101] and MacEwan [102] showed, for the first time, the ability of the formation of IO-hybrid by intercalation of organic cations into layered and charged inorganic hosts and further extended to neutral guest/hosts by Bradley [103]. Owing to the intense interest in new nanocomposite functional hybrid materials for fundamental and device-oriented research, new *intercalation chemistry* has been established [104]. For 2D layered hybrids it is essential to focus on both new hybrids as well as highly ordered films, however, the later one has not been widely considered.

As mentioned before, the kinetics and layer formation during intercalation are critically dependent on the nature and shape of the guest moiety, concentration of guest molecules, thickness of parent films, intercalation time, and the solvent used [7]. The schematic of intercalation strategy of IO-hybrid for a high-quality thin film fabrication is demonstrated in Figure 5. When predeposited layered PbI_2 film is intercalated with presynthesized organic iodide, the structural network of PbI_2 and the conformation of organic chain are changed to form IO-hybrids. Uniform 2D IO-hybrid films can, thus, be fabricated by an appropriate choice of organic moieties. A brief description of the intercalation process is explained here by taking an example of the IO-hybrid 2(1-cyclohexenyl) ethylammonium tetraiodoplumbate ($(\text{C}_6\text{H}_9\text{C}_2\text{H}_4\text{NH}_3)_2\text{PbI}_4$, CHPI) [7]. The organic iodide, 2-(1-cyclohexenyl) ethylammonium iodide ($\text{C}_6\text{H}_9\text{C}_2\text{H}_4\text{NH}_3\text{I}$) (CHI) is formed when 1 mL of 2-(1-cyclohexenyl) ethylamine was added to 2.1 mL of HI (47%). The obtained light yellow precipitate CHI eventually has been filtered and dried for further use. Similar is the method for other organic iodide synthesis. Suitable solvent (such as

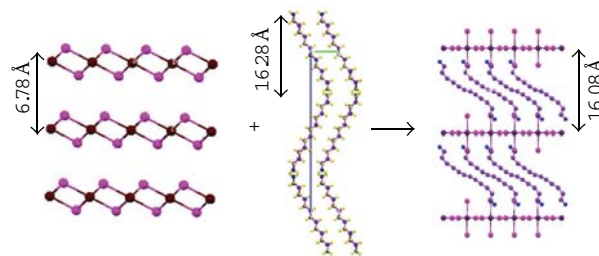


FIGURE 5: Schematic representation of intercalation process for 2D layered IO-hybrid thin films [7]. Essentially the intercalation method involves the intercalation of organic moiety into interstitial spaces of layered inorganic host to obtain desired inorganic-organic exfoliated layered hybrid.

toluene or a combination of toluene and isopropanol) is taken to dissolve organic iodide. Special care has to be taken on the solvent ratio so as to dissolve only the organic iodide but not PbI_2 or the resultant hybrid. Finally, the deposited PbI_2 thin films are dipped into organic iodide films, with a controlled speed and for specific time, to obtain desired IO-hybrid films. The resultant films, fabricated by the intercalation process, were smooth and uniform over a large area and had shown relatively well-stacked ($00l$ oriented) inorganic and organic monolayers [7] (Figure 6).

6. Room-Temperature Optical Exciton Features

Exciton absorption/emission features in these low-dimensional IO-hybrids, especially in 2D hybrids, are significantly enhanced as compared to the 3D counterpart, due to the low-dimensionality. In the PbI based 2D IO-hybrids, electrons are excited from the valence band (VB), consisting of a mixture of Pb (6s) and I (5p) states, to the conduction band (CB), derived mainly from the Pb (6p) states, leaving holes in the VB. An electron and hole pair up to form an exciton via coulomb interaction, and the resulted excitons produce photoluminescence by radiative recombination [105, 106]. The enhancement of exciton features in 2D systems is a well-known phenomenon because of the spatial electron and hole confinement in a very thin and deep quantum wells and, hence, multiples the exciton binding energy, enabling *quantum confinement effect*. Apart from the usual quantum confinement in these natural MQWs, the excitons binding energies are further enhanced due to large contrast in dielectric constants of organic and inorganic layers. Such large binding energy enhancement, leading to strong room-temperature exciton features, often is referred as *dielectric confinement* effects [107, 108]. Ishihara et al. [105] in 1989, reported for the first time the exciton binding energy of $(\text{C}_{10}\text{H}_{21}\text{NH}_3)_2\text{PbI}_4$ (C10PI), which is 370 meV and is much higher than that of bulk PbI_2 , (~ 30 meV) [106]. This was well-accounted from *dielectric confinement* assumption, where the dielectric difference between “well” and “barrier” induces strong coulombic interaction between an electron and a hole

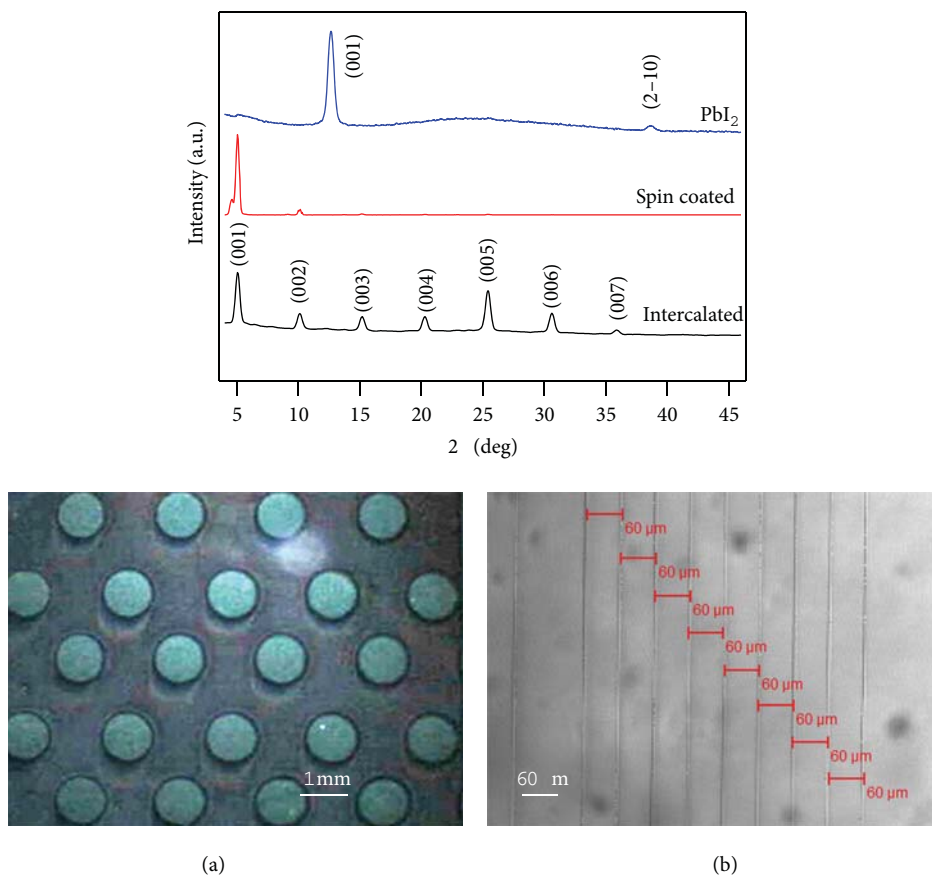


FIGURE 6: X-ray diffraction patterns of pure PbI_2 film, spin-coated CHPI (from synthesized CHPI), and intercalated CHPI films (for 10 seconds) [7]. Bottom microscopic reflection images represent the obtained periodic photonic structures using top-down technology: (a) patterned structures from direct deposition of materials from templates using intercalation technique and (b) femtosecond laser written structures on CHPI thin films.

and as a consequence the binding energy of the exciton is 12 times larger than that of PbI_2 [84, 105, 107–109].

For example, in CAPI (Figure 4), the inorganic and organic layer thicknesses are estimated to be 6 Å and 10 Å. This layered structure resembles MQWs, where inorganic layer has a bandgap of ~ 3 eV forming “well,” and organic layer has a bandgap ~ 6 eV forming “barrier.” Figure 7 shows the typical photoluminescence (PL) and absorption spectra of CAPI thin film.

The room-temperature absorption of CAPI shows two principal absorptions: a broad absorption at ~ 400 nm and a strong narrow peak at ~ 480 nm (Figure 7 (black)). While the former is attributed to the charge-transfer transition between the organic and inorganic layers, the narrow absorption peak at about 480 nm is attributed to the lowest exciton within the inorganic layers [84, 105, 110]. CAPI thin films show strong room-temperature photoluminescence (PL) at ~ 485 nm upon UV excitation (Figure 7 (red)). The PL spectrum of CAPI has narrow line shape with spectral width ~ 15 nm. The oscillator strength of exciton absorption peak peak of CAPI has narrow line shape with spectral width ~ 15 nm. The oscillator strength of exciton absorption peak peak of CAPI has narrow line shape with spectral width ~ 15 nm.

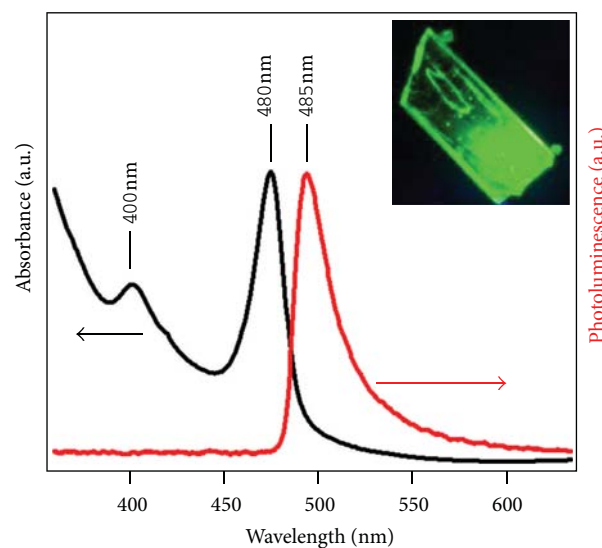


FIGURE 7: Absorption and PL spectra of the 2D layered IO-hybrid, CAPI, thin film [81]. Inset shows typical single crystal PL microscope image.

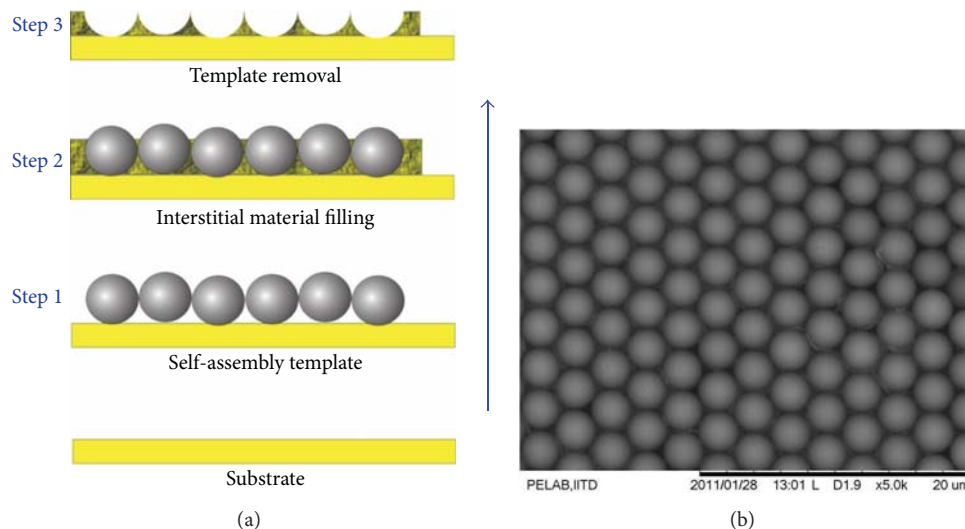


FIGURE 8: (a) Schematic representation of self-assembly template assisted fabrication of photonic structures and (b) polymer microsphere templates.

is $f = 6.5 \times 10^{15} \text{ cm}^{-2}$. Since, for the film thickness of 100nm, there are ~ 70 quantum wells, the oscillator strength per quantum-well $f_{\text{qw}} = 9.2 \times 10^{13} \text{ cm}^{-2}$. This value is an order of magnitude higher than the conventional inorganic quantum wells such as InGaAs structure [111].

Despite some understanding on the dependence of exciton energies of 2D layered IO-hybrids on various parameters like the inorganic *well* width and organic *barrier* separation, the dielectric contrast and the inorganic layer geometrical arrangement, quantitative calculations of exciton binding energies remain out of reach. A systematic correlation between the exciton energies and a specific structural feature has recently been established and discussed [110, 112]. However, the structural features are strongly dependent on several factors such as (1) disorder or conformation of the organic moiety, (2) crystal packing, (3) arrangement of inorganic layers, and (4) position of tagging of ammonium group in organic moiety to the PbI network. As a consequence the optical excitons features are also strongly dependent on the studied IO-hybrid thin films based on organic moiety conformation, solvent used, temperature, and the film thickness [110, 113–115]. Special control over thickness of the IO-hybrid film is critical for device oriented 3D structure fabrication, to avoid the exciton deformation and defect related emission/absorption features.

7. Templated Self-Assembled Microstructures

Carving useful materials itself into the nano to micron-sized structures using simple bottom-up technology is economically viable. This new approach is based on the natural self-assembly of templates and subsequently space filling the voids either by precipitation via chemical routes or by the electrochemical reduction of materials (Figure 8). Therefore, nano-/microstructuring using templates such as artificial polymer opals and liquid crystal is a whole new

class of research. These micro-/nanostructures have potential applications such as tunable plasmonic bandgaps [116], novel types of liquid crystal displays [117], and nanolaser cavities [118]. These macroporous materials are already available in the market as surface enhanced Raman scattering (SERS) devices [119]. Despite the fact that the methodology offers highly ordered structures with very large single-crystalline domains, it has so far been restricted only to metals.

However, fabrication of self-assembled semiconductor photonic structures is still scarce, particularly understanding the chemistry for interstitial filling and deposition for semiconductors and adequate interconnectivity between the pores [120–123]. Electrochemical deposition is one of the low-cost deposition techniques which is an optimal bottom up technique for complete interstitial space filling of desired material through various types of templates. Over the years, conducting thin films (Ag, Au, etc.) were deposited on various semiconducting and conducting substrates utilizing this technique, but the deposition of semiconductors, organic materials, and polymers have always been a formidable task, due to low-conductivity issues. Constant research work on electrodeposition finally emerged out to be more useful than expected when deposition of semiconductors and several organic materials had been possible. However, structural and optoelectronic properties of semiconductors are critically affected by the preparation conditions such as fabrication method, types of substrates, thickness, and annealing conditions. Nevertheless, it is necessary to optimize the fabrication conditions and postprocessing methods for desired applications.

Here the template assisted method to fabricate periodic structures from 50 nm to as big as 20 micron is exemplified. After having optimized electrodeposition conditions, such as electrolyte recipe, surface quality, structural, and optical properties, we have extensively investigated to fabricate 2D and 3D periodic and quasiperiodic nano/micro-structure

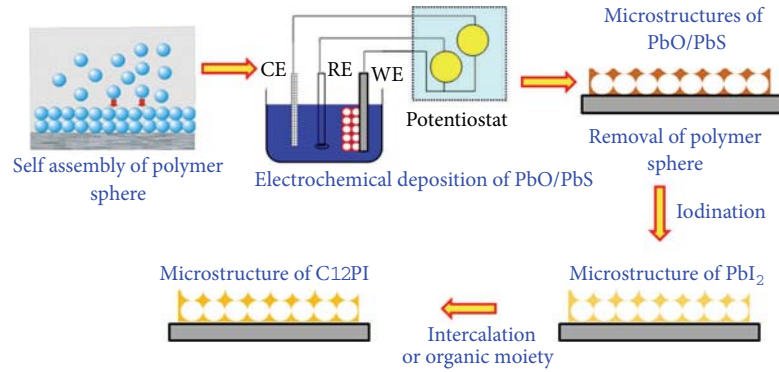


FIGURE 9: Schematic representation of carving naturally self-assembled hybrid systems into 2D/3D microstructures from template self-assembly method.

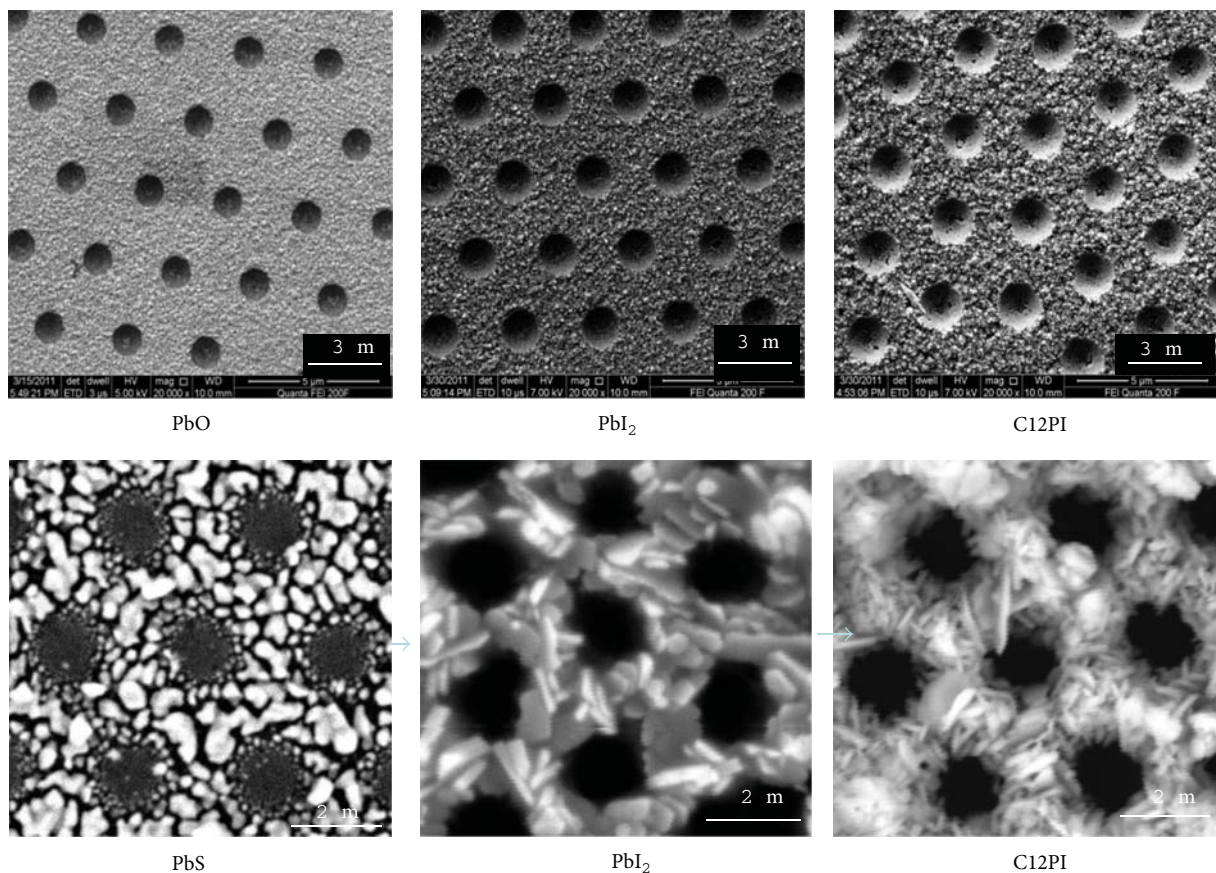


FIGURE 10: Scanning electron microscope images of template-assisted PbO, PbI₂, PbS, and C12PI microstructures [82].

from template-assisted growth techniques [11, 12, 17, 82]. During this investigation, several composite semiconductors such as CdSe, CdTe, ZnO, PbO, PbS, and PbI₂ are successfully fabricated and their optoelectronic properties are thoroughly investigated. We further demonstrated micron-scale 2D periodic highly emitting IO-hybrid structures, using template-assisted electrochemical growth followed by three-step processing, which can be easily extended to wave-length scale and nanoscale structures.

The systematic procedure has been explained in the schematic diagram (Figure 9). Essentially the electrodeposited PbO/PbS microstructures (Figure 10) are iodinated to obtain PbI₂ microstructures, then the presynthesized organic iodide is intercalated into PbI₂ to obtain desired IO-hybrid microstructures. During the process, the thickness of IO-hybrid film has to be fixed and such thickness optimization is required because these type of IO-hybrids are sensitive to thickness induced stacking imperfections, which directly

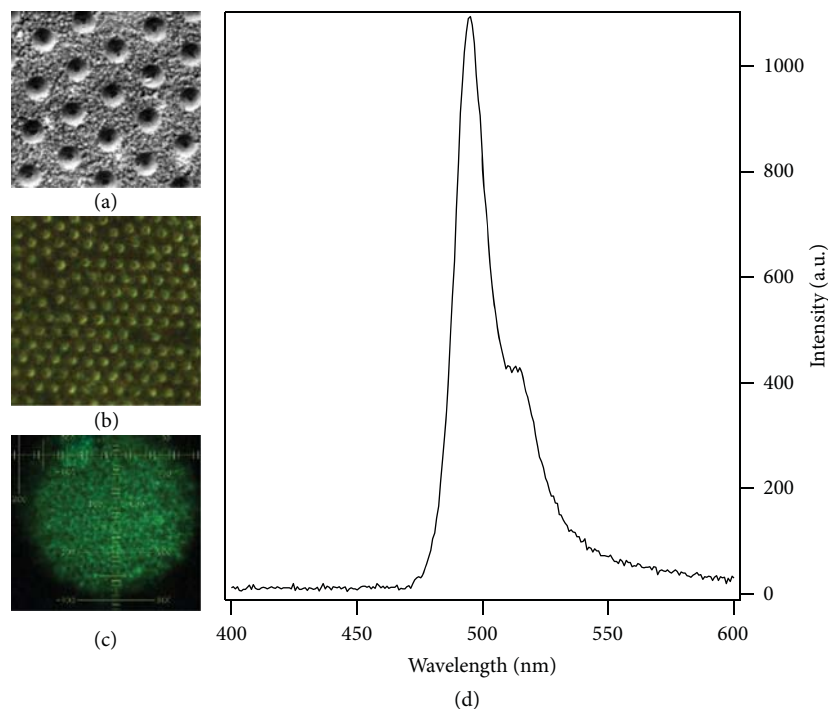


FIGURE 11: (a) SEM, (b) dark field microscope, and (c) PL microscope images ($\lambda_{\text{ex}} \sim 410$ nm), (d) corresponding to the PL spectra from the fabricated C12PI microstructures [82].

results into rapid change in their exciton-related emission/absorption behavior. The thickness-dependent disorder produce uneven crystalline planes, and as a consequence, the shift in the exciton PL peak and/or broad defect emission were observed [81, 113].

The fabricated IO-hybrid microstructures (Figures 10 and 11) are uniform over large areas and are highly luminescent. In general, the fabrication of 3D structures from infiltration methods, using conventionally synthesized hybrids is difficult due to surface morphology issues [81]. In contrast to that, the hybrid structures fabricated from this novel method pave the way for new directions in the fabrication of different photonic structures of IO-hybrids. As a hybrid nanosystem, low-dimensional IO-hybrid systems have shown potential applications and those applications were reviewed in previous sections. Photonic structures of these nano systems could further improve the optical properties and hence would find device applications in the area of optoelectronics.

8. Conclusions

Fabrication, structural and optical exciton features of naturally self-assembled low-dimensional IO-hybrid nano systems were discussed. While the fabrication of these self-assembled systems are usually from solution chemistry techniques, a novel device-compatible thin film fabrication from very inexpensive method, that is, intercalation, was reviewed. Finally, the designing and fabrication of optoelectronic-compatible photonic architectures from these IO-hybrids, especially from template-assisted method, have been clearly discussed.

Acknowledgments

This work is funded from High-impact Research initiative of IIT Delhi, UK-India Education Research Initiative (UKIERI), Nano Research Facility (MCIT, Govt. India funded) of IIT Delhi, and the Department of Science and Technology (DST, Govt. of India). Authors are thankful to Professor Jeremy Baumberg, University of Cambridge, UK, for his valuable support and fruitful discussions.

References

- [1] G. M. Whitesides and M. Boncheva, "Beyond molecules: self-assembly of mesoscopic and macroscopic components," *Proceedings of the National Academy of Sciences of the United States of America*, vol. 99, no. 8, pp. 4769–4774, 2002.
- [2] J. M. Lehn, "Toward self-organization and complex matter," *Science*, vol. 295, no. 5564, pp. 2400–2403, 2002.
- [3] P. Yang, D. Zhao, D. I. Margolese, B. F. Chmelka, and G. D. Stucky, "Block copolymer templating syntheses of mesoporous metal oxides with large ordering lengths and semicrystalline framework," *Chemistry of Materials*, vol. 11, no. 10, pp. 2813–2826, 1999.
- [4] S. Mahima, R. Kannan, I. Komath, M. Aslam, and V. K. Pillai, "Synthesis of platinum Y-junction nanostructures using hierarchically designed alumina templates and their enhanced electrocatalytic activity for fuel-cell applications," *Chemistry of Materials*, vol. 20, no. 3, pp. 601–603, 2008.
- [5] G. S. Attard, C. G. Göltner, J. M. Corker, S. Henke, and R. H. Templer, "Liquid-crystal templates for nanostructured metals," *Angewandte Chemie (International Edition in English)*, vol. 36, no. 12, pp. 1315–1317, 1997.

- [6] K. J. Bachmann and J. L. Shay, "An InGaAs detector for the 1.0–1.7- μm wavelength range," *Applied Physics Letters*, vol. 32, p. 446, 1978.
- [7] K. Pradeesh, J. J. Baumberg, and G. Vijaya Prakash, "In situ intercalation strategies for device-quality hybrid inorganic-organic self-assembled quantum wells," *Applied Physics Letters*, vol. 95, no. 3, Article ID 033309, 2009.
- [8] I. Saikumar, Shahab Ahmad, J. J. Baumberg, and G. Vijaya Prakash, "Fabrication of excitonic luminescent inorganic-organic hybrid nano- and microcrystals," *Scripta Materialia*, vol. 67, no. 10, pp. 834–837, 2012.
- [9] Y. Xia, J. A. Rogers, K. E. Paul, and G. M. Whitesides, "Unconventional methods for fabricating and patterning nanostructures," *Chemical Reviews*, vol. 99, pp. 1823–1848, 1999.
- [10] M. Trupke, F. Ramirez-Martinez, E. A. Curtis et al., "Pyramidal micromirrors for microsystems and atom chips," *Applied Physics Letters*, vol. 88, no. 7, Article ID 071116, 2006.
- [11] G. Vijaya Prakash, R. Singh, A. Kumar, and R. K. Mishra, "Fabrication and characterisation of CdSe photonic structures from self-assembled templates," *Materials Letters*, vol. 60, no. 13–14, pp. 1744–1747, 2006.
- [12] G. Vijaya Prakash, K. Pradeesh, A. Kumar et al., "Fabrication and optoelectronic characterisation of ZnO photonic structures," *Materials Letters*, vol. 62, no. 8–9, pp. 1183–1186, 2008.
- [13] R. V. Nair and R. Vijaya, "Three-dimensionally ordered photonic crystal heterostructures with a double photonic stop band," *Journal of Applied Physics*, vol. 102, Article ID 056102, 3 pages, 2007.
- [14] R. V. Nair and R. Vijaya, "Structural and optical characterization of photonic crystals synthesized using the inward growing self-assembling method," *Applied Physics A*, vol. 90, pp. 559–563, 2008.
- [15] M. C. Gonçalves, L. M. Fortes, R. M. Almeida, A. Chiasera, A. Chiappini, and M. Ferrari, "3-D rare earth-doped colloidal photonic crystals," *Optical Materials*, vol. 31, no. 9, pp. 1315–1318, 2009.
- [16] L. Irimpan, V. P. N. Nampoori, P. Radhakrishnan, A. Deepthy, and B. Krishnan, "Size dependent fluorescence spectroscopy of nanocolloids of ZnO," *Journal of Applied Physics*, vol. 102, no. 6, Article ID 063524, 2007.
- [17] S. Coyle, G. Vijaya Prakash, J. J. Baumberg, M. Abdelsalem, and P. N. Bartlett, "Spherical micromirrors from templated self-assembly: polarization rotation on the micron scale," *Applied Physics Letters*, vol. 83, no. 4, p. 767, 2003.
- [18] V. Bulovic, G. Gu, P. E. Burrows, M. E. Thompson, and S. R. Forrest, "Transparent light-emitting devices," *Nature*, vol. 380, p. 29, 1996.
- [19] G. Gu, V. Bulovic, P. E. Burrows, S. R. Forrest, and M. E. Thompson, "Transparent organic light emitting devices," *Applied Physics Letters*, vol. 68, p. 2606, 1996.
- [20] V. Bulović, V. G. Kozlov, V. B. Khalfin, and S. R. Forrest, "Transform-limited, narrow-linewidth lasing action in organic semiconductor microcavities," *Science*, vol. 279, no. 5350, pp. 553–555, 1998.
- [21] V. G. Kozlov, V. Bulović, P. E. Burrows, and S. R. Forrest, "Laser action, in organic semiconductor waveguide and double-heterostructure devices," *Nature*, vol. 389, no. 6649, pp. 362–364, 1997.
- [22] W. Brütting, Ed., *Physics of Organic Semiconductors*, Wiley-VCH, Weinheim, Germany, 2005.
- [23] M. Furuki, M. Tian, Y. Sato et al., "Observation of sub-100-fs optical response from spin-coated films of squarylium dye J aggregates," *Applied Physics Letters*, vol. 78, no. 18, pp. 2634–2636, 2001.
- [24] K. Misawa, H. Ono, K. Minoshima, and T. Kobayashi, "New fabrication method for highly oriented J aggregates dispersed in polymer films," *Applied Physics Letters*, vol. 63, no. 5, pp. 577–579, 1993.
- [25] F. Sasaki, S. Kobayashi, and S. Haraichi, "Enhancement of the optical nonlinearity in pseudoisocyanine J aggregates embedded in distributed feedback microcavities," *Applied Physics Letters*, vol. 81, p. 391, 2002.
- [26] A. Eilmes, "Excited-state polarizability of J-aggregates," *Chemical Physics Letters*, vol. 347, no. 1–3, pp. 205–210, 2001.
- [27] N. Fukutake, S. Takasaka, and T. Kobayashi, "Energy transfer between two kinds of J-aggregates studied by near-field absorption-fluorescence spectroscopy," *Chemical Physics Letters*, vol. 361, no. 1–2, pp. 42–48, 2002.
- [28] P. Gomez-Romero, "Hybrid organic-inorganic materials-in search of synergic activity," *Advanced Materials*, vol. 13, no. 3, pp. 163–174, 2001.
- [29] E. Fois, A. Gamba, and A. Tilocca, "On the unusual stability of Maya blue paint: molecular dynamics simulations," *Microporous and Mesoporous Materials*, vol. 57, no. 3, pp. 263–272, 2003.
- [30] D. E. Arnold, J. R. Branden, P. R. Williams, G. M. Feinman, and J. P. Brown, "The first direct evidence for the production of Maya Blue: rediscovery of a technology," *Antiquity*, vol. 82, no. 315, pp. 151–164, 2008.
- [31] K. S. Aleksandrov and V. V. Beznosikov, "Hierarchies of perovskite-like crystals," *Physics of the Solid State*, vol. 39, no. 5, pp. 695–715, 1997.
- [32] D. B. Mitzi, "Synthesis, structure, and properties of organic-inorganic perovskites and related materials," *Progress in Inorganic Chemistry*, vol. 48, p. 1, 1999.
- [33] D. B. Mitzi, "Organic-inorganic perovskites containing trivalent metal halide layers: the templating influence of the organic cation layer," *Inorganic Chemistry*, vol. 39, no. 26, pp. 6107–6113, 2000.
- [34] A. Poglitsch and D. Weber, "Dynamic disorder in methylammoniumtrihalogenoplumbates (II) observed by millimeter-wave spectroscopy," *The Journal of Chemical Physics*, vol. 87, no. 11, pp. 6373–6378, 1987.
- [35] D. Weber, " $\text{CH}_3\text{NH}_3\text{PBX}_3$, a Pb(II)-system with cubic perovskite structure," *Zeitschrift für Naturforschung B*, vol. 33, pp. 1443–1445, 1978.
- [36] S. Wang, D. B. Mitzi, G. A. Landrum, H. Genin, and R. Hoffmann, "Synthesis and solid state chemistry of CH_3BiI_2 : a structure with an extended one-dimensional organometallic framework," *Journal of the American Chemical Society*, vol. 119, no. 4, pp. 724–732, 1997.
- [37] D. B. Mitzi, "Synthesis and crystal structure of the alkylbismuth diiodides: a family of extended one-dimensional organometallic compounds," *Inorganic Chemistry*, vol. 35, no. 26, pp. 7614–7619, 1996.
- [38] E. O. Schlemper and W. C. Hamilton, "The crystal structure of dimethyltin difluoride. An example of octahedral coordination of tin," *Inorganic Chemistry*, vol. 5, no. 6, pp. 995–998, 1966.
- [39] X. Huang, J. Li, and H. Fu, "The first covalent organic-inorganic networks of hybrid chalcogenides: structures that may lead to a new type of quantum wells," *Journal of the American Chemical Society*, vol. 122, no. 36, pp. 8789–8790, 2000.

- [40] F. Chiarella, R. Mosca, M. Pavesi, A. Zappettini, P. Ferro, and F. Licci, "Enhanced luminescence of CuCl microcrystals in an organic-inorganic hybrid matrix," *Applied Physics A*, vol. 88, no. 2, pp. 235–237, 2007.
- [41] M. Eraa, K. Miyakea, Y. Yoshidac, and K. Yase, "Orientation of azobenzene chromophore incorporated into metal halide-based layered perovskite having organic-inorganic superlattice structure," *Thin Solid Films*, vol. 393, pp. 24–27, 2001.
- [42] N. F. Stephens, A. M. Z. Slawin, and P. Lightfoot, "A novel scandium fluoride, $[\text{C}_2\text{N}_2\text{H}_{10}]_{(0.5)}[\text{ScF}_4]$, with an unprecedented tungsten bronze-related layer structure," *Chemical Communications*, no. 5, pp. 614–615, 2004.
- [43] M. Szafranski, "Investigation of phase instabilities in guanidinium halogenoplumbates(II)," *Thermochimica Acta*, vol. 307, no. 2, pp. 177–183, 1997.
- [44] R. Kind, "Phase transitions and incommensurability in crystalline model bilayers," *Berichte der Bunsengesellschaft für physikalische Chemie*, vol. 87, pp. 248–254, 1983.
- [45] J. Etzbarria, J. Fernandez, M. A. Arriandiaga, and M. J. Tello, "Influence of the thermal expansion on the piezoelectric photoacoustic detection of ferro-paraelastic phase transition in $(\text{CH}_3\text{CH}_2\text{NH}_3)_2\text{CuCl}_4$," *Journal of Physics C*, vol. 18, no. 1, pp. L13–L17, 1985.
- [46] T. Goto, B. Lthi, R. Geick, and K. Strobel, "Elastic soft mode in perovskite-type layer-structure materials," *Physical Review B*, vol. 22, no. 7, pp. 3452–3458, 1980.
- [47] N. Mercier, N. Louvain, and W. Bi, "Structural diversity and retro-crystal engineering analysis of iodometalate hybrids," *CrystEngComm*, vol. 11, no. 5, pp. 720–734, 2009.
- [48] D. B. Mitzi, "Templating and structural engineering in organic-inorganic perovskites," *Journal of the Chemical Society, Dalton Transactions*, no. 1, pp. 1–12, 2001.
- [49] D. B. Mitzi, C. D. Dimitrakopoulos, and L. L. Kosbar, "Structurally tailored organic-inorganic perovskites: optical properties and solution-processed channel materials for thin-film transistors," *Chemistry of Materials*, vol. 13, no. 10, pp. 3728–3740, 2001.
- [50] T. Fujita, H. Nakashima, M. Hirasawa, and T. Ishihara, "Ultrafast photoluminescence from $(\text{C}_6\text{H}_5\text{C}_2\text{H}_4\text{NH}_3)_2\text{PbI}_4$," *Journal of Luminescence*, vol. 87, pp. 847–849, 2000.
- [51] M. Shimizu, J. Fujisawa, and T. Ishihara, "Photoluminescence of the inorganic-organic layered semiconductor $(\text{C}_6\text{H}_5\text{C}_2\text{H}_4\text{NH}_3)_2\text{PbI}_4$: observation of triexciton formation," *Physical Review B*, vol. 74, Article ID 155206, 6 pages, 2006.
- [52] M. Shimizu, J. I. Fujisawa, and T. Ishihara, "Nonlinear luminescence from an inorganic-organic layered semiconductor," *Journal of Luminescence*, vol. 122–123, no. 1–2, pp. 485–487, 2007.
- [53] T. Ishihara, "Optical properties of PbI-based perovskite structures," *Journal of Luminescence*, vol. 60–61, pp. 269–274, 1994.
- [54] G. A. Mousdis, G. C. Papavassiliou, C. P. Raptopoulou, and A. Terzis, "Preparation and characterization of $[\text{H}_3\text{N}(\text{CH}_2)_6\text{NH}_3]\text{PbI}_4$ and similar compounds with a layered perovskite structure," *Journal of Materials Chemistry*, vol. 10, pp. 515–518, 2000.
- [55] G. C. Papavassiliou, I. B. Koutselas, A. Terzis, and M. H. Whangbo, "Structural and electronic properties of the natural quantum-well system $(\text{C}_6\text{H}_5\text{CH}_2\text{CH}_2\text{NH}_3)_2\text{SnI}_4$," *Solid State Communications*, vol. 91, no. 9, pp. 695–698, 1994.
- [56] A. Lemmerer and D. G. Billing, "Two packing motifs based upon chains of edge-sharing PbI_6 octahedra," *Acta Crystallographica Section C*, vol. 62, no. 12, p. m597, 2006.
- [57] C. P. Raptopoulou, A. Terzis, G. A. Mousdis, and G. C. Papavassiliou, "Preparation, structure and optical properties of $[\text{CH}_3\text{SC}(\text{NH}_2)_2]_3\text{SnI}_5$, $[\text{CH}_3\text{SC}(\text{NH}_2)_2][\text{HSC}(\text{NH}_2)_2]\text{SnBr}_4$, $(\text{CH}_3\text{C}_5\text{H}_4\text{NCH}_3)\text{PbBr}_3$, and $[\text{C}_6\text{H}_5\text{CH}_2\text{SC}(\text{NH}_2)_2]_4\text{Pb}_3\text{I}_{10}$," *Zeitschrift für Naturforschung B*, vol. 57, pp. 645–650, 2002.
- [58] G. C. Papavassiliou, G. A. Mousdis, A. Terzis, and C. P. Raptopoulou, "Crystal structure and optical properties of 4-[4-(dimethylamino)-styryl]-1-methyl-pyridinium lead tribromide," *Zeitschrift für Naturforschung B*, vol. 58, pp. 815–816, 2003.
- [59] G. C. Papavassiliou, G. A. Mousdis, I. Koutselas et al., "Some new synthetic low-dimensional semiconductors based on inorganic units," *Advanced Materials for Optics and Electronics*, vol. 8, no. 5, pp. 263–267, 1998.
- [60] C. Xu, S. Fukuta, H. Sakakura et al., "Anomalous electroabsorption in the low-temperature phase of $(\text{C}_{10}\text{H}_{21}\text{NH}_3)_2\text{PbI}_4$," *Solid State Communications*, vol. 77, pp. 923–926, 1991.
- [61] M. Era, S. Morimoto, T. Tsutsui, and S. Saito, "Organic-inorganic heterostructure electroluminescent device using a layered perovskite semiconductor $(\text{C}_6\text{H}_5\text{C}_2\text{H}_4\text{NH}_3)_2\text{PbI}_4$," *Applied Physics Letters*, vol. 65, pp. 676–3, 1994.
- [62] K. Morii, M. Ishida, T. Takashima et al., "Encapsulation-free hybrid organic-inorganic light-emitting diodes," *Applied Physics Letters*, vol. 89, no. 18, Article ID 183510, 3 pages, 2006.
- [63] K. Chondroudis and D. B. Mitzi, "Electroluminescence from an organic-inorganic perovskite incorporating a quaterthiophene dye within lead halide perovskite layers," *Chemistry of Materials*, vol. 11, no. 11, pp. 3028–3030, 1999.
- [64] T. Hattori, T. Taira, M. Era, T. Tsutsui, and S. Saito, "Highly efficient electroluminescence from a heterostructure device combined with emissive layered-perovskite and an electron-transporting organic compound," *Chemical Physics Letters*, vol. 254, pp. 103–108, 1996.
- [65] K. Saruwatari, H. Sato, T. Idei et al., "Photoconductive properties of organic-inorganic hybrid films of layered perovskite-type niobate," *Journal of Physical Chemistry B*, vol. 109, no. 25, pp. 12410–12416, 2005.
- [66] W. E. Mahmoud, "A novel photodiode made of hybrid organic/inorganic nanocomposite," *Journal of Physics D*, vol. 42, no. 15, Article ID 155502, 2009.
- [67] A. M. Guloy, Z. Tang, P. B. Miranda, and V. I. Srdanov, "A new luminescent organic-inorganic hybrid compound with large optical nonlinearity," *Advanced Materials*, vol. 13, pp. 833–837, 2001.
- [68] M. Shimizu, J. Fujisawa, and J. Ishi-Hayase, "Influence of the dielectric confinement on excitonic nonlinearity in inorganic-organic layered semiconductors," *Physical Review B*, vol. 71, no. 20, Article ID 205306, 9 pages, 2005.
- [69] M. Shimizu, N. A. Gippius, S. G. Tikhodeev, and T. Ishihara, "Coulomb correction to the dressed exciton in an inorganic-organic layered semiconductor: detuning dependence of the Stark shift," *Physical Review B*, vol. 69, no. 15, Article ID 155201, 5 pages, 2004.
- [70] C. Q. Xu, H. Sakakura, T. Kondo et al., "Magneto-optical effects of excitons in $(\text{C}_{10}\text{H}_{21}\text{NH}_3)_2\text{PbI}_4$ under high magnetic fields up to 40 T," *Solid State Communications*, vol. 79, no. 3, pp. 249–253, 1991.
- [71] T. Sekine, T. Okuno, and K. Awaga, "Observation of spontaneous magnetization in the layered perovskite ferromagnet, $(p\text{-Chloroanilinium})_2\text{CuBr}_4$," *Inorganic Chemistry*, vol. 37, no. 9, pp. 2129–2133, 1998.

- [72] K. Tanaka, T. Takahashi, T. Kondo et al., "Electronic and excitonic structures of inorganic-organic perovskite-type quantum-well crystal $(C_4H_9NH_3)_2PbBr_4$," *Japanese Journal of Applied Physics*, vol. 44, no. 8, pp. 5923–5932, 2005.
- [73] J. Fujisawa and T. Ishihara, "Excitons and biexcitons bound to a positive ion in a bismuth-doped inorganic-organic layered lead iodide semiconductor," *Physical Review B*, vol. 70, no. 20, Article ID 205330, 6 pages, 2004.
- [74] Y. Kato, D. Ichii, K. Ohashi et al., "Extremely large binding energy of biexcitons in an organic-inorganic quantum-well material $(C_4H_9NH_3)_2PbBr_4$," *Solid State Communications*, vol. 128, no. 1, pp. 15–18, 2003.
- [75] T. Goto, H. Makino, T. Yao et al., "Localization of triplet excitons and biexcitons in the two-dimensional semiconductor $(CH_3C_6H_4CH_2NH_3)_2PbBr_4$," *Physical Review B*, vol. 73, no. 11, Article ID 115206, pp. 1–5, 2006.
- [76] T. Kondo, T. Azuma, T. Yuasa, and R. Ito, "Biexciton lasing in the layered perovskite-type material $(C_6H_{13}NH_3)_2PbI_4$," *Solid State Communications*, vol. 105, no. 4, pp. 253–255, 1998.
- [77] D. B. Mitzi, K. Chondroudis, and C. R. Kagan, "Organic-inorganic electronics," *IBM Journal of Research and Development*, vol. 45, no. 1, pp. 29–45, 2001.
- [78] C. R. Kagan, D. B. Mitzi, and C. D. Dimitrakopoulos, "Organic-inorganic hybrid materials as semiconducting channels in thin-film field-effect transistors," *Science*, vol. 286, no. 5441, pp. 945–947, 1999.
- [79] K. Shibuya, M. Koshimizu, Y. Takeoka, and K. Asai, "Scintillation properties of $(C_6H_{13}NH_3)_2PbI_4$: exciton luminescence of an organic/inorganic multiple quantum well structure compound induced by 2.0 MeV protons," *Nuclear Instruments and Methods in Physics Research B*, vol. 194, pp. 207–212, 2002.
- [80] D. B. Mitzi, *Functional Hybrid Materials*, Wiley, Weinheim, Germany, 2004, edited by P. G. Romero and C. Sanchez.
- [81] G. Vijaya Prakash, K. Pradeesh, R. Ratnani, K. Saraswat, M. E. Light, and J. J. Baumberg, "Structural and optical studies of local disorder sensitivity in natural organic-inorganic self-assembled semiconductors," *Journal of Physics D*, vol. 42, no. 18, Article ID 185405, 2009.
- [82] V. K. Dwivedi, J. J. Baumberg, and G. Vijaya Prakash, "Direct deposition of inorganic-organic hybrid semiconductors and their template-assisted microstructures," *Materials Chemistry and Physics*, vol. 137, no. 3, pp. 941–946, 2013.
- [83] Y. Kawabata, M. Yoshizawa-Fujita, Y. Takeoka, and M. Rikukawa, "Relationship between structure and optoelectrical properties of organic-inorganic hybrid materials containing fullerene derivatives," *Synthetic Metals*, vol. 159, no. 9–10, pp. 776–779, 2009.
- [84] T. Ishihara, J. Takahashi, and T. Goto, "Optical properties due to electronic transitions in two-dimensional semiconductors $(C_nH_{2n+1}NH_3)_2PbI_4$," *Physical Review B*, vol. 42, pp. 11099–11107, 1990.
- [85] S. Noda, M. Fujita, and T. Asano, "Spontaneous-emission control by photonic crystals and nanocavities," *Nature Photonics*, vol. 1, no. 8, pp. 449–458, 2007.
- [86] D. B. Mitzi, C. A. Feild, W. T. A. Harrison, and A. M. Guloy, "Conducting tin halides with a layered organic-based perovskite structure," *Nature*, vol. 369, no. 6480, pp. 467–469, 1994.
- [87] D. B. Mitzi, S. Wang, C. A. Feild, C. A. Chess, and A. M. Guloy, "Conducting layered organic-inorganic halides containing $\langle 110 \rangle$ -oriented perovskite sheets," *Science*, vol. 267, no. 5203, pp. 1473–1476, 1995.
- [88] Z. Xu, D. B. Mitzi, C. D. Dimitrakopoulos, and K. R. Maxcy, "Semiconducting perovskites $(2-XC_6H_4C_2H_4NH_3)_2SnI_4$ (X = F, Cl, Br): steric interaction between the organic and inorganic layers," *Inorganic Chemistry*, vol. 42, pp. 2031–2039, 2003.
- [89] D. B. Mitzi, D. R. Medeiros, and P. R. L. Malenfant, "Intercalated organic-inorganic perovskites stabilized by fluoroaryl-aryl interactions," *Inorganic Chemistry*, vol. 41, no. 8, pp. 2134–2145, 2002.
- [90] K. Tanakaa, T. Takahashia, T. Bana, T. Kondoa, K. Uchidab, and N. Miura, "Comparative study on the excitons in lead-halide-based perovskite-type crystals $CH_3NH_3PbBr_3$ $CH_3NH_3PbI_3$," *Solid State Communications*, vol. 127, p. 619, 2003.
- [91] Z. Xu, D. B. Mitzi, and D. R. Medeiros, " $[(CH_3)_3NCH_2CH_2NH_3]_2SnI_4$: a layered perovskite with quaternary/primary ammonium dications and short interlayer iodine-iodine contacts," *Inorganic Chemistry*, vol. 42, no. 5, pp. 1400–1402, 2003.
- [92] A. Lemmerer and D. G. Billing, "P-phenylenediammonium tetraiodozincate(II) dihydrate," *Acta Crystallographica Section E*, vol. 62, no. 4, pp. m779–m781, 2006.
- [93] A. Lemmerer and D. G. Billing, "Two packing motifs based upon chains of edge-sharing PbI_6 octahedra," *Acta Crystallographica Section C*, vol. 62, no. 12, pp. m597–m601, 2006.
- [94] H. Krautscheid, C. Lode, F. Vielsack, and H. Vollmer, "Synthesis and crystal structures of iodoplumbate chains, ribbons and rods with new structural types," *Journal of the Chemical Society, Dalton Transactions*, no. 7, pp. 1099–1104, 2001.
- [95] T. Matsui, A. Yamaguchi, Y. Takeoka, M. Rikukawa, and K. Sanui, "Fabrication of two-dimensional layered perovskite $[NH_3(CH_2)_{12}NH_3]PbX_4$ thin films using a self-assembly method," *Chemical Communications*, no. 10, pp. 1094–1095, 2002.
- [96] T. Matsushima, K. Fujita, and T. Tsutsui, "High field-effect hole mobility in organic-inorganic hybrid thin films prepared by vacuum vapor deposition technique," *Japanese Journal of Applied Physics*, vol. 43, pp. L1199–L1201, 2004.
- [97] K. Ikegami, "Spectroscopic study of J aggregates of amphiphilic merocyanine dyes formed in their pure Langmuir films," *Journal of Chemical Physics*, vol. 121, p. 2337, 2004.
- [98] D. B. Mitzi, M. T. Prikas, and K. Chondroudis, "Thin film deposition of organic-inorganic hybrid materials using a single source thermal ablation technique," *Chemistry of Materials*, vol. 11, no. 3, pp. 542–544, 1999.
- [99] Z. Y. Cheng, H. F. Wang, Z. W. Quan, C. K. Lin, J. Lin, and Y. C. Han, "Layered organic-inorganic perovskite-type hybrid materials fabricated by spray pyrolysis route," *Journal of Crystal Growth*, vol. 285, no. 3, pp. 352–357, 2005.
- [100] D. B. Mitzi, D. R. Medeiros, and P. W. DeHaven, "Low-temperature melt processing of organic-inorganic hybrid films," *Chemistry of Materials*, vol. 14, no. 7, pp. 2839–2841, 2002.
- [101] J. E. Gieseking, "The mechanism of cation exchange in the montmorillonite-beidellite-nontronite type of clay minerals," *Soil Science*, vol. 47, no. 1, pp. 1–14, 1939.
- [102] D. M. C. MacEwan, "Identification of the montmorillonite group of minerals by X-rays," *Nature*, vol. 154, no. 3914, pp. 577–578, 1944.
- [103] W. F. Bradley, "Molecular associations between montmorillonite and some polyfunctional organic liquids," *Journal of the American Chemical Society*, vol. 67, no. 6, pp. 975–981, 1945.
- [104] E. Ruiz-Hitzky, *Functional Hybrid Materials*, Wiley, Weinheim, Germany, 2004, edited by P. G. Romero and C. Sanchez.

- [105] T. Ishihara, J. Takahashi, and T. Goto, "Exciton state in two-dimensional perovskite semiconductor $(\text{C}_{10}\text{H}_{21}\text{NH}_3)_2\text{PbI}_4$," *Solid State Communications*, vol. 69, no. 9, pp. 933–936, 1989.
- [106] L. C. Thanh, C. Depeursinge, F. Levy, and E. Mooser, "The band gap excitons in PbI_2 ," *Journal of Physics and Chemistry of Solids*, vol. 36, no. 7-8, pp. 699–702, 1975.
- [107] L. V. Keldysh, "Coulomb interaction in thin semiconductor and semimetal films," *Journal of Experimental and Theoretical Physics*, vol. 29, p. 658, 1979.
- [108] E. Hanamura, N. Nagaosa, M. Kumagai, and T. Takagahara, "Quantum wells with enhanced exciton effects and optical non-linearity," *Materials Science and Engineering B*, vol. 1, no. 3-4, pp. 255–258, 1988.
- [109] A. Piryatinski, S. A. Ivanov, S. Tretiak, and V. I. Klimov, "Effect of quantum and dielectric confinement on the exciton-exciton interaction energy in type II core/shell semiconductor Nanocrystals," *Nano Letters*, vol. 7, pp. 108–115, 2007.
- [110] K. Pradeesh, K. Nageswara Rao, and G. Vijaya Prakash, "Synthesis, structural, thermal and optical studies of inorganic-organic hybrid semiconductors, R-PbI_4 ," *Journal of Applied Physics*, vol. 113, no. 8, Article ID 083523, 9 pages, 2013.
- [111] M. S. Skolnick, T. A. Fisher, and D. M. Whittaker, "Strong coupling phenomena in quantum microcavity structures," *Semiconductor Science and Technology*, vol. 13, p. 645, 1998.
- [112] K. Pradeesh, J. J. Baumberg, and G. Vijaya Prakash, "Exciton switching and Peierls transitions in hybrid inorganic-organic self-assembled quantum wells," *Applied Physics Letters*, vol. 2, no. 10, Article ID 173305, 3 pages, 2009.
- [113] K. Pradeesh, J. J. Baumberg, and G. Vijaya Prakash, "Strong exciton-photon coupling in inorganic-organic multiple quantum wells embedded low-Q microcavity," *Optics Express*, vol. 17, no. 24, pp. 22171–22178, 2009.
- [114] K. Pradeesh, M. Agarwal, K. K. Rao, and G. Vijaya Prakash, "Synthesis, crystal structure and optical properties of quasi-one-dimensional lead (II) iodide: $\text{C}_{14}\text{H}_{18}\text{N}_2\text{Pb}_2\text{I}_6$," *Solid State Sciences*, vol. 12, no. 1, pp. 95–98, 2010.
- [115] K. Pradeesh, G. S. Yadav, M. Singh, and G. Vijaya Prakash, "Synthesis, structure and optical studies of inorganic-organic hybrid semiconductor, $\text{NH}_3(\text{CH}_2)_{12}\text{NH}_3\text{PbI}_4$," *Materials Chemistry and Physics*, vol. 124, no. 1, pp. 44–47, 2010.
- [116] S. Barman, N. V. Venkataraman, S. Vasudevan, and R. Seshadri, "Phase transitions in the anchored organic bilayers of long-chain alkylammonium lead iodides $(\text{C}_n\text{H}_{2n+1}\text{NH}_3)_2\text{PbI}_4$; $n = 12, 16, 18$," *The Journal of Physical Chemistry B*, vol. 107, no. 8, pp. 1875–1883, 2003.
- [117] K. Gauthron, J. S. Lauret, L. Doyennette et al., "Optical spectroscopy of two-dimensional layered $(\text{C}_6\text{H}_5\text{C}_2\text{H}_4\text{-NH}_3)_2\text{-PbI}_4$ perovskite," *Optics Express*, vol. 18, no. 6, pp. 5912–5919, 2010.
- [118] D. G. Billing and A. Lemmerer, "Synthesis, characterization and phase transitions of the inorganic-organic layered perovskite-type hybrids $[(\text{C}_n\text{H}_{2n+1}\text{NH}_3)_2\text{PbI}_4]$ ($n = 12, 14, 16$ and 18)," *New Journal of Chemistry*, vol. 32, pp. 1736–1746, 2008.
- [119] S. Zhang, G. Lanty, J. S. Lauret, E. Deleporte, P. Audebert, and L. Galmiche, "Synthesis and optical properties of novel organic-inorganic hybrid nanolayer structure semiconductors," *Acta Materialia*, vol. 57, no. 11, pp. 3301–3309, 2009.
- [120] I. Zhitomirsky, L. Gal-Or, A. Kohn, and H. W. Henniske, "Electrochemical preparation of PbO films," *Journal of Materials Science Letters*, vol. 14, no. 11, pp. 807–810, 1995.
- [121] T. K. Chaudhuri and H. N. Acharya, "Preparation of lead iodide films by iodination of chemically deposited lead sulphide films," *Materials Research Bulletin*, vol. 17, no. 3, pp. 279–286, 1982.
- [122] G. D. Currie, J. Mudar, and O. Risgin, "Photoconductive and photovoltaic spectral response in PbI_2 crystals," *Applied Optics*, vol. 6, no. 6, pp. 1137–1138, 1967.
- [123] A. E. Dugan and H. K. Hknisch, "Defect energy-level structure of PbI_2 single crystals," *Physical Review*, vol. 171, no. 3, pp. 1047–1051, 1968.

Research Article

Microwave-Assisted Synthesis of Mixed Metal-Oxide Nanoparticles

Akrati Verma,¹ Reena Dwivedi,¹ R. Prasad,¹ and K. S. Bartwal²

¹ School of Chemical Sciences, Devi Ahilya University, Indore 452001, India

² Laser Materials Development & Devices Division, RRCAT, Indore 452013, India

Correspondence should be addressed to K. S. Bartwal; bartwalks@yahoo.co.in

Received 21 January 2013; Accepted 9 February 2013

Academic Editor: Amir Kajbafvala

Copyright © 2013 Akrati Verma et al. This is an open access article distributed under the Creative Commons Attribution License, which permits unrestricted use, distribution, and reproduction in any medium, provided the original work is properly cited.

Nanoparticles of mixed metal oxides, ZrO_2 , $ZrTiO_4$, and ZrV_2O_7 were prepared by microwave-assisted citrate sol-gel and solution combustion method. The prepared nanoparticles were characterized for their structural details using XRD and TEM techniques. The broadening of Raman bands is ascribed to local compositional fluctuations or local positional disordering produced due to random distribution of Zr^{4+} and Ti^{4+} between equivalent sites. The XPS spectra confirm the incorporation of Ti in ZrO_2 and suggest Zr as well as Ti in +4 oxidation state. Gelation and fast combustion seem to be the reason for smaller particle sizes. ZrV_2O_7 nanocrystalline material was synthesized by microwave-assisted solution combustion method. Low angle powder XRD measurements confirm the mesoporous nature of the prepared material. The effect of calcination temperature on the phase transformation of the materials has been investigated. Among tetragonal, monoclinic, and cubic phases, the monoclinic phase is predominant at higher calcinations temperature. The XPS confirms the incorporation of V_2O_5 in ZrO_2 and suggests that Zr and V are in the same oxidation state (+4). The average particle sizes for ZrO_2 , $ZrTiO_4$, and ZrV_2O_7 were found to be in the ranges of 5–10 nm, 2–5 nm, and 10–50 nm, respectively.

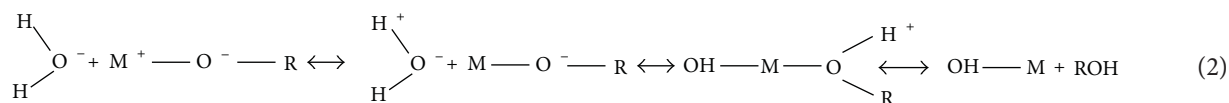
1. Introduction

Combination of two metal oxides M_1O and M_2O can be either a simple mechanical mixing involving weak van der Waals forces or a chemical possessing chemical linkages of the type M_1-O-M_2 . The physicochemical properties of the latter combination will be entirely different from the simple combination of individual oxides (mechanical mixture). The degree of dispersion in the chemical route depends on preparation method and synthetic conditions. Because of this, many different synthetic routes for mixed metal oxides have been developed. Some of the popular routes for preparation of mixed oxides are coprecipitation, sol-gel method, condensed phase combustion, and microwave-assisted solution combustion method.

Coprecipitation (wet precipitation) is the most widely used method for oxide synthesis. In this method hydroxide of the metals is precipitated from an aqueous solution of the metal salt by titrating it with ammonia solution. The hydroxide is washed, dried, and calcined to get the metal oxide. Sol-gel method is used to prepare metal oxides by hydrolysis and condensation of metal alkoxides $M(OR)_z$:



The reaction follows an SN^2 mechanism in which the nucleophile OH^- adds to the M^+ and increases its coordination number in the transition state:



The H^+ changes its position to alkoxy group producing a protonated ROH species which is subsequently eliminated, and metal hydroxide is produced. Production of MgO is a typical example. The rate of hydrolysis and condensation depends on (1) electronegativity of the metals atom, (2) ability of the metal atom to increase its coordination number, (3) steric hindrance of the alkoxy group, (4) solvents, (5) molecular structure of the metal alkoxide, (6) hydrolysis ratio $h = H_2O/Metal$, and (7) catalyst. The rate of hydrolysis of $Ti(OEt)_4$ is 10^7 times faster than that of $Si(OEt)_4$. This can be attributed to the ability of Ti to expand its coordination number from 4 to 6. For the same reason the hydrolysis of $Sn(OR)_4$ is much faster compared to $Si(OR)_4$.

Most advanced ceramics are multicomponent systems having two or more types of cations in the lattice. It is therefore necessary to prepare gels of high homogeneity in which cations of various kinds are distributed uniformly at an atomic scale through M-O-M bridges. A major problem in forming homogeneous multicomponent gel is the unequal hydrolysis and condensation rates of the metal alkoxides. This may result in chemical inhomogeneities, leading to higher crystallization temperatures or even undesired crystalline phases. Several approaches have been attempted to overcome this problem including partial prehydrolysis of less reactive precursors, matching of hydrolysis rates by chemical modification with chelating ligands, and synthesis of heterometallic alkoxides. Conventional self-propagating high temperature synthesis (SHS) or condensed phase combustion is associated with difficulties like large particle size of nanomaterials and high reaction temperature of about $2000^\circ C$. Combustion of metal oxides by Mg in the presence of NaCl produces small particles of metals coated with NaCl. Subsequent treatment of the powder with dilute acid removes MgO impurity. Metal can be recovered by washing the sample with water.

Microwave-assisted method of oxide synthesis is gaining popularity because of its high rate of reaction, efficient heat transfer, and environmental friendly nature. In this process material is directly heated by radiation instead of indirect heating by thermal sources leading to higher temperature homogeneity in the reaction mixture. In this process of heating, microwave radiation interacts with the polar molecules possessing dipole moment and makes them reorient through rotation. A large number of molecules try to orient together resulting in collision and production of heat. Thus microwave heating is energy conversion method in which electromagnetic radiation is converted into heat energy rather than heat transfer by convection in conventional heating. In microwave-assisted solution combustion synthesis (MWSCS) an aqueous solution of metal nitrate (oxidant) and fuel (urea, citric acid) is subjected to a microwave heating for few minutes to obtain a viscous gel which on drying and calcination produces the metal oxide/mixed metal oxide. The solution combustion method seems to be modification of the conventional oxalate method which is used for preparing metal oxides and supported metal oxides. The citrate gel decomposition process is better known as a thermally induced anionic oxidation-reduction reaction. In the process chelates are formed between metal ions facilitating atomic scale distribution of ions in a polymer network. Heating of this resin

causes the breakdown of the polymer, and a solid amorphous precursor material is finally obtained. On subsequent heating between 500 and $900^\circ C$, the cations are oxidized to form the respective metal oxides. Microwave-assisted MVSCS technique can be used for preparing materials or catalysts, catalyst support, fuel cells, capacitors, Li-ion rechargeable batteries, dye-sensitized solar cells, solid oxide fuel cells (SOFC), and direct methanol fuel cells (DMFCs).

The development of zirconia (ZrO_2) nanoparticles has attracted much attention due to their multifunctional characteristics. Nanoparticles have been recognized to have potential in the area of photonic applications. It has several applications such as solid oxide fuel cell, biosensors, H_2 gas storage material, oxygen sensor, catalyst, and catalyst support [2–5]. In addition, zirconia is used as piezoelectric material, electrooptic material, and dielectric material [6–8]. It is also used as support to disperse various noble and transition metals for distinct catalytic applications. Zirconia is a well-known solid acid catalyst and an n-type semiconductor material. ZrO_2 is also used as toughening ceramics in thighbone and oral planting [9]. The existence of metastable tetragonal ($t-ZrO_2$) at low temperature has been synthesized by several methods. Some of the methodologies such as oxidation of $ZrCl_2$ by molecular oxygen [10], molten hydroxides method [11], nonhydrolytic sol-gel reaction between isopropoxide and $ZrCl_4$ [12], and sol-gel template technique [13, 14] are developed to prepare nanocrystalline ZrO_2 .

The traditional preparation of zirconium titanate ($ZrTiO_4$) ceramic is based on solid-state reaction between the TiO_2 and ZrO_2 powders at high temperatures (above $1400^\circ C$) [15]. In order to improve the functional properties of the ceramic material, heat treatments are generally necessary which consume high amount of energy. Chemical method based on Coprecipitation of the reactive precursors was developed to prepare powders with a high purity and low treatment cost after reaction [16]. Low temperature synthesis of zirconium titanate has been reported by Karakchiev et al. [1] and Dos Santos et al. [17]. Zirconium titanate possessing a layered wolframite-type structure (ABO_4) with space group $P2_1/a$ finds applications as microwave components. As catalyst and catalyst supports, $ZrTiO_4$ is employed for a wide variety of catalytic applications both in liquid and gaseous phases [18, 19]. Recently it has been reported that the oxide nanoparticles are promising for photonics, and their monodispersion and appropriate contact with the surrounding medium are very crucial parameters [20, 21].

Vanadium incorporated zirconia ($V_2O_5-ZrO_2$) is a mesoporous material and is very useful catalyst. Nanoporous materials consist of a regular organic or inorganic framework supporting a regular, porous structure. A mesoporous material is a material containing pores with diameters between 2 and 50 nm. The α -phase (cubic) of ZrV_2O_7 is the stable structure at ambient conditions. It consists of ZrO_6 octahedra whose corners share their oxygen atoms with VO_4 tetrahedra. Vanadium oxide catalysts supported on different metal oxides are widely used in many industrial reactions, such as selective catalytic reduction of NO with NH_3 , ammoxidation of alkyl aromatics, and the selective oxidation of hydrocarbons. Properties of supported vanadium catalysts depend on a variety

of factors, such as percentage of vanadium loading, method of preparation interaction, and nature of the support [22]. Various supporting oxides used for vanadium loading include Al_2O_3 , TiO_2 , SiO_2 , ZrO_2 , MgO , and HfO_2 [23, 24]. Among all these oxides, ZrO_2 is a better choice as it interacts with vanadium relatively strongly, preventing its sintering, and helps in producing highly dispersed vanadium on ZrO_2 . Besides, ZrO_2 is thermally and chemically stable at the different reaction conditions. Solution combustion synthesis is a versatile, low-cost, simple, and rapid process, which allows effective synthesis of a variety of nanosize materials. This process involves a self-sustained reaction in homogeneous solution of different oxidizers (e.g., metal nitrates) and fuels (e.g., urea, glycine, and hydrazides) [25, 26].

The objective of the present work is to synthesize zirconium oxide, zirconium titanate, and zirconium vanadate nanocrystalline powder by microwave-assisted method. The combustion synthesis for preparing ZrO_2 has been performed under microwave using citric acid as fuel and zirconium oxychloride as oxidizer. The ZrTiO_4 particles were prepared using titanyl nitride and zirconium oxychloride as precursors. The ZrV_2O_7 nanoparticles were synthesized by microwave-assisted solution combustion method. The prepared nanoparticles were characterized for their structure-property relationship. The particle size and crystalline phase of the catalysts were determined by powder X-ray diffraction (XRD). The TEM technique was used to confirm the formation of single phase material with nanocrystalline particles. Raman and XPS spectroscopy techniques were used to characterize the structure and electronic properties. The present problem was undertaken with an aim (1) to develop a versatile, effective, low-cost, simple, and fast solution combustion assisted method for synthesis of these zirconia-based oxide nanoparticles and (2) to characterize the prepared nanoparticles by employing various physicochemical methods.

2. Experimental Details

Zirconia (ZrO_2) nanoparticles were prepared by citrate sol-gel method. High purity chemicals, zirconium oxychloride (S.D. Fine Chemicals), and anhydrous citric acid (LOBA Chemie Pvt. Ltd.) were used as precursors. In the present set of experiments, 9.78 g of zirconium oxychloride ($\text{ZrOCl}_2 \cdot 8\text{H}_2\text{O}$) was mixed with 7.68 g of citric acid ($\text{C}_2\text{O}_4\text{H}_2$) in a 250 mL corning glass beaker. Demineralized water was added to have homogeneous slurry of pH 2. The solution was evaporated to dryness by exposing it to microwave for 2 min. The material swells into a white colored gel. The product obtained was ground and kept for calcination in a tubular furnace at a temperature of 450°C for 4 h. On calcinations a black colored residue was obtained which was ground in a motor pastel to make a fine powder. Similarly, zirconium titanate (ZrTiO_4) nanoparticles were prepared by citrate sol-gel method. Zirconium oxychloride, anhydrous citric acid, and titanyl nitrate were used as starting materials. The titanyl nitrate was prepared by reacting tetrabutyl orthotitanate with nitric acid and evaporating the resulting mixture to dryness. The replacement of Zr by Ti was optimized, and two sets of

compositions in Zr : Ti ratio, 1 : 0.1 and 1 : 1, were prepared. In a typical preparation, 3.2 g of $\text{ZrOCl}_2 \cdot 8\text{H}_2\text{O}$, 0.29 g of titanyl nitrate, and 3.5 g of citric acid were used for 1 : 0.1 ratio of Zr : Ti (named ZT1), and 3.2 g of $\text{ZrOCl}_2 \cdot 8\text{H}_2\text{O}$, 2.95 g of titanyl nitrate, and 6.15 g of citric acid were used for the 1 : 1 ratio of Zr : Ti (named ZT2). These precursors were mixed in a 250 mL corning glass beaker, and enough demineralized water was added to have homogeneous slurry of 2 pH. The well-mixed solution was evaporated to dryness by exposing it to microwave for 2 min. This step of drying in microwave oven was optimized, and the time of 2 min was found suitable for this composition. The dried material was ground and kept for calcination in a resistive heating tubular furnace at a temperature of 400°C for 4 h. A grayish colored residue was obtained on calcination which was again ground in a motor pastel to make a fine powder. Both compositions of ZrTiO_4 with Zr : Ti ratio 1 : 0.1 and Zr-Ti ratio 1 : 1 were prepared with the same procedure in similar conditions. These samples were named as ZT1 and ZT2, respectively, and were used for various physicochemical studies.

Mesostructured vanadium oxide supported on zirconium oxide was synthesized by microwave-assisted solution combustion method [25, 27]. Zirconium oxychloride (S.D. Fine Chemicals) and ammonium metavanadate and urea (LOBA Chemie Pvt. Ltd.) were used as starting materials. In a typical preparation of 10% vanadium doped zirconia (ZV10), a solution of zirconium nitrate (prepared by mixing 5.8 g of zirconium oxychloride with 12 mL of 1 : 2 HNO_3) is mixed with another solution prepared by mixing 0.23 g of NH_4VO_4 in 50 mL of water. The final solution was mixed with 1.2 g of urea and fired in a muffle furnace at 200°C for 15 min. The material swells into a yellow colored gel. The product obtained was ground and kept for calcination in a tubular furnace at a temperature of 400°C for 4 h. On calcination a green colored residue was obtained. The prepared powder was ground several times before putting it in specimen holder to minimize the possible preferred orientation effects. For the preparation of all the ZV_x materials, 1 : 1 molar ratio of urea to metal oxide ($\text{Zr} + \text{V}$)_x was taken. Four different samples with varying V_2O_7 concentrations were prepared. The samples were named according to V_2O_7 concentrations of 2, 5, 8 and 10 mol% and named as ZV2, ZV5, ZV8, and ZV10, respectively.

The crystallite sizes and structural morphology were investigated by transmission electron microscopy (TEM) in high-resolution mode. Philips make, Tecnai G²-20 (FEI) electron microscope operating at 200 kV was used for TEM experiments. Sample for TEM observation was prepared by suspending the particles in ethanol by ultrasonification and drying a drop of the suspension on a carbon coated copper grid. Raman spectrum in the range $50\text{--}4000\text{ cm}^{-1}$ was recorded using Labram HR 800 micro-Raman spectrometer with 488 nm wavelength Ar^+ laser source at the energy of 2.53 eV with recording time of 10 sec. The core level X-ray photoelectron spectroscopy (XPS) spectra of ZrTiO_4 and ZrV_2O_7 were measured using Omicron Nanotechnology (EAI-25) photoelectron spectrometer with Al K_α radiation ($E = 1486.6\text{ eV}$) as excitation source. The base pressure of the analysis chamber of the system was less than 5×10^{-10} mbar

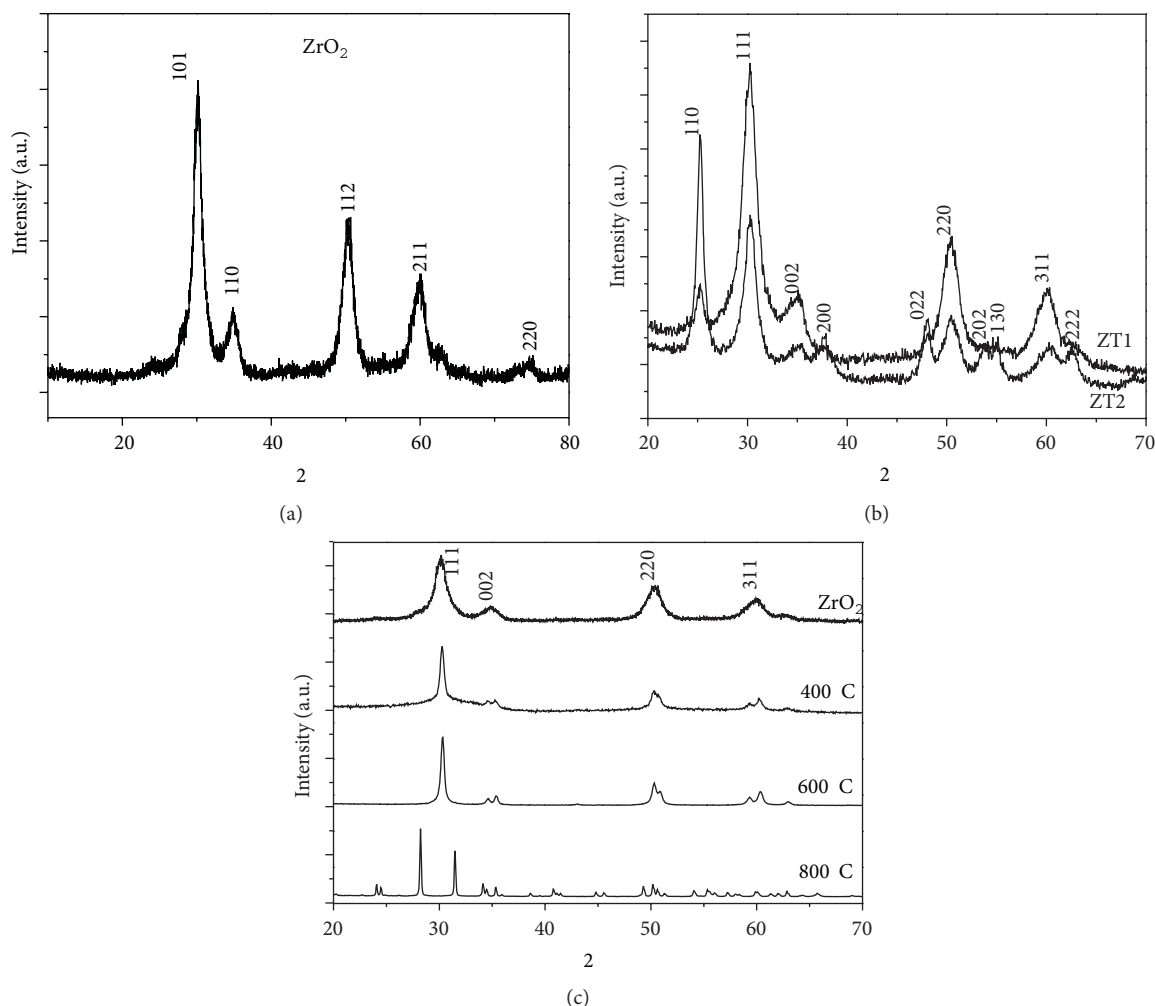


FIGURE 1: Representative powder XRD pattern for (a) ZrO₂, (b) ZrTiO₄ (ZT1 and ZT2) nanoparticles calcined at 400°C, and (c) ZrV₂O₇ (ZV10) nanoparticles calcined at different temperatures.

during the experiments. Energy scale of the spectrometer was calibrated by setting the measured Au 4f_{7/2} and Cu 2p_{3/2} binding energies to 84.00 ± 0.05 and 932.66 ± 0.05 eV, respectively, with regard to E_F. The energy drift due to charging effects was calibrated taking the XPS, C 1s (285.0 eV) core-level spectrum of hydrocarbons.

3. Results and Discussion

It is known that the main crystal phases of ZrO₂ are cubic (c), tetragonal (t), and monoclinic (m). The IR frequencies for cubic, tetragonal, and monoclinic phases are 480, 435, and 270 cm⁻¹, respectively. This indicates that phonon energy of the ZrO₂ host varies in the crystal phases. The monoclinic phase is thermodynamically stable up to 1100°C, the tetragonal phase exists in the temperature range 1100–2370°C, and the cubic phase is found above 2370°C. The nanoparticles of tetragonal zirconium oxide (t-ZrO₂) were prepared by microwave-assisted citrate sol-gel technique. Zirconium titanate, ZrTiO₄, with two different Zr : Ti ratios was prepared

to understand the complete replacement of Zr ion by Ti. The Zr : Ti ratios taken were 1:0.1 (ZT1) and 1:1 (ZT2). These samples were prepared by microwave-assisted citrate sol-gel method. The microwave was used during the sol-gel drying process to make the particles more homogeneous in Zr/Ti ionic ratio. The prepared samples were subjected to various characterization studies to understand dispersion of Ti ions and the role of microwave in preparation. Zirconia supported vanadate (ZrV₂O₇) was synthesized by microwave-assisted solution combustion method. The two-dimensional vanadia species with tetrahedral coordination appear on the surface of the ZrO₂ and expand in size with increasing V₂O₅ concentration. ZrV₂O₇ is formed as a consequence of zirconia migration into the V₂O₅ crystallites. The prepared nanoparticles were found having mesoporous structure. The structures of the zirconia support and of the dispersed vanadia were characterized. The prepared nanoparticles were investigated for their phase and structure by powder XRD using Cu K_α radiation (λ = 1.5406 Å, Rigaku Geiger Flex X-ray diffractometer). The powder XRD data were collected in the 2θ range from 20 to 80 degrees with the scan rate of 2° per minute.

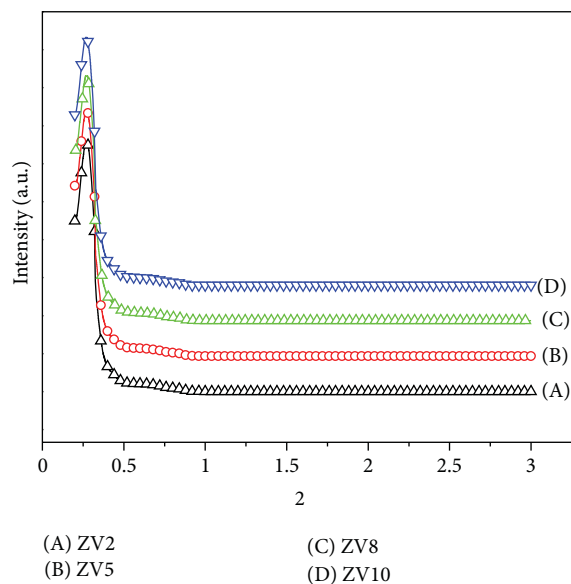


FIGURE 2: Low angle XRD pattern of ZV2, ZV5, ZV8, and ZV10 calcined at 400°C.

The prepared powder was ground several times before putting it in specimen holder to minimize the possible preferred orientation effects. Powder XRD patterns of the prepared ZrV_2O_7 nanoparticles calcined at different temperatures were recorded. The representative powder XRD for all the three samples is shown in Figures 1(a), 1(b), and 1(c). XRD pattern shown in Figure 1(a), reveals the fact that the single tetragonal phase of ZrO_2 is crystallized. The calcination temperature has important role to play in formation of crystalline phase and the particle size. The calcination temperature was optimized, and 450°C was found to be effective to crystallize the desired tetragonal phase. It was observed that the full width at half maximum of the reflection peaks decreases and also becomes sharp as the calcining temperature increases. This suggests that the crystallinity of prepared zirconia nanoparticles is increasing at higher temperatures. The XRD patterns have been indexed and found matching with the t- ZrO_2 (JCPDF card file no. 79-1771). The lattice parameters were calculated for t- ZrO_2 from the XRD data. The parameters were $a = 5.083 \text{ \AA}$, $c = 5.185 \text{ \AA}$ and the tetragonality, $c/a = 1.0201$. The diffraction characteristic peaks were obtained with the (h k l) values of (101), (110), (112), (211), and (220). The particle sizes were calculated from FWHM (full width half maximum) of reflections of t- ZrO_2 structured zirconia nanoparticles using Debye-Scherrer formula [28]:

$$D = \frac{0.9\lambda}{(\beta \cos \theta)}, \quad (3)$$

where D is the average crystallite size in nm, λ is the wavelength of source X-ray (0.154 nm), and β (in radian) is the full peak width at half maximum. The particle sizes were found varying ~5–10 nm range.

It is known that the zirconium titanate solid solution with Zr:Ti molar ratio ranging from 1:1 to 1:2 is the only stable binary compound in the Zr-Ti-O system. Two

structural modifications known for this system are high-temperature disordered $Zr_{1-x}Ti_xO_4$ (Ti-excess) and low-temperature ordered $ZrTiO_4$. The XRDs for the samples ZT1 and ZT2 are reproduced in Figure 1(b), which indicate the formation of $ZrTiO_4$ orthorhombic phase, which is closely matching with JCPDS file no. 34-415. To a first approximation, this major phase has orthorhombic structure of α - PbO_2 with space group $Pbcn$, with the cell parameters $a = 4.80 \text{ \AA}$, $b = 5.49 \text{ \AA}$, and $c = 5.03 \text{ \AA}$. Most of the peaks for the samples ZT1 and ZT2 are matching, the only difference being the intensity of the peaks which is different for Zr-rich composition (ZT1). The diffraction characteristic peaks for this phase were obtained with the (h k l) values of (011), (111), (200), (220), (022), and (311). The doublets observed in the XRD pattern for $ZrTiO_4$ at 2θ values 35, 37, and 54 are due to the presence of small amount of secondary phase ($Zr_5Ti_7O_{24}$) of Ti-rich phase in Zr-Ti system. It has been known that some small amounts equation of ZrO_2 and TiO_2 are also expected to be formed during the process. The average particle size was calculated from (111) diffraction peak using Scherrer's, and the average particle size was calculated to be ~4.8 nm ZT1 and ~6.14 nm for ZT2.

XRD pattern for pure ZrO_2 material calcined at 400°C and 10 wt% V_2O_5 supported on ZrO_2 calcined at different temperatures in the range of 20°–70° is shown in Figure 1(c). The pattern has been indexed with the tetragonal ZrO_2 (JCPDS card file no. 81-1551) and cubic ZrV_2O_7 (JCPDS card file no. 16-0422). The absence of vanadia or vanadate peaks ($2\theta = 20.3^\circ$ and 26.2°) in the sample calcined at 400°C and 600°C can be noticed. The appearance of the vanadia peaks in the samples calcined at 800°C is clearly seen. The presence of these peaks with lower intensity in the sample calcined at 800°C confirms that the vanadium ions have occupied the zirconium ions at their lattice positions and high dispersion of vanadia ions on zirconium oxide surface [29]. On calcination at higher temperatures the full width at half maximum of the diffraction peaks decreases. This decrease in FWHM suggests that the sizes of prepared zirconium vanadate nanoparticles are increasing at higher temperatures. When zirconium vanadate sample was calcined at 400°C and 600°C, a very sharp peak appeared at 30.34° which can be ascribed to tetragonal phase. On calcination at 800°C, two sharp peaks appeared at 28.2° and 31° which is ascribed to the monoclinic phase of ZrO_2 [30]. The average particle size was calculated from (111) diffraction peak using Scherrer's equation and the average particle size was calculated to be 16 nm, 27 nm, and 49.63 nm, respectively, for 10 wt% zirconium vanadate samples calcined at 400°C, 600°C, and 800°C. Low angle powder XRD pattern of the prepared nanoparticles calcined at 400°C for 4 h was recorded in order to explore structural feature of zirconium supported mesoporous vanadium materials. Figure 2 shows the low angle powder XRD pattern. The appearance of peak in low angle region at 0.3° confirms the mesoporous nature. It has been known that the presence of sharp peak in low angle region confirms the disordered wormhole type mesoporosity in ZrV_2O_7 [31]. The increase in the intensity of the peak present at 0.3° , with increasing V concentration, suggests the enhancement in mesoporosity in the material.

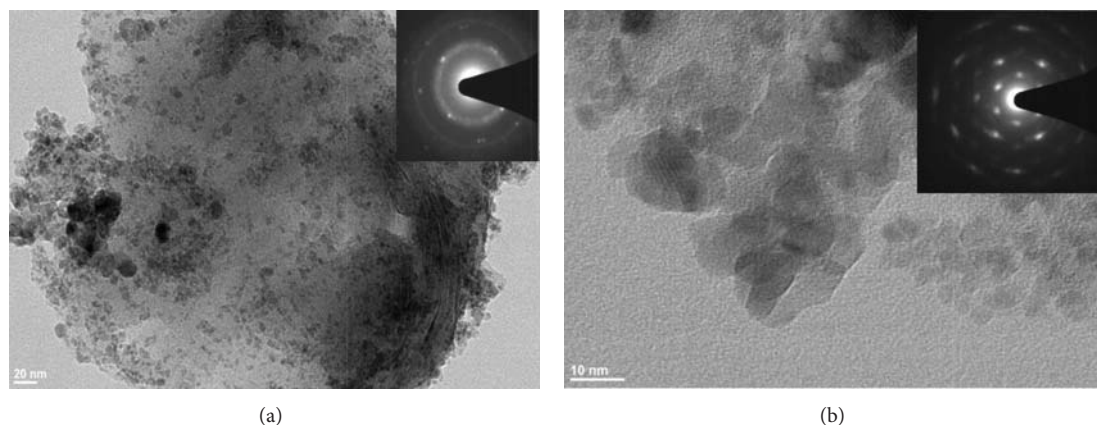


FIGURE 3: (a) Representative TEM micrograph for ZrO_2 sample annealed at $450^\circ C$. (b) High-resolution TEM micrograph for samples annealed at $450^\circ C$. The corresponding SAED patterns are inserted into micrographs.

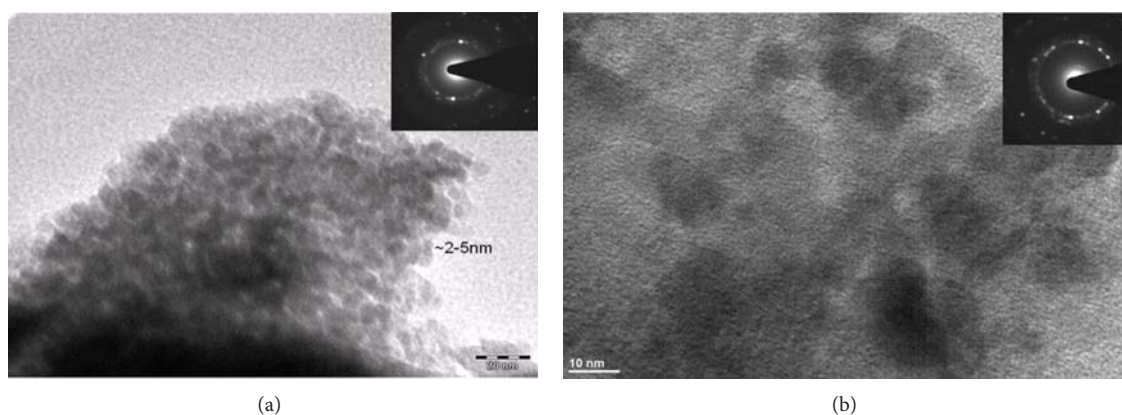


FIGURE 4: (a) Representative TEM micrograph for $ZrTiO_4$ sample. (b) High-resolution TEM micrograph for the same sample. The corresponding SAED patterns are inserted into micrographs.

Transmission electronic microscopy (TEM) in high-resolution mode is the best tool to analyze the morphology and the sizes of the prepared nanoparticles [32–34]. Figures 3(a) and 3(b) show the representative TEM micrographs taken for the ZrO_2 samples calcined at $450^\circ C$. The corresponding selected area electron diffraction (SAED) patterns are inserted into the micrographs. Figure 3(a) shows a typical TEM image for the dried powders. The powders are very fine and agglomerated. Electron diffraction analysis reveals that they have amorphous characteristics due to small particle sizes. The micrograph shown in Figure 3(a) indicates the formation of nanoparticles with sizes ranging from few nanometers to few tens of nanometers. The corresponding diffraction pattern shows few clear spots along with connecting diffraction rings. The presence of spots along with the streaks shows the presence of crystallite of reasonably sufficient sizes to diffract. The connecting streaks indicate the short-range order due to presence of some smaller size particles as well. The high-resolution electron micrograph for the samples annealed at $450^\circ C$ is shown in Figure 3(b). The clarity in the fringe patterns inside the crystallite indicates the formation of

single phase ZrO_2 with the long-range order in the structure. The corresponding SAED pattern is inserted into the micrograph. The clear spots in SAED pattern suggest that the crystallites are of sufficiently large size. The absence of rings in the SAED pattern is indicative of the crystalline order, larger particle size, and long-range order in the crystallites. The TEM results also suggest the successful preparation of tetragonal phase of ZrO_2 nanocrystals with the crystallite sizes ranging ~ 5 – 10 nm.

The samples of $ZrTiO_4$ (ZT2) with the Zr : Ti ratio of 1 : 1 calcined at $400^\circ C$ were also analysed using TEM, and the micrographs taken are shown in Figures 4(a) and 4(b). Corresponding selected area electron diffraction (SAED) patterns are inserted into the micrographs. The micrograph shown in Figure 4(a) shows the formation of nanoparticles. The SAED pattern inserted into the micrograph shows the few sharp spots along with connecting diffuse rings. The smaller size particles are responsible for the connecting rings which suggests the short-range order. The high-resolution electron micrograph (HRTEM) for the sample $ZrTiO_4$ (ZT2) is shown in Figure 4(b). The fringe patterns indicate the formation

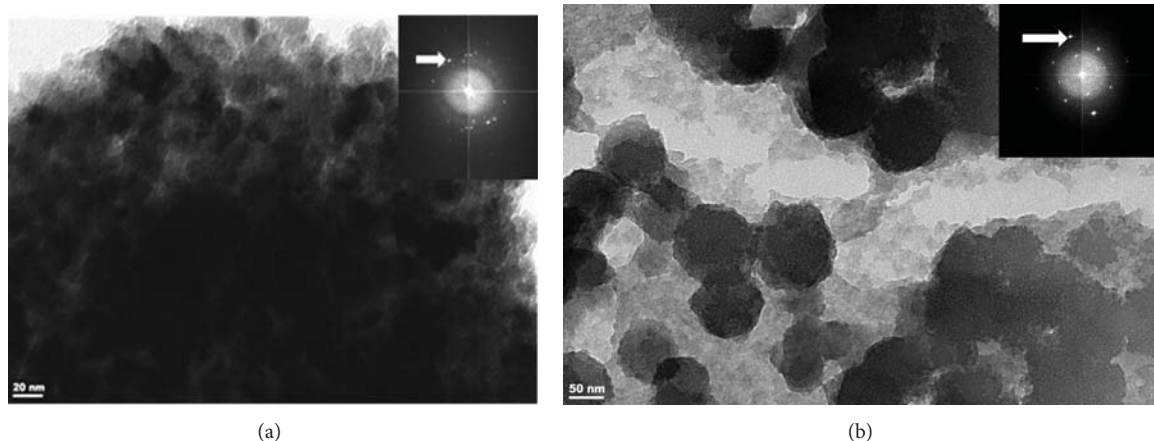


FIGURE 5: Representative HRTEM images of (a) ZV8 and (b) ZV10 compositions. The corresponding SAED patterns are inserted into the micrograph.

of single phase ZrTiO_4 with the long-range ordering in the structure. The corresponding SAED pattern is inserted into the micrograph. Spots along with rings in the SAED pattern suggest the larger particle size and short-range order in the crystallites. These results on TEM suggest the preparation of the desired phase of ZrTiO_4 nanocrystals with the crystallite sizes ranging $\sim 2\text{--}5$ nm.

The high-resolution TEM images and corresponding selected area electron diffraction (SAED) patterns for ZrV_2O_7 samples (ZV8 and ZV10) calcined at 400°C are shown in Figures 5(a) and 5(b). HRTEM micrograph shown in Figure 5(a) confirms the formation of nanoparticles with varying sizes. The particle sizes are in $\sim 20\text{--}30$ nm range and sufficient to diffract and produce SAED pattern. The SAED diffraction pattern inserted into the micrograph (Figure 5(a)) shows the presence of few sharp spots along with diffuse spots and connecting ring. The position of the reflections (shown by arrow) in the electron diffraction pattern and broadening of the rings indicate the presence of small randomly oriented V-Zr mixed oxide particles. The HRTEM for ZV10 shown in Figure 5(b) shows that the particle sizes increase with increasing V concentration. Sharp and clear spots along the SAD pattern in Figure 5(b) suggest the long-range order between the crystallites. The particle sizes are in $\sim 20\text{--}50$ nm range and sufficient to diffract and produce sharp and clear SAED pattern compared to ZV8. The previous TEM results of diffraction and high-resolution mode suggest the successful preparation of the cubic ZrV_2O_7 nanoparticles with the particle sizes ranging $\sim 20\text{--}50$ nm. The TEM results show that there is no secondary phase formation due to vanadia separation. The formation of well-crystallized ZV nanoparticles is clearly seen in the micrographs. The particle size of the as-prepared materials was found to increase with the increase in the V concentration.

It has been known that the Raman spectroscopy can be used to determine the symmetry of a crystal system for oxide materials as it is very sensitive to the polarizability of the oxygen ions. In fact Raman spectroscopy is a technique more sensitive to short-range order than X-ray diffraction, and it can show the peaks for anatase or rutile as well as monoclinic

zirconia along with that of tetragonal zirconia. Raman spectroscopy has been performed on all the nanocrystalline samples of ZrO_2 and ZrTiO_4 samples. The Raman spectra of ZrO_2 calcined at the temperatures of 600°C and 800°C are plotted in Figure 6(a). The assignment of the observed bands was made on the basis of the comparison of the observed spectra with those of reported in the literature [1, 35, 36]. The vibrational Raman active modes are classified as

$$\Gamma = A_{1g} + 2B_{1g} + 3E_g. \quad (4)$$

In A_{1g} mode oxygen atoms move in the z -direction only. The B_{1g} modes also involve motion in the z -direction; however now both Zr and O atoms participate. In E_g modes, Zr as well as O atoms move in the x - y plane. In Figure 6(a), the plot (A) represents the Raman spectra for the sample calcined at 400°C . The band that appeared at 643 cm^{-1} can be assigned to A_{1g} mode since it involves movement of two oxygen atoms only and is expected to appear at higher wavenumber. The next two bands that appeared at 470 and 382 cm^{-1} are assigned to doubly degenerate E_g modes on the simple reasoning that these two modes also do not involve movement of Zr atoms. The remaining three modes, namely, two B_{1g} modes and one E_g modes are assigned to the remaining three bands appeared at 259 , 146 , and 123 cm^{-1} , respectively. The spectrum of sample calcined at 600°C is shown as curve (B) in Figure 6(a). The previous bands that appeared in the Raman spectra for both samples are assigned to $t\text{-ZrO}_2$. In addition, few faint bands at 563 , 536 , 381 , 293 , and 176 cm^{-1} have appeared which are due to the coexistence of small amount of monoclinic phase.

The Raman spectra of ZrTiO_4 (ZT1 and ZT2) are shown in Figures 6(b) and 6(c). The location of band positions is shown in Table 1. The band positions recorded by Karakchiev et al. [1] for ZrO_2 are shown in Table 1 for comparison. ZrTiO_4 with orthorhombic symmetry (space group $Pbcn$, point group mmm) and two formula units in a unit cell have 33 optically active modes of vibration, 18 of which are Raman active and 15 are infrared active phonon modes. Their distributions are as follows: Raman: $4A_g$, $5B_{1g}$, $4B_{2g}$,

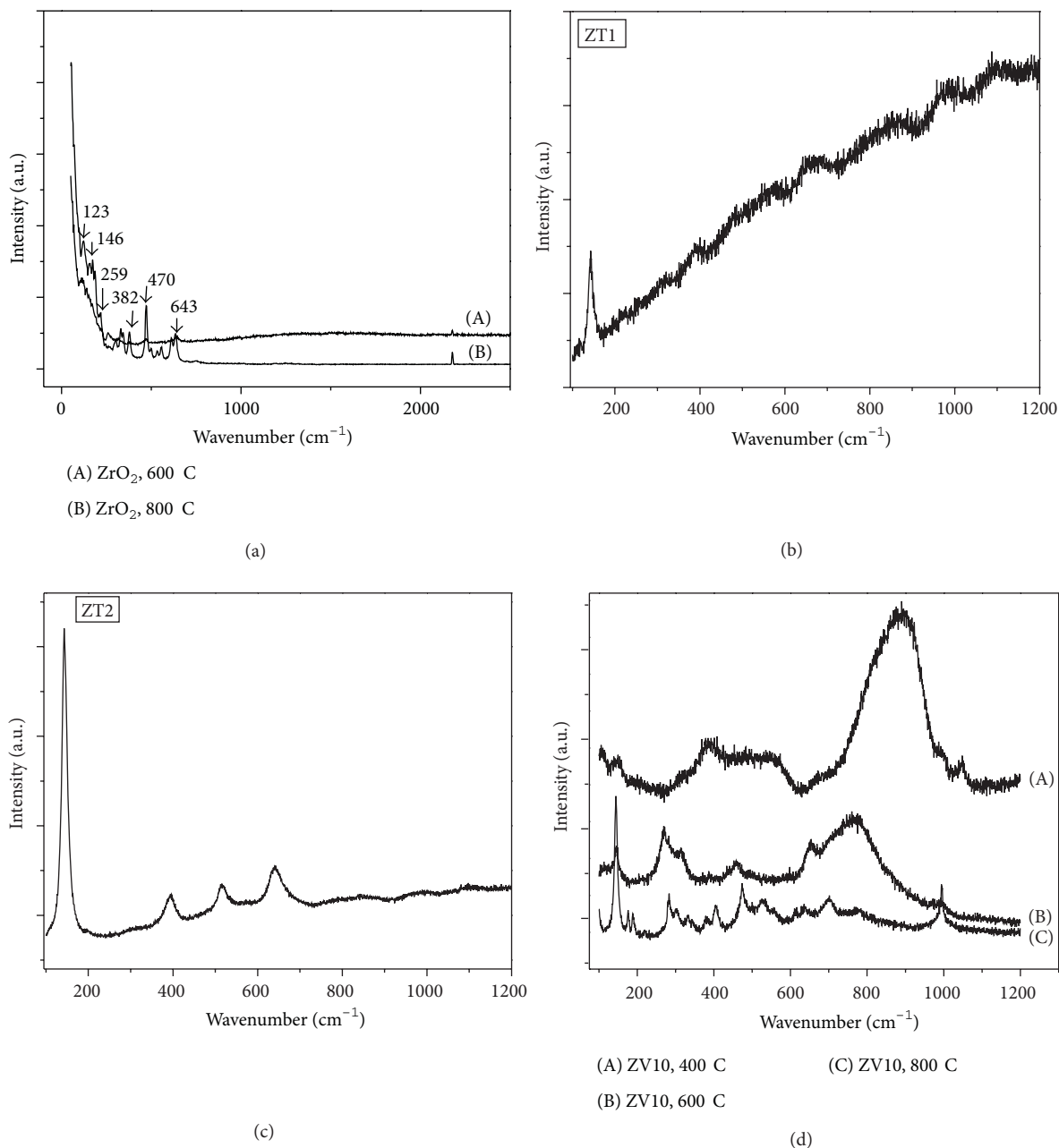


FIGURE 6: Raman spectra of (a) ZrO₂ precipitated at pH 2 and calcined at different temperatures, (b) ZT1 and (c) ZT2 calcined at 400°C, and (d) ZV10 calcined at (A) 400°C, (B) 600°C, and (C) 800°C.

$5B_{3g}$ and Infrared: $4A_u$, $4B_{1u}$, $3B_{2u}$, $4B_{3u}$. Raman line shape analysis has also been studied by Kim et al. [37, 38] and Krebs and Condrate [39]. The number of observed bands in the present recording is much less as compared to those obtained for the samples prepared by ceramics due to the fact that (a) band positions are at lower wavenumbers, (b) bands are too weak to be observed (c) bands are hidden due to overlap by other bands and, (d) lower degree of ordering in nanocrystalline ZrTiO₄. The bands due to that appeared in nanocrystalline ZrTiO₄ samples are broader compared to those in ZrO₂ and can be attributed to local compositional fluctuations or local positional disordering produced due to

random distribution of Zr⁴⁺ and Ti⁴⁺ between equivalent sites in the crystal lattice.

In the similar experimental setup, the representative Raman spectra for ZrV₂O₇ (ZV10) samples calcined at 400°C, 600°C, and 800°C are plotted in Figure 6(d), and the assignments of bands are made on the basis of reported assignments [1, 35–39] and are given in Table 2. 14 Raman-active modes centred at 144, 176, 187, 269, 282, 384, 406, 474, 654, 705, 773, 889, 996, and 1044 cm⁻¹ were detected. The ZrV₂O₇ crystals contain the VO₄ tetrahedra and ZrO₆ octahedra in the structure. The modes centred at 889, 996, and 1044 cm⁻¹ are assigned to symmetric stretching of the VO₄ tetrahedra.

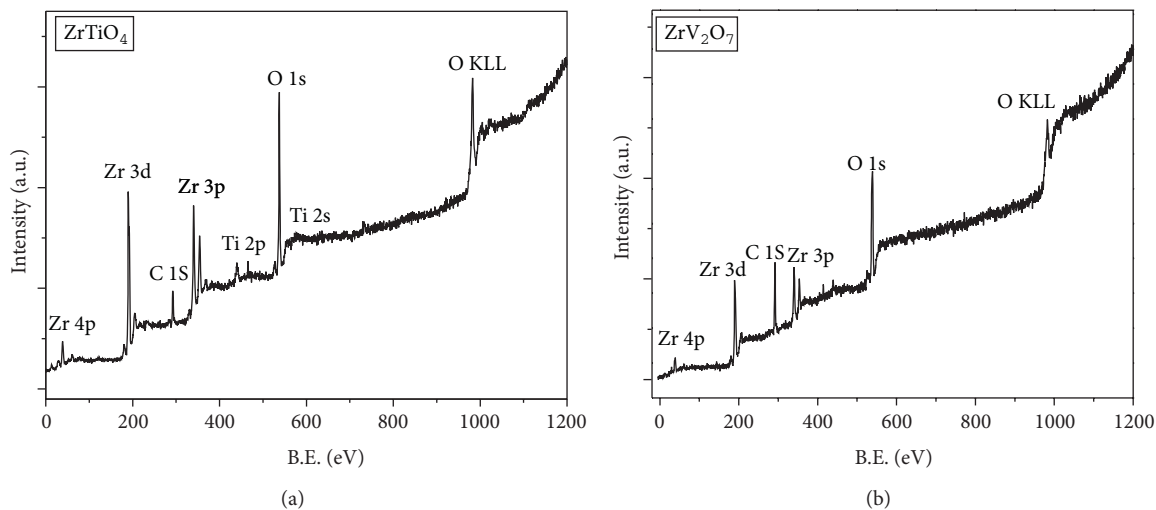


FIGURE 7: Representative survey XPS spectra of (a) ZrTiO_4 and (b) ZrV_2O_7 nanoparticles calcined at 400°C .

TABLE 1: Observed bands (cm^{-1}) and their assignments in ZT1, ZT2, and ZrO_2 .

ZT1	ZT2	ZrO_2	Reference [1]
141 (VS)	141 (VS)	146 (VS)	145 (VS)
388 (S)	395 (S)	382 (S)	405 (S)
		470 (M)	
572 (M)	514 (S)		515 (M)
652 (M)	642 (S)	643 (M)	635 (S)
850 (W)	839 (VVW)		
986 (W)			
1085 (W)			

VS: very sharp; S: sharp; M: medium; W: weak; VVW: very very weak.

The modes centred at 705 and 773 cm^{-1} are assigned to the asymmetric stretching of the VO_4 tetrahedra. The modes centred at 269 , 282 , and 384 cm^{-1} are assigned to the symmetric ZrO_6 octahedral stretching and at 406 cm^{-1} to the asymmetric ZrO_6 octahedral bending. The modes centred at 474 and 654 cm^{-1} are assigned to ZrO_2 tetragonal stretching. The low frequency bands that appeared at 144 , 176 , and 187 cm^{-1} are assigned to lattice vibrations. The sharpness in the peaks is observed with the increase in calcination temperature indicating increase in particle size with temperature. These results are consistent with previous studies of $\text{V}_2\text{O}_5/\text{ZrO}_2$ which have also confirmed the formation of ZrV_2O_7 on calcination at high temperatures [40, 41].

X-ray photoelectron spectroscopy (XPS) method has been used to study experimentally the valence-band and core-level spectra as well as the energy distribution of some occupied valence states of the constituent atoms of ZrTiO_4 . XPS valence-band and core-level spectra of ZrTiO_4 were measured using the UHV analysis system. $\text{Al K}\alpha$ radiation ($E = 1486.6\text{ eV}$) and hemispherical analyzer operating at constant pass energy of 40 eV were used as a source of XPS spectra excitation. The XPS survey spectrum of ZrTiO_4 (ZT2)

TABLE 2: Observed Raman bands (cm^{-1}) and their assignment for ZrV_2O_7 calcined at 800°C .

Observed bands (cm^{-1})	Assignment
144 (s), 176 (w), 187 (w)	Lattice
889 (s), 993 (s), 1044 (m)	VO_4 (symmetric)
705 (m), 773 (m)	VO_4 (asymmetric)
474 (s), 654 (m)	ZrO_2 (tetragonal)
269 (s), 282 (m), 384 (w)	ZrO_6 (symmetric)
406 (m)	ZrO_6 (asymmetric)

s: strong; m: medium; w: weak.

is shown in Figure 7(a). It has been reported that the X-ray emission of $\text{Ti L}\alpha$, $\text{Zr L}\beta_{2,15}$, and $\text{O K}\alpha$ bands on a common energy scale indicates that Ti 3d , Zr 4d , and O 2p states contribute throughout the valence-band region of ZrTiO_4 [42]. The XPS spectra show that the XPS bands for Zr 3d , Zr 3p , and Ti 2p core-level spectra are simple spin doublets with the XPS $\text{Zr 3d}_{5/2}$, $\text{Zr 3p}_{3/2}$, and $\text{Ti 2p}_{3/2}$ core-level binding energies appearing at 190 , 342 , and 440 eV , respectively, which correspond to those of titanium and zirconium in the formal valence state of Zr^{4+} and Ti^{4+} [43]. The previous results reveal that in ZrTiO_4 the binding energy positions of Ti 2p and O 1s core levels match well with the reported values. Similarly, the XPS of ZrV_2O_7 was taken using UHV analysis system with $\text{Al K}\alpha$ radiation ($E = 1486.6\text{ eV}$) and hemispherical analyzer operating at constant pass energy of 25 eV being used as a source of XPS spectra excitation. Figure 7(b) shows the XPS survey spectrum of ZrV_2O_7 . The spectra confirm the presence of vanadium, zirconium, carbon, and oxygen [42, 44]. The peak at 517 eV is due to $\text{V 2p}_{3/2}$ and indicates the presence of V^{5+} species. The peak that appeared at 524.4 eV can be assigned to $\text{V 2p}_{1/2}$, and shift in this peak from 523 eV to 524.4 eV can be ascribed to change in the oxidation state from V^{4+} to V^{5+} . The strong peak that appeared at 537.6 eV is assigned to O 1s . The peak at 291.5 is due to C 1s , and

the doublet that appeared at 340.1 eV and 353.3 eV can be assigned to Zr 3p_{3/2} and Zr 3p_{1/2}, respectively. The binding energy positions of the species (V, O and Zr) obtained in the present investigations match well with the reported values.

4. Conclusion

Microwave-assisted method of oxide synthesis is important due to its high reaction rate, efficient heat transfer, and environmental friendly nature. In this process material is directly heated by radiation leading to higher temperature homogeneity. ZrO₂ and ZrTiO₄ nanoparticles were synthesized by microwave assisted citrate sol-gel method. Nanoparticles of V₂O₅ supported on ZrO₂ were synthesized by microwave-assisted solution combustion method. The formation of tetragonal crystalline phase (t-ZrO₂) was confirmed by powder XRD analysis. The low angle powder XRD measurements confirm the mesoporous nature of ZrV₂O₇ and formation of single phase material up to 10 wt% of vanadium incorporation. The morphology, particle size, and microstructure were analyzed using high-resolution transmission electron microscopy. The HRTEM data also confirms the formation of single phase t-ZrO₂. Raman spectra further support and confirm the crystalline phase as well as the specific bands to show the modes of vibration in Zr-O system, whereas the specific bands indicate the modes of vibration in Zr-Ti-O and ZrV₂O₇ systems. The XPS results show that the X-ray emission of Ti L_α, Zr L_{β2,15}, and O K_α bands on a common energy scale indicates that Ti 3d, Zr 4d, and O 2p states contribute throughout the valence-band region of ZrTiO₄. The Raman spectra show the specific bands indicative of the modes of vibration in Zr-V-O system and presence of VO₄ tetrahedra and ZrO₆ octahedra in the crystal structure. XPS results show that the X-ray emission of V, Zr, and O bands on a common energy scale indicates that V 2p, Zr 3p, and O 1s states contribute throughout the valence-band region. The crystallite sizes were found to be in the ranges of ~5–10 nm, ~2–5 nm, and ~20–50 nm for ZrO₂, ZrTiO₄, and ZrV₂O₇, respectively.

References

- [1] L. G. Karakchiev, T. M. Zima, and N. Z. Lyakhov, "Low-temperature synthesis of zirconium titanate," *Inorganic Materials*, vol. 37, no. 4, pp. 386–390, 2001.
- [2] G. K. Chuah, S. Jaenicke, and B. K. Pong, "The preparation of high-surface-area zirconia: II. Influence of precipitating agent and digestion on the morphology and microstructure of hydrous zirconia," *Journal of Catalysis*, vol. 175, no. 1, pp. 80–92, 1998.
- [3] N. Q. Minh, "Ceramic fuel cells," *Journal of the American Ceramic Society*, vol. 76, no. 3, pp. 563–588, 1993.
- [4] A. B. F. Martinson, J. W. Elam, J. T. Hupp, and M. J. Pellin, "ZnO nanotube based dye-sensitized solar cells," *Nano Letters*, vol. 7, no. 8, pp. 2183–2187, 2007.
- [5] E. C. Subbarao and H. S. Maiti, "Oxygen sensors and pumps," *Advanced Ceramic*, vol. 24, pp. 731–748, 1988.
- [6] J. D. Kim, S. Hana, S. Kawagoe, K. Sasaki, and T. Hata, "Preparation of perovskite, Pb(Zr, Ti)O₃ thin-films on YSZ(11)/Si(111) substrates by post-deposition annealing," *Thin Solid Films*, vol. 385, no. 1-2, pp. 293–297, 2001.
- [7] M. Laurent, U. Schreiner, P. A. Langjahr, A. E. Glazounov, and M. J. Hoffmann, "Microstructural and electrical characterization of La-doped PZT ceramics prepared by a precursor route," *Journal of the European Ceramic Society*, vol. 21, no. 10-11, pp. 1495–1498, 2001.
- [8] J. T. Kim, G. G. Hong, and H. L. Lee, "Properties of the powders of the system Al₂O₃-ZrO₂-Y₂O₃ prepared by precipitation method," *Journal of the Korean Ceramic Society*, vol. 25, pp. 117–124, 1988.
- [9] K. Prabhakaran, S. Kannan, and S. Rajeswari, "Development and characterisation of zirconia and hydroxyapatite composites for orthopaedic applications," *Trends in Biomaterials and Artificial Organs*, vol. 18, no. 2, pp. 114–116, 2005.
- [10] J. L. Gole, S. M. Prokes, J. D. Stout, O. J. Glembocki, and R. Yang, "Unique properties of selectively formed zirconia nanostructures," *Advanced Materials*, vol. 18, no. 5, pp. 664–667, 2006.
- [11] L. Wang, K. F. Cai, Y. Y. Wang, J. L. Yin, H. Li, and C. W. Zhou, "Preparation and characterization of tetragonal-ZrO₂ nanoparticles by a molten hydroxides method," *Ceramics International*, vol. 35, no. 6, pp. 2499–2501, 2009.
- [12] J. Joo, T. Yu, Y. W. Kim et al., "Multigram scale synthesis and characterization of monodisperse tetragonal zirconia nanocrystals," *Journal of the American Chemical Society*, vol. 125, no. 21, pp. 6553–6557, 2003.
- [13] H. Cao, X. Qiu, B. Luo et al., "Synthesis and room-temperature ultraviolet photoluminescence properties of Zirconia nanowires," *Advanced Functional Materials*, vol. 14, no. 3, pp. 243–246, 2004.
- [14] S. Shukla and S. Seal, "Mechanisms of room temperature metastable tetragonal phase stabilisation in zirconia," *International Materials Reviews*, vol. 50, no. 1, pp. 45–64, 2005.
- [15] N. Vittayakorn, "Synthesis and a crystal structural study of microwave dielectric Zirconium Titanate (ZrTiO₄) powders via a mixed oxide synthesis route," *Journal of Ceramic Processing Research*, vol. 7, no. 4, pp. 288–291, 2006.
- [16] S. V. Pol, V. G. Pol, and A. Gedanken, "Encapsulating ZnS and ZnSe nanocrystals in the carbon shell: a RAPET approach," *Journal of Physical Chemistry C*, vol. 111, no. 36, pp. 13309–13314, 2007.
- [17] V. Dos Santos, M. Zeni, J. M. Hohemberger, and C. P. Bergmann, "Preparation of crystalline ZrTiO₄ at low thermal treatment temperatures," *Reviews on Advanced Materials Science*, vol. 24, no. 1-2, pp. 44–47, 2010.
- [18] B. M. Reddy, P. M. Sreekanth, Y. Yamada, Q. Xu, and T. Kobayashi, "Surface characterization of sulfate, molybdate, and tungstate promoted TiO₂-ZrO₂ solid acid catalysts by XPS and other techniques," *Applied Catalysis A*, vol. 228, no. 1-2, pp. 269–278, 2002.
- [19] B. M. Reddy and A. Khan, "Recent advances on TiO₂-ZrO₂ mixed oxides as catalysts and catalyst supports," *Catalysis Reviews*, vol. 47, no. 2, pp. 257–296, 2005.
- [20] A. Majchrowski, J. Ebothe, E. Gondek et al., "Photoinduced nonlinear optical effects in the Pr doped BiB₃O₆ glass nanoparticles incorporated into the polymer matrices," *Journal of Alloys and Compounds*, vol. 485, no. 1-2, pp. 29–32, 2009.
- [21] Y. Djaoued, K. Ozga, A. Wojciechowski, A. H. Reshak, J. Robichaud, and I. V. Kityk, "Photoinduced effects in TiO₂

- nanocrystalline films with different morphology," *Journal of Alloys and Compounds*, vol. 508, no. 2, pp. 599–605, 2010.
- [22] A. Adamski, Z. Sojka, K. Dyrek, M. Che, G. Wendt, and S. Albrecht, "Surface heterogeneity of zirconia-supported V₂O₅ catalysts. The link between structure and catalytic properties in oxidative dehydrogenation of propane," *Langmuir*, vol. 15, no. 18, pp. 5733–5741, 1999.
- [23] E. V. Kondratenko, M. Cherian, and M. Baerns, "Oxidative dehydrogenation of propane over differently structured vanadia-based catalysts in the presence of O₂ and N₂O," *Catalysis Today*, vol. 112, no. 1–4, pp. 60–63, 2006.
- [24] R. Sasikala, V. Sudarsan, T. Sakuntala, J. C. Sudakar, R. Naik, and S. R. Bharadwaj, "Nanoparticles of vanadia-zirconia catalysts synthesized by polyol-mediated route: enhanced selectivity for the oxidative dehydrogenation of propane to propene," *Applied Catalysis A*, vol. 350, no. 2, pp. 252–258, 2008.
- [25] J. J. Kingsley and K. C. Patil, "A novel combustion process for the synthesis of fine particle α -alumina and related oxide materials," *Materials Letters*, vol. 6, no. 11–12, pp. 427–432, 1988.
- [26] S. T. Aruna and A. S. Mukasyan, "Combustion synthesis and nanomaterials," *Current Opinion in Solid State and Materials Science*, vol. 12, no. 3–4, pp. 44–50, 2008.
- [27] S. Kumarsrinivasan, A. Verma, and S. G. Chinnakonda, "Molecular oxygen-assisted oxidative dehydrogenation of ethylbenzene to styrene with nanocrystalline Ti_{1-x}V_xO₂," *Green Chemistry*, vol. 14, pp. 461–471, 2012.
- [28] B. D. Cullity, *Elements of X-Ray Diffraction*, Addison-Wesley, Reading, Mass, USA, 2nd edition, 1978.
- [29] M. De and D. Kunzru, "Effect of calcium and potassium on V₂O₅/ZrO₂ catalyst for oxidative dehydrogenation of propane: a comparative study," *Catalysis Letters*, vol. 102, no. 3–4, pp. 237–246, 2005.
- [30] A. Khodakov, J. Yang, S. Su, E. Iglesia, and A. T. Bell, "Structure and properties of vanadium oxide-zirconia catalysts for propane oxidative dehydrogenation," *Journal of Catalysis*, vol. 177, no. 2, pp. 343–351, 1998.
- [31] S. Biz and M. L. Occelli, "Synthesis and characterization of mesostructured materials," *Catalysis Reviews*, vol. 40, no. 3, pp. 329–407, 1998.
- [32] K. S. Bartwal, S. Kar, N. Kaithwas et al., "Synthesis and characterization of Y₃Al₅O₁₂ nanocrystals," *Advanced Materials Research*, vol. 24–25, pp. 665–670, 2007.
- [33] N. Kaithwas, M. Dave, S. Kar, S. Verma, and K. S. Bartwal, "Preparation of Nd:Y₃Al₅O₁₂ nanocrystals by low temperature glycol route," *Crystal Research and Technology*, vol. 45, no. 11, pp. 1179–1182, 2010.
- [34] S. Kar, S. Verma, and K. S. Bartwal, "Preparation of Mn doped Li₂B₄O₇ nanoparticles by glass quenching," *Journal of Alloys and Compounds*, vol. 495, no. 1, pp. 288–291, 2010.
- [35] K. J. Rao and P. D. Ramesh, "Use of microwaves for the synthesis and processing of materials," *Bulletin of Materials Science*, vol. 18, no. 4, pp. 447–465, 1995.
- [36] S. Park, D. W. Lee, J. C. Lee, and J. H. Lee, "Photocatalytic silver recovery using ZnO nanopowders synthesized by modified glycine-nitrate process," *Journal of the American Ceramic Society*, vol. 86, no. 9, pp. 1508–1512, 2003.
- [37] B. K. Kim, J. W. Hahn, and K. R. Han, "Quantitative phase analysis in tetragonal-rich tetragonal/monoclinic two phase zirconia by Raman spectroscopy," *Journal of Materials Science Letters*, vol. 16, no. 8, pp. 669–671, 1997.
- [38] Y. K. Kim and H. M. Jang, "Raman line-shape analysis of nanostructural evolution in cation-ordered ZrTiO₇-based dielectrics," *Solid State Communications*, vol. 127, no. 6, pp. 433–437, 2003.
- [39] M. A. Krebs and R. A. Condrate, "A Raman spectral characterization of various crystalline mixtures in the ZrO₂-TiO₂ and HfO₂-TiO₂ systems," *Journal of Materials Science Letters*, vol. 7, no. 12, pp. 1327–1330, 1988.
- [40] C. V. Ramana, R. J. Smith, O. M. Hussain, M. Massot, and C. M. Julien, "Surface analysis of pulsed laser-deposited V₂O₅ thin films and their lithium intercalated products studied by Raman spectroscopy," *Surface and Interface Analysis*, vol. 37, no. 4, pp. 406–411, 2005.
- [41] U. L. C. Hemamala, F. El-Ghoussein, D. V. S. Muthu et al., "High-pressure Raman and infrared study of ZrV₂O₇," *Solid State Communications*, vol. 141, no. 12, pp. 680–684, 2007.
- [42] A. A. Lavrentyev, B. V. Gabrelian, P. N. Shkumat et al., "Electronic structure of ZrTiO₄ and HfTiO₄: self-consistent cluster calculations and X-ray spectroscopy studies," *Journal of Physics and Chemistry of Solids*, vol. 72, no. 2, pp. 83–89, 2011.
- [43] I. F. Moulder, W. E. Sticlke, P. E. Sobol, and K. E. Bomben, *Handbook of X-Ray Photoelectron Spectroscopy*, Edited by J. Chastian, Perkin-Elmer, Eden Prairie, Minn, USA, 1992.
- [44] M. Kantcheva, "Spectroscopic characterization of vanadium(v) oxo species deposited on zirconia," *Physical Chemistry Chemical Physics*, vol. 2, no. 13, pp. 3043–3048, 2000.

Research Article

Selective Hydrogenation of *p*-Chloronitrobenzene on Nanosized PdNiB Catalysts

Yu-Wen Chen and Der-Shing Lee

Department of Chemical Engineering, National Central University, Chung-Li 320, Taiwan

Correspondence should be addressed to Yu-Wen Chen; ywchen@ncu.edu.tw

Received 10 January 2013; Accepted 1 February 2013

Academic Editor: Mohammad H. Maneshian

Copyright © 2013 Y.-W. Chen and D.-S. Lee. This is an open access article distributed under the Creative Commons Attribution License, which permits unrestricted use, distribution, and reproduction in any medium, provided the original work is properly cited.

A series of PdNiB bimetallic nanoalloy catalysts with various Pd contents was prepared. Pd was well dispersed in NiB. Even adding a small amount of Pd in NiB had a significant effect on activity and selectivity in hydrogenation of *p*-chloronitrobenzene (*p*-CNB) to *p*-chloroaniline (*p*-CAN). High activity and selectivity on PdNiB could be attributed to both ensemble effect and electronic effect. The particle size in PdNiB decreased with an increase in Pd content. Electron-enriched Ni could activate the polar-NO₂ groups of *p*-CNB and depress the dehalogenation of *p*-CAN.

1. Introduction

Bimetallic nanoparticle catalysts have received increasing attention [1–9]. The most remarkable features of nanoscopic materials are that their chemical and physical properties are quite different from those of bulk solids and those of atoms. This phenomenon has been known as a quantum effect [10–13]. Magnetic enhancement has been expected in Pd clusters owing to their finite size because Pd does not polarize magnetically in bulk metal state, but has giant magnetic moment in the presence of ferromagnetic 3d transition metals [14–18]. One could successfully prepare chemically monodispersed ultrafine Pd and bimetallic PdNi particles [17–19].

The addition of the second metal plays a key role in controlling the activity, selectivity, and stability of catalysts in certain reactions. However, little is known about the electronic structures of bimetallic clusters of groups 8–10. Since both Ni and Pd belong to the same group 10 in the periodic table, the increase (mixing) between Ni 3d⁸4s² electrons and Pd 4d¹⁰5s⁰ electrons is very likely involved in intermetallic Ni-Pd bonding [19]. Such effect on the catalysis by nanosized NiPd clusters is certainly interesting.

Aromatic chloramines are important intermediates in the synthesis of dyes, drugs, herbicides, and pesticides [20–34]. At present, these organic amines are generally

produced through selective hydrogenation of the corresponding aromatic chloronitro compounds over transition metal catalysts such as Pt and Ni [35–39]. In this process, the hydrodechlorination of the aromatic chloramines often occurs over most metal catalysts because of the electron-donating effect of amino group in the aromatic ring. Keane [40] reported that in the continuous gas phase hydrogenation of *p*-chloronitrobenzene (*p*-CNB) over several supported Ni catalysts, *p*-chloroaniline (*p*-CAN) was produced as the main product at *p*-CNB conversion of about 15%, which is enlightening for the development of a clean route to produce chloroanilines. It has been reported by this lab [41–43] that NiB is more active and selective than Raney nickel catalyst for hydrogenation of *p*-CNB to *p*-CAN. Many modifiers were added on NiB for hydrogenation of chloronitrobenzene [44–70]. Although intensive efforts have been made to solve the problem of hydrodechlorination in CNB hydrogenation, it is still a challenge to create novel catalysts for further improving the selectivity to CAN at complete conversion of the substrates and intermediates and simultaneously maintaining the high catalytic activity [20–32].

Usually the desired selectivity can be achieved by the addition of some inhibitors or some modifiers such as base or other electron-donating compounds to the catalyst or to the solution phase. By alloying a second metal to platinum, Coq

et al. [71, 72] obtained good results in the hydrogenation of *p*-CNB over PtSn/Al₂O₃ catalysts, with 97.5% *p*-CAN selectivity at >98% conversion. Comparing with Pt catalysts, Pd catalysts exhibit low selectivity of CAN in the hydrogenation of CNB because the concomitant hydrodechlorination reactions are serious over Pd-based catalysts. The most attractive advantage of Pd-based catalysts over Pt-based ones is its low cost. In order to improve the selectivity to CAN in the hydrogenation of CNB over Pd catalysts, several strategies have been developed, such as introducing some promoting or inhabiting additives to the solution phase or to the catalysts, alloying Pd with other metals, applying partly poisoned catalysts, and modulating the metal/support interaction in supported Pd catalysts. PdB has been reported to be an active catalyst than Pd [14–19].

In a previous paper [9], one of the authors has reported the Pt-NiB catalyst for hydrogenation of *p*-CNB. However, Pt was too active to have high selectivity to the *p*-CAN product. Pd was chosen as the dopant of NiB in this study because its hydrogenation capability was not too high to have high selectivity to *p*-CAN and not too low to have low activity. By adding suitable amount of Pd in NiB, it was expected to have high conversion of *p*-CNB and high selectivity of *p*-CAN.

The objective of this study was to synthesize PdNiB bimetallic nanocatalysts and to investigate the effect of Pd content on the catalytic properties of PdNiB catalysts in liquid-phase hydrogenation of *p*-CNB to *p*-CAN.

2. Experimental

2.1. Materials. *p*-CNB, with a purity of >99%, was obtained from Acros (Belgium). High-purity hydrogen gas (>99.99% from Air Product) was used without further purification. Palladium nitrate and nickel acetate (>98%) were supplied by Showa Chemicals (Tokyo, Japan), and sodium borohydride was purchased from Lancaster (Morecambe, UK). Sodium hydroxide, methanol, and ammonia solutions were purchased from Tedia Co. (OH, USA). Ethanol was purchased from Showa Chemicals (Tokyo, Japan). Raney nickel catalyst was obtained from Merck. All other solvents and reagents were of analytical grade quality, purchased commercially, and used without any further purification. Water used in the whole process was doubly distilled water.

2.2. Catalysts Preparation. A series of PdNiB catalysts was prepared by the chemical reduction method. Pd/Ni atomic ratios were between 0.001 and 0.02 for investigation. Nickel acetate and palladium nitrate were added to the 50% methanol/water solution (both were 0.1M) at room temperature under vigorous stirring and used nitrogen stream to remove air. The solution of reduction agent, sodium borohydride (1M), was added with the microtubing pump into the solution drop by drop. The atomic ratio of (Ni + Pd) to B was fixed at 1 : 3. Excess amount of sodium borohydride was used to ensure that all nickel and palladium cations were reduced to metals. When no bubbles were released, the black powders were centrifuged and were washed to remove the impurities, that is, Na⁺ ions and the excess amount boride

species, by hot deionized water for three times and with methanol twice. Since all catalysts were easily oxidized in air, care must be taken to avoid their exposure to air. Generally, the catalysts were kept in methanol until further use.

2.3. Catalyst Characterization. The catalysts were characterized by XRD, TEM, and XPS. The crystalline structure of the catalysts was characterized by XRD using a Siemens D500 powder X-ray diffractometer. The XRD patterns were collected by using Cu K_α radiation ($\lambda = 0.15418$ nm). The tube voltage and current were 40 kV and 40 mA, respectively. The scanning rate was 0.05° s⁻¹.

The morphologies of the catalysts were determined by TEM (Jeol JEM-2000 FX II). TEM was operated at 160 kV and the magnification was 200 K. A small amount of sample was put into the sample tube filled with a 95% ethanol solution. After agitation under ultrasonic environment for 90 min, one drop of the dispersed slurry was dipped onto a carbon coated copper mesh (300#) (Ted Pella Inc., CA, USA) and dried at room temperature in vacuum overnight.

The compositions and the electronic state of each element on the surface of the catalysts were studied by XPS on a Thermo VG Scientific Sigma Probe spectrometer. Al K_α radiation was used as the excitation source ($h\nu = 1486.6$ eV) (20 kV, 30 mA). The sample was pressed as a self-supported plate and was mounted on the sample cell. It was degassed in the pretreatment chamber at 343 K for 2 h and then it was transferred into the analyzing chamber where the background pressure was lower than 10⁻⁷ Pa. Before the XPS test, the sample was sputtered using Ar⁺ ions for 15 min to remove the oxidation parts, which were formed during the XPS operation. All the binding energies were calibrated by using the contaminant carbon (C1s = 284.6 eV). The XPS spectrum of each element was deconvoluted using a Gaussian-Lorentz curve-fitting program, the background was corrected using a Shirley-type baseline, and the peak type was Gaussian-Lorentz (7 : 3). The surface composition of each sample was calculated using the corresponding peak areas of Ni, Pd, and B, and the PHI sensitive factors were applied in the calculation. It should be noted that, for Ni, only the 2p_{3/2} subbands were studied instead of the 2p_{1/2} subbands, because the former have a much higher signal-to-noise ratio and provide the same information.

2.4. Reaction Test. All the experiments were carried out in the cylindrical stirred-tank reactor (Parr Instrument Model 4842). A four-bladed pitched impeller was placed for effective agitation, and the agitator was connected to an electric motor with variable speed up to 1700 rpm. A pressure transmitter and an automatic temperature controller were also provided. Hydrogen was introduced at the bottom of the reactor. A separate tube was used as sampling tube for the liquid phase. The reactor was charged by 0.002 mol Ni catalyst and 2.54 g *p*-CNB in 80 mL methanol; the concentration of *p*-CNB was 0.2M. It was reported that methanol was a better reaction medium than ethanol for the hydrogenation reaction. The reaction was operated in reaction-controlled regime, as confirmed by using the different particle size and

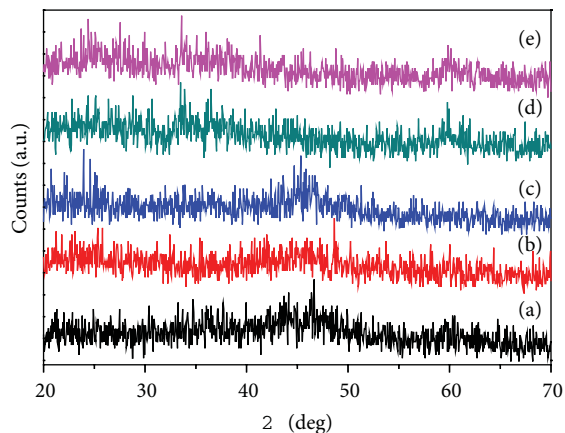


FIGURE 1: XRD patterns of catalyst samples, (a) NiB, (b) 0.001Pd-NiB, (c) 0.005Pd-NiB, (d) 0.01Pd-NiB, and (e) 0.02Pd-NiB.

stirring rate. The results showed that 400 rpm was enough to free from external diffusion. Therefore, 500 rpm stirring speed was used in this study. PdNiB sample was in nanosize range; one can conclude that the pore diffusion was not important in this study. During the reaction run, the samples were withdrawn periodically (every 10 min) and analyzed by a gas chromatograph equipped with a flame ionization detector and a 3 m × 1/8 inch stainless steel column packed with 5% OV-101 on Chromosorb WAW-DMSC (80–100 mesh). The conversion and the selectivity of each product were calculated as follows:

$$\begin{aligned}
 & \text{conversion (\%)} \\
 & = \left(1 - \frac{C_{p\text{-CNB}}}{C_{\text{AN}} + C_{\text{NB}} + C_{p\text{-CAN}} + C_{p\text{-CNB}}} \right) \times 100\%, \\
 & S_{\text{AN}} (\%) = \left(\frac{C_{\text{AN}}}{C_{\text{AN}} + C_{\text{NB}} + C_{p\text{-CAN}}} \right) \times 100\%, \\
 & S_{\text{NB}} (\%) = \left(\frac{C_{\text{NB}}}{C_{\text{AN}} + C_{\text{NB}} + C_{p\text{-CAN}}} \right) \times 100\%, \\
 & S_{p\text{-CAN}} (\%) = \left(\frac{C_{p\text{-CAN}}}{C_{\text{AN}} + C_{\text{NB}} + C_{p\text{-CAN}}} \right) \times 100\%,
 \end{aligned} \tag{1}$$

where C_{AN} , C_{NB} , $C_{p\text{-CAN}}$, and $C_{p\text{-CNB}}$ represented the concentration of aniline, nitrobenzene, *p*-chloroaniline, and *p*-chloronitrobenzene, respectively.

3. Results and Discussion

3.1. XRD. XRD was used to characterize the structure of the Pd-NiB bimetallic nanoparticles. The XRD patterns of NiB and Pd-NiB samples with various contents of Pd are shown in Figure 1. The broad peak at $2\theta = 45^\circ$ in each pattern indicates the amorphous phase in all the as-prepared samples, in consistent with those in the literature [9, 11, 12]. It is further evidenced by a diffuse Debye ring rather than

distinct dots in their SAED patterns. It has been reported that Ni can form several types of compounds with B such as NiB, Ni₂B, and Ni₃B. After adding the Pd, the intensities of this peak decreased. This shows that the presence of Pd could suppress the crystalline growth (long-range order) of NiB. No diffraction peak corresponding to crystalline Pd was found, indicating a high dispersion of Pd in NiB. No other crystalline phases (including palladium-related compounds, elemental Ni, B, and the corresponding oxides and hydroxides) were observed. One can conclude that PdNiB possessed short-range order and long range disorder, resulting in more surface coordinating unsaturated sites, more crystalline defects, and isotropic structure. Alloying Pd interrupts the long-range order of NiB, resulting in the characteristics of small cluster of NiB. Wang et al. [73] reported that a metal can disperse on the surface of another metal to form a highly dispersed bimetallic system due to the formation of bonds between the two metals. They noted that a highly dispersed Pd-Ni system occurred when <2.0 wt% Pd was loaded on a Pd/Ni catalyst. Our results are in accord.

3.2. TEM. Figure 2 shows the morphology of the as-prepared samples. With the addition of Pd, the particle size tends to decrease. Due to the high surface energy of the nanosized amorphous alloys, metal metalloids prepared by chemical reduction with borohydride are inclined to aggregate to form larger particles with diameters of several 10s to several 100s nanometers. Each sample was composed of many small particles, and the size of the aggregates was about 50 nm. It was difficult to obtain detailed information on the TEM photos because of the aggregation of the particles by the very strong van der Waals force and magnetization. One was not able to see any Pd particles due to very low concentration in the sample. After adding Pd on NiB, it became difficult to sediment in water, indicating that Pd-NiB particles were smaller than NiB particles. The primary particles of PdNiB were very fine. One could conclude that the size of primary particles of PdNiB was much smaller than 50 nm. Moreover, the magnetization of ultrafine particles remarkably increased with doping Pd into NiB.

3.3. XPS. The compositions and the electronic structure of each species on the surface of the samples were determined by XPS analysis. All of the spectra were deconvoluted, and the amount of each species in each state was calculated based on the corresponding peak area. The XPS spectra of Ni_{2p} and B_{1s} are shown in Figures 3 and 4. The binding energy of Ni_{2p} level is ascribed to 856.8, 857.7, 856.0, 853.4, 856.3, and 856.7 eV, respectively, for the samples of NiB, 0.001Pd-NiB, 0.005Ni-Pd, 0.01Pd-NiB, and 0.02Pd-NiB. These are assigned to the metallic nickel. The peak around 862.2 eV is ascribed to nickel oxide (it was simply donated as Ni²⁺ for the oxidized state of Ni; similar notations were used for the other elements). Tolman et al. [74] investigated a variety of Ni⁰ organometallic compounds and found that in zero-valence state Ni complexes, the Ni_{2p_{3/2}} binding energies span a range of 853.6–856.0 eV, while higher binding energy peaks were observed in a range of 855.0–857.2 eV in Ni²⁺ complexes, and even higher

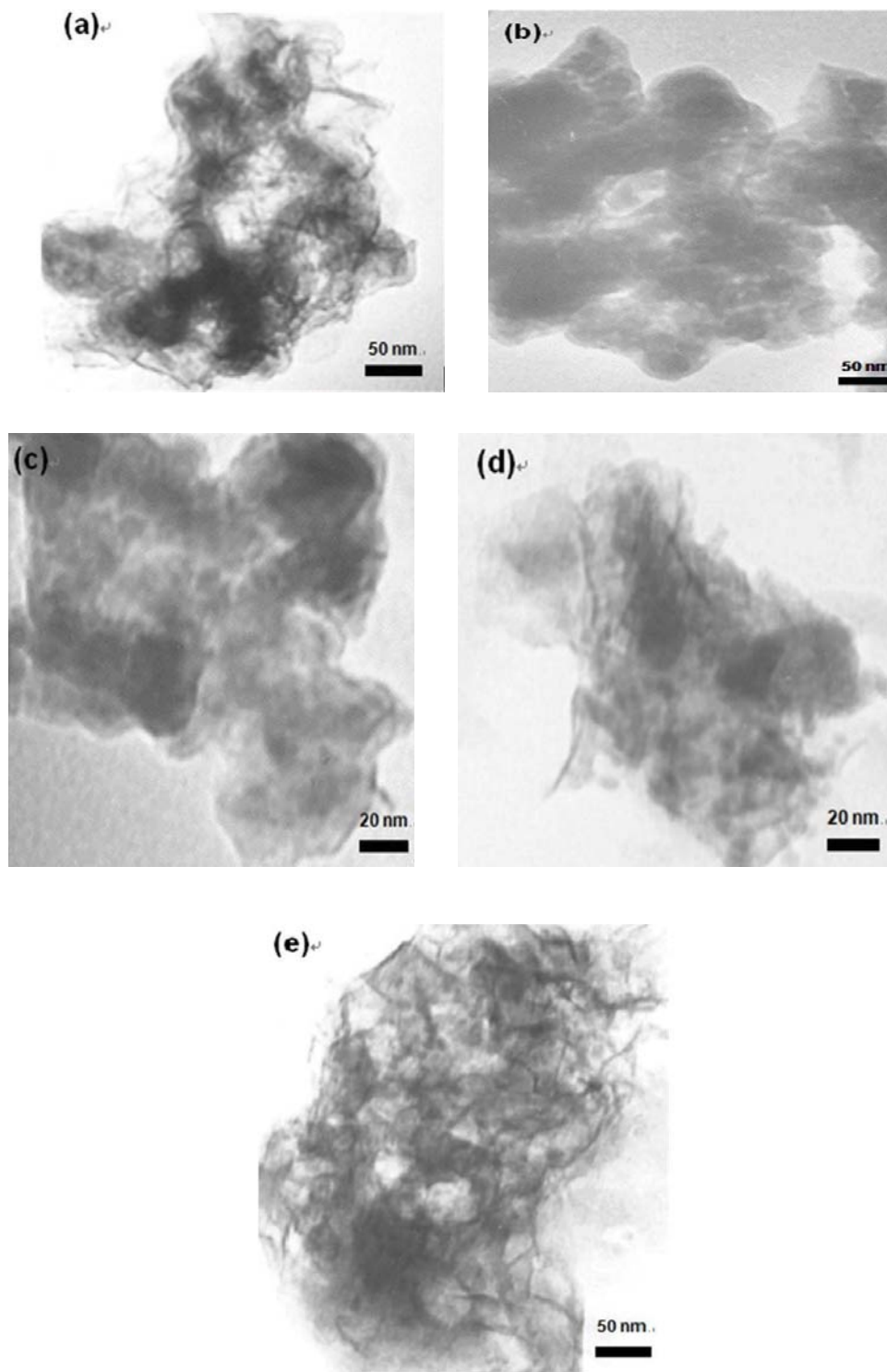


FIGURE 2: TEM images of (a) NiB, (b) 0.001Pd-NiB, (c) 0.005Pd-NiB, (d) 0.01Pd-NiB, and (e) 0.02Pd-NiB.

binding energy peaks were observed for Ni^{4+} compounds [74]. Matienzo et al. [75] also extensively studied a series of nickel compounds in all of the oxidation states by XPS. In NiO, binding energy values of 854.0 and 872.0 eV were found for $\text{Ni}_{2p3/2}$ and $\text{Ni}_{2p1/2}$ peaks, respectively. Furthermore, in

the case of NiO and tetrahedral Ni^{2+} compounds, obvious shake-up (satellite) peaks can be found in the region at about 6 eV higher than a normal $\text{Ni}_{2p3/2}$ or $\text{Ni}_{2p1/2}$ band because such compounds are paramagnetic, whereas Ni^0 compounds and square-planar complexes of Ni^{2+} do not produce satellite

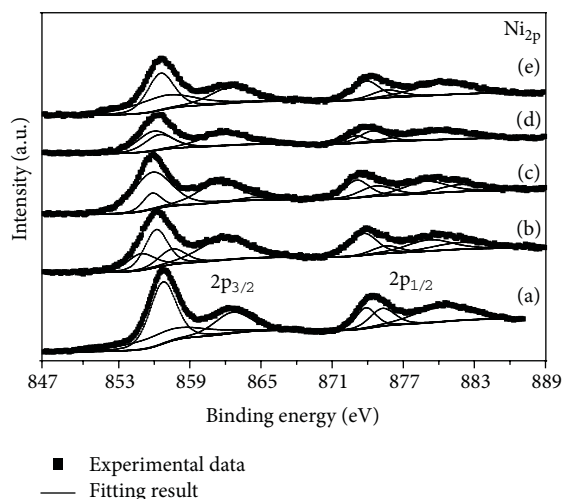


FIGURE 3: XPS spectra of Ni_{2p} for (a) NiB, (b) 0.001Pd-NiB, (c) 0.005Pd-NiB, (d) 0.01Pd-NiB, and (e) 0.02Pd-NiB.

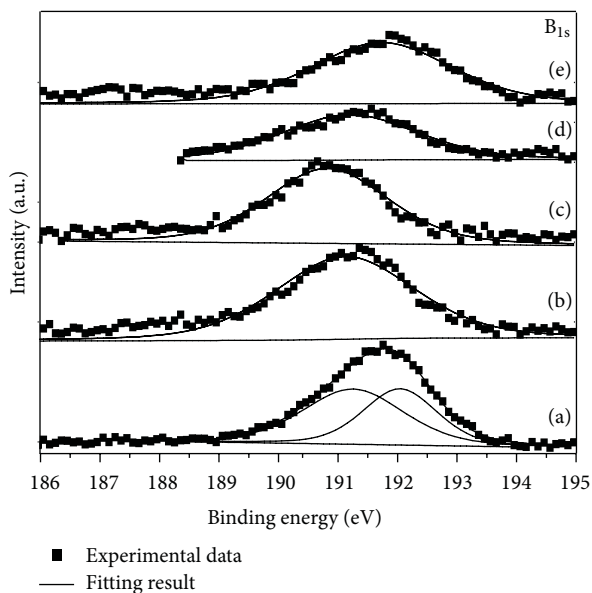


FIGURE 4: XPS spectra of B_{1s} for (a) NiB, (b) 0.001Pd-NiB, (c) 0.005Pd-NiB, (d) 0.01Pd-NiB, and (e) 0.02Pd-NiB.

peaks, because they are diamagnetic. Therefore, the Ni_{2p} bands in Figure 3 show low binding energy values and essentially no satellites features inferring that Ni exists mainly as zero-valence state inside PdNiB rather than in NiO-Pd-B form. The PdNiB catalysts exhibited electron-enriched state and effectively dispersed the Ni nanoparticles, resulting in more metallic Ni atoms on the surface. It is consistent with the results in the literature [76]. No obvious shift was presented in the XPS spectra, and those present in metallic state are not very close to the standard value 853.1 eV [77], which was attributed to the quantum size effect. It is known that hydrogen molecules adsorbed on the Ni^0 sites are activated to proceed hydrogenation reaction. Therefore, the amount of

Ni^0 on the surface of catalyst is crucial for its catalytic activity in hydrogenation reaction.

There are two peaks in the B_{1s} spectra. The peak near 187.1 eV is attributed to elemental B, and the peak near 192.5 eV is attributed to B^{3+} . The peak with the binding energy around 192.5 eV is related to the presence of the oxidized B species, which may be attributed to the interaction between BH_4^- and H_2O during the reduction of Pd^{2+} ions by BH_4^- in alkali solution or the surface boron oxide in the Pd-NiB alloy oxidized by air. It should be noted that most of B species is in oxidation state. The binding energies of B_{1s} are 191.6, 191.2, 190.9, 191.2, and 191.8 eV for the samples of NiB, 0.001PdNiB, 0.005PdNiB, 0.01PdNiB, and 0.02PdNiB, respectively. The decreased BE's resulted from acceptance of electrons of B from other metal atoms. Strong interaction and interdiffusion between Pd and B substrate at room temperature have been reported [18, 78]. Here the change in BE's should be due to the interaction of Ni, Pd, and B. In conclusion, the amorphous structure of NiB and the presence of B promoted the surface-alloying effect of Pd and Ni. Pd peak was not observed due to the low loadings in these samples.

3.4. Hydrogenation Reaction. The catalytic activities of the as-prepared catalysts were investigated on the hydrogenation of *p*-CNB. There are two kinds of reactions in the hydrogenation process: selected hydrogenation of $-\text{NO}_2$ group and dehalogenation of $-\text{Cl}$ group. In order to obtain high *p*-CAN yield, the dechlorination of *p*-CNB and *p*-CAN should be restrained; only the hydrogenation of $-\text{NO}_2$ group of *p*-CNB is desired [79]. The simplified reaction route is displayed in Scheme 1.

Figure 5 shows the conversion of *p*-CNB and the corresponding selectivity of *p*-CAN over these catalysts. The yields of *p*-CAN, NB, and AN are also shown in Figure 5. In each case, the concentration of NB increased at the first 30 min and then decreased and converted to AN and became zero eventually. There are two possible explanations the other one is that *p*-CNB only followed path (1) in reaction scheme in the first 30 min; is that the rate of the hydrogenation on the path (3) is faster than path (1). Since the increasing rate of aniline is not obvious, so the possibility of the latter case is low.

Figure 5 shows the *p*-CNB conversion and the selectivity of *p*-CAN versus reaction time. The reaction rate was zeroth order to *p*-CNB concentration. The activity of PdNiB was greater than NiB even with very small amount of Pd. The reaction results of the catalysts are listed in Table 1. The sample 0.02Pd-NiB had the highest reaction rate, which achieved 100% conversion within 30 min. The results showed that the activities increased with an increase in Pd content in the range of Pd/Ni atomic ratios between 0 and 0.01. Even adding small amount of Pd could enhance the activity and selectivity of *p*-CAN greatly. The hydrogenation of *p*-CNB on PdNiB catalysts was very selective to *p*-CAN. The results demonstrated that PdNiB can have the advantages of both metals, that is, high activity of Pd and high selectivity of Ni.

Both Ni^0 and Pd^0 are the active sites. Since only very small amount of Pd was added, the reaction was mainly on the surface of Ni. The surface concentration and electron

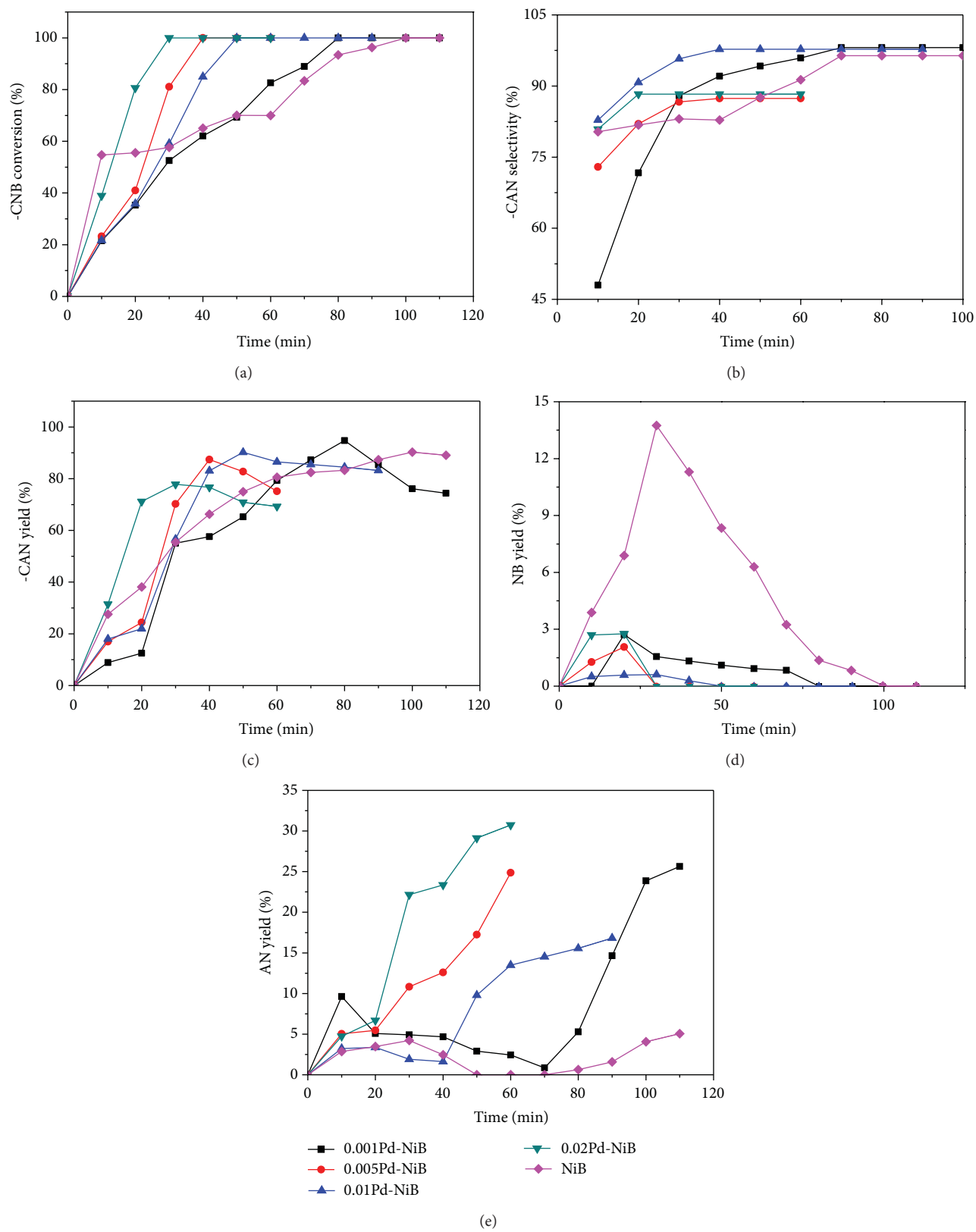
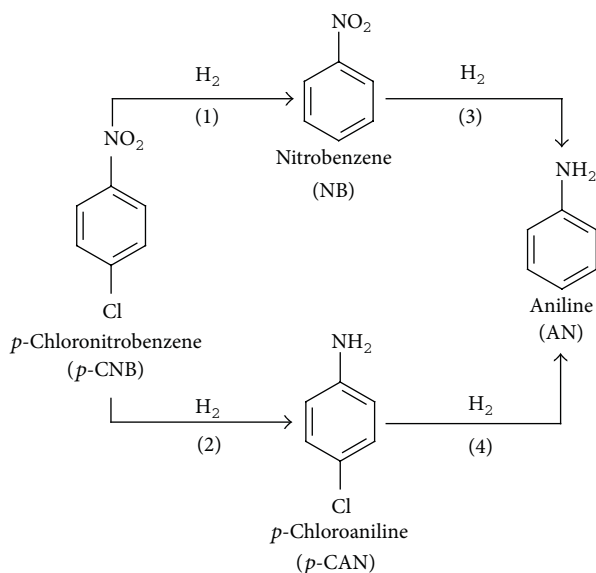


FIGURE 5: The relations of (a) *p*-CNB conversion, (b) *p*-CAN selectivity, (c) *p*-CAN yield, (d) NB yield, and (e) AN yield with reaction time on PdNiB catalysts. * Reaction conditions: 2 mmol NiPdB catalyst; 16 mmol *p*-CNB; 80 mL methanol; 80 °C; 1.2 MPa hydrogen pressure; 500 rpm.

SCHEME 1: Simplified reaction scheme of hydrogenation of *p*-CNB.

density of Ni⁰ are the important factors for the reaction. A higher Ni⁰ content would favor the dissociative adsorption of H₂ molecules. According to the XPS analysis, one could find out that all the prepared samples had high densities of the elemental Ni. Thus, the -NO₂ group in the reactant *p*-CNB can be activated by the positive-charged Pd. The ability of the nearby dissociated H atoms to attack the O and N atoms of -NO₂ groups to form -NH₂ is enhanced, which benefits the high selectivity of *p*-CAN [33, 35, 80]. With the addition of Pd, the binding energy of Ni shifted to a lower value, indicating that Ni received more electrons from Pd. Combining the structure effect, palladium species could make the Ni particles smaller. This would increase the dispersion of Ni active sites and make the surface of the catalyst highly unsaturated, which favors the hydrogenation of *p*-CNB. The nitro group owned two different elements, N and O; both are highly electronegative. With the electrons donation from alloying B and Pd to Ni, the Ni on the catalyst surface became more electron enriched. Higher electronegativity of -NO₂ would be adsorbed on the surface easily, and the active sites would activate the N=O bond, which was polarized. The para-substituted nitro group had the higher electron negativity, resulting from the combination of both inductive and resonance effects. Since the -NO₂ group was more electronegative than -Cl, -NO₂ was supposed to occupy the active site on Ni surface at the start of the reaction. -NO₂ adsorbed on the catalyst surface is hydrogenated to form *p*-CAN, which is further desorbed. In addition, oxygen was more electronegative and alloying Pd and B could engage the oxygen to activate the polar -NO₂ group of *p*-CNB. The -NH₂ of *p*-CAN might adsorb on the surface alloying B and Pd and coordinate with each other. It would improve the selectivity of *p*-CAN by depressing the dehalogenation reaction. Pd-dopant in the NiB catalysts would increase the electron density of Ni and make the activity increase

TABLE 1: The Effect of Pd content on the hydrogenation of *p*-CNB over PdNiB catalysts^a.

Sample	Reaction time (min) to 100% conversion ^a	Selectivity (%)			Reaction rate constant (s ⁻¹)
		<i>p</i> -CAN ^b	AN ^b	NB ^b	
NiB	95.6	96.9	5.5	0	0.0298
0.001Pd-NiB	80.0	94.7	5.3	0	0.0167
0.005Pd-NiB	40.0	75.1	24.9	0	0.0119
0.01Pd-NiB	50.0	90.2	9.8	0	0.0127
0.02Pd-NiB	28.6	77.8	22.2	0	0.0112

^aReaction condition: 1.2 MPa hydrogen pressure, 353 K reaction temperature, absolute methanol was medium, 500 rpm stirring speed, and 0.2 mmol Ni catalyst.

^b*p*-CAN: *p*-chloroaniline; AN: aniline; NB: nitrobenzene.

significantly. In addition, PdNiB is paramagnetic; it is easier to separate after reaction.

The results presented herein show that metal catalyst could be affected by the formation of the bimetallic colloid or by the addition of metal cations. The mechanism of the hydrogenation of *p*-CNB over the bimetallic colloid system is very complicated and is affected by the electronic and conformation properties of the components as well as the composition on the metal surface.

3.5. Reaction Kinetics. One could calculate the reaction rate constant for each catalyst. Based on the conversion-time curves in the hydrogenation of *p*-CNB (Figure 5), it shows that the reaction was of first order with respect to the concentration of *p*-CNB [81]. The reaction rate can be expressed as

$$-r_A = kC_{A0} \cdot (1 - X_A), \quad (2)$$

where k is the reaction rate constant, s⁻¹; C_{A0} is the initial concentration of reactant at $t = 0$; X_A is the conversion of A.

Since the reaction was carried out in a constant-volume batch reactor, so

$$-r_A = C_{A0} \frac{dX_A}{dt}, \quad (3)$$

where C_{A0} is the initial concentration of reactant at $t = 0$; X_A is the conversion of A; t is the reaction time.

Combining the above two equations and using integral method of analysis of data, one could get

$$-\ln(1 - X_A) = kt. \quad (4)$$

A plot of $-\ln(1 - X_A)$ versus t could derive the slope which represents the reaction rate constant. Because of the induction period appeared in the initial stage of reaction, the data in the initial stage were neglected. The results are tabulated in Table 1. As expected, the rate constant of NiPdB catalyst was higher than that of NiB.

4. Conclusion

A series of PdNiB nanoalloy catalysts with various Pd contents was prepared by chemical reduction method with

NaBH₄ as the reducing agent. The catalysts were characterized by XRD, TEM, and XPS. The catalytic properties of these catalysts were tested in the hydrogenation of *p*-CNB. NiB was amorphous as indicated by the broad peak around $2\theta = 45^\circ$. Upon modification with Pd, it could maintain NiB in the amorphous structure and decrease the crystallinity. With the addition of Pd, the particle size of NiB decreased. PdNiB formed nanoalloy and no discrete phase was found. The addition of Pd could reduce the particle size of NiB and improve the Ni dispersion. The binding energy of elemental Ni and B in the PdNiB is negatively shifted, indicating that Ni and B accepted partial electrons from Pd. The magnetization of PdNiB remarkably increased with doping Pd into NiB.

Since the $-\text{NO}_2$ was more electronegative than $-\text{Cl}$, $-\text{NO}_2$ was supposed to occupy the active site on Ni surface in the beginning of the reaction. $-\text{NO}_2$ adsorbed on the surface is hydrogenated to form *p*-CAN which is then desorbed. In addition, oxygen is more electronegative and the alloying B could engage the oxygen to activate the polar $-\text{NO}_2$ group of *p*-CNB. The $-\text{NH}_2$ of *p*-CAN might adsorb on the alloying B and coordinate with each other. Hence, it could improve the selectivity of *p*-CAN by suppressing the dehalogenation reaction.

High activity and selectivity on PdNiB in the hydrogenation of *p*-CNB could be attributed to both ensemble effect and electronic effect. Alloying Pd interrupts the long-range order of NiB, resulting in the characteristics of small cluster of NiB. On the other hand, B and Pd could partially donate electrons to Ni. Electron-enriched Ni could activate the polar $-\text{NO}_2$ groups of *p*-CNB and depress the dehalogenation of *p*-CAN. The results described here showed that PdNiB nanoalloy catalyst is a promising catalyst for industrial application.

Acknowledgment

This research was supported by the Ministry of Economical Affairs, Taiwan, under Contract no. 101-EC-17-A-09-S1-022.

References

- [1] J. Q. Du, Y. Zhang, T. Tian, S. C. Yan, and H. T. Wang, "Microwave irradiation assisted rapid synthesis of Fe-Ru bimetallic nanoparticles and their catalytic properties in water-gas shift reaction," *Materials Research Bulletin*, vol. 44, no. 6, pp. 1347–1351, 2009.
- [2] J. C. S. Wu and H. C. Chou, "Bimetallic Rh-Ni/BN catalyst for methane reforming with CO₂," *Chemical Engineering Journal*, vol. 148, no. 2-3, pp. 539–545, 2009.
- [3] N. He, P. Li, Y. Zhou, W. Ren, S. Fan, and V. A. Verkhozina, "Catalytic dechlorination of polychlorinated biphenyls in soil by palladium-iron bimetallic catalyst," *Journal of Hazardous Materials*, vol. 164, no. 1, pp. 126–132, 2009.
- [4] G. Bernardotto, F. Menegazzo, F. Pinna, M. Signoreto, G. Cruciani, and G. Strukul, "New Pd-Pt and Pd-Au catalysts for an efficient synthesis of H₂O₂ from H₂ and O₂ under very mild conditions," *Applied Catalysis A*, vol. 358, no. 2, pp. 129–135, 2009.
- [5] S. Penner, H. Lorenz, W. Jochum et al., "Pd/Ga₂O₃ methanol steam reforming catalysts, part I: morphology, composition and structural aspects," *Applied Catalysis A*, vol. 358, no. 2, pp. 193–202, 2009.
- [6] N. M. Bertero, A. F. Trasarti, B. Moraweck, A. Borgna, and A. J. Marchi, "Selective liquid-phase hydrogenation of citral over supported bimetallic Pt-Co catalysts," *Applied Catalysis A*, vol. 358, no. 1, pp. 32–41, 2009.
- [7] M. P. Latusek, R. M. Heimerl, B. P. Spigarelli, and J. H. Holles, "Synthesis and characterization of supported bimetallic overlayer catalysts," *Applied Catalysis A*, vol. 358, no. 1, pp. 79–87, 2009.
- [8] N. Gyoryffy, I. Bakos, S. Szabo et al., "Preparation, characterization and catalytic testing of GePt catalysts," *Journal of Catalysis*, vol. 263, no. 2, pp. 372–379, 2009.
- [9] Y. W. Chen, N. Sasirekha, and Y. C. Liu, "Hydrogenation of *p*-chloronitrobenzene over NiPtB nanoalloy catalysts," *Journal of Non-Crystalline Solids*, vol. 355, no. 22-23, pp. 1193–1201, 2009.
- [10] G. C. Bond and D. E. Webster, "Mixed metal catalysts in catalytic hydrogenation," *Annals of the New York Academy of Sciences*, vol. 158, pp. 540–559, 1969.
- [11] L. F. Chen and Y. W. Chen, "Effect of additive (W, Mo, and Ru) on Ni-B amorphous alloy catalyst in hydrogenation of *p*-chloronitrobenzene," *Industrial & Engineering Chemistry Research*, vol. 45, no. 26, pp. 8866–8873, 2006.
- [12] Y. Chen, "Chemical preparation and characterization of metal-metalloid ultrafine amorphous alloy particles," *Catalysis Today*, vol. 44, no. 1-4, pp. 3–16, 1998.
- [13] X. F. Chen, H. X. Li, H. S. Luo, and M. H. Qiao, "Liquid phase hydrogenation of furfural to furfuryl alcohol over Mo-doped Co-B amorphous alloy catalysts," *Applied Catalysis A*, vol. 233, no. 1-2, pp. 13–20, 2002.
- [14] T. Ding, Y. N. Qin, and M. A. Zhi, "Study of the Pd-B/ γ -Al₂O₃ amorphous alloy catalyst," *Chinese Chemical Letters*, vol. 14, no. 3, pp. 319–322, 2003.
- [15] X. Yu, M. Wang, and H. Li, "Study on the nitrobenzene hydrogenation over a Pd-B/SiO₂ amorphous catalyst," *Applied Catalysis A*, vol. 202, no. 1, pp. 17–22, 2000.
- [16] W. X. Tu, S. J. Cao, L. P. Yang, and W. C. Wang, "Modification effects of magnetic supports and bimetallic structures on palladium nanocluster catalysts," *Chemical Engineering Journal*, vol. 143, no. 1-3, pp. 244–248, 2008.
- [17] F. J. Urbano and J. M. Marinas, "Hydrogenolysis of organohalogen compounds over palladium supported catalysts," *Journal of Molecular Catalysis A*, vol. 173, no. 1-2, pp. 329–345, 2001.
- [18] D. H. Shen, P. A. Kearney, J. M. Slaughter, and C. M. Falco, "Chemical interaction at the Pd-B interface," *Journal of Magnetism and Magnetic Materials*, vol. 126, no. 1-3, pp. 25–27, 1993.
- [19] S. U. Son, Y. Jang, J. Park et al., "Designed synthesis of atom-economical Pd/Ni bimetallic nanoparticle-based catalysts for sonogashira coupling reactions," *Journal of the American Chemical Society*, vol. 126, no. 16, pp. 5026–5027, 2004.
- [20] B. Coq, G. Ferrat, and F. Figueras, "Conversion of chlorobenzene over palladium and rhodium catalysts of widely varying dispersion," *Journal of Catalysis*, vol. 101, no. 2, pp. 434–445, 1986.
- [21] B. Coq, A. Tijani, and F. Figueras, "Hydrogenation of *para*-chloronitrobenzene over supported ruthenium-based catalysts," *Applied Catalysis*, vol. 76, no. 2, pp. 255–266, 1991.
- [22] N. Lingaiah, N. S. Babu, R. Gopinath, P. S. S. Reddy, and P. S. S. Prasad, "Hydrodechlorination of chlorobenzene over supported metal catalysts," *Catalysis Surveys from Asia*, vol. 10, no. 1, pp. 29–39, 2006.

- [23] L. M. Sikhwihilu, N. J. Coville, B. M. Pulimaddi, J. Venkatreddy, and V. Vishwanathan, "Selective hydrogenation of *o*-chloronitrobenzene over palladium supported nanotubular titanium dioxide derived catalysts," *Catalysis Communications*, vol. 8, no. 12, pp. 1999–2006, 2007.
- [24] M. Liu, W. Yu, H. Liu, and J. Zheng, "Preparation and characterization of polymer-stabilized ruthenium–platinum and ruthenium–palladium bimetallic colloids and their catalytic properties for hydrogenation of *o*-chloronitrobenzene," *Journal of Colloid and Interface Science*, vol. 214, no. 2, pp. 231–237, 1999.
- [25] M. H. Liu, W. Y. Yu, and H. F. Liu, "Selective hydrogenation of *o*-chloronitrobenzene over polymer-stabilized ruthenium colloidal catalysts," *Journal of Molecular Catalysis A*, vol. 138, no. 2-3, pp. 295–303, 1999.
- [26] Y. W. Chen and D. S. Lee, "Hydrogenation of *p*-chloronitrobenzene on nanosized modified NiMoB catalysts," *Catalysis Survey in Asia*, vol. 16, pp. 198–209, 2012.
- [27] Y. Monguchi, A. Kume, K. Hattori, T. Maegawa, and H. Sajiki, "Pd/C–Et₃N-mediated catalytic hydrodechlorination of aromatic chlorides under mild conditions," *Tetrahedron*, vol. 62, no. 33, pp. 7926–7933, 2006.
- [28] V. Vishwanathan, V. Jayasri, P. M. Basha, N. Mahata, L. Sikhwihilu, and N. J. Coville, "Gas phase hydrogenation of *ortho*-chloronitrobenzene (O-CNB) to *ortho*-chloroaniline (O-CAN) over unpromoted and alkali metal promoted-alumina supported palladium catalysts," *Catalysis Communications*, vol. 9, no. 3, pp. 453–458, 2008.
- [29] C. Y. Xi, H. Y. Cheng, J. M. Hao, S. X. Cai, and F. Y. Zhao, "Hydrogenation of *o*-chloronitrobenzene to *o*-chloroaniline over Pd/C in supercritical carbon dioxide," *Journal of Molecular Catalysis A*, vol. 282, no. 1-2, pp. 80–84, 2008.
- [30] X. L. Yang, H. F. Liu, and H. Zhong, "Hydrogenation of *o*-chloronitrobenzene over polymer-stabilized palladium–platinum bimetallic colloidal clusters," *Journal of Molecular Catalysis A*, vol. 147, no. 1-2, pp. 55–62, 1999.
- [31] Z. K. Yu, S. J. Liao, Y. Xu, B. Yang, and R. Yu, "A remarkable synergic effect of polymer-anchored bimetallic palladium–ruthenium catalysts in the selective hydrogenation of *p*-chloronitrobenzene," *Journal of the Chemical Society, Chemical Communications*, no. 11, pp. 1155–1156, 1995.
- [32] Z. K. Yu, S. J. Liao, Y. Xu, B. Yang, and D. R. Yu, "Hydrogenation of nitroaromatics by polymer-anchored bimetallic palladium–ruthenium and palladium–platinum catalysts under mild conditions," *Journal of Molecular Catalysis A*, vol. 120, no. 1–3, pp. 247–255, 1997.
- [33] X. X. Han, R. X. Zhou, G. H. Lai, B. H. Yue, and X. M. Zheng, "Effect of transition metal (Cr, Mn, Fe, Co, Ni and Cu) on the hydrogenation properties of chloronitrobenzene over Pt/TiO₂ catalysts," *Journal of Molecular Catalysis A*, vol. 209, no. 1-2, pp. 83–87, 2004.
- [34] J. R. Kosak, "Catalytic hydrogenation of aromatic halonitro compounds," *Annals of the New York Academy of Sciences*, vol. 172, pp. 175–185, 1970.
- [35] H. Li, Q. F. Zhao, and H. X. Li, "Selective hydrogenation of *p*-chloronitrobenzene over Ni–P–B amorphous catalyst and synergistic promoting effects of B and P," *Journal of Molecular Catalysis A*, vol. 285, no. 1-2, pp. 29–35, 2008.
- [36] N. Mahata, A. F. Cunha, J. J. M. Órfão, and J. L. Figueiredo, "Hydrogenation of chloronitrobenzenes over filamentous carbon stabilized nickel nanoparticles," *Catalysis Communications*, vol. 10, no. 8, pp. 1203–1206, 2009.
- [37] M. H. Lin, B. Zhao, and Y. W. Chen, "Hydrogenation of *p*-chloronitrobenzene over Mo-modified NiCoB nanoalloy catalysts: effect of Mo content," *Industrial & Engineering Chemistry Research*, vol. 48, no. 15, pp. 7037–7043, 2009.
- [38] B. Zhao, C. J. Chou, and Y. W. Chen, "Hydrogenation of *p*-chloronitrobenzene on tungsten-modified NiCoB catalyst," *Industrial & Engineering Chemistry Research*, vol. 49, no. 4, pp. 1669–1676, 2010.
- [39] B. Zhao and Y. W. Chen, "Hydrogenation of *p*-chloronitrobenzene on Mo, La, Fe, and W-modified NiCoB nanoalloy catalysts," *Journal of Non-Crystalline Solids*, vol. 356, no. 18-19, pp. 839–847, 2010.
- [40] M. A. Keane, "A review of catalytic approaches to waste minimization: case study-liquid-phase catalytic treatment of chlorophenols," *Journal of Chemical Technology and Biotechnology*, vol. 80, no. 11, pp. 1211–1222, 2005.
- [41] Y. C. Liu, C. Y. Huang, and Y. W. Chen, "Hydrogenation of *p*-chloronitrobenzene on Ni–B nanometal catalysts," *Journal of Nanoparticle Research*, vol. 8, no. 2, pp. 223–234, 2006.
- [42] Y. C. Liu, C. Y. Huang, and Y. W. Chen, "Liquid-phase selective hydrogenation of *p*-chloronitrobenzene on Ni–P–B nanocatalysts," *Industrial & Engineering Chemistry Research*, vol. 45, no. 1, pp. 62–69, 2006.
- [43] Y. C. Liu and Y. W. Chen, "Hydrogenation of *p*-chloronitrobenzene on lanthanum-promoted NiB nanometal catalysts," *Industrial & Engineering Chemistry Research*, vol. 45, no. 9, pp. 2973–2980, 2006.
- [44] J. F. Deng, J. Yang, S. Sheng, and H. Chen, "The study of ultrafine Ni–B and Ni–P amorphous alloy powders as catalysts," *Journal of Catalysis*, vol. 150, no. 2, pp. 434–438, 1994.
- [45] J. F. Deng, H. Li, and W. J. Wang, "Progress in design of new amorphous alloy catalysts," *Catalysis Today*, vol. 51, no. 1, pp. 113–125, 1999.
- [46] S. P. Lee and Y. W. Chen, "Nitrobenzene hydrogenation on Ni–P, Ni–B and Ni–P–B ultrafine materials," *Journal of Molecular Catalysis A*, vol. 152, no. 1-2, pp. 213–223, 2000.
- [47] C. P. Li, Y. W. Chen, and W. J. Wang, "Nitrobenzene hydrogenation over aluminum borate-supported platinum catalyst," *Applied Catalysis A*, vol. 119, no. 2, pp. 185–194, 1994.
- [48] H. Li, H. X. Li, W. L. Dai, W. J. Wang, and Z. G. Fang, "XPS studies on surface electronic characteristics of Ni–B and Ni–P amorphous alloy and its correlation to their catalytic properties," *Applied Surface Science*, vol. 152, no. 1-2, pp. 25–34, 1999.
- [49] H. Li, H. X. Li, W. J. Wang, J. F. Deng, and J. F., "Excellent activity of ultrafine Co–B amorphous alloy catalyst in glucose hydrogenation," *Chemistry Letters*, no. 7, pp. 629–630, 1999.
- [50] H. X. Li, H. S. Luo, L. Zhuang, W. L. Dai, and M. H. Qiao, "Liquid phase hydrogenation of furfural to furfuryl alcohol over the Fe-promoted Ni–B amorphous alloy catalysts," *Journal of Molecular Catalysis A*, vol. 203, no. 1-2, pp. 267–275, 2003.
- [51] H. X. Li, H. Li, W. L. Dai, and M. H. Qiao, "Preparation of the Ni–B amorphous alloys with variable boron content and its correlation to the hydrogenation activity," *Applied Catalysis A*, vol. 238, no. 1, pp. 119–130, 2003.
- [52] H. X. Li, Y. D. Wu, J. Zhang, W. L. Dai, and M. H. Qiao, "Liquid phase acetonitrile hydrogenation to ethylamine over a highly active and selective Ni–Co–B amorphous alloy catalyst," *Applied Catalysis A*, vol. 275, no. 1-2, pp. 199–206, 2004.
- [53] H. Li, J. Zhang, and H. X. Li, "Ultrasound-assisted preparation of a novel Ni–B amorphous catalyst in uniform nanoparticles

- for *p*-chloronitrobenzene hydrogenation," *Catalysis Communications*, vol. 8, no. 12, pp. 2211–2216, 2007.
- [54] L. H. Lu, Y. H. Ma, F. Guo et al., "Structural characteristics of Mo modified skeletal Ni and its catalysis for liquid phase hydrogenation of nitro T-acid to T-acid," *Fine Chemicals*, vol. 25, no. 3, pp. 251–255, 2008.
- [55] Y. F. Ma, W. Li, M. G. Zhang, Y. Zhou, and K. Y. Tao, "Preparation and catalytic properties of amorphous alloys in hydrogenation of sulfolene," *Applied Catalysis A*, vol. 246, no. 2, pp. 215–223, 2003.
- [56] F. Cardenas-Lizana, S. Gomez-Quero, and M. A. Keane, "Clean production of chloroanilines by selective gas phase hydrogenation over supported Ni catalysts," *Applied Catalysis A*, vol. 334, no. 1-2, pp. 199–206, 2008.
- [57] X. X. Han, R. X. Zhou, X. M. Zheng, and H. Jiang, "Effect of rare earths on the hydrogenation properties of *p*-chloronitrobenzene over polymer-anchored platinum catalysts," *Journal of Molecular Catalysis A*, vol. 193, no. 1-2, pp. 103–108, 2003.
- [58] X. X. Han, R. X. Zhou, G. H. Lai, and X. M. Zheng, "Influence of support and transition metal (Cr, Mn, Fe, Co, Ni and Cu) on the hydrogenation of *p*-chloronitrobenzene over supported platinum catalysts," *Catalysis Today*, vol. 93–95, pp. 433–437, 2004.
- [59] R. Hara, K. Sato, W. H. Sun, and T. Takahashi, "Catalytic dechlorination of aromatic chlorides using Grignard reagents in the presence of $(C_5H_5)_2TiCl_2$," *Chemical Communications*, vol. 12, no. 9, pp. 845–846, 1999.
- [60] M. L. Hitchman, R. A. Spackman, N. C. Ross, and C. Agra, "Disposal methods for chlorinated aromatic waste," *Chemical Society Reviews*, vol. 24, no. 6, pp. 423–430, 1995.
- [61] Y. J. Hou, Y. Q. Wang, F. He et al., "Liquid phase hydrogenation of 2-ethylanthraquinone over La-doped Ni–B amorphous alloy catalysts," *Materials Letters*, vol. 58, no. 7-8, pp. 1267–1271, 2004.
- [62] G. Junfeng, A. J. David, and G. G. J. Brian, "Exploring the structural complexities of metal-metalloid nanoparticles: the case of Ni · B as catalyst," *Chemistry*, vol. 15, no. 5, pp. 1134–1143, 2009.
- [63] V. Kratky, M. Kralik, M. Mecarova, M. Stolcova, L. Zalibera, and M. Hronec, "Effect of catalyst and substituents on the hydrogenation of chloronitrobenzenes," *Applied Catalysis A*, vol. 235, no. 1-2, pp. 225–231, 2002.
- [64] I. H. Liu, C. Y. Chang, S. C. Liu, I. C. Chang, and S. M. Shih, "Absorption removal of sulfur dioxide by falling water droplets in the presence of inert solid particles," *Atmospheric Environment*, vol. 28, no. 21, pp. 3409–3415, 1994.
- [65] Z. B. Yu, M. H. Qiao, H. X. Li, and J. F. Deng, "Preparation of amorphous Ni–Co–B alloys and the effect of cobalt on their hydrogenation activity," *Applied Catalysis A*, vol. 163, no. 1-2, pp. 1–13, 1997.
- [66] H. Yamashita, H. Yoshikawa, T. Funabiki, and S. Yoshida, "Catalysis by amorphous metal alloys, part 4: structural modification towards metastable states and catalytic activity of amorphous $Ni_{62}B_{38}$ ribbon alloy," *Journal of the Chemical Society, Faraday Transactions I*, vol. 82, no. 6, pp. 1771–1780, 1986.
- [67] X. Yan, M. Liu, H. Liu, and K. Y. Liew, "Role of boron species in the hydrogenation of *o*-chloronitrobenzene over polymer-stabilized ruthenium colloidal catalysts," *Journal of Molecular Catalysis A*, vol. 169, no. 1-2, pp. 225–233, 2001.
- [68] X. H. Yan, J. Q. Sun, Y. W. Wang, and J. F. Yang, "A Fe-promoted Ni–P amorphous alloy catalyst (Ni–Fe–P) for liquid phase hydrogenation of *m*- and *p*-chloronitrobenzene," *Journal of Molecular Catalysis A*, vol. 252, no. 1-2, pp. 17–22, 2006.
- [69] X. H. Yan, J. Q. Sun, Y. H. Xu, and J. F. Yang, "Liquid-phase hydrogenation of chloronitrobenzene to chloroaniline over Ni–Co–B amorphous alloy catalyst," *Chinese Journal of Catalysis*, vol. 27, no. 2, pp. 119–123, 2006.
- [70] J. Chen, N. Yao, R. Wang, and J. Zhang, "Hydrogenation of chloronitrobenzene to chloroaniline over Ni/TiO₂ catalysts prepared by sol-gel method," *Chemical Engineering Journal*, vol. 148, pp. 164–172, 2009.
- [71] B. Coq, A. Tijani, and F. Figueras, "Influence of alloying platinum for the hydrogenation of *p*-chloronitrobenzene over PtM/Al₂O₃ catalysts with M = Sn, Pb, Ge, Al, Zn," *Journal of Molecular Catalysis*, vol. 71, no. 3, pp. 317–333, 1992.
- [72] B. Coq, A. Tijani, R. Dutartre, and F. Figueras, "Influence of support and metallic precursor on the hydrogenation of *p*-chloronitrobenzene over supported platinum catalysts," *Journal of Molecular Catalysis*, vol. 79, no. 1-3, pp. 253–264, 1993.
- [73] M. G. Wang, H. X. Li, Y. D. Wu, and J. Zhang, "Comparative studies on the catalytic behaviors between the Ni–B amorphous alloy and other Ni-based catalysts during liquid phase hydrogenation of acetonitrile to ethylamine," *Materials Letters*, vol. 57, no. 19, pp. 2954–2964, 2003.
- [74] C. A. Tolman, W. H. Riggs, W. J. Lin, C. M. King, and R. C. Wendt, "Electron spectroscopy for chemical analysis of nickel compounds," *Inorganic Chemistry*, vol. 12, no. 12, pp. 2770–2778, 1973.
- [75] L. J. Matienzo, L. I. Yin, S. O. Grim, and W. E. Swartz Jr., "X-ray photoelectron spectroscopy of nickel compounds," *Inorganic Chemistry*, vol. 12, no. 12, pp. 2762–2769, 1973.
- [76] W. L. Dai, M. H. Qiao, and J. F. Deng, "XPS studies on a novel amorphous Ni–Co–W–B alloy powder," *Applied Surface Science*, vol. 120, no. 1-2, pp. 119–124, 1997.
- [77] J. F. Moulder, W. F. Stickle, P. E. Sobol, and K. D. Bomben, *Handbook of X-Ray Photoelectron Spectroscopy*, Physical Electronics, Chanhassen, Minn, USA, 1995.
- [78] J. Tamaki, S. Nakayama, M. Yamamura, and T. Imanaka, "Preparation and catalytic properties of palladium-(boron, phosphorus) thin films using an RF sputtering method," *Journal of Materials Science*, vol. 24, no. 5, pp. 1582–1588, 1989.
- [79] J. H. Shen and Y. W. Chen, "Catalytic properties of bimetallic NiCoB nanoalloy catalysts for hydrogenation of *p*-chloronitrobenzene," *Journal of Molecular Catalysis A*, vol. 273, no. 1-2, pp. 265–276, 2007.
- [80] H. Noller and W. M. Lin, "Activity and selectivity of Ni = Cu/Al₂O₃ catalysts for hydrogenation of crotonaldehyde and mechanism of hydrogenation," *Journal of Catalysis*, vol. 85, no. 1, pp. 25–30, 1984.
- [81] O. Levenspiel, *Chemical Reaction Engineering*, John Wiley & Sons, New York, NY, USA, 1999.

Research Article

Tuning the Pore Size in Ionic Nanoparticle Networks

Marie-Alexandra Neouze Gauthey,¹ Marco Litschauer,¹ Michael Puchberger,¹
Martin Kronstein,¹ and Herwig Peterlik²

¹ Vienna University of Technology, Institute of Materials Chemistry, 1060 Vienna, Austria

² University of Vienna, Faculty of Physics, 1090 Vienna, Austria

Correspondence should be addressed to Marie-Alexandra Neouze Gauthey; maiaatneouze@hotmail.com

Received 11 January 2013; Accepted 1 February 2013

Academic Editor: Amir Kajbafvala

Copyright © 2013 Marie-Alexandra Neouze Gauthey et al. This is an open access article distributed under the Creative Commons Attribution License, which permits unrestricted use, distribution, and reproduction in any medium, provided the original work is properly cited.

Highly promising hybrid materials consisting of silica, titania, or zirconia nanoparticles linked with ionic liquid-like imidazolium units have been developed. The nanoparticle networks are prepared by click-chemistry-like process through a nucleophilic substitution reaction. The type of metal oxide nanoparticles appears to play a key role regarding the pore size of the hybrid material.

1. Introduction

Recently the materials community is focusing on the development of specific materials based on assemblies of nanoparticles. These new materials aim at making use of nanoparticle collective properties. In this context, various synthetic pathways were proposed, such as template-assisted synthesis [1, 2], layer-by-layer deposition [3], or using covalent organic mediator [4–8]. These nanoparticle assemblies are already highly promising for numerous applications, like plasmonics, catalysis, or gas sorption/gas sequestration applications.

For catalysis and gas sorption/sequestration applications, the porosity of these materials is an important aspect [9, 10]. Wacker et al. developed a purely inorganic porous nanoparticle assembly, by the bridging of magnetite nanoparticle with silica colloids, for catalytic applications [11], while Gao and coworkers prepared porous magnetite nanochain assemblies for water treatment [12].

However, for such applications like catalysis and gas separation, the use of hybrid inorganic-organic porous materials can be even more interesting, as the organic counterpart is able to interact with gas molecules or precursors. Thus, it was shown that the presence of ionic linker can enhance the adsorbent-adsorbate interactions through charge-induced forces [13]. In particular, ionic liquid-like linkers were pointed out to be extremely interesting [14–18]. More specifically, the high affinity of carbon dioxide for imidazolium moieties was evidenced [8, 19, 20]. For example, Lee et al. have reported

the effective absorption of carbon dioxide over methane by copper imidazolium microporous frameworks [21]. This separation is enabled by the effects of both the metal site and the ionic imidazolium species.

In this context, we have already reported the synthesis of titania Ionic Nanoparticle Networks (INNs), where the titania nanoparticles are covalently linked by means of imidazolium bridges [22]. The titania INNs have shown to possess pores with a diameter centred on 2 nm.

The present communication describes a new INN material based on zirconia nanoparticles and compares the porous characteristics of different INNs, with various metal oxide nanoparticles. In these materials, the linking imidazolium moieties are maintained in the network and thus remained accessible to adsorbed molecules.

2. Experimental Section

2.1. Chemicals. Chemicals unless otherwise stated were used without further purification. Titanium isopropoxide ($\text{Ti}(\text{O}^i\text{Pr})_4$), 1,3-dibromopropane, bromotrimethylsilane, potassium tert-butoxide, dimethylphosphite, 1-bromo-3-chloropropane, sodiumhydride, triethylphosphite, dimethylformamide (DMF), tetrahydrofuran (THF), Na_2SO_4 , P_2O_5 , and zirconium oxychloride octahydrate ($\text{ZrOCl}_2 \cdot 8\text{H}_2\text{O}$) were obtained from Sigma-Aldrich, ammonia (32%) and hydrochloric acid (37%) from VWR, imidazole, sodium iodide, and tetraethylorthosilicate from Fluka, nitric acid

(53%), dichloromethane, and ethanol from Merck, acetone, chloroform, diethylether, ethanol, methanol, and toluene from Donau Chemie, and 3-chloropropyltrimethoxysilane (**Si-Cl**) from ABCR.

2.2. Measurements. Transmission Electron Microscopy (TEM) measurements: samples for transmission electron microscopy measurements were prepared by dispersing the particles in ethanol prior to deposition on a carbon-coated TEM Cu grid. TEM measurements were performed on a JEOL JEM-100CX (USTEM, Vienna University of Technology).

X-ray powder diffraction (XRD) measurements were performed on a Philips X'Pert diffractometer using the Cu-K α radiation ($\lambda = 1.542 \text{ \AA}$).

Small-angle X-ray scattering (SAXS) was performed using a rotating anode generator equipped with a pinhole camera (Nanostar from Bruker AXS, Karlsruhe, with Cu K α radiation from crossed Göbel mirrors). The X-ray patterns were recorded with an area detector (VANTEC 2000) and radially averaged to obtain the scattering intensity in dependence on the scattering vector $q = (4\pi/\lambda) \sin \theta$, with 2θ being the scattering angle and $\lambda = 0.1542 \text{ nm}$ the X-ray wavelength.

Diffraction light scattering (DLS): for the measurement, the solid was dissolved in ethanol. The DLS experiments were carried out without previous sonication of the samples. The run time of the measurements was 10 seconds. Every size distribution curve was obtained by averaging 10 measurements. The apparatus is an ALV/CGS-3 compact goniometer system, equipped with an ALV/LSE-5003 light scattering electronics and multiple τ digital correlator and a 632,8 nm JDSU laser 1145P.

N₂ sorption isotherms were obtained from N₂-adsorption/desorption experiments at 77 K using a Micrometrics ASAP 2020 analyzer. Specific surface areas were calculated from the BET equation, with the average pore diameter being evaluated by the BJH equation on the desorption branch of the isotherm. Before analysis, the samples were evacuated overnight at room temperature.

Fourier transform infrared (FT-IR) spectra: the products were pelletized in KBr before measurement. The spectrometer is a Bruker Tensor-27-DTGS equipped with an Interferometer RockSolid and a DigiTect detector system, high-sensitivity DLATGS, using the OPUSTM software.

Nuclear Magnetic Resonance (NMR): solid-state NMR spectra were recorded on a Bruker AVANCE 300 (¹H at 299.85 MHz and ¹⁵N at 30.38 MHz) equipped with a 4 mm broadband MAS probe head. ¹⁵N spectra were recorded with ramped CP MAS experiments (Cross Polarization and Magic Angle Spinning). The sample holders were spun at 6 kHz for the ¹⁵N. Liquid-state NMR spectra were recorded on a Bruker AVANCE 250 (¹H at 250.13 MHz, ¹³C at 62.90 MHz, ³¹P at 101.25 MHz) equipped with a 5 mm QNP probe head.

2.3. Syntheses

2.3.1. Modification of the Silica Nanoparticles with Si-Im or Si-Cl and Formation of SiO₂-INN. The synthesis of *N*-(trimethoxysilylpropyl)imidazole (**Si-Im**) as well as the synthesis of

the silica nanoparticles were already reported [6]. **Si-Im** is colourless liquid.

¹H NMR (250.13 MHz, CDCl₃): 0.54 (t, 2H, Si-CH₂), 1.83 (q, 2H, N-CH₂-CH₂), 3.53 (s, 9H, Si-O-CH₃), 3.88 (t, 2H, N-CH₂), 6.88 (s, 1H, N-CH-CH-N), 7.01 (s, 1H, N-CH-CH-N), 7.54 (s, 1H, N-CH-N) ppm.

¹³C NMR (62.90 MHz, CDCl₃): 7.4 (Si-CH₂), 25.1 (N-CH₂-CH₂), 55.7 (N-CH₂), 56.2 (Si-O-CH₃), 120.7 (N-CH-CH-N), 128.1 (N-CH-CH-N), 136.8 (N-CH-N) ppm.

16 mL of a previously prepared silica nanoparticles suspension was transferred into a Schlenk tube and degassed in vacuum several minutes to remove excessive ammonia. Either 1.42 g (7.147 mmol) of 3-chloropropyltrimethoxysilane (**Si-Cl**) or 1.65 g (7.147 mmol) of *N*-(trimethoxysilylpropyl)imidazole (**Si-Im**) was added dropwise. The solutions were stirred in argon atmosphere at room temperature overnight.

The networking reaction (**SiO₂-INN**) was carried out in argon atmosphere. 5 mL suspension of silica nanoparticles modified with *N*-(trimethoxysilylpropyl)imidazole (**SiO₂-Im**) and 5 mL suspension of silica nanoparticles modified with 3-chloropropyltrimethoxysilane (**SiO₂-Cl**) were introduced in a 50 mL round bottom flask. Additionally 10 mL of dry methanol was added. The solution was refluxed over 2 days and finally the solvent was removed in vacuum (3 mbar). A translucent gel was obtained, washed with acetone, ethanol, and water, 20 mL, respectively. The final product was dried in a desiccator over P₂O₅ in vacuum.

2.3.2. Synthesis of P-Im or P-Cl: Synthesis of 3-Chloropropylphosphonic Acid (P-Cl)³

Synthesis of Dimethyl-3-chloropropylphosphonate. 18 g (160.41 mmol) potassium tert-butoxide was suspended in 150 mL THF. Afterwards, 22.01 g (200 mmol) dimethylphosphite was slowly added under vigorous stirring. After 2 hours of stirring, the whole suspension was slowly added to a stirred suspension of 47.23 g (300 mmol) 1-bromo-3-chloropropane in 120 mL THF in a 500 mL round bottom flask. A white suspension was formed immediately. The mixture was heated to reflux for 20 minutes. After cooling to room temperature, the formed precipitate, potassium bromide, was filtered off and washed twice with 100 mL diethylether. Then the solvents and by-products were removed under vacuum (20 mbar at 170°C). A slightly coloured liquid was obtained. Yield: 17.9 g (60%, 96.25 mmol).

¹H NMR (250 MHz, CDCl₃): 1.82–1.92 (m, 2H, P-CH₂-CH₂), 1.93–2.10 (m, 2H, P-CH₂), 3.58 (t, 2H, Cl-CH₂), 3.72 (d, 6H, P-O-CH₃) ppm.

³¹P NMR (250 MHz, CDCl₃): 45.99 ppm.

Synthesis of 3-Chloropropylphosphonic Acid. 6.169 g (33.07 mmol) dimethyl-3-chloropropylphosphonate was mixed with 40 mL hydrochloric acid (37%) and heated to reflux for 24 hours. Afterwards, the solvent was removed under reduced pressure, and the residues of water were removed through azeotropic distillation by adding 20 mL of toluene. The yellowish liquid residue was crystallized from 50 mL chloroform and filtered. The colourless crystalline product

was dried in a desiccator over P_2O_5 under vacuum. Yield: 3.73 g (70%, 23.53 mmol).

P-Cl is colourless crystalline product.

1H NMR (250 MHz, DMSO-*d*6): 1.63–1.69 (m, 2H, P-CH₂-CH₂), 1.83–1.90 (m, 2H, P-CH₂), 3.67 (t, 2H, Cl-CH₂), 7.29 (s, 2H, P-OH) ppm.

^{31}P NMR (101.25 MHz, DMSO-*d*6): 37.85 ppm.

^{13}C -NMR (62.90 MHz, DMSO-*d*6): 24.2 (P-CH₂-CH₂), 26.4 (P-CH₂), 46.1 (Cl-CH₂) ppm.

*Synthesis of N-Imidazolylpropylphosphonic Acid (P-Im)*³: *Synthesis of Diethyl-3-Bromopropylphosphonate*. 30 g (180.55 mmol) triethylphosphite and 150 g (722.20 mmol) 1,3-dibromopropane were heated under vigorous stirring to 160°C for 30 minutes. Unreacted 1,3-dibromopropane was removed under reduced pressure and diethyl-3-bromopropylphosphonate distilled under vacuum (2 mbar at 165°C). A colorless liquid was obtained. Yield: 23.45 g (50%, 90.5 mmol).

1H NMR (250 MHz, CDCl₃): 1.20 (t, 6H, P-O-CH₂-CH₃), 1.80 (m, 2H, P-CH₂-CH₂), 1.99 (m, 2H, Br-CH₂), 3.35 (t, 2H, P-CH₂), 3.97 (m, 4H, P-O-CH₂) ppm.

^{31}P NMR (250 MHz, CDCl₃): 30.48 ppm.

^{13}C NMR (250 MHz, CDCl₃): 16.3 (P-O-CH₂-CH₃), 23.1 (P-CH₂-CH₂), 25.8 (P-CH₂), 33.5 (Br-CH₂), 61.5 (P-O-CH₂-CH₃) ppm.

Synthesis of Sodium Imidazolidine. Under argon, 1.2 g (50 mmol) sodiumhydride was suspended in 150 mL dry THF. This suspension was cooled to 4°C with an ice bath, and 3.404 g (50 mmol) imidazole was added over a period of 30 minutes. The suspension was further stirred for 2 hours until no evolution of hydrogen is visible. Afterwards, the white product was filtered off and dried in a desiccator over P_2O_5 under vacuum. Yield: 4.41 g (98%, 49 mmol).

Synthesis of Dimethyl-N-Imidazolpropylphosphonate. Under argon in a 25 mL round bottom flask, 0.9 g (10 mmol) of sodium imidazolidine was dissolved in 5 mL dry DMF. The solution was cooled to 4°C with an ice bath, and 2.59 g (10 mmol) diethyl-3-bromopropylphosphonate was added at once. Afterwards, the ice bath is removed and the suspension is heated to 55°C for 8 hours under vigorous stirring. The solvent was removed under reduced pressure at 40°C. The liquid residue was extracted with chloroform and water, 3 times, with 10 mL, respectively. The collected organic phases were dried over MgSO₄ and the solvent evaporated under vacuum. A colorless liquid was obtained. Yield: 0.78 g (26%, 3.16 mmol).

1H NMR (250 MHz, CDCl₃): 1.26 (t, 6H, P-O-CH₂-CH₃), 1.61 (m, 2H, P-CH₂-CH₂), 1.99 (m, 2H, P-CH₂-CH₂-CH₂), 3.98 (m, 4H, P-CH₂, P-O-CH₂), 6.91 (d, 2H, N-CH-CH-N), 7.43 (s, 1H, N-CH-N) ppm.

^{31}P NMR (250 MHz, CDCl₃): 30.21 ppm.

^{13}C NMR (250 MHz, CDCl₃): 16.3 (P-O-CH₂-CH₃), 21.1 (P-CH₂-CH₂), 24.4 (P-CH₂), 46.7 (N-CH₂), 61.7 (P-O-CH₂-CH₃), 118.7 (N-CH-CH-N), 129.5 (N-CH-CH-N), 137.1 (N-CH-N) ppm.

Synthesis of N-Imidazolylpropylphosphonic Acid. Under argon in a 10 mL round bottom flask, 0.43 g (1.75 mmol) of dimethyl-N-imidazolpropylphosphonate was dissolved in 5 mL dry dichloromethane and stirred for 5 minutes. Afterwards, 0.80 g (5.24 mmol) bromotrimethylsilane was added and stirred for 24 hours. Then the solvent was removed under reduced pressure and the brownish viscous liquid was dissolved in 5 mL dry methanol. Afterwards, the excessive methanol was removed under reduced pressure. **P-Im** is a viscous brown liquid. Yield: 0.213 g (64%, 1.12 mmol).

1H NMR (250.13 MHz, D₂O): 1.58 (m, 2H, P-CH₂-CH₂), 1.98 (m, 2H, P-CH₂-CH₂-CH₂), 4.20 (t, 2H, P-CH₂), 7.38 (d, 2H, P-CH₂, N-CH-CH-N), 8.63 (s, 1H, N-CH-N) ppm.

^{31}P NMR (101.25 MHz, D₂O): 27.19 ppm.

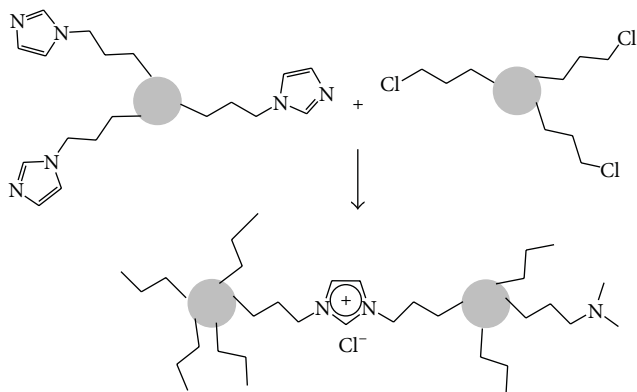
^{13}C NMR (62.90 MHz, D₂O): 22.2 (P-CH₂-CH₂), 24.3 (P-CH₂), 49.4 (N-CH₂), 119.8 (N-CH-CH-N), 121.9 (N-CH-CH-N), 135.5 (N-CH-N) ppm.

Synthesis of the Zirconia Nanoparticles and Modification with P-Im or P-Cl: Formation of TiO₂_INN. Synthesis of Titania Nanoparticles. 10 mL (33.96 mmol) of Ti(O¹Pr)₄ was dissolved in 25 mL dry ethanol. This mixture was added dropwise under vigorous stirring to 250 mL water and adjusted to a pH of 1.7 with 1 mL nitric acid (53%). During the addition, the reaction mixture was cooled to 4°C using an ice bath. After complete addition the ice bath was removed and the mixture stirred for 3 days at room temperature. Then, the solvent was removed under reduced pressure and the white crystalline product was dried in a desiccator over P_2O_5 under vacuum.

Formation of TiO₂_INN. 1 g of previously synthesised TiO₂ nanoparticles was dispersed in 50 mL water. To this suspension, either 0.244 g (1.54 mmol) of 3-chloropropylphosphonic acid (**TiO₂_Cl**) or 0.293 g (1.54 mmol) of N-imidazolylpropylphosphonic acid (**TiO₂_Im**), dissolved in 100 mL distilled water, respectively, was added. The white suspensions were stirred at room temperature for 24 hours. For analysis, the modified particles were isolated *via* centrifugation, washed several times with ethanol and water, and finally dried in a desiccator over P_2O_5 under vacuum. The networking nucleophilic substitution reaction (**TiO₂_INN**) was carried out by transferring 75 mL of the modified particles suspensions, **TiO₂_Cl** and **TiO₂_Im**, to a 250 mL round bottom flask and refluxed for 24 hours. Afterwards, the connected particles were centrifuged, washed two times with ethanol, and finally dried a desiccator over P_2O_5 in vacuum.

Synthesis of the Zirconia Nanoparticles and Modification with P-Im or P-Cl: Formation of ZrO₂_INN. ZrO₂ nanoparticles were synthesized by heating 20 mL of an aqueous 4 molar solution of ZrOCl₂·8H₂O (80 mmol) to 200°C for 72 hours in a stainless-steel autoclave with a PTFE inlay. The particles were collected through precipitation with acetone and centrifugation. Afterwards, the nanoparticles were washed 3 times with ethanol and acetone, 20 mL, respectively. Finally, the crystalline, white powder was dried in a desiccator over P_2O_5 under vacuum.

For surface modification, 0.5 g of ZrO₂ nanoparticles was dispersed in 50 mL water. To this suspension either 80 mg



SCHEME 1: The 3-dimaensonal networking of nanoparticles by means of nucleophilic substitution to form INN hybrid material.

(0.5 mmol) of 3-chloropropylphosphonic acid ($\text{ZrO}_2\text{-Cl}$) or 95 mg (0.5 mmol) of *N*-imidazolylpropylphosphonic acid ($\text{ZrO}_2\text{-Im}$), dissolved in 50 mL distilled water, respectively, was added. The white suspensions were stirred at room temperature for 24 hours. For analysis, the modified particles were isolated via centrifugation, washed several times with water, ethanol, and acetone, and finally dried in a desiccator over P_2O_5 in vacuum. The networking nucleophilic substitution reaction ($\text{ZrO}_2\text{-INN}$) was carried out by transferring the two differently modified zirconia nanoparticle suspensions to a 250 mL round bottom flask and refluxed for 24 hours. Afterwards, the connected particles were centrifuged, washed two times with ethanol, and finally dried a desiccator over P_2O_5 in vacuum.

3. Results and Discussion

The various INN materials were prepared by reacting imidazole-modified nanoparticle with chloroalkyl-modified nanoparticles (Scheme 1) [6, 7].

The modified nanoparticles were on the one hand silica, for which the anchoring group was a functional trimethoxysilane, and on the other hand titania or zirconia, for which the anchoring group was a functional phosphonic acid [23]. The spherical silica and titania nanoparticles have a main diameter of 15 nm and 4 nm, respectively (see Supplementary Information in the supplementary material available online at <http://dx.doi.org/10.1155/2013/682945>). The zirconia nanoparticles are 100% made of the monoclinic baddeleyite phase as verified with powder X-ray diffraction (bars: JCPDS no. 01-0750 for baddeleyite in Figure 1). The monoclinic zirconia nanoparticles are not spherical but elongated; from the DLS and XRD, their spherical equivalent diameter can be estimated to be 6 nm (Figure 1).

The anchoring of the functional groups onto the surface of the nanoparticles can be verified by ^{29}Si NMR, for the alkoxy silane onto silica [6]. The anchoring of functionalized phosphonic acid onto titania or zirconia surface was verified by FTIR (see Supplementary Information). The band of the PO_3 environment at 950 cm^{-1} is shifted to 1030 cm^{-1} after anchoring, while the strength of the phosphorous–oxygen

bonds is almost lowering due to the formation of titanium/zirconium oxygen bonds. In the same time, the bands at 770 cm^{-1} and 1150 cm^{-1} characteristic of the P–OH and P=O bonds, respectively, are disappearing due to the formation of the P–O–Ti liaisons. However in the case of $\text{ZrO}_2\text{-Im}$ and $\text{ZrO}_2\text{-Cl}$, the band at 750 cm^{-1} is hidden by the strong absorption band for the Zr–O–Zr bonds.

The functional groups, imidazole and chloroalkyl, at the surface of the nanoparticles are reacting with each other in a nucleophilic substitution reaction. The organic bridging molecule formed between two nanoparticles is an imidazolium chloride unit, as described in Scheme 1. This reaction occurs at low temperature (under 70°C) in environmental friendly solvent (methanol or ethanol) and without formation of side-product. Thus, the reaction can be considered as a click-chemistry-like reaction.

The INN hybrid materials formation obtained from imidazole and chloroalkyl anchored on silica nanoparticles ($\text{SiO}_2\text{-INN}$) or titania nanoparticles ($\text{TiO}_2\text{-INN}$) were characterized in previous works by means of ^{15}N NMR spectroscopy and/or anion exchange experiments [22, 24].

The formation of the zirconia nanoparticle network ($\text{ZrO}_2\text{-INN}$) by reaction of imidazole with chloropropyl functional groups anchored on zirconia nanoparticles was verified by anion metathesis. The metathesis reaction is obtained by reaction with sodium tetrafluoroborate in an acetone suspension of the INN. During the metathesis, the chloride imidazolium counter anion is exchanged by the tetrafluoroborate, leading to the formation of sodium chloride as side-product. After filtration of the hybrid material, as sodium chloride is not soluble in acetone, the presence of sodium chloride could be evidenced by X-ray diffraction (Figure 2, bars). The reflections at values of 2θ of 32° , 46° , and 57° are characteristic for NaCl (while the other reflections on the pattern can be assigned to NaCl but also to the excess of NaBF_4 used in excess for the metathesis reaction). The formation of sodium chloride is the proof that anionic chloride was present in the hybrid material. Indeed, if no reaction occurred, only covalent chlorine species would be present. Such covalently bonded chlorine atoms cannot be exchanged by anion metathesis. Thus, the anion metathesis reaction indicates clearly that the imidazolium formation took place.

In addition to the anion metathesis, solid-state nuclear magnetic resonance of ^{15}N was performed on the hybrid material $\text{ZrO}_2\text{-INN}$. Despite performing the experiment under cross-polarization, the signal to noise ratio of the spectrum is quite poor due to three effects. The first two effects are the low gyromagnetic constant of the ^{15}N ($-2.7126 \times 10^7\text{ rad}\cdot\text{T}^{-1}\cdot\text{s}^{-1}$) and the very low natural abundance of the isotope (0,368%) [25]. The first aspect inducing a low signal to noise ratio is the low amount of nitrogen atoms in the sample: 2 nitrogen atoms per imidazolium chain in a material containing only 10 wt% organic (see Supplementary Information). Nevertheless, a clear peak can be observed at a chemical shift of 142 ppm in Figure 2. Reference experiments have shown that the reaction of imidazole to imidazolium results in a slight but characteristic shift of the nitrogen peak in the ^{15}N NMR spectrum, from 133 ppm to 142 ppm [22].

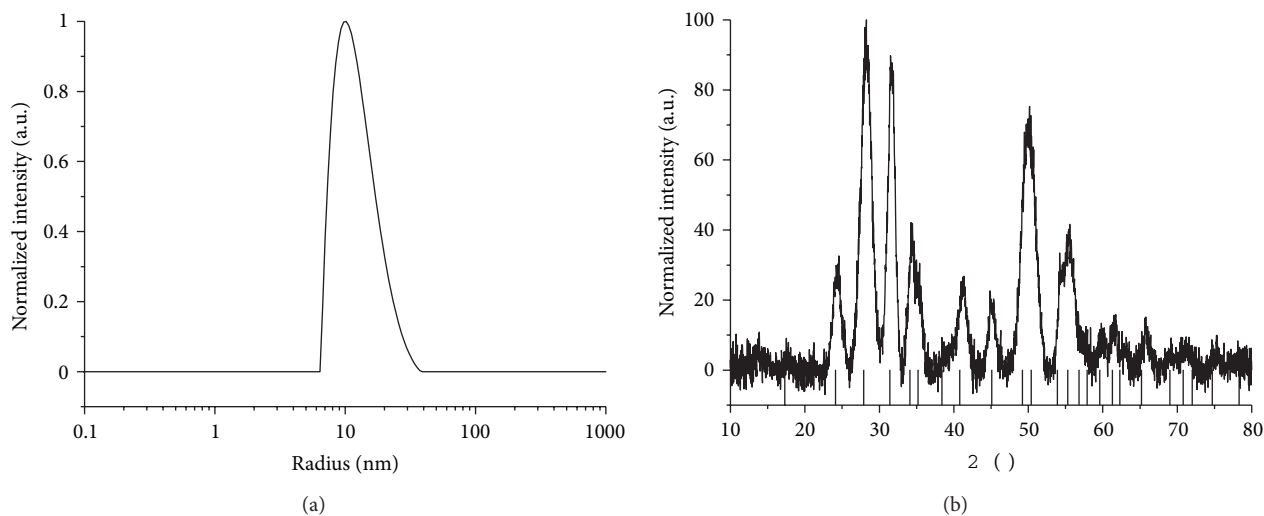


FIGURE 1: (a) DLS and (b) XRD patterns of the nonmodified zirconia nanoparticles.

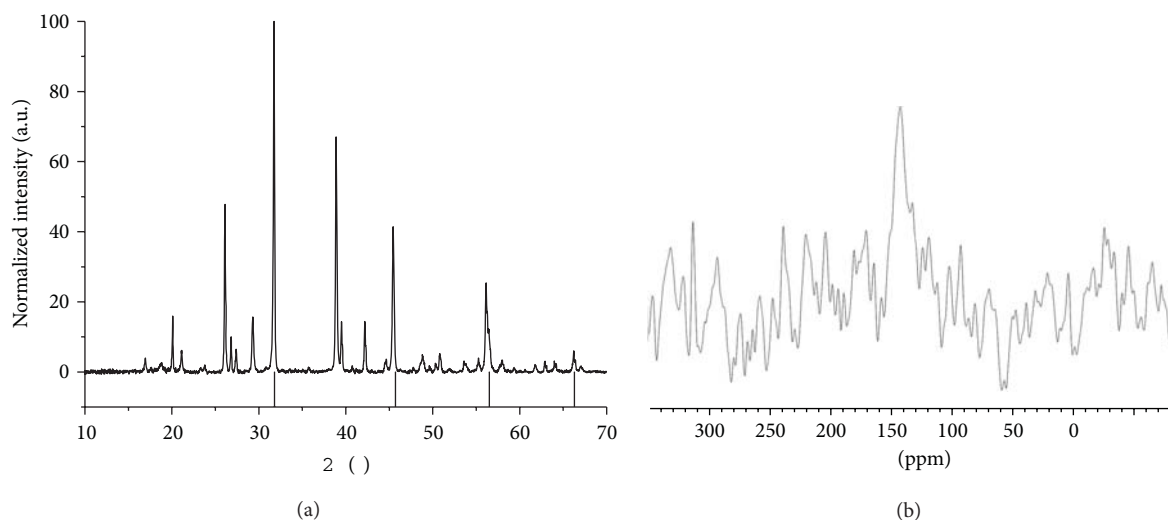


FIGURE 2: (a) XRD diffractogram of the anion exchange washing phase of $\text{ZrO}_2\text{-INN}$ (bars: JCPDS no. 74-0199 for NaCl) and (b) CP MAS ^{15}N NMR of $\text{ZrO}_2\text{-INN}$.

Thus, the peak observed at 142 ppm for $\text{ZrO}_2\text{-INN}$ is the signature for the formation of an imidazolium species.

SAXS investigations could allow verifying the presence of nonagglomerated nanoparticles within the INN materials, as also discussed in the works of Feichtenschlager et al. and Pabisch et al. [26, 27]. Indeed, differences in the scattering intensities can be observed corresponding to the typical size and distance of single nanoparticles present in the hybrid material, at about $q = 0.4 \text{ nm}^{-1}$ for silica, 2 nm^{-1} for titania, and 1.0 nm^{-1} for zirconia (arrows on Figure 3). These peaks correspond in real space in a first approximation to a typical size of about 15 nm, 4 nm, and 6 nm for SiO_2 , TiO_2 , and ZrO_2 , respectively. To be more precise, the scattering curves were fitted by a formal factorization with a mean form factor and an effective structure factor [27, 28]. As form factor we used the unified function from Beaucage [29, 30] and as structure

a hard sphere model [31]. These fits give a typical radius of gyration r_g of the particles, from which the equivalent spherical diameter d_p is obtained by $d_p = 2r_g \text{ Sqrt}(5/3)$, a typical distance D (twice the hard sphere radius r_{HS}), and a packing density (the hard sphere volume factor η). At large scattering vectors, at $q > 10 \text{ nm}^{-1}$, the scattering peaks are corresponding either to amorphous silica, crystalline titania, or crystalline zirconia.

The porous characteristics of the three INN materials were measured by means of nitrogen sorption at 77 K after degassing in vacuum overnight at 75°C (Figure 4). The three materials present very different profiles.

The isotherm of $\text{SiO}_2\text{-INN}$ is a type II isotherm [32] characteristic for macroporous materials (Figure 3 top). The calculated BET surface area is very low, around $5 (\pm 1) \text{ m}^2 \cdot \text{g}^{-1}$, which is consistent with the presence of macropores. The high

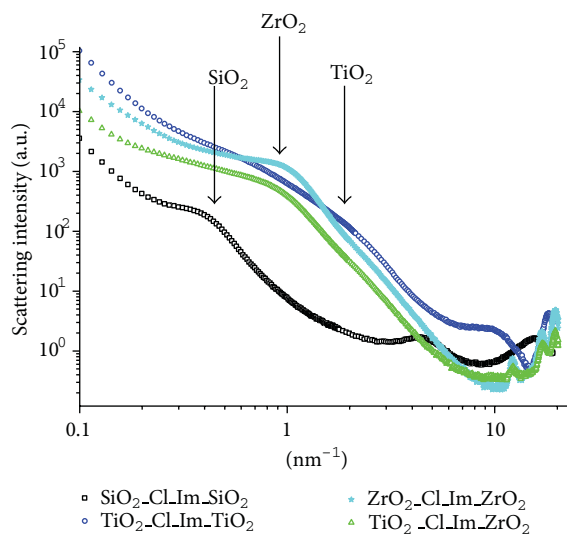


FIGURE 3: SAXS curves for various INNs (black squares for SiO_2 -INN, blue triangles for TiO_2 -INN, and green stars for ZrO_2 -INN).

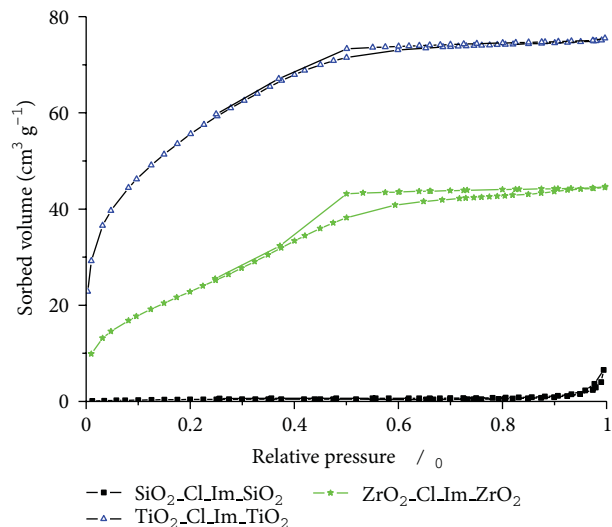
uncertainty on the surface area is due to the fact that the nitrogen sorption experiments are not suited for the determination of specific surface areas for macroporous materials and in consequence underestimate the values. The graph of the BJH method plotted for the desorption branch (Figure 4(b)) confirmed the presence of large pores, macropores, from around 20 nm diameter and broadly distributed toward larger pores.

The TiO_2 -INN in contrary shows a type I isotherm (Figure 3 top) [32], classical for microporous structures, with pore diameters centred on 2 nm and distributed toward smaller pores (Figure 4(b)). For this TiO_2 -INN hybrid material, the BET-specific surface area of the material reaches $205 (\pm 5) \text{ m}^2 \cdot \text{g}^{-1}$. A relatively high specific surface area is characteristic of microporous materials.

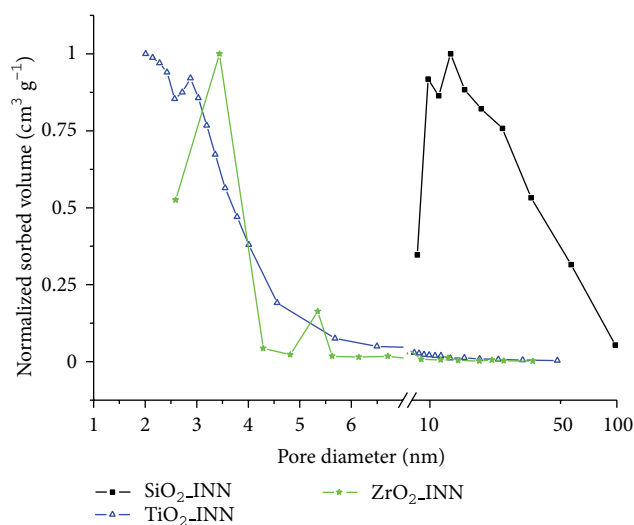
The hybrid material ZrO_2 -INN represents an intermediary case. Here the nitrogen sorption isotherm (Figure 4(a)) is of type IV. This type IV isotherm corresponds to mesoporous materials. A BET-specific surface area of $90 (\pm 4) \text{ m}^2 \cdot \text{g}^{-1}$ was estimated. The BJH plotted for the desorption branch (Figure 4(b)) indicated the presence of mesopores centred on 4 nm with a quite narrow distribution.

The INNs were also observed through transmission electronic microscopy. The TEM images are presented in Figure 5. The size and shape of the nanoparticles can be observed in the micrographs. However, the organic link cannot be distinguished. In the TEM micrographs, the pores which were characterized by nitrogen sorption experiments cannot be distinguished from defects in the network. Moreover, in the case of TiO_2 -INN, the pores are of around 2 nm and thus can hardly be observed by TEM.

We interpret the difference in the pore sizes as a consequence of the nanoparticle size or shape and the derived nanoparticle curvature. The silica nanoparticles in SiO_2 -INN are relatively large: a fit of the SAXS intensities gave a size



(a)



(b)

FIGURE 4: (a) Nitrogen sorption isotherms and (b) BJH pore size distribution (on the abscissa axis: linear scale before the break and log scale after the break) of various INNs (black squares for SiO_2 -INN, blue triangles for TiO_2 -INN, and green stars for ZrO_2 -INN).

of 13.1 nm, a distance of 13.8 nm, and relatively high packing density (hard sphere volume ratio $\eta = 0.17$). Therefore, the curvature of the nanoparticle is very low and the ligands are facing an almost plane surface. It follows that in SiO_2 -INN, the ligands can be organized between the nanoparticles. This short-range ordering of the ligands can be detected by the scattering peak observed around 5 nm^{-1} in the SAXS curve (Figure 3) [33]. The organized ligands between the nanoparticles are then building a relatively dense organic phase (size and distance 1.1 nm, $\eta = 0.18$) and preclude the formation of small cavities (Scheme 2, top left). The good networking is directly visible in Figure 3 by the relatively strong intensity of the peak corresponding to the silica nanoparticles at 0.4 nm^{-1}

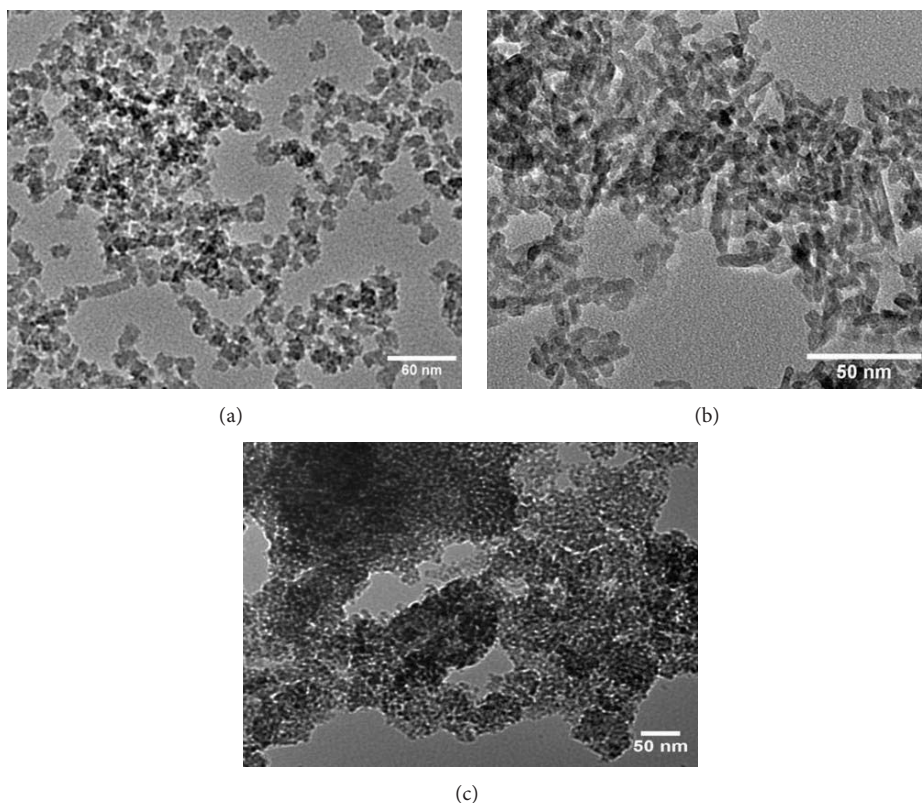
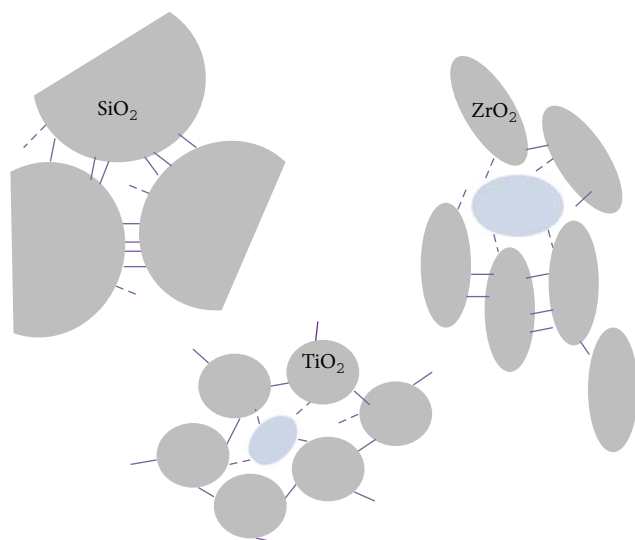


FIGURE 5: TEM micrographs of the Ionic Nanoparticle Networks (a) SiO_2 -INN, (b) ZrO_2 -INN, and (c) TiO_2 -INN.



SCHEME 2: Network porosity (striped circles) for (top left) SiO_2 -INN, (bottom centre) TiO_2 -INN, and (top right) ZrO_2 -INN.

(Figure 3) [26, 27]. The macropores, larger than 20 nm, are formed in regions of the network where some ligands did not react.

In contrary to the titania nanoparticle networks TiO_2 -INN, the nanoparticles, 4 nm diameter, are small enough to present a strong curvature, with regard to the

imidazolium ligands. Thus, more unreacted ligands could be observed, by means of solid-state ^{15}N NMR where a clear peak for the imidazole could be observed at 131 ppm next to the imidazolium peak at 142 ppm [22]. The presence of these un-reacted ligands allows the formation of interparticle cavities having sizes slightly larger than the ionic liquid-like imidazolium bridging units (Scheme 2, bottom right). The SAXS intensity of TiO_2 -INN also highlights a more loose network with a broad size distribution, as a possible short range order peak at 2 nm^{-1} is weak (Figure 3) [22].

The case of ZrO_2 -INN is slightly different. Indeed, if the nanoparticles are of comparable size with the titania nanoparticles, they are not spherical any more but elongated (Figure 5(b)). It results in an overall better networking of the particles, revealed by a distinct short-range order peak of the zirconia nanoparticles at 1.0 nm^{-1} (Figure 3) with $\eta = 0.08$.

The fit results in a typical particle diameter of 5.2 nm, whereas the effective distance obtained from the structure factor is about 4.8 nm and therefore is slightly smaller than the spherical equivalent diameter of 5.2 nm. This seems to be surprising, but a reasonable interpretation is that, on the one hand, the particles are elongated (TEM image, Figure 5(b)) and, on the other hand, the particles face mostly each other's long side. When two neighbouring nanoparticles are connected over a long face, similarly as for the silica nanoparticles, no space is left. But when two nanoparticles are connected by the shorter faces, mesopores can be formed in the nanoparticle interspace (Scheme 2, top right), somehow similarly as for titania nanoparticle-based materials.

4. Conclusion

In this paper we have presented a new Ionic Nanoparticle Network (INN) based on zirconia nanoparticles linked by ionic liquid-like imidazolium bridging units. The porous characteristics of the new zirconia INN were compared to those of titania- and silica-based INN.

It was shown that the porous characteristics of the INN depend on the size and shape of the nanoparticles. INNs based on large spherical nanoparticles, like SiO₂, are macroporous, while INNs based on small spherical nanoparticles, like TiO₂, are microporous. The use of elongated small zirconia nanoparticles drives to the formation of a mesoporous hybrid material.

The porosity observed in the INN materials should ensure accessibility of the functional units for catalysis experiments.

Conflict of Interests

The authors declare having no direct financial relation with the trademarks mentioned in the paper.

Acknowledgment

This work was financially supported by the Austrian Fonds zur Förderung der Wissenschaftlichen Forschung (FWF, Project P21190–N17).

References

- [1] Gacoin, Besson, and Boilot, "Organized mesoporous silica films as templates for the elaboration of organized nanoparticle networks," *Journal of Physics Condensed Matter*, vol. 18, no. 13, pp. S85–S95, 2006.
- [2] S. Siavoshi, C. Yilmaz, S. Somu et al., "Size-selective template-assisted electrophoretic assembly of nanoparticles for biosensing applications," *Langmuir*, vol. 27, no. 11, pp. 7301–7306, 2011.
- [3] B. Basnar, M. Litschauer, S. Abermann, E. Bertagnolli, G. Strasser, and M. A. Neouze, "Layer-by-layer assembly of titania nanoparticles based ionic networks," *Chemical Communications*, vol. 47, pp. 361–363, 2011.
- [4] S. Easwaramoorthi, P. Kim, J. M. Lim et al., "The self-assembly and photophysical characterization of tri(cyclopenta[def]phenanthrene)-derived nanoparticles: a template free synthesis of hollow colloidosomes," *Journal of Materials Chemistry*, vol. 20, no. 43, pp. 9684–9694, 2010.
- [5] D. Jańczewski, N. Tomczak, S. Liu, M. Han, and G. J. Vancso, "Covalent assembly of functional inorganic nanoparticles by "click" chemistry in water," *Chemical Communications*, vol. 46, no. 19, pp. 3253–3255, 2010.
- [6] M. Litschauer and M. Neouze, "Nanoparticles connected through an ionic liquid-like network," *Journal of Materials Chemistry*, vol. 18, no. 6, pp. 640–646, 2008.
- [7] M. A. Neouze, "About the interactions between nanoparticles and imidazolium moieties: emergence of original hybrid materials," *Journal of Materials Chemistry*, vol. 20, no. 43, pp. 9593–9607, 2010.
- [8] L. Wang, J. Luo, M. J. Schadt, and C. Zhong, "Thin film assemblies of molecularly-linked metal nanoparticles and multifunctional properties," *Langmuir*, vol. 26, no. 2, pp. 618–632, 2010.
- [9] K. Moller, B. Yilmaz, U. Muller, and T. Bein, "Hierarchical zeolite beta via nanoparticle assembly with a cationic polymer," *Chemistry of Materials*, vol. 23, no. 19, pp. 4301–4310, 2011.
- [10] Q. Yao and S. L. Brock, "Porous CdTe nanocrystal assemblies: ligation effects on the gelation process and the properties of resultant aerogels," *Inorganic Chemistry*, vol. 50, no. 20, pp. 9985–9992, 2011.
- [11] J. B. Wacker, V. K. Parashar, and M. A. M. Gijs, "Anisotropic magnetic porous assemblies of oxide nanoparticles interconnected via silica bridges for catalytic application," *Langmuir*, vol. 27, no. 8, pp. 4380–4385, 2011.
- [12] M. R. Gao, S. R. Zhang, J. Jiang, Y. R. Zheng, D. Q. Tao, and S. H. Yu, "One-pot synthesis of hierarchical magnetite nanochain assemblies with complex building units and their application for water treatment," *Journal of Materials Chemistry*, vol. 21, no. 42, pp. 16888–16892, 2011.
- [13] S. Chen, J. Zhang, T. Wu, P. Feng, and X. Bu, "Multiroute synthesis of porous anionic frameworks and size-tunable extraframework organic cation-controlled gas sorption properties," *Journal of the American Chemical Society*, vol. 131, no. 44, pp. 16027–16029, 2009.
- [14] R. S. Crees, M. L. Cole, L. R. Hanton, and C. J. Sumbly, "Synthesis of a zinc(II) imidazolium dicarboxylate ligand metal-organic framework (MOF): a potential precursor to MOF-tethered N-heterocyclic carbene compounds," *Inorganic Chemistry*, vol. 49, no. 4, pp. 1712–1719, 2010.
- [15] S. U. Hong, D. Park, Y. Ko, and I. Baek, "Polymer-ionic liquid gels for enhanced gas transport," *Chemical Communications*, no. 46, pp. 7227–7229, 2009.
- [16] D. Kerlé, R. Ludwig, A. Geiger, and D. Paschek, "Temperature dependence of the solubility of carbon dioxide in imidazolium-based ionic liquids," *Journal of Physical Chemistry B*, vol. 113, no. 38, pp. 12727–12735, 2009.
- [17] A. Mavrandonakis, E. Klontzas, E. Tylianakis, and G. E. Froudakis, "Enhancement of hydrogen adsorption in metal-organic frameworks by the incorporation of the sulfonate group and Li cations. A Multiscale Computational Study," *Journal of the American Chemical Society*, vol. 131, no. 37, pp. 13410–13414, 2009.
- [18] M. P. Stracke, G. Ebeling, R. Cataluña, and J. Dupont, "Hydrogen-storage materials based on imidazolium ionic liquids," *Energy and Fuels*, vol. 21, no. 3, pp. 1695–1698, 2007.
- [19] A. Revelli, F. Mutelet, and J. Jaubert, "High carbon dioxide solubilities in imidazolium-based ionic liquids and in poly(ethylene glycol) dimethyl ether," *Journal of Physical Chemistry B*, vol. 114, no. 40, pp. 12908–12913, 2010.
- [20] W. Shi and D. C. Sorescu, "Molecular simulations of CO₂ and H₂ sorption into ionic liquid 1-n-hexyl-3-methylimidazolium bis(trifluoromethylsulfonyl)amide ([hmim][Tf₂N]) confined in carbon nanotubes," *Journal of Physical Chemistry B*, vol. 114, no. 46, pp. 15029–15041, 2010.
- [21] J. Y. Lee, J. M. Roberts, O. K. Farha, A. A. Sarjeant, K. A. Scheidt, and J. T. Hupp, "Synthesis and gas sorption properties of a Metal-Azoliium Framework (MAF) material," *Inorganic Chemistry*, vol. 48, no. 21, pp. 9971–9973, 2009.
- [22] M. A. Neouze, M. Litschauer, M. Puchberger, and H. Peterlik, "Porous titania ionic nanoparticle networks," *Langmuir*, vol. 27, no. 7, pp. 4110–4116, 2011.
- [23] M. Neouze and U. Schubert, "Surface modification and functionalization of metal and metal oxide nanoparticles by organic ligands," *Monatshfte fur Chemie*, vol. 139, no. 3, pp. 183–195, 2008.

- [24] M. Litschauer, M. Puchberger, H. Peterlik, and M. Neouze, "Anion metathesis in ionic silica nanoparticle networks," *Journal of Materials Chemistry*, vol. 20, no. 7, pp. 1269–1276, 2010.
- [25] H. Friebolin, *Basic One- and Two- Dimensional NMR Spectroscopy*, Wiley-VCH, Weinheim, Germany, 4th edition, 2004.
- [26] B. Feichtenschlager, S. Pabisch, H. Peterlik, and G. Kickelbick, "Nanoparticle assemblies as probes for self-assembled monolayer characterization: correlation between surface functionalization and agglomeration behavior," *Langmuir*, vol. 28, no. 1, pp. 741–750, 2012.
- [27] S. Pabisch, B. Feichtenschlager, G. Kickelbick, and H. Peterlik, "Effect of interparticle interactions on size determination of zirconia and silica based systems—a comparison of SAXS, DLS, BET, XRD and TEM," *Chemical Physics Letters*, vol. 521, pp. 91–97, 2012.
- [28] J. Brunner-Popela, R. Mittelbach, R. Strey, K. V. Schubert, E. W. Kaler, and O. Glatter, "Small-angle scattering of interacting particles. III. D₂O-C₁₂E₅ mixtures and microemulsions with n-octane," *Journal of Chemical Physics*, vol. 110, no. 21, pp. 10623–10632, 1999.
- [29] G. Beaucage, "Approximations leading to a unified exponential/power-law approach to small-angle scattering," *Journal of Applied Crystallography*, vol. 28, pp. 717–728, 1995.
- [30] G. Beaucage and D. W. Schaefer, "Structural studies of complex systems using small-angle scattering: a unified Guinier/power-law approach," *Journal of Non-Crystalline Solids*, vol. 172, no. 2, pp. 797–805, 1994.
- [31] D. J. Kinning and E. L. Thomas, "Hard-sphere interactions between spherical domains in diblock copolymers," *Macromolecules*, vol. 17, no. 9, pp. 1712–1718, 1984.
- [32] F. Rouquerol, J. Rouquerol, and K. Sing, *Adsorption by Powders and Porous Solids: Principles, Methodology and Applications*, Academic Press, London, UK, 1999.
- [33] M. Czakler, M. Litschauer, K. F. Föttinger, H. Peterlik, and M. A. Neouze, "Photoluminescence as complementary evidence for short-range order in ionic silica nanoparticle networks," *The Journal of Physical Chemistry C*, vol. 114, no. 49, pp. 21342–21347, 2010.

Research Article

Photocatalytic Properties of Microwave-Synthesized TiO₂ and ZnO Nanoparticles Using Malachite Green Dye

A. K. Singh^{1,2} and Umesh T. Nakate¹

¹ Nanomaterials and Sensors Laboratory, Defence Institute of Advanced Technology, Girinagar, Pune, Maharashtra 411025, India

² DRDO Centre for Piezoceramics and Devices, ARDE, Pashan, Pune, Maharashtra 411021, India

Correspondence should be addressed to A. K. Singh; aksingh@diat.ac.in

Received 11 January 2013; Accepted 17 January 2013

Academic Editor: Amir Kajbafvala

Copyright © 2013 A. K. Singh and U. T. Nakate. This is an open access article distributed under the Creative Commons Attribution License, which permits unrestricted use, distribution, and reproduction in any medium, provided the original work is properly cited.

TiO₂ and ZnO nanoparticles (NPs) were synthesized using microwave-assisted method. Synthesized NPs were characterized for their structure, morphology, and elemental composition using X-ray diffraction (XRD), scanning electron microscopy (SEM), and energy dispersive spectroscopy (EDS). The crystallite size of synthesized NPs of TiO₂ and ZnO was about 12.3 and 18.7 nm as obtained from the Scherrer formula from the most intense XRD peak. The synthesized NPs have been found to be in stoichiometric ratio having anatase and hexagonal wurtzite structure for TiO₂ and ZnO, respectively, and are spherical in shape. Surface area of TiO₂ and ZnO NPs was found to be about 43.52 m²/g and 7.7 m²/g. Photocatalytic (PC) properties of synthesized NPs were studied for malachite green (MG) dye under UV light. TiO₂ NPs were found to be highly photocatalytically active among the two, having efficiency and apparent photodegradation rate of 49.35% and 1.32×10^{-2} , respectively.

1. Introduction

Nowadays, organic pollutants like dyes are becoming a serious health problem, which are being discharged by many industries and houses through wastewater in the environment. The discharged wastes containing dyes are toxic to microorganisms and aquatic life [1]. Malachite green (MG) dye is an extensively used biocide in the global aquaculture industry. It is also used as a food colouring agent, food additive, medical disinfectant, and anthelmintic as well as in silk, wool, jute, leather, cotton, paper, and acrylic industries. However, MG has now become a highly controversial compound due to the risks it poses to the consumers of treated fish, including its effects on the immune system and reproductive system and its genotoxic and carcinogenic properties [2]. In the light of the basic and applied researches reviewed, PC oxidation method appears to be a promising route for the treatment of wastewater contaminated with phenols and dyes. In recent years, there has been a wide research interest in developing semiconductor photocatalysts having high PC activities for environmental applications such as water disinfection, hazardous waste remediation, and

water purification [3–5]. It is reported that nanosize semiconductors act as an efficient PC agent resulting from either an extremely large-surface-area-to-volume ratio or quantum confinement effects of charge carriers for the degradation of organic pollutants in water under UV irradiation [6–10]. PC function is similar to the chlorophyll in the photosynthesis. In a PC system, photo-induced molecular transformation or reaction takes place at the surface of the catalyst. A basic mechanism of PC reaction on the generation of electron-hole pair and its destination is as follows: when a photocatalyst is illuminated by the light stronger than its bandgap energy, electron-hole pairs diffuse out to the surface of the PCs and participate in the chemical reaction with the electron donor and acceptor. Those free electrons and holes transform the surrounding oxygen or water molecules into OH free radicals with super strong oxidation [11]. One of the major problems in the PC process is the electron-hole recombination. To avoid this problem, UV irradiation source stands up among other sources [12] because the energy of the UV irradiation is large compared to the bandgap energy of the catalysts. The problem of electron-hole recombination is not fully solved but largely avoided with the use of UV source.

Many photocatalysts like TiO₂, ZnO, ZrO₂, CeO₂, Fe₂O₃, CdS, and ZnS have been attempted for the PC degradation of a wide variety of environmental contaminants. TiO₂ [7] is one of the most widely used semiconductors for PC degradation of waste due to its biological and chemical inertness, high photoreactivity, nontoxicity, and photostability. It is proven that among the three crystalline polymorphs of TiO₂, that is, rutile, anatase, and brookite, the anatase phase or the mixed anatase/rutile phase exhibits better PC properties. The anatase form of TiO₂ has the desirable properties of being chemically stable, readily available, and active as a catalyst for oxidation processes. Bandgap of about 3.2 eV matches the output of a wide variety of readily available lamps. Recently, ZnO [13–17] has also been reported for PC activity having bandgap close to TiO₂. However, only a handful of studies have been attempted which compare the efficiency of different catalysts for a particular organic compound under identical experimental conditions. Serpone and Pelizzetti [18] have reported that TiO₂ and ZnO are the two most active catalysts.

During the recent past, ZnO and TiO₂ were the most widely investigated [19, 20] semiconductors. There are several reported methods of NPs synthesis such as sol-gel [21], organometallic [22], hydrothermal [23, 24], and microwave methods [25–27]. Due to the intense friction and the collision of molecules created by microwave irradiation, microwave irradiation not only provides the energy for heating but also greatly accelerates the nucleation. With microwave irradiation on the reactant solution, temperature and concentration gradients can be avoided leading to uniform nucleation. Microwave-based synthesis method is one of the easiest, energy-saving, green, and quick methods for large-scale production of nanomaterials. Microwave synthesis is the novel route of synthesis of metal oxide semiconductor NPs which is a clean, cost-effective, energy-efficient, eco-friendly, rapid, and convenient method of heating and results in higher yields in shorter reaction times [26, 27].

In the present work, TiO₂ and ZnO NPs were synthesized using the microwave method. These NPs were characterized using XRD, SEM, and EDS. The PC activity of these NPs was studied for MG dye under UV light.

2. Experimental

2.1. Synthesis. For the synthesis of TiO₂, 0.5 M titanium butoxide solution was prepared in 100 mL butanol and stirred for 15 min; further 30 mL deionized water was added dropwise in the above solution to allow hydrolysis. This solution was stirred for 30 min which gave rise to white precipitation. The obtained white precipitate was microwave irradiated for 5 min at 700 W power using Raga's microwave system. The microwave used for this experiment was having a power range of 140 W to 700 W. This obtained solution was left 24 hr for aging at room temperature and then centrifuged at 2000 rpm for 15 min. Obtained precipitate was dried at 80°C for 12 hrs. After complete drying, powder was crushed and calcinated in air at 500°C for 2 hr to remove hydroxide impurities and recrystallization.

For the synthesis of ZnO, NaOH (0.4 M), and zinc acetate (0.2 M), solutions were mixed slowly with molar ratio of 2 : 1,

respectively. The above solution was stirred for 10 min. After that, a small quantity of tea was added, and stirring continued for another 10 min. This solution was put for microwave irradiation at 700 W in two steps, that is, 40°C for 20 min and 60°C for 30 min. Resulting precipitate was washed with DI water 2-3 times before drying at 70°C for 4 hr, then crushed using mortar pestle, and calcinated in air at 500°C for 1 hr.

2.2. Characterization. The prepared samples were characterized for their structure, morphology, and elemental composition using X-ray diffraction (XRD) analysis, scanning electron micrograph (SEM), and energy dispersive spectrometry (EDS), respectively. XRD was performed using Bruker AXS, Germany (Model D8 Advanced), diffractometer in the scanning range of 20–70° (2θ) using Cu Kα radiations of wavelength 1.5406 Å. A JEOL ASM 6360A SEM was used to study the morphology and elemental analysis of the NPs. Measurement of BET surface area was carried out for nitrogen adsorption using a Micromeritics Ins., USA.

2.3. Photocatalytic Activity. Synthesized NPs were used for the photodegradation of MG dye, chemical formula: [C₆H₅C(C₆H₄N(CH₃)₂)₂]Cl-4, IUPAC name: [(4-dimethylaminophenyl)phenyl-methyl]-N,N-dimethylaniline, under UV light. In each experiment, 40 mL of MG solution of 0.025 g mL⁻¹ concentration and 0.005 gr of catalyst were used. This solution was stirred for 10 minutes in the dark for equilibrium of adsorption and desorption process of MG with NPs. After stirring, the solution was irradiated by UV lamp (DYMAX Corporation) under medium intensity spot lamp. The UV lamp was having radiation wavelength range of 200 nm–600 nm with nominal intensity 1000–2000 mW/cm². The intensity of absorption peaks, and peak absorbance of NPs was examined by an Ocean Optics UV-Vis high-resolution spectrophotometer (Ocean Optics HR 4000). From which concentrations of MG solution initially and after every 4 minutes of irradiation of UV light were measured from the Lambert–Beer Law [28] that is the absorbance (*A*) of MG solution is proportional to its concentration (*c*), which generally followed the following equation:

$$A = \epsilon bc, \quad (1)$$

where ϵ is the molar absorption coefficient, and *b* is the thickness of the absorption cell. In our experiment, all the testing parameters were kept constant, so that ϵ and *b* could be considered constant. Therefore, changes in the concentration of MB aqueous solution can be determined by a UV-Vis spectrophotometer.

3. Results and Discussion

3.1. X-Ray Diffraction (XRD). XRD spectra of calcinated samples of TiO₂ and ZnO are shown in Figures 1(a) and 1(b). The obtained diffraction pattern has been compared with JCPDS datasheet JCPDS-080-0074 and JCPDS-84-1284, respectively. From Figures 1(a) and 1(b), it is confirmed from the XRD spectra that the given phase of TiO₂ and ZnO is anatase and hexagonal wurtzite, respectively. The crystallite

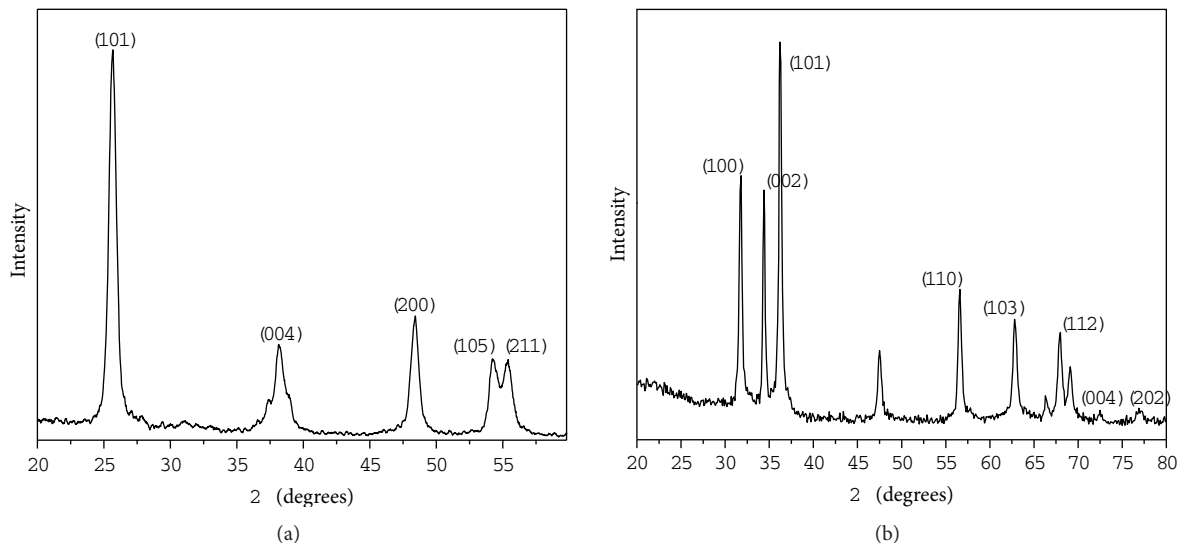


FIGURE 1: XRD of microwave-synthesized NPs: (a) TiO₂ and (b) ZnO.

TABLE 1: PC degradation of MG dye performance parameters of all the samples.

Sample	Crystallite size (nm)	K_{app} ($\times 10^{-2}$)	$X_{(32 \text{ min})}$ (%)
TiO ₂	12.3	1.32	49.35
ZnO	18.7	0.84	23.31

size, D , of NPs has been calculated by XRD line broadening of the most intense peak using the Scherrer formula [29]

$$D = \frac{K\lambda}{\beta \cos \theta}, \quad (2)$$

where λ is the wavelength of X-ray, β is the full width and half maxima, θ is Bragg's angle, and K is the shape factor. The dimensionless shape factor has a typical value of about 0.9 but varies with the actual shape of the crystallite. Here, K is taken as 0.9. Crystallite sizes for these NPs are about 12.3 nm and 18.7 nm for TiO₂ and ZnO, respectively, calculated from the most intense peak and shown in Table 1. The sharpness of peaks shows that TiO₂ NPs are highly crystalline in nature.

3.2. Morphology and Elemental Analysis. Morphology of synthesized NPs was studied using scanning electron microscope (SEM) and is shown in Figures 2(a), 2(b), 2(c), and 2(d) at two different magnifications for TiO₂ and ZnO, respectively. Synthesized NPs of TiO₂ and ZnO were found to be spherical in shape, and ZnO NPs are of lower size than TiO₂ with size uniformity. Some agglomeration was also observed in the SEM image of TiO₂, which may be due to calcination NPs. The measured BET surface area of TiO₂ and ZnO NPs has been found to be, respectively, 43.52 m²/g and 7.7 m²/g. Elemental analysis of NPs was done by using energy dispersive spectrometer (EDS); the plot of spectrum is shown in Figures 3(a) and 3(b), for TiO₂ and ZnO, respectively. For TiO₂ and ZnO, respectively, the at% of elements detected

from EDX is Ti, and O is 54.29 and 45.71; Zn and O are 43.09 and 56.91, respectively, which shows that synthesized NPs are in stoichiometric ratio. The peaks of the plot show the presence of titanium and oxygen elements, zinc and oxygen elements in the corresponding images, that is, Figures 3(a) and 3(b), respectively.

3.3. Photocatalytic Activity. The UV-visible absorbance spectra for photodegradation of MG dye using TiO₂ and ZnO are shown in Figures 4(a) and 4(b), respectively, and corresponding UV-visible spectra of TiO₂ and ZnO are shown in Figure 5. From the plot, it is observed that as irradiation time increases, the concentration of MG dye decreases, which is shown by the decrease in UV-absorbance spectra. The absorption of photon leads to charge separation due to promotion of an electron (e^-) from the valence band of the semiconductor catalyst to the conduction band, thus generating a hole (h^+) in the valence band. Light source provides photon energy required to excite the semiconductor electron from the valence band (VB) region to the conduction band (CB) region. With the increase in irradiation having sufficient intensity, photodegradation efficiency increases because electron-hole formation is predominantly increasing, and electron-hole recombination is negligible at sufficiently higher intensity, whereas at lower light intensity, electron-hole pair separation competes with recombination which in turn decreases the formation of free radicals, thereby, causing less effect on the percentage degradation of the dyes.

Mechanism for photodegradation of MG dye can be explained as follows. On illumination of catalyst surface with enough energy (equals or higher than the bandgap energy, E_{bg} , of the catalyst), it leads to the formation of a hole (h^+) in the valence band and an electron (e^-) in the conduction band. The hole oxidizes either pollutant directly or water to produce OH^\cdot radicals, whereas the electron in the conduction band reduces the oxygen adsorbed on the catalyst. The activation

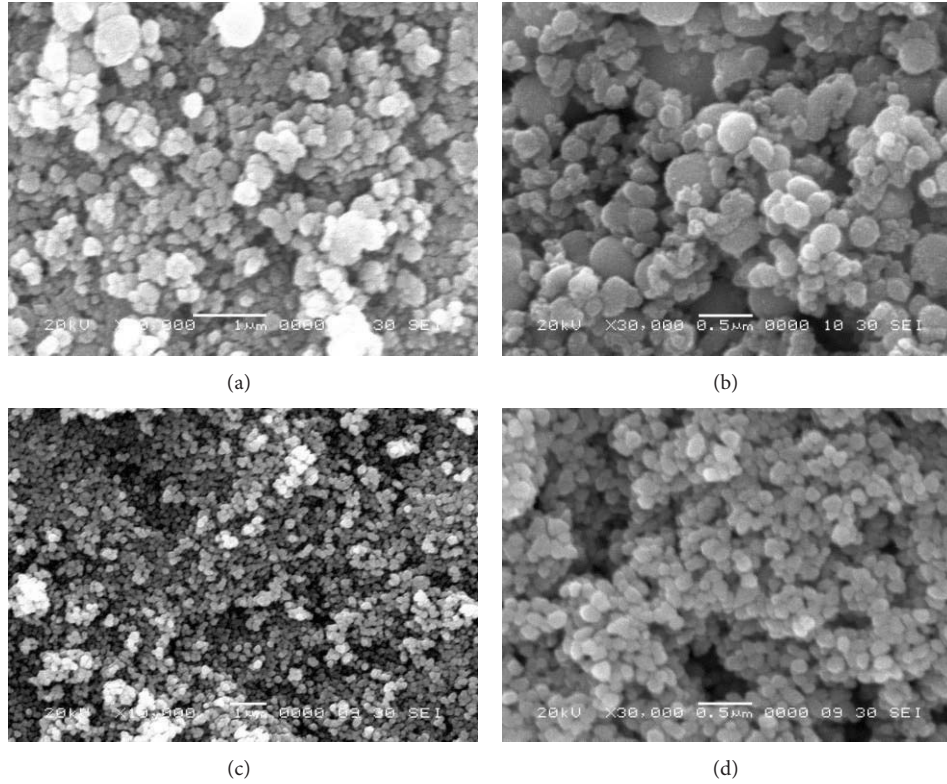


FIGURE 2: SEM image of microwave-synthesized NPs at different magnifications: (a)-(b) for TiO_2 and (c)-(d) for ZnO NPs.

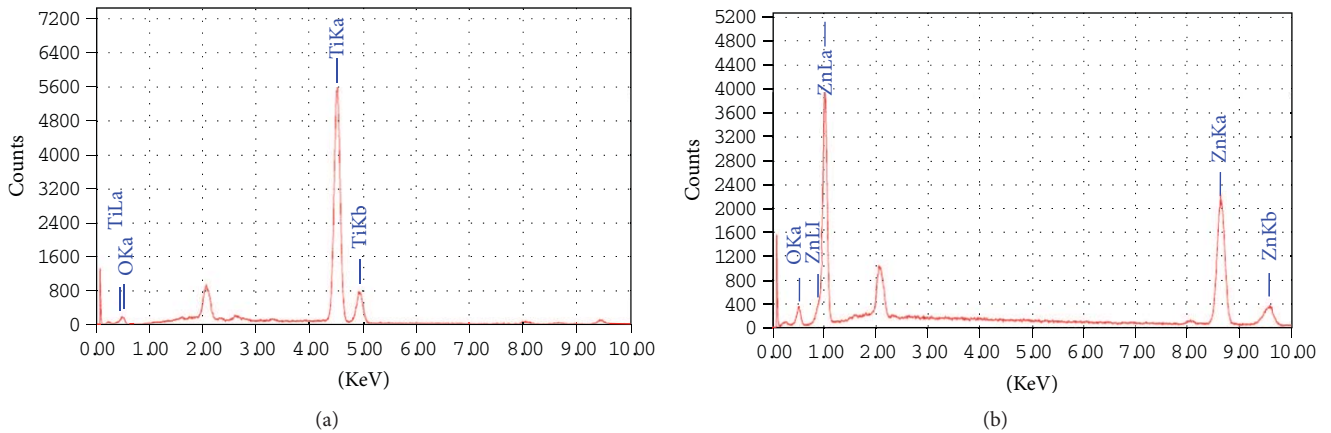
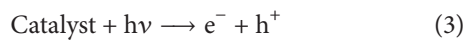
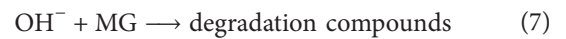
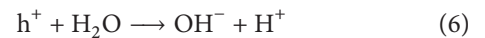


FIGURE 3: EDS spectrum of microwave-synthesized samples: (a) TiO_2 and (b) ZnO NPs.

of catalyst (TiO_2 or ZnO) by UV light can be represented by the following steps:



In this reaction, h^+ and e^- are powerful oxidizing and reductive agents, respectively. The oxidative and reductive reaction steps are expressed as follows:



One of the major problems in the photocatalytic process is the electron-hole recombination. To avoid this problem, UV irradiation source stands up among other sources [12]. The energy of UV irradiation is large compared to the bandgap energy of the catalysts. Hence, the problem of electron-hole recombination is not fully but largely avoided with UV

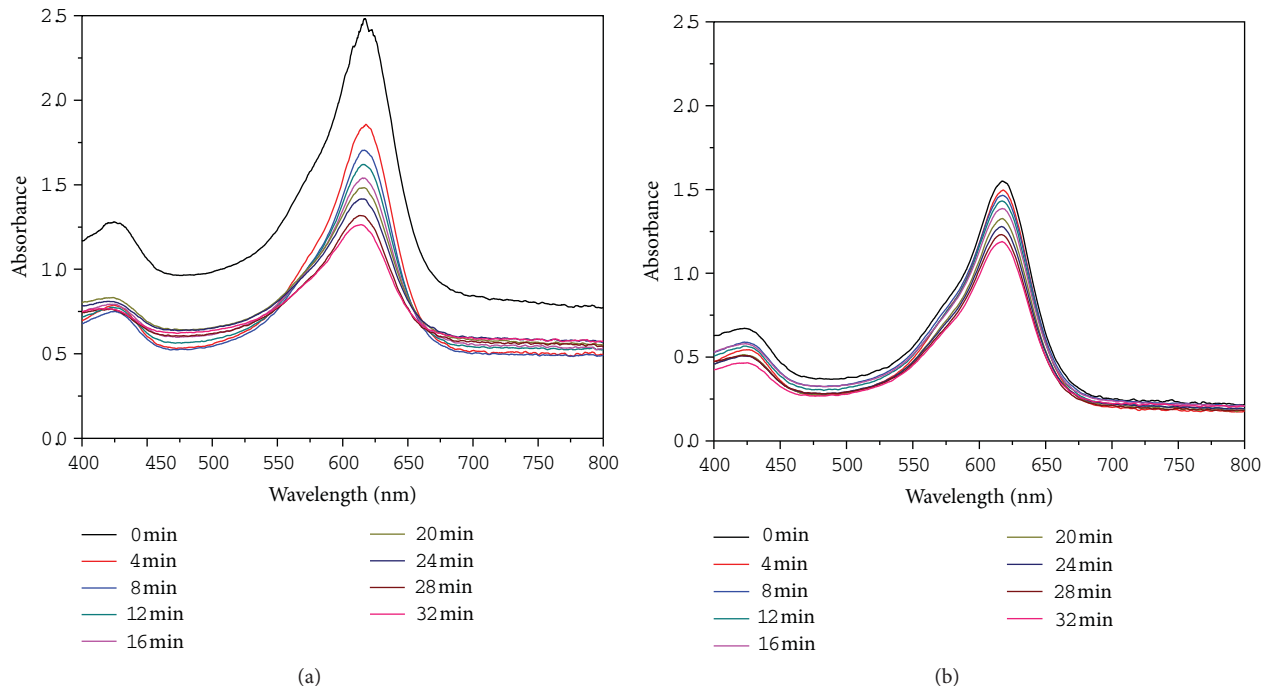


FIGURE 4: UV absorbance spectra of catalyst during photodegradation of MG dye for (a) TiO₂ NPs and (b) ZnO NPs.

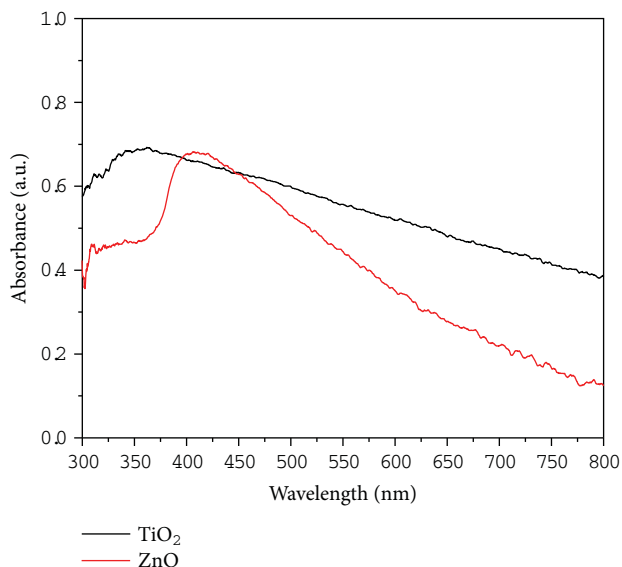


FIGURE 5: UV absorbance spectra of synthesized TiO₂ NPs and ZnO NPs.

source. The percentage efficiency of photodegradation was determined using the following equation [30]:

$$X = \frac{C_0 - C}{C_0} \times 100, \tag{8}$$

where C_0 is the initial solution concentration of MG and C is the solution concentration of MG after degradation. The graph of percentage efficiency with irradiation time is shown

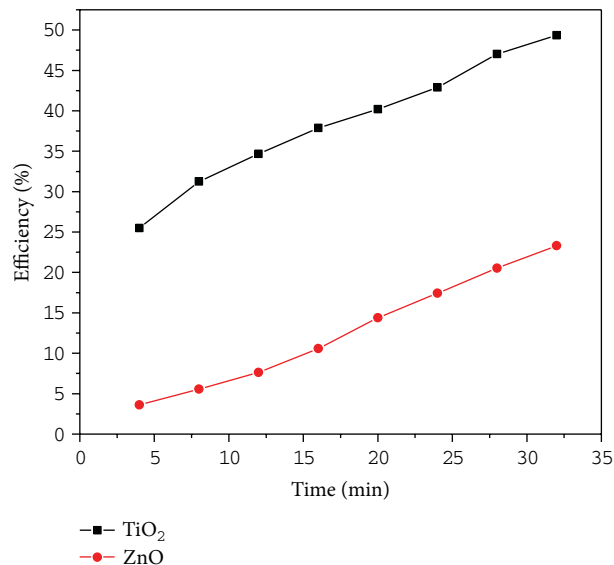


FIGURE 6: Photodegradation percentage efficiency for TiO₂ and ZnO catalysts.

in Figure 6. It is clear from the figure that as irradiation time increases the efficiency of nanoparticles to degrade MG dye also increases. Here, TiO₂ NPs are found to be more efficient catalysts than ZnO NPs. The apparent rate constant for degradation of MG was determined using the following equation [30]:

$$\ln\left(\frac{C_0}{C}\right) = K_{app}t. \tag{9}$$

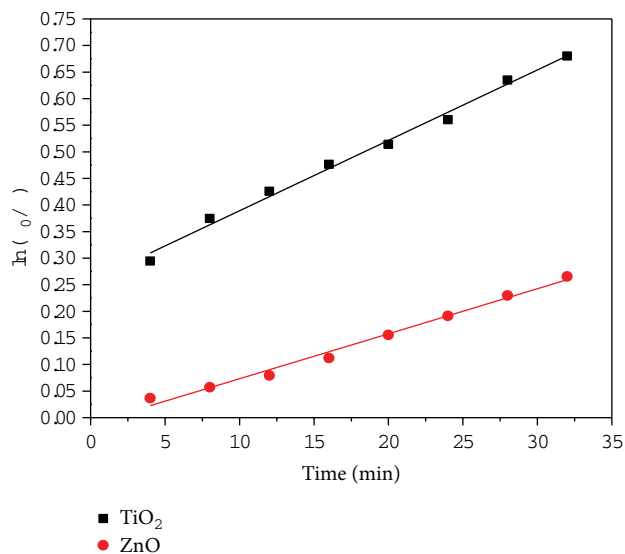


FIGURE 7: Apparent rate constant for degradation of MG dye by synthesized TiO₂ and ZnO NPs catalysts.

K_{app} (min^{-1}) is the observed first-order rate constant. In the early stage of the reaction (i.e., up to 30 min), MG degradation is found to follow first-order kinetics according to the equation. This empirical equation has been used from common first-order kinetics and proposed for the simple description of the decay process [31]. The plot of $\ln(C_0/C)$ with irradiation time is shown in Figure 7 where the slopes represent the apparent rate constant for degradation of MG dye. The apparent rate constants of TiO₂ and ZnO catalysts are given in Table 1. Here, we found that TiO₂ NPs have higher apparent rate constant than other ZnO NPs; this is due to TiO₂ having wide bandgap and highly sensitivity to UV radiations, as can be seen in Figure 5. The bandgap value of anatase TiO₂ is around 3.2 eV, which enables UV light of wavelengths smaller than 400 nm to activate the catalyst [32].

4. Conclusions

In this study, synthesis of uniform size TiO₂ and ZnO nanoparticles was achieved using microwave synthesis which is considered to be a green, efficient, and cost-effective method having potential for large-scale synthesis. Photocatalytic properties of synthesized TiO₂ and ZnO nanoparticles were studied which shows that TiO₂ and ZnO nanoparticles have 49.35% and 23.31% photodegradation efficiency, respectively, for MG dye under UV light. TiO₂ nanoparticles show more than two-order photodegradation property for MG dye as compared to ZnO.

Acknowledgments

The authors are thankful to the director of ARDE, Pashan, Pune, for granting permission to publish this work. Thanks are also due to the Department of Physics, University of Pune, for SEM and XRD of samples.

References

- [1] P. Borker and A. V. Salker, "Photocatalytic degradation of textile azo dye over Ce_{1-x}Sn_xO₂ series," *Materials Science and Engineering B*, vol. 133, pp. 55–60, 2006.
- [2] C. C. Chen, C. S. Lu, Y. C. Chung, and J. L. Jan, "UV light induced photodegradation of malachite green on TiO₂ nanoparticles," *Journal of Hazardous Materials*, vol. 141, no. 3, pp. 520–528, 2007.
- [3] A. Fujishima, T. N. Rao, and D. A. Tryk, "Titanium dioxide photocatalysis," *Journal of Photochemistry and Photobiology C*, vol. 1, pp. 1–21, 2000.
- [4] C. Kormann, D. W. Bahnemann, and M. R. Hoffmann, "Photolysis of chloroform and other organic molecules in aqueous TiO₂ suspensions," *Environmental Science and Technology*, vol. 25, no. 3, pp. 494–500, 1991.
- [5] J. Peral and D. F. Ollis, "Heterogeneous photocatalytic oxidation of gas-phase organics for air purification: acetone, 1-butanol, butyraldehyde, formaldehyde, and m-xylene oxidation," *Journal of Catalysis*, vol. 136, no. 2, pp. 554–565, 1992.
- [6] S. Chakrabarti and B. K. Dutta, "Photocatalytic degradation of model textile dyes in waste water using ZnO as semiconductor catalyst," *Journal of Hazardous Materials B*, vol. 112, pp. 269–278, 2004.
- [7] G. P. Fotou and S. E. Pratsinis, "Photocatalytic destruction of phenol and salicylic acid with aerosol-made and commercial titania powders," *Chemical Engineering Communications*, vol. 151, pp. 251–269, 1996.
- [8] M. L. Curridal, R. Comparelli, P. D. Cozzli, G. Mascolo, and A. Agostiano, "Colloidal oxide nanoparticles for the photocatalytic degradation of organic dye," *Materials Science and Engineering C*, vol. 23, no. 1-2, pp. 285–289, 2003.
- [9] S. B. Park and Y. C. Kang, "Photocatalytic activity of nanometer size ZnO particles prepared by spray pyrolysis," *Journal of Aerosol Science*, vol. 28, pp. S473–S474, 1997.
- [10] R. Y. Hong, T. T. Pan, J. Z. Qian, and H. Z. Li, "Synthesis and surface modification of ZnO nanoparticles," *Chemical Engineering Journal*, vol. 119, no. 2-3, pp. 71–81, 2006.
- [11] Y. J. Jang, C. Simer, and T. Ohm, "Comparison of zinc oxide nanoparticles and its nano-crystalline particles on the photocatalytic degradation of methylene blue," *Materials Research Bulletin*, vol. 41, no. 1, pp. 67–77, 2006.
- [12] B. Neppolian, H. C. Choi, S. Sakthivel, B. Arabindoo, and V. Murugesan, "Solar/UV-induced photocatalytic degradation of three commercial textile dyes," *Journal of Hazardous Materials B*, vol. 89, no. 2-3, pp. 303–317, 2002.
- [13] Y. Zhang, F. Zhu, J. Zhang, and L. Xia, "Converting layered zinc acetate nanobelts to one-dimensional structured ZnO nanoparticle aggregates and their photocatalytic activity," *Nanoscale Research Letters*, vol. 3, no. 6, pp. 201–204, 2008.
- [14] M. Zhang, G. Sheng, J. Fu, T. An, X. Wang, and X. Hu, "Novel preparation of nanosized ZnO–SnO₂ with high photocatalytic activity by homogeneous co-precipitation method," *Materials Letters*, vol. 59, no. 28, pp. 3641–3644, 2005.
- [15] C. Wang, X. Wang, B. Q. Xu et al., "Enhanced photocatalytic performance of nanosized coupled ZnO/SnO₂ photocatalysts for methyl orange degradation," *Journal of Photochemistry and Photobiology A*, vol. 168, no. 1-2, pp. 47–52, 2004.
- [16] W. Cun, Z. Jincai, W. Xinming et al., "Preparation, characterization and photocatalytic activity of nano-sized ZnO/SnO₂ coupled photocatalysts," *Applied Catalysis B*, vol. 39, no. 3, pp. 269–279, 2002.

- [17] A. Kajbafvala, H. Ghorbani, A. Paravar, J. P. Samberg, E. Kajbafvala, and S. K. Sadrnezhad, "Effects of morphology on photocatalytic performance of Zinc oxide nanostructures synthesized by rapid microwave irradiation methods," *Superlattices and Microstructures*, vol. 51, no. 4, pp. 512–522, 2012.
- [18] N. Serpone and E. Pelizzetti, Eds., *Photocatalysis: Fundamentals and Applications*, Wiley, New York, NY, USA, 1989.
- [19] A. K. Singh, "Synthesis, characterization, electrical and sensing properties of ZnO nanoparticles," *Advanced Powder Technology*, vol. 21, pp. 609–613, 2010.
- [20] J. Wang, J. Polleux, J. Lim, and B. Dunn, "Pseudocapacitive contributions to electrochemical energy storage in TiO₂ (anatase) nanoparticles," *Journal of Physical Chemistry C*, vol. 111, no. 40, pp. 14925–14931, 2007.
- [21] T. Sugimoto, X. Zhou, and A. Muramatsu, "Synthesis of uniform anatase TiO₂ nanoparticles by gel-sol method: 3. Formation process and size control," *Journal of Colloid and Interface Science*, vol. 259, no. 1, pp. 43–52, 2003.
- [22] J. Tang, F. Redl, Y. Zhu, T. Siegrist, L. E. Brus, and M. L. Steigerwald, "An organometallic synthesis of TiO₂ nanoparticles," *Nano Letters*, vol. 5, no. 3, pp. 543–548, 2005.
- [23] S. Jeon and P. V. Braun, "Hydrothermal synthesis of Er-doped luminescent TiO₂ nanoparticles," *Chemistry of Materials*, vol. 15, no. 6, pp. 1256–1263, 2003.
- [24] S. K. Sahoo, M. Mohapatra, A. K. Singh, and S. Anand, "Hydrothermal synthesis of single crystalline nano CeO₂ and its structural, optical, and electronic characterization," *Materials and Manufacturing Processes*, vol. 25, no. 9, pp. 982–989, 2010.
- [25] A. K. Singh, "Microwave synthesis, optical, structural and magnetic properties of ZnO/Mn doped ZnO nanostructures," *Journal of Optoelectronics and Advanced Materials*, vol. 12, pp. 2255–2260, 2010.
- [26] P. Periyat, N. Leyland, D. E. McCormack, J. Colreavy, D. Corr, and S. C. Pillai, "Rapid microwave synthesis of mesoporous TiO₂ for electrochromic displays," *Journal of Materials Chemistry*, vol. 20, no. 18, pp. 3650–3655, 2010.
- [27] A. Kajbafvala, J. P. Samberg, H. Ghorbani, E. Kajbafvala, and S. K. Sadrnezhad, "Effects of initial precursor and microwave irradiation on step-by-step synthesis of zinc oxide nanoarchitectures," *Materials Letters*, vol. 67, no. 1, pp. 342–345, 2012.
- [28] H. Kumazawa, M. Inoue, and T. Kasuya, "Photocatalytic degradation of volatile and nonvolatile organic compounds on titanium dioxide particles using fluidized beds," *Industrial and Engineering Chemistry Research*, vol. 42, no. 14, pp. 3237–3244, 2003.
- [29] P. B. Bagdare, S. B. Patil, and A. K. Singh, "Phase evolution and PEC performance of Zn_xCd_(1-x)S nanocrystalline thin films deposited by CBD," *Journal of Alloys and Compounds*, vol. 506, no. 1, pp. 120–124, 2010.
- [30] S. Ghasemi, S. Rahimnejad, S. Rahman Setayesh, S. Rohani, and M. R. Gholami, "Transition metal ions effect on the properties and photocatalytic activity of nanocrystalline TiO₂ prepared in an ionic liquid," *Journal of Hazardous Materials*, vol. 172, no. 2–3, pp. 1573–1578, 2009.
- [31] G. Mascolo, R. Comparelli, M. L. Curri, G. Lovecchio, A. Lopez, and A. Agostiano, "Photocatalytic degradation of methyl red by TiO₂: comparison of the efficiency of immobilized nanoparticles versus conventional suspended catalyst," *Journal of Hazardous Materials*, vol. 142, no. 1–2, pp. 130–137, 2007.
- [32] A. H. C. Chan, C. K. Chan, J. P. Barford, and J. F. Porter, "Solar photocatalytic thin film cascade reactor for treatment of benzoic acid containing wastewater," *Water Research*, vol. 37, no. 5, pp. 1125–1135, 2003.

Research Article

Rapid Green Synthetic Protocol for Novel Trimetallic Nanoparticles

B. Karthikeyan and B. Loganathan

Department of Chemistry, Annamalai University, Annamalai Nagar, Tamil Nadu 608 002, India

Correspondence should be addressed to B. Karthikeyan; bkarthi_au@yahoo.com

Received 31 December 2012; Accepted 16 January 2013

Academic Editor: Hamed Bahmanpour

Copyright © 2013 B. Karthikeyan and B. Loganathan. This is an open access article distributed under the Creative Commons Attribution License, which permits unrestricted use, distribution, and reproduction in any medium, provided the original work is properly cited.

Metallic nanocomposites and nanotubes can be rapidly prepared under microwave irradiation (MW) from an aqueous solution of metallic precursors in the presence of trisodium citrate as a reductant. For the nanotubes nanoparticles are stabilized by poly(N-vinyl-2-pyrrolidone) (PVP), a protecting agent. PVP is a typical capping and structure-directing agent used for the synthesis of various metallic nanostructures. In this work, we have demonstrated for the first time an MW irradiation approach for the synthesis of trimetallic nanocomposites and nanotubes. The resulting nanohybrids were characterized by UV-Vis spectroscopic analysis, high-resolution scanning electron microscopy (HR-SEM), energy dispersive X-ray spectroscopic analysis (EDX), and X-ray diffractometer (XRD) techniques.

1. Introduction

Over the past decade there has been an increased emphasis on the topic of green chemistry and chemical processes [1]. Colloidal metallic nanoparticles are emerging as an important family of multifunctional nanoscale materials that assist diverse applications in various fields [2–7]. For these essential applications, a variety of preparation routes have been reported for the syntheses of metallic nanosized particles. In order to increase the efficiency of Pt-based bimetallic and trimetallic nanoparticles catalysts have been prepared [8, 9]. Because, in usual metal catalysts, addition of other element can often improve the catalytic activity and selectivity, from the same viewpoint bimetallic and trimetallic nanoparticles are also often investigated. Trimetallic nanoparticles retain an ever greater degree of catalytic activity than the bimetallic and monometallic ones. However, there have been only few reports of trimetallic nanoparticles in the literature. The reported trimetallic nanoparticles were synthesized by only thermal heating method [10–14].

On the other hand, microwave (MW) dielectric heating is fast emerging as a widely accepted rapid processing technology for a variety of synthesis of nanoparticles. In the MW-assisted syntheses of nanoparticles, we found that

MW heating is a rapid technology and it can control the size distribution of the nanoparticles than the conventional heating by thermal convection [15].

In the present work on the preparation of nanosized trimetallic nanocomposites and trimetallic nanotubes from an aqueous solution of corresponding metallic precursors, we have employed trisodium citrate as a reducing agent for the preparation of different combinations of trimetallic nanoparticles and poly(N-vinyl-2-pyrrolidone) (PVP) as a stabilizing agent. Using MW irradiation as a heating source, the rapid, homogeneous, and selective heating in the reaction system at the molecular level for rapid and size-controlled preparation of nanosized particles, which has never been achieved by other conventional methods is reported for the first time.

2. Materials and Methods

2.1. Materials. Hydrogen tetrachloroaurate (III) trihydrate ($\text{HAuCl}_4 \cdot 3\text{H}_2\text{O}$), hydrated hexachloroplatinic (IV) acid ($\text{H}_2\text{PtCl}_6 \cdot 6\text{H}_2\text{O}$), silver nitrate (AgNO_3), Palladium chloride (PdCl_2) trisodium citrate ($\text{C}_6\text{H}_5\text{Na}_3\text{O}_7 \cdot 2\text{H}_2\text{O}$), poly(N-vinyl-2-pyrrolidone) (PVP; $K = 30$, $M_w = 40000$), and

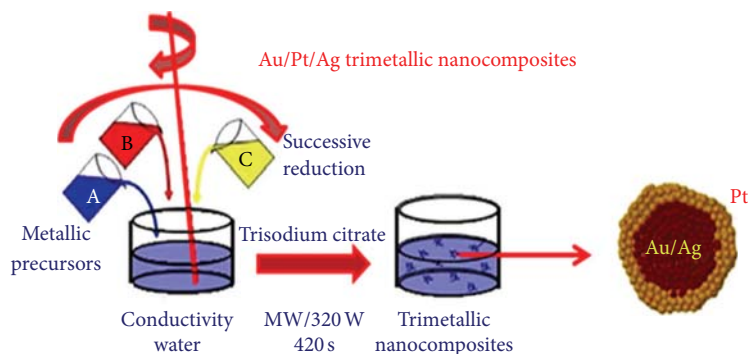


FIGURE 1: MW irradiation method for the preparation of Au-Pt-Ag trimetallic nanoparticles.

all other chemicals used were of analytical grade and the chemicals were purchased from HiMedia Laboratories Pvt. Ltd. (Mumbai, India). All chemicals were used as received without further purification. Conductivity water was used in all experiments.

2.2. Synthesis of Trimetallic Nanoparticles. The Au-Pt-Ag trimetallic nanocomposites and Au-Pd-Pt trimetallic nanotubes are prepared by MW irradiation method. This procedure was carried out in an MW oven (LG Grill, Intellrowave, 160–800 W, consumption 800 W, output power 320 W, and frequency 2450 MHz) operating in a cyclic mode (ON 15 s, OFF 5 s) to prevent intense boiling of sol as well as aggregation. As synthesized trimetallic nanoparticles were sonicated in a Fast Clean-Ultrasonicator.

2.2.1. Synthesis of Au-Pt-Ag Trimetallic Nanocomposites. Citrate-stabilized Au nanoparticles were prepared according to the reported method by us [16]. Briefly, 10 mL of aqueous 0.1% $\text{HAuCl}_4 \cdot 3\text{H}_2\text{O}$ was heated to a boiling and 2 mL of 1% trisodium citrate was then added with stirring. The reaction mixture was heated for 4 min (240 sec) and cooled to room temperature. The solution was turned to vivid magenta from slight yellow, indicating the formation of Au nanoparticles. 10 mL of 0.1% $\text{H}_2\text{PtCl}_6 \cdot 6\text{H}_2\text{O}$ was then added to the Au nanoparticles followed by the addition of 2 mL 1% trisodium citrate with stirring. Finally 10 mL of 0.1% AgNO_3 was added into the Au/Pt nanoparticles. The overall reaction time for the preparation of trimetallic nanocomposites are 420 sec. Then the prepared sol was sonicated for 1 hr.

2.2.2. Synthesis of Au-Pd-Pt Trimetallic Nanotubes. In atypical synthesis of Pd containing trimetallic nanotubes, 45 mL of aqueous 1.20 mM $\text{HAuCl}_4 \cdot 3\text{H}_2\text{O}$ was heated to a boil and 2 mL of 1% trisodium citrate was then added with stirring. The reaction mixture was heated for 4 min (240 s) and cooled to room temperature. The solution was turned to vivid magenta from slight yellow, indicating the formation of Au nanoparticles. 3 mL of 1% PVP was then added to the solution and stirred at room temperature overnight. The prepared sol was sonicated for 40 min. Deaerated aqueous PdCl_2 (2.0 mL of 35 mM) was added to PVP-stabilized Au nanoparticles, with stirring under nitrogen atmosphere

(3 min). After 15 min 2.0 mL of a 1% trisodium citrate solution was again added dropwise to the solution with constant stirring. The vivid magenta coloured solution turned brown indicating the formation of nano-Pd on the PVP-stabilized Au nanoparticles. The stirring was continued for an additional 3 hr. Then 2.0 mL of 20 mM $\text{H}_2\text{PtCl}_6 \cdot 6\text{H}_2\text{O}$ was added and the solution was stirred for another 2 hr at room temperature. Finally the prepared Au-Pd-Pt sol was sonicated for 1 hr to get the fine dispersion of nanoparticles.

2.3. Characterization of Nanoparticles. UV-vis (ultraviolet and visible light) absorbance spectra were measured over a range of 200–800 nm with a Shimadzu UV-1650PC recording spectrometer using a quartz cell with 10 mm of optical path length. High-resolution scanning electron microscopy (HR-SEM), elementary dispersive X-ray analysis (EDX) experiments were carried out on a FEI Quanta FEG 200 instrument with EDX analysis facility at 25°C. Wide-angle powder X-ray diffraction (XRD) pattern was recorded with an XPERT-PRO diffractometer equipped with monochromatic $\text{Cu K}\alpha$ radiation by using a step scan programme.

3. Results and Discussion

The MW irradiation method for the preparation of Au-Pt-Ag trimetallic nanocomposites and Au-Pd-Pt trimetallic nanotubes is shown in Figures 1 and 2. From the viewpoint of sequential electron transfer [17], we chose the combination of the trimetals. The ionization potentials of Au, Pt, Ag, and Pd are known to be 9.225, 8.620, 7.576, and 8.340 eV, respectively. Ionization energy of the corresponding bulk metals is also shown for the comparison in Figure 3 [18].

3.1. UV-Vis Spectral Studies

3.1.1. Au-Pt-Ag Trimetallic Nanocomposites. The absorbance spectrum of the sols containing various nanoparticles for the comparison has been given in Figure 4. The absorbance studies have been carried out after ensuring complete reduction of the metal ions based on the kinetics of reduction of individual metal ions. Absorbance spectra corresponding to the individual Au, Pt, and Ag nanoparticles are also given

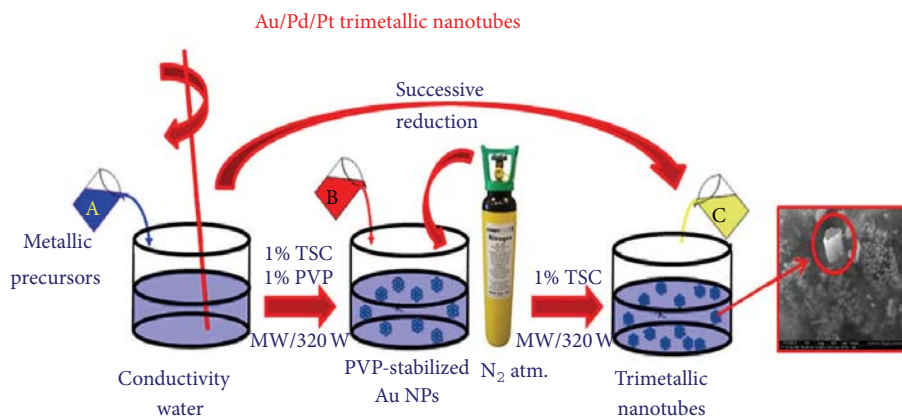


FIGURE 2: MW irradiation method for the preparation of Au-Pd-Pt trimetallic nanotubes.

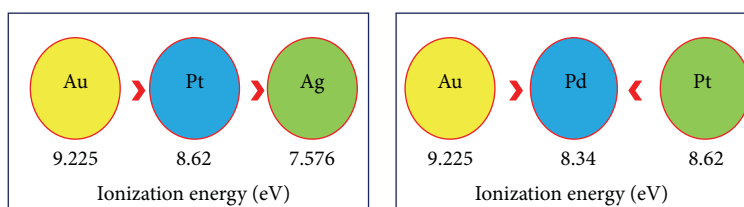


FIGURE 3: Ionization energy of the corresponding bulk metals.

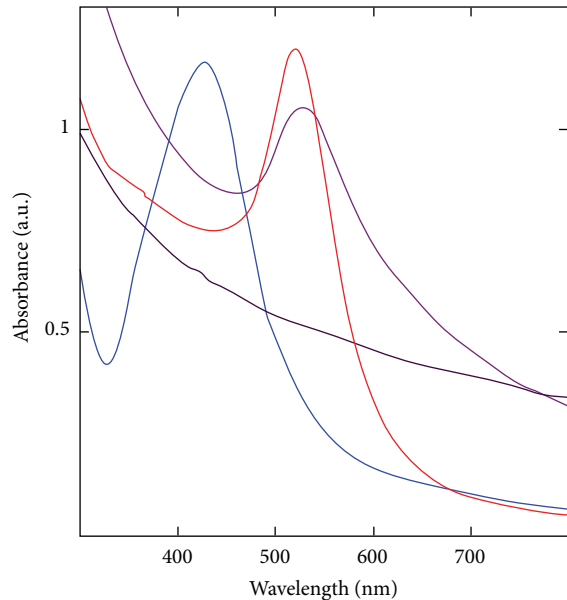


FIGURE 4: UV-vis spectrum of the colloidal dispersion of polymer protected Au nanoparticles.

for comparison. The absorption peak at 530 nm and 430 nm can be attributed to the surface plasmon absorption of Au and Ag nanoparticles (note that Pt colloids do not have an individual visible absorbance). The absence of peaks at 310 nm, characteristic of unreduced Au (III) ion, and peaks at

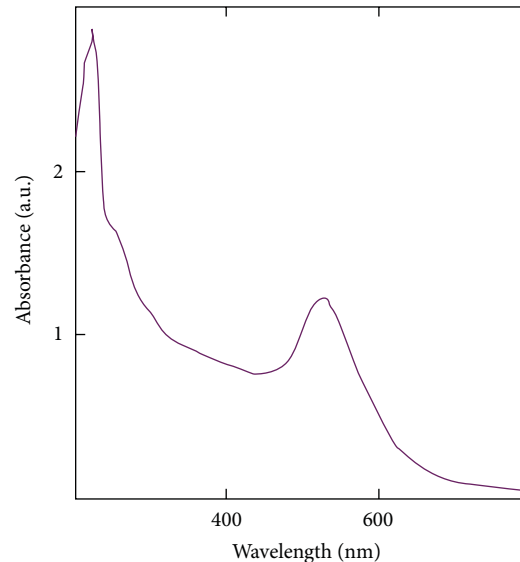


FIGURE 5: UV-vis spectrum of the colloidal dispersion of polymer protected Au nanoparticles.

378, 460 nm indicates the complete reduction of Pt (IV) ion [19]. But, in the case of Au-Pt-Ag trimetallic nanocomposites, a clear single absorbance at 528 nm was attributed to the surface plasmon resonance of trimetallic nanoparticles. The absence of multiple bands in the spectrum also rules out the presence of individual Au, Pt, and Ag nanoparticles in the dispersion [16].

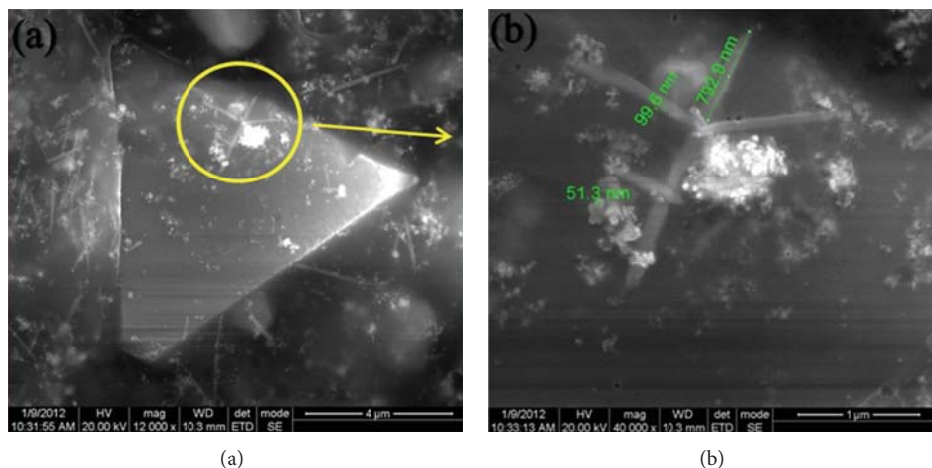


FIGURE 6: A typical HR-SEM image of Au-Pt-Ag trimetallic nanocomposites. Magnifications at (a) 12000x (20 kV) and (b) 20000x (20 kV). Scale bars (a) 4 μm and (b) 1 μm .

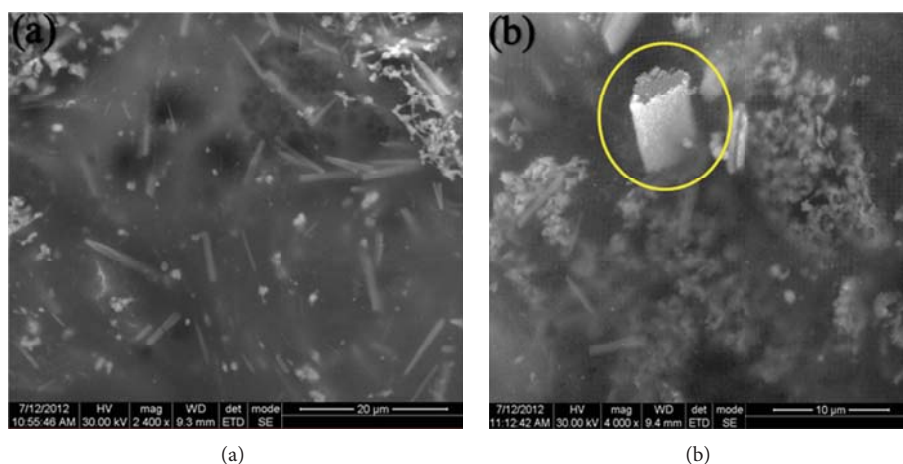


FIGURE 7: A typical HR-SEM image of Au-Pd-Pt trimetallic nanotubes. Magnifications at (a) 2400x (30 kV) and (b) 7000x (30 kV). Scale bars (a) 20 μm and (b) 10 μm .

3.1.2. Au-Pd-Pt Trimetallic Nanotubes. Figure 5 shows the UV-Vis spectrum of the colloidal dispersion of polymer protected Au nanoparticles (note that Pd and Pt colloids do not have an individual visible absorbance). A clear surface plasmon absorbance peak which appeared at 528 nm is corresponding to the presence of Au nanoparticles and the vivid magenta in colour sol also indicating the presence of Au nanoparticles.

3.2. High-Resolution Scanning Electron Microscopic (HR-SEM) Studies

3.2.1. Au-Pt-Ag Trimetallic Nanocomposites. HR-SEM images indicate that the particles are nearly nanowires (Au) and nanocomposite (Ag-Pt) structure, the length of the nanowire is 792 nm and the width is 99 and 51 nm (Figure 6(b)). From Figure 6(a), it is inferred that the nanocomposites are not well dispersed as individual nanoparticles and showed Au nanowires and Ag-Pt bimetallic nanoparticles. The length

and width of the nanoparticles (Figure 6(b)) are indicated on the shape of the nanoparticles.

3.2.2. Au-Pd-Pt Trimetallic Nanotubes. Figure 7 shows HR-SEM images of as-synthesized Au-Pd-Pt trimetallic nanotubes. HR-SEM investigation clearly reveals that the nanoparticles were uniformly having nanotube shape. The length of the nanotube is 141 nm (Figure 7(b)) and width of that one is 152 nm.

3.3. Energy Dispersive X-Ray Microanalysis (EDX). One of the most revealing analytical methods for the composition of trimetallic nanoparticle is energy dispersive X-ray spectroscopy (EDX). Figures 8 and 9 show the EDX elemental analysis of as-synthesized Au-Pt-Ag trimetallic nanocomposites and Au-Pd-Pt trimetallic nanotubes. All the K and L emission peaks for trimetals are observed. The carbon and copper peaks are due to the HR-SEM holding grid. No other obvious peak attributable to impurity is detected.

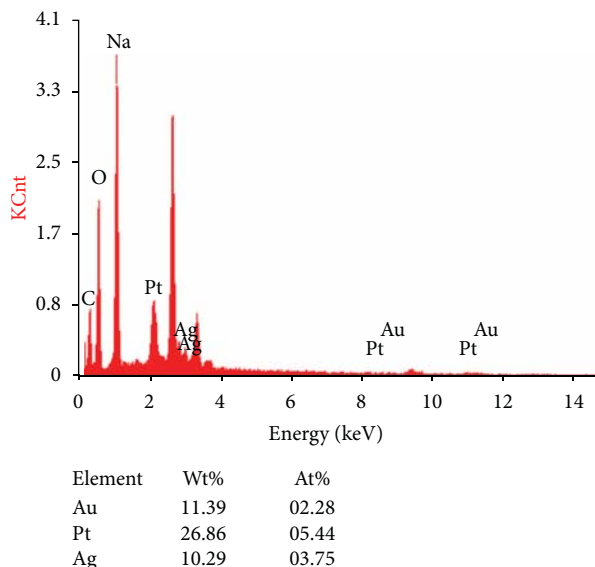


FIGURE 8: EDX elemental data of Au-Pt-Ag trimetallic nanocomposites.

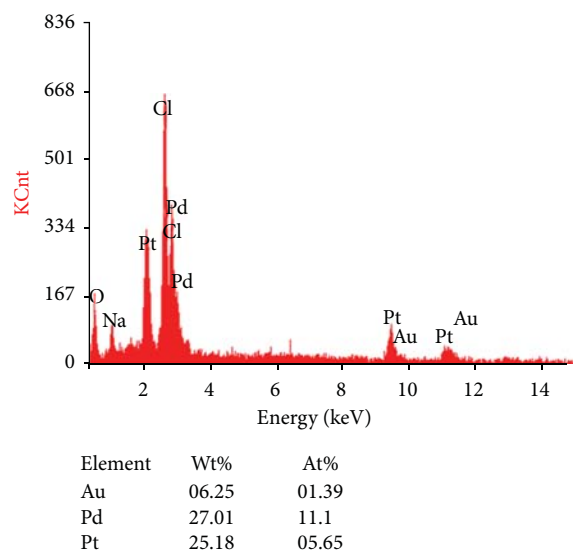


FIGURE 9: EDX elemental data of Au-Pd-Pt trimetallic nanotubes.

This result indicates that as-synthesized product is composed of high purity trimetallic nanoparticles. The carbon and oxygen signals were most likely due to the reducing agents on the surface of the prepared nanoparticles. EDX analysis of Au-Pt-Ag trimetallic nanocomposites gave weight of 11.39% Au, 26.86% Pt, and 10.23% Ag in the sample. It indicated the formation of trimetallic nanocomposites in the ratio of 1:3:1. For Au-Pd-Pt trimetallic nanotubes EDX analysis gave 6.25% Au, 25.18% Pd, and 27.01% Pt. It indicated the formation of trimetallic nanotubes in the ratio of 1:4:4. From the above results, the maximum percentage of Pt nanoparticles is present on the surface of Au-Pt-Ag trimetallic nanocomposites and Pd and Pt nanoparticles are present on the surface of as-synthesised Au-Pd-Pt trimetallic nanotubes.

3.4. XRD Studies. The diffractograms of the trimetallic combinations generally show broad bands while their monometallic counterparts exhibit fairly sharp bands [19]. The particle sizes of the trimetallic combinations determined from the XRD spectra correlate well with the sizes obtained from HR-SEM measurements. The particle size is calculated based on the Scherrer's equation:

$$D = \frac{K\lambda}{\beta_s \cos \theta}, \quad (1)$$

where D corresponds to the particle size, K is the shape-dependent Scherrer's constant, λ is the wavelength of radiation, β_s is the full peak width at half-maximum (FWHM) of the peak, and θ is the Bragg diffraction angle [20].

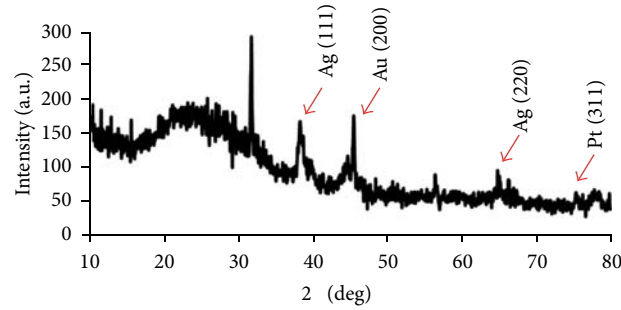


FIGURE 10: Wide-angle XRD pattern of Au-Pt-Ag trimetallic nanocomposites.

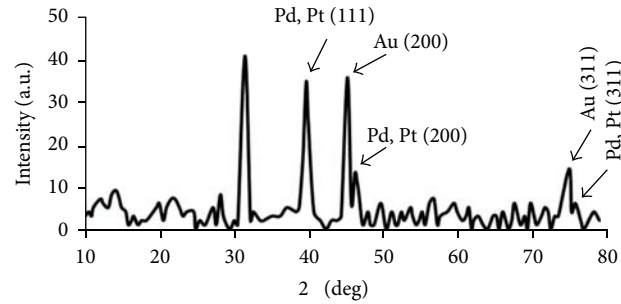


FIGURE 11: Wide-angle XRD pattern of Au-Pd-Pt trimetallic nanotubes.

3.4.1. Au-Pt-Ag Trimetallic Nanocomposites. Figure 10 shows the XRD of Au-Pt-Ag trimetallic nanocomposites. The diffraction patterns indicate a broad diffraction peak (2θ about 45.4°) corresponding to (2 0 0) reflection. This suggested that the prepared particles have a very small size and a face-centered cubic (fcc) structure. The XRD also indicated the reflection peak that appears at 38.12° (2θ) corresponds to the (1 1 1) crystallographic plane and the peak at 64.83° (2θ) corresponds to the (2 2 0) plane. The diffractograms show that (3 1 1) crystallographic surface is marked for Pt ($2\theta = 75.29^\circ$). The above crystalline data are verified by JCPDS card number of Au, Pt, and Ag. Table 1 shows the crystalline sizes of nanoparticles and identification of nanoparticles present in trimetallic nanocomposites.

3.4.2. Au-Pd-Pt Trimetallic Nanotubes. Figure 11 shows the XRD pattern of Au-Pd-Pt trimetallic nanotubes. The wide-angle XRD pattern showed randomly oriented fcc crystals. A diffraction peak which appeared at $2\theta = 45.17^\circ$ and 75.02° corresponds to Au (2 0 0) and Au (3 1 1) planes. The XRD also indicated that the reflection peaks that appeared at $2\theta = 39.62^\circ$, 46.68° , and 75.32° ascribed to Pd/Pt (1 1 1), Pd/Pt (2 0 0), and Pd/Pt (3 1 1) planes. Owing to the lattice mismatch factor [21], it was very difficult to resolve the peaks for Pd and Pt in the XRD pattern, whereas the peaks of Au and Pd/Pt could be readily distinguished by XRD. Table 2 shows the crystalline sizes of nanoparticles and the identification of nanoparticles present in trimetallic nanotubes. From all of

TABLE 1: The crystalline sizes of nanoparticles and identification of nanoparticles present in Au-Pt-Ag trimetallic nanocomposites.

Sl. no.	2 Theta ($^\circ$)	d (Å)	FWHM (deg)	Crystalline size (nm)
1	38.12	2.27293	0.49	3.66
2	45.40	2.00579	0.20	4.25
3	64.83	1.94330	0.79	4.79
4	75.29	1.26514	0.59	7.85

TABLE 2: The crystalline sizes of nanoparticles and identification of nanoparticles present in Au-Pd-Pt trimetallic nanotubes.

Sl. no.	2 Theta ($^\circ$)	d (Å)	FWHM (deg)	Crystalline size (nm)
1	39.62	2.27293	0.500	3.67
2	45.17	2.00579	0.304	4.80
3	46.68	1.94330	0.110	4.33
4	75.02	1.26514	0.310	7.47

the above observation, Au in the prepared Au-Pd-Pt trimetallic nanotubes was confirmed as forming inner core.

3.5. Surface Energy. The surface energy of selected 4d and 5d metals is given in Table 3. In addition to that cohesive energy and atomic radius are also tabulated. From this viewpoint, Pt has more surface energy compared with Au, Ag, and Pd. So, it is one of the reasons for Pt is present on the surface.

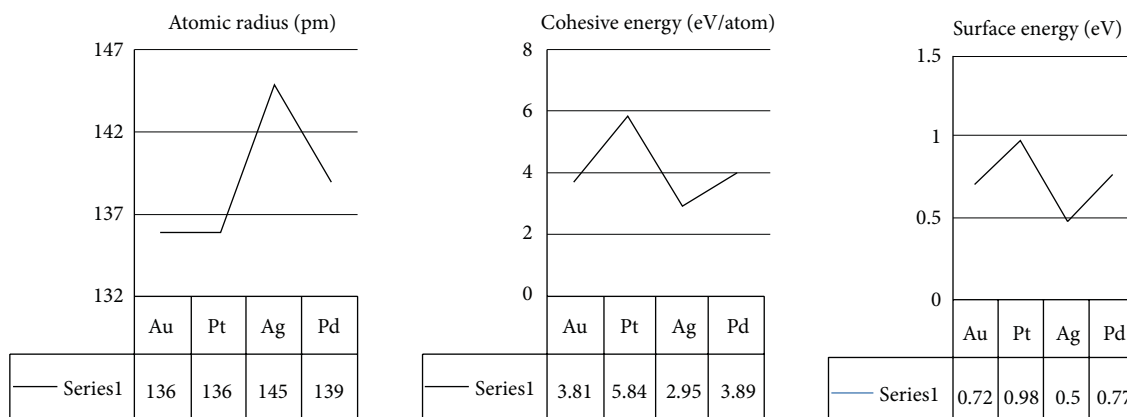


FIGURE 12: Surface energy, cohesive energy, and atomic radius are shown for comparison of Au, Pt, Ag, and Pd metals.

TABLE 3: Surface energy, cohesive energy and atomic radius of the Au, Pt, Ag and Pd metals.

Property	Au	Pt	Ag	Pd
Surface energy	0.72 eV	0.98 eV	0.50 eV	0.77 eV
Cohesive energy	3.81 eV/atom	5.84 eV/atom	2.95 eV/atom	3.89 eV/atom
Atomic radius	136 pm	136 pm	145 pm	139 pm

Surface energy, cohesive energy, and atomic radius are shown for comparison (Figure 12) of Au, Pt, Ag, and Pd metals.

4. Conclusions

In conclusion, for the first time, simple MW-irradiated syntheses of Au-Pt-Ag trimetallic nanocomposites and Au-Pd-Pt trimetallic nanotubes are reported. The UV-visible and HR-SEM confirmed the formation of nanocomposites and nanotube-shaped nanoparticles. EDX analysis confirmed that the percentage of Pt is maximum on the surface of trimetallic nanoparticles and nanotubes. XRD crystal data revealed that the particles are very small in size. The results reported here will inspire the further design of multilayered metallic nanoparticles.

Acknowledgments

The author (B. Karthikeyan) is highly thankful for UGC, New Delhi, for granting a major research project. Electron microscopy was performed at the DSTUNS and SAIF-IIT Madras. XRD data were recorded at the Department of Physics, Alagappa University, Karaikudi. The coauthor (B. Loganathan) is thankful for UGC for the award of BSR-SAP fellowship.

References

- [1] P. Raveendran, J. Fu, and S. L. Wallen, "Completely "green" synthesis and stabilization of metal nanoparticles," *Journal of the American Chemical Society*, vol. 125, no. 46, pp. 13940–13941, 2003.
- [2] M. R. Buck, J. F. Bondi, and R. E. Schaak, "A total-synthesis framework for the construction of high-order colloidal hybrid nanoparticles," *Nature Chemistry*, vol. 4, no. 1, pp. 37–44, 2012.
- [3] C. Xu, J. Xie, D. Ho et al., "Au-Fe₃O₄ dumbbell nanoparticles as dual-functional probes," *Angewandte Chemie International Edition*, vol. 47, pp. 173–176, 2008.
- [4] J. Choi, Y. Jun, S. Yeon, H. C. Kim, J. Shin, and J. Cheon, "Biocompatible heterostructured nanoparticles for multimodal biological detection," *Journal of the American Chemical Society*, vol. 128, no. 50, pp. 15982–15983, 2006.
- [5] C. Xu, B. Wang, and S. Sun, "Dumbbell-like au-fe₃O₄ nanoparticles for target-specific platinum delivery," *Journal of the American Chemical Society*, vol. 131, no. 12, pp. 4216–4217, 2009.
- [6] H. Yin, C. Wang, H. Zhu, S. H. Overbury, S. Sun, and S. Dai, "Colloidal deposition synthesis of supported gold nanocatalysts based on Au-Fe₃O₄ dumbbell nanoparticles," *Chemical Communications*, no. 36, pp. 4357–4359, 2008.
- [7] T. Mokari, E. Rothenberg, I. Popov, R. Costi, and U. Banin, "Selective growth of metal tips onto semiconductor quantum rods and tetrapods," *Science*, vol. 304, no. 5678, pp. 1787–1790, 2004.
- [8] B. Karthikeyan and M. Murugavelu, "Nano bimetallic Ag/Pt system as efficient opto and electrochemical sensing platform towards adenine," *Sensors and Actuators B: Chemical*, vol. 163, no. 1, pp. 216–223, 2012.
- [9] S. Patra and H. Yang, "Synthesis of trimetallic Au@Pb@Pt core-shell nanoparticles and their electrocatalytic activity toward formic acid and methanol," *Bulletin of the Korean Chemical Society*, vol. 30, no. 7, pp. 1485–1488, 2009.
- [10] H. Zhang, M. Okumura, and N. Toshima, "Stable dispersions of PVP-protected Au/Pt/Ag trimetallic nanoparticles as highly active colloidal catalysts for aerobic glucose oxidation," *Journal of Physical Chemistry C*, vol. 115, no. 30, pp. 14883–14891, 2011.

- [11] P. Venkatesan and J. Santhanalakshmi, "Core-shell bimetallic Au-Pd nanoparticles: synthesis, structure, optical and catalytic properties," *Journal of Nanoscience and Nanotechnology*, vol. 1, pp. 43–47, 2011.
- [12] B. N. Wanjala, J. Luo, R. Loukrakpam et al., "Nanoscale alloying, phase-segregation, and core-shell evolution of gold-platinum nanoparticles and their electrocatalytic effect on oxygen reduction reaction," *Chemistry of Materials*, vol. 22, no. 14, pp. 4282–4294, 2010.
- [13] L. Wang and Y. Yamauchi, "Strategic synthesis of trimetallic Au@Pd@Pt core-shell nanoparticles from poly(vinylpyrrolidone)-based aqueous solution toward highly active electrocatalysts," *Chemistry of Materials*, vol. 23, no. 9, pp. 2457–2465, 2011.
- [14] P. Fang, S. Duan, X. Lin et al., "Tailoring Au-core Pd-shell Pt-cluster nanoparticles for enhanced electrocatalytic activity," *Chemical Science*, vol. 2, no. 3, pp. 531–539, 2011.
- [15] H. Yin, T. Yamamoto, Y. Wada, and S. Yanagida, "Large-scale and size-controlled synthesis of silver nanoparticles under microwave irradiation," *Materials Chemistry and Physics*, vol. 83, no. 1, pp. 66–70, 2004.
- [16] B. Karthikeyan and B. Loganathan, "Strategic green synthesis and characterization of Au/Pt/Ag trimetallic nanocomposites," *Materials Letters*, vol. 85, pp. 53–56, 2012.
- [17] N. Toshima, *Macromolecular Complexes: Dynamic Interactions and Electronic Processes*, edited by E. Tsuchida, Japan Scientific Societies Press, Tokyo, Japan, 1991.
- [18] N. Toshima, "Polymer-assisted composites of trimetallic nanoparticles with a three-layered core-shell structure for catalyses," *Nanohybridization of Organic-Inorganic Materials. Advances in Materials Research*, vol. 13, pp. 55–79, 2009.
- [19] T. Yonezawa and N. Toshima, "Mechanistic consideration of formation of polymer-protected nanoscopic bimetallic clusters," *Journal of the Chemical Society, Faraday Transactions*, vol. 91, no. 22, pp. 4111–4119, 1995.
- [20] D. S. Shenoy, J. Mathew, and D. Philip, "Phytosynthesis of Au, Ag and Au-Ag bimetallic nanoparticles using aqueous extract and dried leaf of *Anacardium occidentale*," *Spectrochimica Acta A: Molecular and Biomolecular Spectroscopy*, vol. 79, no. 1, pp. 254–262, 2011.
- [21] S. E. Habas, H. Lee, V. Radmilovic, G. A. Somorjai, and P. Yang, "Shaping binary metal nanocrystals through epitaxial seeded growth," *Nature Materials*, vol. 6, no. 9, pp. 692–697, 2007.

Research Article

Synthesis of ZnO Nanostructures by Microwave Irradiation Using Albumen as a Template

T. Prakash,¹ R. Jayaprakash,¹ G. Neri,² and Sanjay Kumar³

¹ Nanotechnology Laboratory, Department of Physics, Sri Ramakrishna Mission Vidyalaya College of Arts and Science, Coimbatore, Tamil Nadu 641020, India

² Department of Electronic Engineering, Chemistry and Industrial Engineering, University of Messina, 98166 Messina, Italy

³ Department of Physics, B. R. Ambedkar Bihar University, Muzaffarpur, Bihar 842001, India

Correspondence should be addressed to R. Jayaprakash; jprakash_jpr@rediffmail.com

Received 10 January 2013; Accepted 1 February 2013

Academic Editor: Amir Kajbafvala

Copyright © 2013 T. Prakash et al. This is an open access article distributed under the Creative Commons Attribution License, which permits unrestricted use, distribution, and reproduction in any medium, provided the original work is properly cited.

ZnO nanostructures have been successfully prepared by a microwave irradiation method. The role of albumen as a template in addressing the size and morphology of ZnO has been investigated by X-ray diffraction (XRD), Fourier transform infrared spectroscopy (FT-IR), thermogravimetric analysis (TG-DTA), scanning electron microscopy (SEM), and transmission electron microscopy (TEM) techniques. A heterogeneous mixture of Zn(OH)₂ and ZnO was obtained in absence of albumen. Pure ZnO nanostructures, consisting of rod- and whisker-like nanoparticles embedded in a sheet matrix, were obtained in the presence of albumen. Optical and photoluminescence (PL) properties of the synthesized samples were also compared. Results obtained indicate that the microwave-assisted method is a promising low temperature, cheap, and fast method for the production of ZnO nanostructures.

1. Introduction

Recently, metal oxides which exhibit morphologies at the nanoscale (<100 nm) have become increasingly important. One of them is ZnO, a wide band gap n-type semiconductor (3.37 eV) with large exciton binding energy of (60 meV) at room temperature, which has attracted much attention due to its unique properties. ZnO nanoparticles have found numerous applications, such as in gas sensors [1], transparent electrodes [2], pH sensors [3], biosensors [4], acoustic wave devices [5], and UV photodiodes [6].

Up to now, a number of investigations have focused on the synthesis of nano- and microarchitectures through different methods like hydrothermal [7], sol-gel [8], electrochemical deposition [9], and vapor-phase process [10]. Previous studies on the microwave radiation synthesis of ZnO with a variety of morphologies, such as nanowires [11], nanorods [12], nanoneedles [13], hollow structures, and self-assembled architectures [14], were widely reported.

In this work, we synthesized ZnO nanostructures via a microwave irradiation method in the presence of albumen as a biotemplate. Microwave irradiation as a heating method has found a number of applications in chemistry. The utilization of microwave irradiation in the preparation of nanoparticles has been reported in recent years [15]. Compared to the conventional methods, the microwave synthesis has the advantages of producing small particle size metal oxides with high purity owing to short reaction time [15–19]. Due to the “*in situ*” mode of energy conversion, the microwave heating process is fundamentally different from conventional heating processes. Heat will be generated internally within the material, instead of originating from external sources. By means of this method, many functional materials and compounds with novel structures and properties have been obtained [20]. In recent studies, it has been shown that nanoparticles, such as Co₃O₄ [21], LiMn_{2-x}Cr_xO₄ [22], SnO₂ [23] Ce_{1-x}Gd_xO_{2-1/2x} [24], MgO [25], ZnO [26], and TiO₂ [27], can be prepared by the microwave synthesis process. Though the application

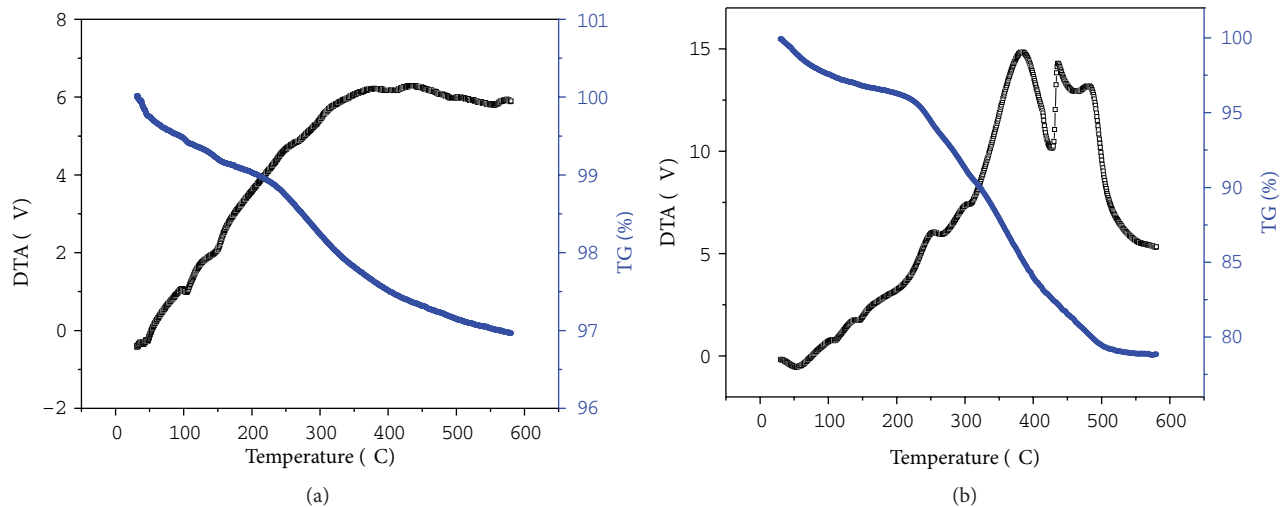


FIGURE 1: TG-DTA analysis of microwave synthesized samples: (a) sample A, (b) sample B.

of microwave irradiation in synthetic chemistry started in 1980s, only in the recent years, its use has provided a new, efficient, and environmentally benign methodology for the synthesis of various metal oxide nanoparticles of diverse morphologies and sizes. These radiations have unique properties like homogenous volumetric heating, which causes heating directly inside the sample, high reaction rate, selectivity, and increased product yield. Moreover, it is an energy saving process [14, 28, 29].

The process here proposed to synthesize ZnO nanostructures by a microwave-assisted process is simple, cheap, and fast and is characterized by a low synthesis temperature (130°C). As compared to conventional heating, microwaves cause the uniform distribution of temperature between the surface and the bulk material thereby leading to the fast formation of ZnO nanoparticles [30, 31]. Another advantage is that no postannealing process is necessary to obtain ZnO crystalline nanometer-sized structures compared to other microwave irradiation methods reported in the literature [32, 33]. To investigate the role of template in the synthesis of ZnO nanostructure by this method, a comparative study has been carried out characterizing the products obtained in the presence or not of albumen as a biotemplate. The ZnO nanostructures obtained were thoroughly characterized through X-ray diffraction (XRD), Fourier transform infrared spectroscopy (FT-IR), thermogravimetric analysis (TG-DTA), scanning electron microscopy (SEM), and transmission electron microscopy (TEM) techniques. Furthermore, their optical properties were assessed by UV-Vis DRS spectra and photoluminescence (PL) measurements.

2. Experimental Procedure

2.1. Materials. Zinc nitrate $Zn(NO_3)_2$ and ammonia solution (NH_4OH) were supplied from (Merk, 98%) Mumbai, India. All the chemicals were of analytical grade and used as received without further purification. The albumen, extracted

from white part of egg, was used for the synthesis. Double distilled water was used through the experiments.

2.2. Synthesis. The synthesis of ZnO nanostructures by the microwave irradiation method was carried out as follows. First, a 0.1M of zinc hydroxyl solution was prepared by dissolving zinc nitrate ($Zn(NO_3)_2$) in deionized water. Then pH of the solution was maintained at 8 by adding liquid ammonia solution dropwise. The resulting product was filtered and washed with double distilled water and ethanol until it became free from impurities. The precipitate was irradiated for 5 minutes in household microwave (radiation frequency 2.45 GHz, Power up to 1KW) with convection mode, giving a white product. Finally the sample was dried at 130°C (sample A) for 5 hours.

The same experimental procedure was followed for the synthesis of ZnO nanostructures carried out in the presence of albumen (sample B), by adding drop by drop 5 mL of freshly extracted albumen, mixed with 25 mL of deionized water and stirred, to 0.1M zinc hydroxyl solution.

2.3. Characterization. The sample microstructure was analyzed by X-ray diffraction (XRD) using a Bruker AXS D8 Advance instrument and the monochromatic $CuK_{\alpha 1}$ wavelength of 1.5406 Å. The average crystalline size of the crystallites was evaluated using Scherrer's formula, $d = K\lambda/\beta \cos \theta$, where d is the mean crystalline size, K is a grain shape dependent constant (0.9), λ is the wavelength of the incident beam, θ is a Bragg reflection angle, and β is the full width at half maximum (FWHM) of the main diffraction peak. The sample morphology was observed by scanning electron microscopy (SEM), using a JEOL 5600LV microscope at an accelerating voltage of 10 kV. High resolution transmission electron microscopy (HRTEM) and selected-area electron diffraction (SAED) were recorded on a Tecnai G20-stwin

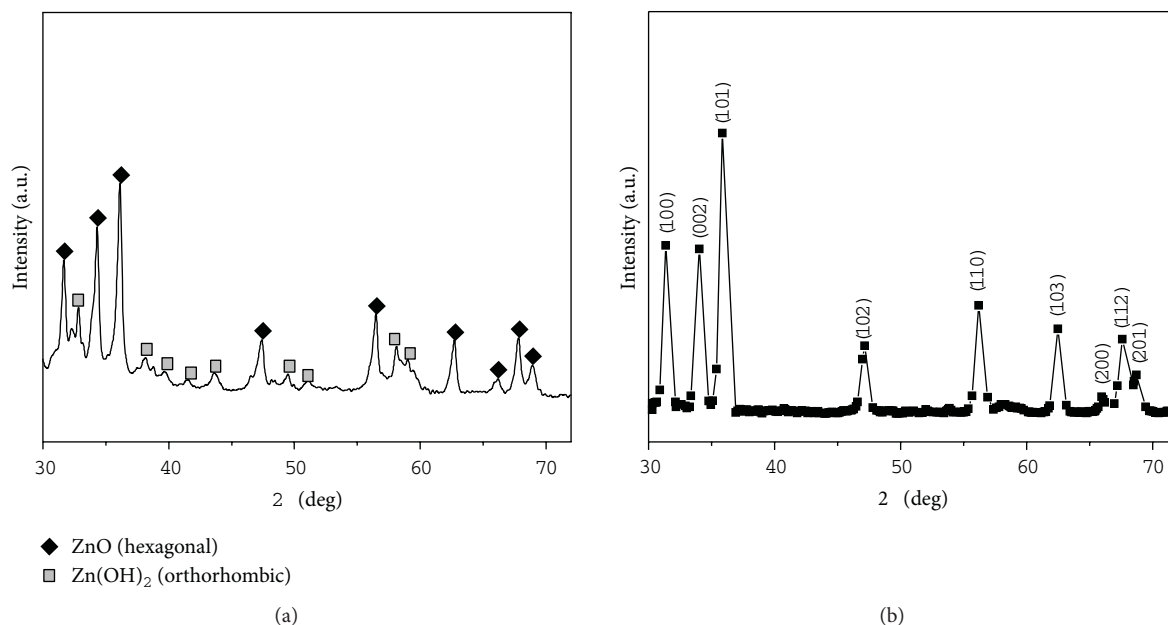


FIGURE 2: XRD analysis of microwave synthesized samples: (a) sample A, (b) sample B.

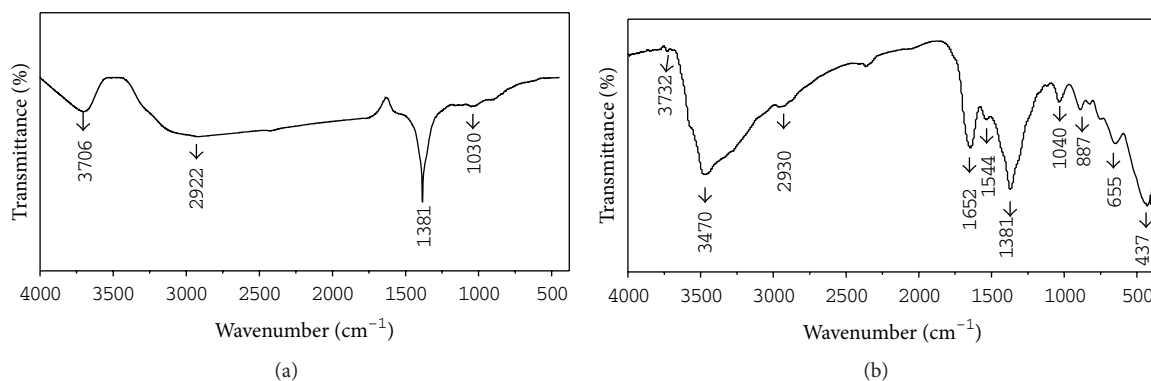


FIGURE 3: FT-IR spectra of microwave synthesized samples: (a) sample A, (b) sample B.

using an accelerating voltage of 200 kV. The Fourier transform infrared spectra (FT-IR) of the samples were recorded by using a Nicolet 5DX FTIR spectrometer. Thermal analysis was carried out by using a thermogravimetric and differential scanning calorimeter apparatus (TG-DSC Netzsch—Model STA 409PC). The analyses were carried out with a heating rate of 10°C/min in static air up to 800°C. The ultraviolet (UV) spectrum of the ZnO samples was recorded on a Perkin Elmer UV-visible DRS spectrophotometer. The room-temperature PL spectrum was performed on a spectrofluorometer instrument (JY Fluorolog-FL3-11).

3. Results and Discussion

3.1. Morphological and Microstructural Analysis

3.1.1. Thermogravimetric Analysis. The thermal behavior of ZnO samples synthesized has been first investigated by TG-DTA. Figure 1(a) shows the TG-DTA curves of sample A.

The weight loss monitored in the range 25–600°C is low and has been calculated to be less than 3.3% in total. This weight loss is ascribed to the removal of adsorbed water molecules and ethanol and the loss of hydroxyl ions. The final step at higher temperature is attributed to the burnout of organic species still remained in the dried powder. By focusing the attention on sample B, TGA indicated that the weight loss is higher (about 20% in total). The first weight loss in the temperature range between 25°C and 150°C is ascribed to the removal of adsorbed water molecules. The second weight loss in the range between 230°C and 520°C comes from the decomposition of the organic template, which is also confirmed by the exothermic peak at about 384°C in the DTA curve.

3.1.2. X-Ray Diffraction. The phase identification of the synthesized ZnO nanostructures was determined by X-ray diffraction (XRD). Figures 2(a) and 2(b) show the XRD

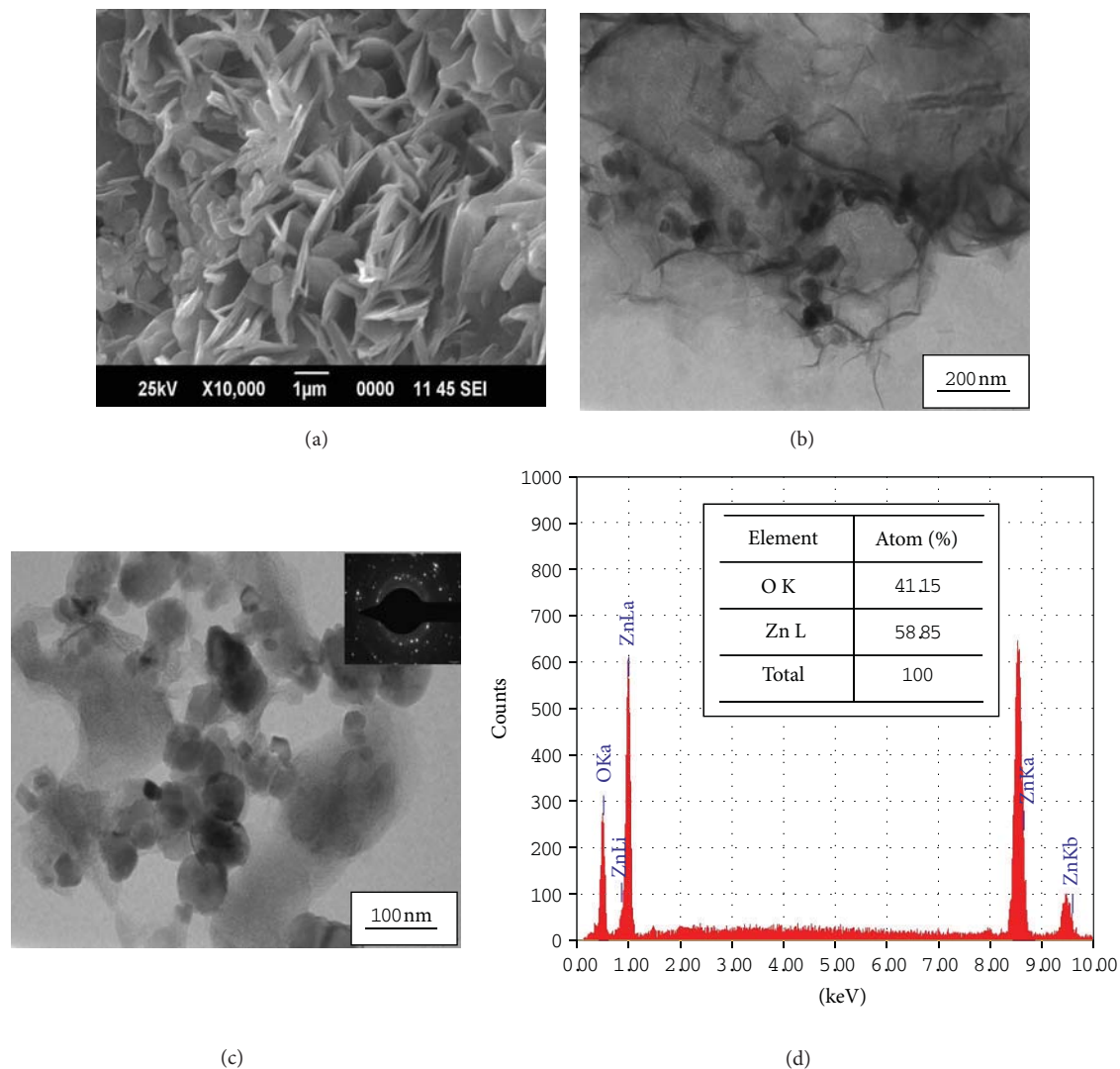


FIGURE 4: SEM and TEM micrographs of sample A. (a) SEM image, (b) and (c) TEM images of the sheet-like and spherical-like ZnO nanostructure, and (d) EDX analysis. Inset in Figure (c) shows the SAED pattern.

patterns of both samples. In Figure 2(a), XRD of sample A indicated that two phases, like ZnO hexagonal wurtzite phase structure (JCPDS number 897102) and $\text{Zn}(\text{OH})_2$ orthorhombic phase structure (JCPDS number 890138), are present. On the basis of diffraction peaks intensity, ZnO is the predominant phase. According to Scherrer's equation, the average particle size of ZnO nanoparticles is about 29 nm.

Figure 2(b) shows the XRD pattern of sample B. The diffraction planes (100), (002), (101), (102), (110), (103), (200), (112), and (201) in the patterns can be perfectly indexed to the hexagonal wurtzite phase structure (JCPDS number 897102). Also no diffraction peaks corresponding to Zn, $\text{Zn}(\text{OH})_2$, and other impurities are observed. The value of lattice parameters ($a = 3.2896 \text{ \AA}$ and $c = 5.2624 \text{ \AA}$), as calculated by the XRD data, is in good agreement with those reported by other authors [33]. The average particle size of ZnO is estimated to be around 14 nm.

XRD analysis indicates that the pure ZnO phase is obtained only in the presence of albumen. Furthermore, the average particle size of ZnO phase is markedly lower. It can be supposed that, in the formation processes in absence of albumen, the zinc hydroxide species was first produced step by step by the reaction between the Zn species and the hydroxyl ions coming from dissociation of hydrated ammonia molecules, and then in a consecutive reaction ZnO nanoparticles are formed. In the presence of template molecules, it appears that this second reaction is strongly promoted; so all initial zinc hydroxide species are transformed into ZnO.

3.1.3. Fourier Transform Infrared Spectroscopy. Figure 3(a) shows the typical FT-IR spectrum of sample A. The broad peak at 3706 cm^{-1} corresponds to the vibrational mode of O-H bond, indicating the presence of zinc hydroxide. The

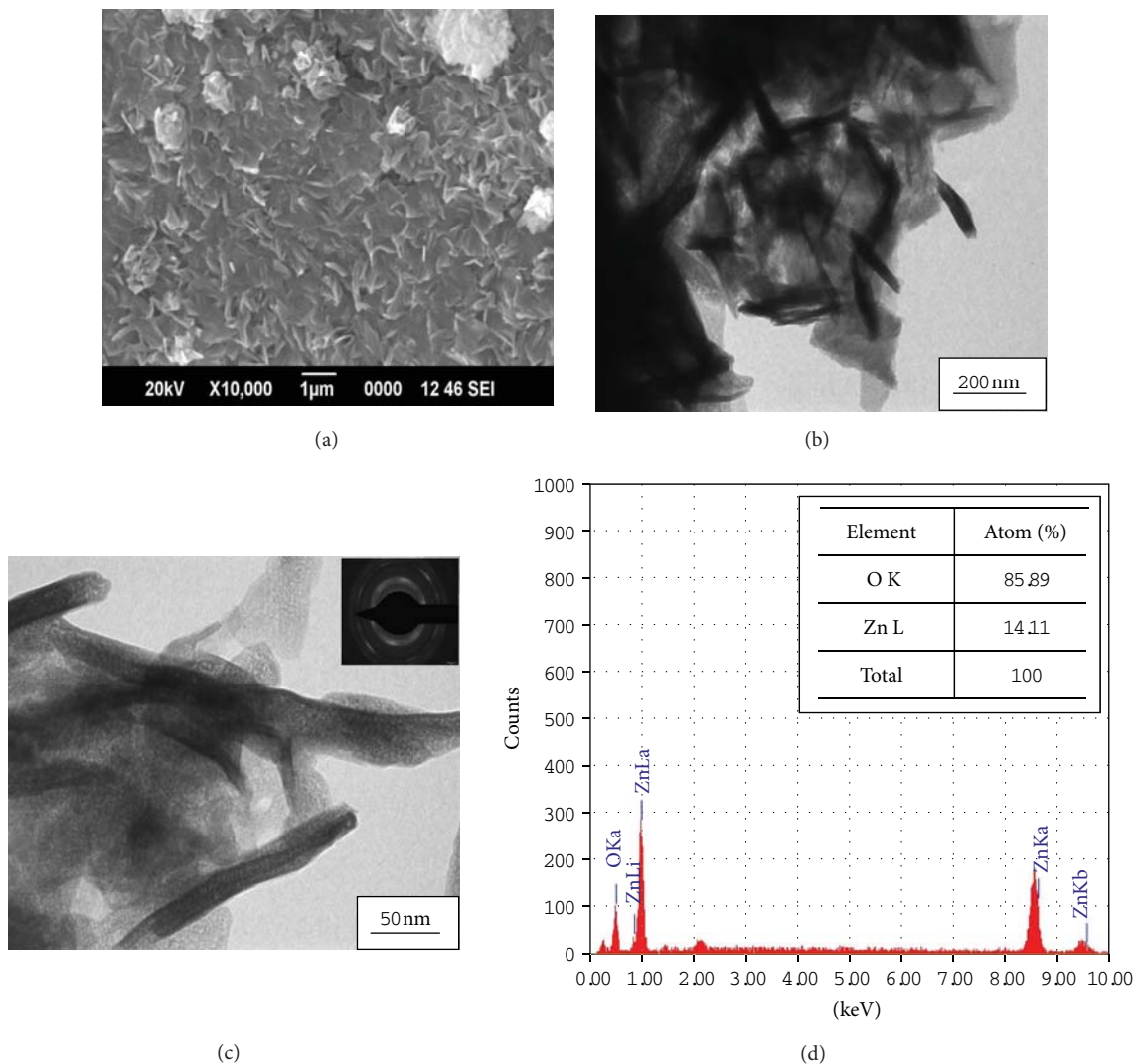


FIGURE 5: SEM and TEM micrographs of sample B. (a) SEM image, (b) and (c) TEM images of the whisker-like and rod-like ZnO nanostructure, and (d) EDX analysis. Inset in Figure (c) shows the SAED pattern.

stretching mode of vibrations in asymmetric and symmetric C=O bonds that is observed at 1381 cm^{-1} is associated with residual organic impurity in the dried powder as suggested by TG-DTA analysis.

In the spectrum of sample B (Figure 3(b)), the appearance of a sharp band at 437 cm^{-1} in the FT-IR spectrum, characteristic for the Zn–O stretching vibration [34], confirms the presence of well-crystallized ZnO. Additionally broad absorption peaks centered at around 3470 cm^{-1} and 1652 cm^{-1} are caused by the O–H stretching of the absorbed water reabsorption during the storage of the sample in ambient air [35]. The absence of features at 3706 cm^{-1} is an indication of the absence of $\text{Zn}(\text{OH})_2$ phase on this sample. In this sample are also seen the signatures of the organic template. The broad peak at 3470 cm^{-1} is in fact due to superimposition of N–H stretching of amide group at 3449 cm^{-1} of the biotemplate and O–H stretching mode of water molecules. Also some of the absorption bands in the

range $1000\text{--}1600\text{ cm}^{-1}$ are due to C=O and C=C stretching vibrational modes of albumen, as well the weak peaks located at 2930 cm^{-1} are due to symmetric and asymmetric C–H bonds, respectively [36]. A very small band originated at 887 cm^{-1} is probably due to the carbonate moieties which are generally observed when FT-IR samples are measured in air [37, 38].

3.1.4. Scanning and Transmission Electron Microscopy. SEM and TEM images of sample A are reported in Figure 4. SEM analysis shows extensive sheet-like nanostructure where spherical-shaped particles are also present. TEM analysis evidences clearly this composite structure and the large diameter distribution of the spherical-shaped nanoparticles. No attempt has been made to assign the two phases present, ZnO and $\text{Zn}(\text{OH})_2$, to each of these nanostructures. The thickness of the sheets and spherical particles is in the range of about 13–50 nm. The SAED pattern taken from one of

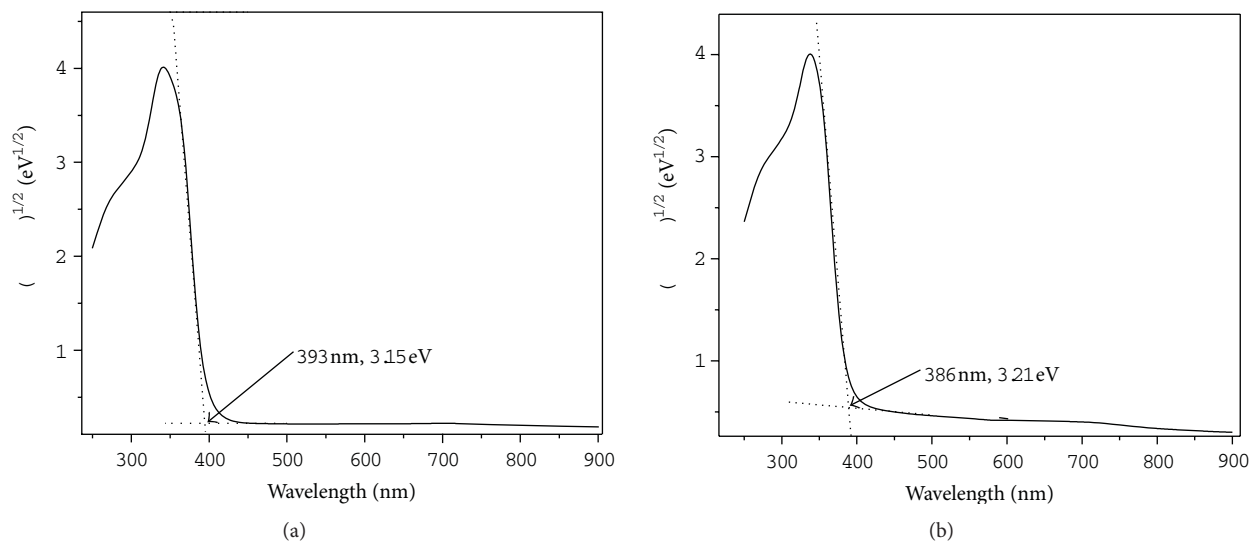


FIGURE 6: UV-Vis DRS of the typical ZnO nanoparticles: (a) sample A, (b) sample B. Extrapolation of the linear portion to the photon energy axis to obtain the E_g value is shown.

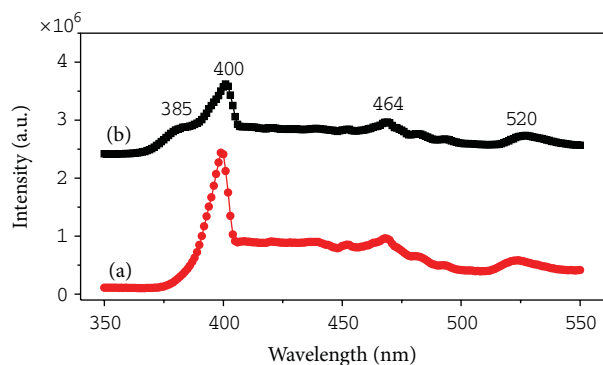


FIGURE 7: PL spectra of (curve a) sample A and (curve b) sample B.

the particles is shown in the inset, and it further confirms the crystalline nature of the sample. In addition, the EDS spectrum of the sample confirms the presence of Zn and O in sample without any other element contamination. The atomic percent ratio of O and Zn in dried sample is 41.15 : 58.85, which might indicate that there is a small content of oxygen vacancy defects on the surface of as-obtained product.

Figure 5 shows SEM and TEM images of sample B. SEM analysis shows that this sample is characterized by a more uniform surface sheet-like nanostructure. TEM analysis revealed the presence of nanowhiskers and nanorods of different length and diameter embedded within the sheet matrix. The thickness of the nanorods and nanowhiskers is in the range of about 10–57 nm. The SAED pattern of ZnO nanostructures further confirms the crystalline nature of the sample. EDS analysis reports that the atomic percent ratio of O and Zn in the dried sample is 85.59 : 14.11, which might indicate that there is a larger content of oxygen on the surface with respect to sample A.

3.2. Optical Properties. In order to determine the precise value of optical band gap UV-visible DRS of the ZnO nanoparticles in samples A and B, we used the optical absorption method on reflectance spectrum. The reflectance values were converted to absorbance by application of the Kubelka-Munk function [39–42]. The Kubelka-Munk theory is generally used for analyzing the diffuse reflectance spectra obtained from weakly absorbing samples. The Kubelka-Munk formula can be expressed by the following relation [43]:

$$K = \frac{(1 - R)^2}{2R}, \quad (1)$$

where K is the reflectance transformed according to Kubelka-Munk and R is the reflectance (%).

The relationship $(k * h\nu)^{1/2} = f(h\nu)$ is shown in Figures 6(a) and 6(b). The E_g value can be obtained by extrapolating the linear portion to the photon energy axis. The reflectance shoulder onset peaks are located at 393 nm and 386 nm corresponding to the band gaps of 3.15 eV and 3.21 eV, respectively. The E_g values are smaller than that of 3.3 eV reported for single crystalline ZnO samples. On comparison with ZnO nanoparticles prepared by other methods, ZnO nanoparticles are obtained by this microwave irradiation method showing larger band gap energy. It is well known that the difference in the band gap is related to the presence of vacancies and dopants [44]. The red shift of the band gap energy also relates to structural morphologies, particle size, and surface microstructures [45]. Then, the higher value of band gap of the sample B synthesized in the presence of albumen can be attributed to a minor amount of defects, due essentially to its more ordered crystalline structure.

The study of the photoluminescence properties is interesting because it can provide valuable information on the quality, purity, and the structural properties of the material. Moreover, recording PL spectrum is of paramount importance for evaluating their optical characteristics for various

applications. The PL spectra of samples A and B are depicted in Figures 7(a) and 7(b). On sample A, three emission peaks, a blue light at 400 nm, a blue-green around 464 nm, and a green light at around 520 nm, were recorded. The main strong UV emission at 400 nm corresponds to the near-band-edge emission, while the blue-green and green emission peaks at 464 nm and 520 nm are instead possibly associated with oxygen vacancies [46, 47]. Specifically, the blue-green transition at 464 nm is caused due to transition from the level of ionized oxygen vacancy to the valence band, while the green emission, called deep-level emission, occurs by the recombination of the photogenerated holes with singly ionized oxygen vacancies in ZnO. On sample B, an additional UV emission peak at 385 nm, due to the recombination of photogenerated electrons and holes, appears as a shoulder of the main peak at 400 nm. The higher intensity of near-band-edge emission peaks compared to green emission peaks is an indication of the good quality of ZnO nanostructures produced.

4. Conclusions

The morphology, structure, and optical properties of ZnO nanostructures synthesized by microwave irradiation have been investigated in detail. The composition and morphology of the nanostructures are affected by the presence of albumen as a template. The optical band gap of the polycrystalline ZnO nanoparticles increases from 3.22 to 3.25 eV for the sample synthesized in the presence of albumen because of the defects' decrease. The good quality of ZnO nanostructures produced was also demonstrated by PL studies which evidenced a higher intensity of near-band-edge emission peaks compared to green emission peaks. In summary, results obtained indicate that the microwave-assisted method is a promising low temperature, cheap, and fast method for the production of ZnO nanostructures.

References

- [1] B. B. Rao, "Zinc oxide ceramic semi-conductor gas sensor for ethanol vapour," *Materials Chemistry and Physics*, vol. 64, no. 1, pp. 62–65, 2000.
- [2] W. H. G. Horsthuis, "ZnO processing for integrated optic sensors," *Thin Solid Films*, vol. 137, no. 2, pp. 185–192, 1986.
- [3] Asif, Nur, Willander, and Danielsson, "Selective calcium ion detection with functionalized ZnO nanorods-extended gate MOSFET," *Biosensors and Bioelectronics*, vol. 24, no. 11, pp. 3379–3382, 2009.
- [4] C. Xia, N. Wang, L. Lidong, and G. Lin, "Synthesis and characterization of waxberry-like microstructures ZnO for biosensors," *Sensors and Actuators B*, vol. 129, no. 1, pp. 268–273, 2008.
- [5] Krishnamoorthy and Iliadis, "Development of high frequency ZnO/SiO₂/Si Love mode surface acoustic wave devices," *Solid-State Electronics*, vol. 50, no. 6, pp. 1113–1118, 2006.
- [6] Liu, Zhang, Lu et al., "Fabrication and characterization of ZnO film based UV photodetector," *Journal of Materials Science*, vol. 20, no. 3, pp. 197–201, 2009.
- [7] Y. Wang and M. Li, "Hydrothermal synthesis of single-crystalline hexagonal prism ZnO nanorods," *Materials Letters*, vol. 60, no. 2, pp. 266–269, 2006.
- [8] Lee, Easteal, Pal, and Bhattacharyya, "Evolution of ZnO nanostructures in sol-gel synthesis," *Current Applied Physics*, vol. 9, no. 4, pp. 792–796, 2009.
- [9] Wang, Liu, Chang, and Tang, "Synthesis of sulfur-doped ZnO nanowires by electrochemical deposition," *Materials Science in Semiconductor Processing*, vol. 10, no. 6, pp. 241–245, 2007.
- [10] J. Park, Y. Choi, and J. Park, "Synthesis of ZnO nanowires and nanosheets by an O₂-assisted carbothermal reduction process," *Journal of Crystal Growth*, vol. 280, no. 1-2, pp. 161–167, 2005.
- [11] H. Cheng, J. Cheng, Y. Zhang, and Q. Wang, "Large-scale fabrication of ZnO micro-and nano-structures by microwave thermal evaporation deposition," *Journal of Crystal Growth*, vol. 299, no. 1, pp. 34–40, 2007.
- [12] J. Liu, J. Cao, Z. Li, G. Ji, and M. Zheng, "A simple microwave-assisted decomposing route for synthesis of ZnO nanorods in the presence of PEG400," *Materials Letters*, vol. 61, no. 22, pp. 4409–4411, 2007.
- [13] S. Cho, D. Shim, S. Jung, E. Oh, B. R. Lee, and K. Lee, "Fabrication of ZnO nanoneedle arrays by direct microwave irradiation," *Materials Letters*, vol. 63, no. 9-10, pp. 739–741, 2009.
- [14] Krishnakumar, Jayaprakash, N. Pinna, Singh, Mehta, and Phani, "Microwave-assisted synthesis and characterization of flower shaped zinc oxide nanostructures," *Materials Letters*, vol. 63, no. 2, pp. 242–245, 2009.
- [15] I. Y. Y. Bu, "Rapid synthesis of ZnO nanostructures through microwave heating process," *Ceramics International*, vol. 39, pp. 1189–1194, 2013.
- [16] S. T. Aruna and A. S. Mukasyan, "Combustion synthesis and nanomaterials," *Current Opinion in Solid State and Materials Science*, vol. 12, no. 3-4, pp. 44–50, 2008.
- [17] Mohebbi, Ebadzadeh, and Hesari, "Synthesis of nanocrystalline (Ni/NiO)-YSZ by microwave-assisted combustion synthesis method: the influence of pH of precursor solution," *Journal of Power Sources*, vol. 178, no. 1, pp. 64–68, 2008.
- [18] M. A. Bhosale, K. D. Bhatte, and B. M. Bhanage, "A rapid, one pot microwave assisted synthesis of nanosize cuprous oxide," *Powder Technology*, vol. 235, pp. 516–519, 2013.
- [19] P. Dinka and A. S. Mukasyan, "In situ preparation of oxide-based supported catalysts by solution combustion synthesis," *Journal of Physical Chemistry B*, vol. 109, no. 46, pp. 21627–21633, 2005.
- [20] Kasapoğlu, Baykal, Köseoğlu, and Toprak, "Microwave-assisted combustion synthesis of CoFe₂O₄ with urea, and its magnetic characterization," *Scripta Materialia*, vol. 57, no. 5, pp. 441–444, 2007.
- [21] L. Ai and Jiang, "Rapid synthesis of nanocrystalline Co₃O₄ by a microwave-assisted combustion method," *Powder Technology*, vol. 195, no. 1, pp. 11–14, 2009.
- [22] Y. Fu, Y. Su, and C. Lin, "Comparison of microwave-induced combustion and solid-state reaction for synthesis of LiMn_{2-x}CrxO₄ powders and their electrochemical properties," *Solid State Ionics*, vol. 166, no. 1-2, pp. 137–146, 2004.
- [23] A. Srivastava, Lakshmikummar, Srivastava, Rashmi, and K. Jain, "Gas sensing properties of nanocrystalline SnO₂ prepared in solvent media using a microwave assisted technique," *Sensors and Actuators B*, vol. 126, no. 2, pp. 583–587, 2007.

- [24] Y. Fu, Y. Chang, and S. Wen, "Microwave-induced combustion synthesis and electrical conductivity of $Ce_{1-x}Gd_xO_{2-1/2x}$ ceramics," *Materials Research Bulletin*, vol. 41, no. 12, pp. 2260–2267, 2006.
- [25] E. Esmaeili, A. Khodadadi, and Y. Mortazavi, "Microwave-induced combustion process variables for MgO nanoparticle synthesis using polyethylene glycol and sorbitol," *Journal of the European Ceramic Society*, vol. 29, no. 6, pp. 1061–1068, 2009.
- [26] C. Hwang and T. Wu, "Combustion synthesis of nanocrystalline ZnO powders using zinc nitrate and glycine as reactants - Influence of reactant composition," *Journal of Materials Science*, vol. 39, no. 19, pp. 6111–6115, 2004.
- [27] M. Selvakumar and D. K. Bhat, "Microwave synthesized nanostructured TiO_2 -activated carbon composite electrodes for supercapacitor Selvakumar," *Applied Surface Science*, vol. 263, pp. 236–241, 2012.
- [28] I. Bilecka, P. Elser, and M. Niederberger, "Kinetic and thermodynamic aspects in the microwave-assisted synthesis of ZnO nanoparticles in benzyl alcohol," *ACS Nano*, vol. 3, no. 2, pp. 467–477, 2009.
- [29] P. Zhu, J. Zhang, Z. Wu, and Z. Zhang, "Microwave-assisted synthesis of various ZnO hierarchical nanostructures: effects of heating parameters of microwave oven," *Crystal Growth and Design*, vol. 8, no. 9, pp. 3148–3153, 2008.
- [30] N. F. Hamedani, A. R. Mahjoub, A. A. Khodadadi, and Y. Mortazavi, "Microwave assisted fast synthesis of various ZnO morphologies for selective detection of CO, CH₄ and ethanol," *Sensors and Actuators B*, vol. 156, no. 2, pp. 737–742, 2011.
- [31] J. ZHU, J. ZHANG, H. ZHOU, W. QIN, L. CHAI, and Y. HU, "Microwave-assisted synthesis and characterization of ZnO-nanorod arrays," *Transactions of Nonferrous Metals Society of China (English Edition)*, vol. 19, no. 6, pp. 1578–1582, 2009.
- [32] Savary, Marinel, Colder, Harnois, Lefevre, and Retoux, "Microwave sintering of nano-sized ZnO synthesized by a liquid route," *Powder Technology*, vol. 208, no. 2, pp. 521–525, 2011.
- [33] L. C. Nehru, V. Swaminathan, and C. Sanjeeviraja, "Rapid synthesis of nanocrystalline ZnO by a microwave-assisted combustion method," *Powder Technology*, vol. 226, pp. 29–33, 2012.
- [34] Al-Hajry, A. Umar, Hahn, and Kim, "Growth, properties and dye-sensitized solar cells-applications of ZnO nanorods grown by low-temperature solution process," *Superlattices and Microstructures*, vol. 45, no. 6, pp. 529–534, 2009.
- [35] T. Prakash, R. Jayaprakash, D. Sathya Raj et al., "Sensing properties of ZnO nanoparticles synthesized by using albumen as a biotemplate for acetic acid monitoring in aqueous mixture," *Sensors and Actuators B*, vol. 176, pp. 560–568, 2013.
- [36] Vafaei and M. S. Ghamsari, "Preparation and characterization of ZnO nanoparticles by a novel sol-gel route," *Materials Letters*, vol. 61, no. 14–15, pp. 3265–3268, 2007.
- [37] A. Umar, Rahman, M. Vaseem, and Y. Hahn, "Ultra-sensitive cholesterol biosensor based on low-temperature grown ZnO nanoparticles," *Electrochemistry Communications*, vol. 11, no. 1, pp. 118–121, 2009.
- [38] A. Umar, Rahman, Al-Hajry, and Hahn, "Highly-sensitive cholesterol biosensor based on well-crystallized flower-shaped ZnO nanostructures," *Talanta*, vol. 78, no. 1, pp. 284–289, 2009.
- [39] A. E. Morales, E. S. Mora, and U. Pal, "Use of diffuse reflectance spectroscopy for optical characterization of unsupported nanostructures," *Revista Mexicana De Fisica S*, vol. 53, pp. 18–22, 2007.
- [40] Senthilkumar, Vickraman, and Ravikumar, "Synthesis of fluorine doped tin oxide nanoparticles by sol-gel technique and their characterization," *Journal of Sol-Gel Science and Technology*, vol. 53, no. 2, pp. 316–321, 2010.
- [41] F. Yakuphanoglu, "Electrical characterization and device characterization of ZnO microring shaped films by sol-gel method," *Journal of Alloys and Compounds*, vol. 507, no. 1, pp. 184–189, 2010.
- [42] Yakuphanoglu, Mehrotra, Gupta, and M. Oz, "Nanofiber organic semiconductors: the effects of nanosize on the electrical charge transport and optical properties of bulk polyanilines," *Journal of Applied Polymer Science*, vol. 114, no. 2, pp. 794–799, 2009.
- [43] J. Tauc, R. Grigorovici, and A. Vancu, "Optical properties and electronic structure of amorphous germanium," *Physica Status Solidi B*, vol. 15, pp. 627–637, 1966.
- [44] Wang, Chen, and Yang, "Microstructure and optical properties of polycrystalline ZnO films sputtered under different oxygen flow rates," *Journal of Alloys and Compounds*, vol. 488, no. 1, pp. 232–237, 2009.
- [45] A. K. Zak, M. E. Abrishami, W. H. Abd Majid, R. Yousefi, and S. M. Hosseini, "Effects of annealing temperature on some structural and optical properties of ZnO nanoparticles prepared by a modified sol-gel combustion method," *Ceramic International*, vol. 37, pp. 393–398, 2011.
- [46] P. Yang, H. Yan, S. Mao et al., "Controlled growth of ZnO nanowires and their optical properties," *Journal of Advanced Functional Materials*, vol. 12, pp. 323–331, 2002.
- [47] P. Jiang, J. Zhou, H. Fang, C. Wang, Z. L. Wang, and S. Xie, "Hierarchical shelled ZnO structures made of bunched nanowire arrays," *Advanced Functional Materials*, vol. 17, no. 8, pp. 1303–1310, 2007.

Research Article

Microwave Assisted Growth of ZnO Nanorods and Nanopolypods Nanostructure Thin Films for Gas and Explosives Sensing

A. K. Singh^{1,2}

¹ Nanomaterials and Sensors Laboratory, Defence Institute of Advanced Technology, Girinagar, Pune, Maharashtra 411025, India

² DRDO Centre for Piezoceramics and Devices, ARDE, Pashan, Pune, Maharashtra 411021, India

Correspondence should be addressed to A. K. Singh; aksingh@diat.ac.in

Received 16 December 2012; Accepted 2 January 2013

Academic Editor: Amir Kajbafvala

Copyright © 2013 A. K. Singh. This is an open access article distributed under the Creative Commons Attribution License, which permits unrestricted use, distribution, and reproduction in any medium, provided the original work is properly cited.

The growth of uniformly distributed and densely packed array of zinc oxide (ZnO) nanorods (NRs) and nanorods (NRs)/nanopolypods (NPPs) was successfully achieved through microwave-assisted chemical route at low temperature. The ZnO NRs and NRs/NPPs were characterized using X-ray diffraction (XRD), scanning electron microscope (SEM), energy dispersive X-ray analysis (EDX), and UV-Vis absorption spectroscopy. The ZnO NRs were of 100–150 nm diameter and 0.5–1 μm length, while the NPPs were of diameter about 150–200 nm and 1.5–2 μm pod length. The prepared films are polycrystalline in nature and highly oriented along (002) plane with a hexagonal wurtzite structure. These films were studied for the sensing properties of liquefied petroleum gas (LPG), oxygen, and hazardous explosives, that is, 2,4,6-trinitrotoluene (TNT) and cyclotrimethylenetrinitramines (RDX), in the temperature ranges of 25–425 °C and 100–200 °C, respectively. The grown nanostructure films showed reliable stable response to several on-off cycles, and reduction in sensor recovery time was found with the increase in temperature. ZnO NRs and NRs/NPPs showed better sensitivity and recovery time for both LPG and oxygen, as compared to the literature-reported results for ZnO thin films.

1. Introduction

Numerous materials have been reported to be usable as metal-oxide chemical sensors including both single-component (e.g., ZnO, SnO₂, WO₃, TiO₂, and Fe₂O₃) and multicomponent oxides (BiFeO₃, MgAl₂O₄, SrTiO₃, and Sr_{1-y}Ca_yFeO_{3-x}). The metal-oxide semiconductors like ZnO, SnO₂, or TiO₂ react with atmospheres like oxygen, carbon monoxide, or carbon dioxide which has been known for years and investigated intensively. The metal-oxide semiconductors are high gap metal oxides in which the semiconducting behavior arises from the deviation of stoichiometry. Conductometric metal-oxide-semiconductor thin films are the most promising devices among solid state chemical sensors, due to their small dimensions, low cost, low power consumption, on-line operation, and high compatibility with microelectronic processing. The hazardous gas detection spans from environmental monitoring, automotive applications, air conditioning in airplanes, spacecrafts and houses, explosive

detection of sensors networks, and so forth. Historically, ZnO is one of the first materials studied as a gas sensor. ZnO is also a promising material for the realization of electronic and optoelectronic devices due to its specific chemical, electrical, surface, and microstructural properties. ZnO is a wide band gap semiconductor, having high exciton binding energy of 60 meV which allows excitonic transitions at room temperature, meaning high radiative recombination efficiency for spontaneous emission as well as lower threshold voltage for emission, and has a stable wurtzite structure with lattice spacing $a = 0.325$ nm and $c = 0.521$ nm. It has attracted intensive research efforts for its unique properties and versatile applications in antireflection coatings, transparent electrodes in solar cells, ultraviolet (UV) light emitters, diode lasers, varistors, piezoelectric devices, spin electronics, surface acoustic wave propagator [1], photonic applications [2], and gas sensing [3].

For gas sensing, ZnO is good candidate to replace the toxic and expensive materials like SnO₂ generally used for

gas sensing applications [4]. The ZnO is particularly useful to gas sensors because of its typical properties such as resistivity control over the range of 10^{-3} to $10^5 \Omega\text{m}$, high electrochemical stability, absence of toxicity, and abundant availability in nature [5]. This is primarily due to the high mobility of conduction electrons in the material and good chemical and thermal stability under operating conditions. ZnO-based gas sensors have been fabricated using powders, pellets, thick and thin films, and so forth. Thin films are found to be suitable for such sensors, since the gas sensing properties of metal oxides are related to the material surface and the species are adsorbed and react with the surface [3, 6], leading to change in the resistance of sensor element [7]. Instead of the sensors measuring the change of electrical conductance, there are several other kinds of sensors, such as photoluminescence (PL) sensors, nanostructured ZnO coated quartz crystal microbalance (QCM) sensors, and plasmon surface resonance-based sensors [8]. However, compared with the electrical conductance-based sensors, these sensors are complicated and expensive. The mechanism for gas detection in these conductometric materials is based, in large part, on reactions that occur at the sensor surface, resulting in a change in the concentration of adsorbed oxygen. Variation in conductivity is due to the adsorption of atmospheric oxygen on the oxide surface that extracts electrons from the semiconducting material leading to change in carrier density and conductivity.

The fundamental sensing mechanism of metal-oxide-based gas sensors relies on a change in electrical conductivity due to the interaction process between the surface complexes such as O^- , O^{2-} , H^+ , and OH^- reactive chemical species and the gas molecules to be detected. For example, changes in the electron density at the semiconductor surface are due to the presence of oxidizing and reducing gases, because of the adsorption and desorption of O^- , O^{2-} , and O_2^- . Oxygen ions adsorb onto the material's surface, removing electrons from the bulk and creating a potential barrier that limits electron movement and conductivity. On interaction with oxidizing or reducing gases, adsorbed oxygen concentration and thereby conductivity change. The change in conductivity is a measure of gas concentration. For reducing gases such as H_2 , H_2S , LPG, CO, CO_2 , $\text{C}_2\text{H}_5\text{OH}$, and NH_3 , the conductivity increases for *n*-type materials (ZnO) and reduces for *p*-type materials (such as Te). The effect of oxidizing gases such as NO_2 is opposite to that of reducing gases. Adsorbed oxygen gives rise to potential barriers at grain boundaries and thus increases the resistance of sensor surface. On the other hand reducing gas decreases the oxygen surface concentration and hence the surface resistance; magnitude of the response depends on the nature and concentration of the volatile molecules and on the type of metal oxide. This change in conductivity is directly related to the amount of a specific gas present in the environment, resulting in a quantitative determination of gas presence and concentration.

The low selectivity is a well-known problem of these sensors, and its improvement is a research field open to different solutions. An improvement in selectivity can be obtained by changing the sensor temperature during measurements.

These gas-sensor reactions typically occur at elevated temperatures (150–600°C), requiring the sensors to be internally heated for maximum response. The operating temperature must be optimized for both the sensor material and the gas being detected. In addition, to maximize the opportunities for surface reactions, a high ratio of surface area to volume is needed. As an inverse relationship exists between surface area and particle size, nanoscale materials, which exhibit high surface area, are highly desirable. The effects of the microstructure, namely, ratio of surface area to volume, grain size, and pore size of the metal oxide particles, as well as film thickness of the sensor performance are well recognized. Since the gas sensing mechanism is a surface reaction, use of nanostructured materials is expected to improve gas sensing characteristics. Many recent reports have confirmed the benefits of nanotechnology to sensor performance. The most recent research has been devoted to nanostructured oxides, since reactions at grain boundaries and complete depletion of carriers in the grains can strongly modify the material transport properties. Unfortunately the high temperature required for the surface reactions to take place induces a grain growth by coalescence and prevents the achievement of stable materials.

ZnO exhibits a wide range of novel structures which include NRs, belts, rings, spheres, and core shells that can be grown by tuning the growth rates along these directions. One of the most profound factors determining the morphology involves the relative surface activities of various growth facets under given conditions. The use of ZnO nanostructures like NRs, and nanowires, nanotetrapods having higher surface area to volume (aspect ratio) can give even better sensitivity response, compared to ZnO nanoparticles/thin films, because the interaction between the adsorbed gases and the sensors surface will be stronger for the nanostructures as the complete particle contributes to the gas sensing phenomenon as $D \sim 2L$, where D is the particle diameter and L is the Debye length. The larger surface area of the materials synthesized also facilitates the gas detection at much lower temperatures [9]. The development of ZnO nanostructure-based gas sensors has attracted intensive research interest in the last several years because of their selective and rapid detection of various gases specified by novel nanostructures. ZnO NRs with excellent gas sensing properties have been reported by Sun et al. [10].

Various ZnO nanostructures have been prepared using both physical as well as chemical methods, which include chemical vapor deposition [11], physical vapor deposition [12], laser ablation [13], and chemical synthesis [14, 15]. Among them, chemical synthesis is much simpler and the reaction is performed at much lower temperatures [16, 17]. Recently, microwave irradiation has been widely applied to synthesis of nanomaterials. Due to intense friction and the collision of molecules created by microwave irradiation, microwave irradiation not only provides the energy for heating but also greatly accelerates the nucleation. With microwave irradiation on the reactant solution, temperature and concentration gradients can be avoided leading to uniform nucleation. Microwave-based synthesis method is one of the

easiest, energy-saving, green, and quick methods for large-scale production of nanomaterials [18].

Li et al. [19] have used ZnO nanorods for H₂, NH₃, and C₂H₅OH chemical sensing. Wang et al. [20] have used vertically oriented ZnO nanorods for H₂ sensing and have also reported detection of NH₃ and CO. Sun et al. [10] have used ZnO nanorods for H₂, NH₃, LPG, and CH₃CH₂OH whereas Lv et al. [21] reported use of ZnO nanorods for benzene and ethanol gas. Zhang et al. [22] have synthesized 3D microspheres for ethanol and ammonia sensing. Baratto et al. [23] have used ZnO nanostructured fibers for NO₂ sensing. Kenanakis et al. [24] have synthesized ZnO nanosponge/rod for ozone detection. Recently, Choi and Jang [25] have reviewed the use of 1D oxide nanostructures for chemical sensing. To the author's knowledge there is hardly any report on the usage of ZnO NRs and NPPs for explosive sensing. In the present paper, ZnO NRs and ZnO NRs/NPPs were grown on glass substrate using microwave-assisted chemical synthesis method. The gas (LPG and oxygen) and RDX and TNT explosive sensing properties of ZnO NRs and NRs/NPPs have been investigated.

2. Experimental

All substrates were thoroughly cleaned by the following sequence: cleaned by labolene detergent and then rinsed with double-distilled (DD) water; then boiled with dilute chromic acid for 15 minutes and thoroughly rinsed with DD water; after that, ultrasonicated for 10 min in acetone and then in methanol, and finally all substrates were dried in an oven.

The ZnO NRs and NPPs on glass substrates were grown using microwave-assisted chemical method in place of conventional heating [26]. The growth of ZnO NRs was carried out in two steps.

2.1. First Step: Synthesis of ZnO Seed Layer. Two samples of ZnO sol were prepared, one without capping agent and another with triethanolamine (TEA) as capping agent. In the first case (without capping agent), solution of 0.03 M sodium hydroxide (NaOH, Merck) in methanol (CH₃OH, Merck) was added slowly to a continuously stirred solution of 0.01 M zinc acetate dihydrate (CH₃COO)₂Zn·2H₂O (Merck) in methanol at 60°C. The formed sol is designated as sample S1 hereafter. In the second case, 0.24 mL TEA (Merck) was added after a gap of 5 min to a continuously stirred solution of 0.03 M sodium hydroxide and 0.01 M zinc acetate dihydrate (CH₃COO)₂Zn·2H₂O in methanol at 60°C. The formed sol is designated as sample S2 hereafter. For the growth of ZnO nanoparticles, the operation temperature of solution was uniformly maintained at 60°C for 01 h, using 2.54 GHz microwave radiations. The 5 min delay in addition of TEA resulted in the formation of ZnO and (ZnOH)⁺ cations from the chemical reaction of zinc acetate dihydrate and sodium hydroxide and prevented the agglomeration of colloidal particles.

The prepared sol S1 and S2 were spin-cast four times on glass substrate at 3000 RPM for 20 s each time to form uniform ZnO seed layer. Between coatings, the substrates

were annealed in open air at 150°C–160°C for 15 min to ensure particle adhesion onto the substrate surface.

2.2. Second Step: Growth of ZnO NRs and NPPs. Growth of NRs and NPPs was carried out by suspending the substrates with crystal seed layer upside down in an aqueous solution containing 0.025 M Zinc nitrate hexahydrate, Zn(NO₃)₂·6H₂O (Merck), 2.58 mL of diethylenetriamine, and C₄H₁₃N₃ (Burgoyne Mk) in DD water at 90°C. The required operation temperature was maintained using 2.54 GHz microwave radiations. After 5 hrs the substrates were removed, rinsed thoroughly with DD water, and dried at room temperature. The prepared ZnO film on glass substrate without capping agent is defined as “F1” and another with capping agent defined as “F2.”

The prepared samples S1-S2 and films F1-F2 were characterized at different stages of synthesis and growth. The UV-Vis spectroscopy of samples was done in the range of about 300–700 nm with the help of spectrometers (NanoDrop-1000 and HPX-2000). The particles size of ZnO nanoparticles was measured using particle sizing system (Nicom-p-380ZLS). The structural and morphological study of samples was carried out using Xpert PRO Panalytical Powder X-ray diffractometer (XRD) in the scanning range of 20–80° (2θ) using Cu K_α radiations with wavelength 1.54 Å (JOEL, JSM-6360A, and Philips XL-30) and analytical scanning electron microscope (SEM).

The gas (LPG and oxygen) and explosives sensing properties of film F1 (ZnO nanorods, NRs) and film F2 (ZnO nanopolydops, NPPs) samples was carried out in a custom designed gas sensor assembly [3]; it comprises a temperature controller, a copper-constantan thermocouple, an electric heating plate, a gas chamber, and a volume measurement unit. The two-probe DC measurement technique was used to measure the electrical resistance in air and in the presence of target gas at constant voltage of 6 V. For electric measurements, silver paste contacts separated by a gap of 5 mm were used to form ohmic contacts on the films F1 and F2. The electrical resistance of film F1 or F2 in air (R_a) and in the presence of target gas (R_g) was measured to evaluate the sensor response/sensitivity (S), percentage sensor sensitivity ($S\%$), and recovery time (t) as follows [27]:

$$S = \frac{R_g}{R_a}, \quad (1)$$

$$S\% = (1 - S) \times 100, \quad (2)$$

$$t = t_2 - t_1, \quad (3)$$

where t_1 is the moment the target gas is switched off and t_2 is the moment the sample regains its initial resistance, while the difference of both these times gives the recovery time.

3. Characterization

3.1. UV-Visible Absorption Spectra and Particle Size of ZnO Nanoparticles. Figure 1 shows UV-Visible absorption spectra

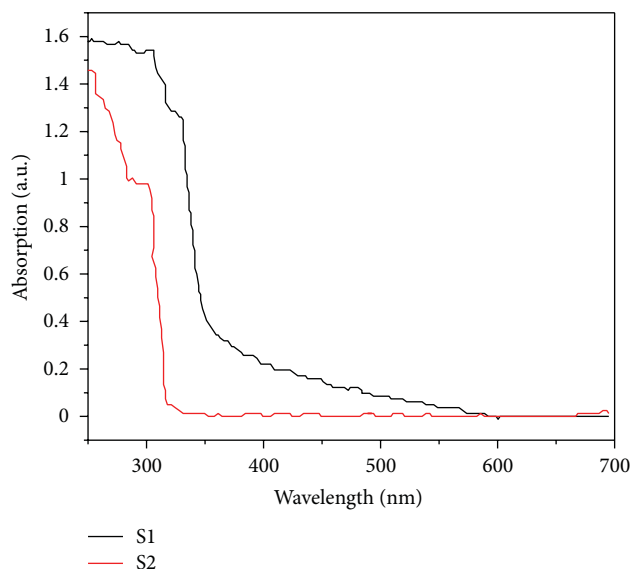


FIGURE 1: UV-Vis absorption spectra of ZnO nanoparticles of samples S1 and S2.

of the samples S1 and S2. It is clear from the figure that the absorbance peak for sample S1 is at 329 nm and for S2 is at 302 nm. The blue shift in the optical absorption can be attributed to the use of TEA as a capping agent. Similar result has been reported by Singh et al. [28]. To confirm the blue shift in the optical absorption particle size distribution was recorded on the particle size analyzer and is shown in Figure 2. The particle size distribution for the sample S1 was observed to be around 942 nm whereas for S2, 190 nm as can be seen from Figure 2. The agglomeration of particles was noticed in the case of S1 as evident from Figure 2(a). Thus the blue shift is supported by the size distribution analysis. Reduction of the particle size from 942 nm to 190 nm was observed in the case of S2 because of TEA which prevents the agglomeration.

3.2. UV-Vis Optical Absorption of ZnO Nanostructures. Figure 3 shows the UV-Vis optical absorption spectra of films F1 and F2 with absorption edge at 373 nm and 370 nm, respectively. These values are found to be less than 380 nm which corresponds to bulk ZnO, indicating that ZnO nanostructures grown are smaller than bulk ZnO particles [29].

3.3. Structural Analysis. Figures 4(a) and 4(b) show the X-ray diffraction patterns for the films F1 and F2, respectively. The diffraction peaks observed at 32.4° , 34.4° , 36.7° , 48.2° , 57.3° , and 63.6° are attributed to the (100), (002), (101), (102), (110), and (103) planes, respectively, of hexagonal wurtzite structure [30], as can be seen in comparison with the JCPDS card nos. 00-003-0752/01-075-1526 and 01-077-2414 for F1 and F2. Both the films F1 and F2 are polycrystalline in nature and highly oriented along (002) plane. The crystallite sizes were calculated using Scherrer's formula using information

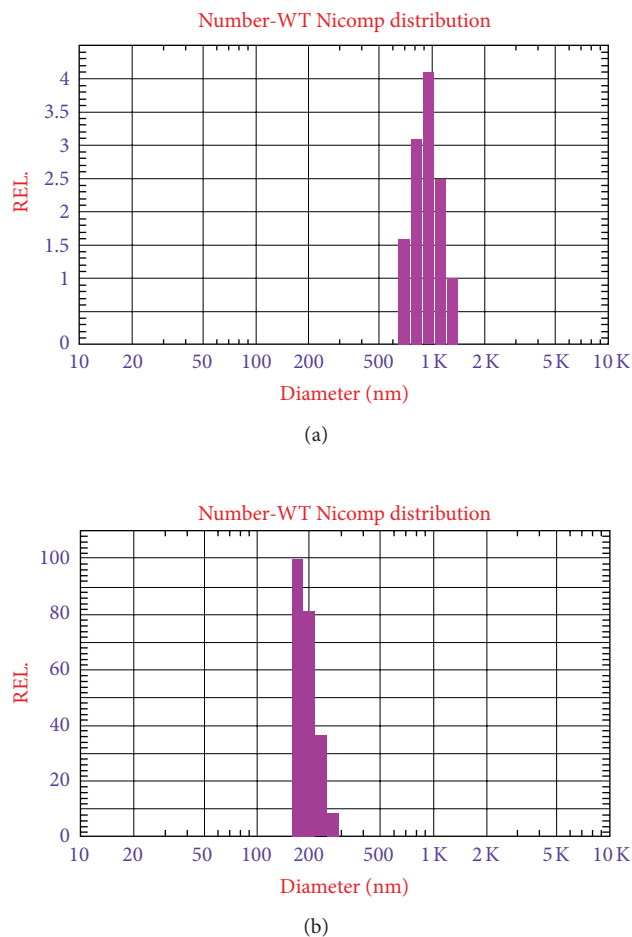


FIGURE 2: Particles size distribution of ZnO nanoparticles (based on number-weight distribution): (a) without capping agent sample S1 (Av. particle size: 942 nm) and (b) with capping agent sample S2 (Av. particle size: 190 nm).

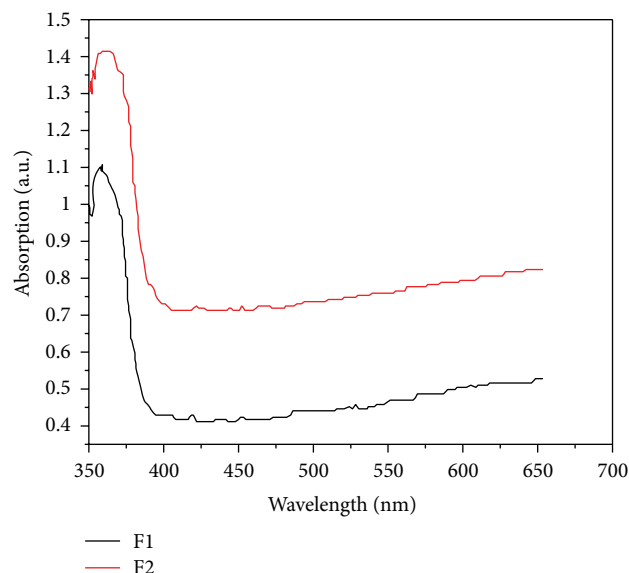


FIGURE 3: Optical absorption spectra of ZnO films F1 and F2.

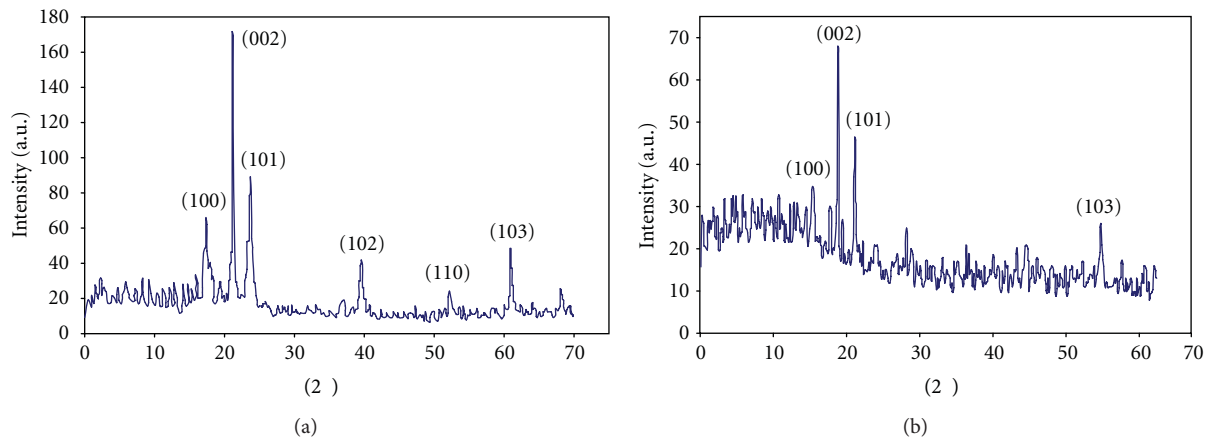
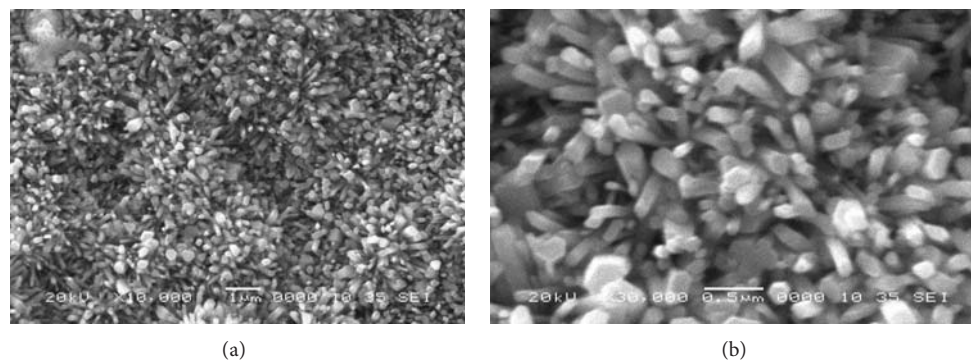


FIGURE 4: XRD of (a) ZnO film F1 and (b) ZnO film F2.

FIGURE 5: SEM images of ZnO film F1: (a) ZnO nanorods (NRs) with scale 1.0 μm and (b) enlarged view of nanorods (NRs) with scale 0.5 μm .

on broadening of diffraction peak (β), X-ray wavelength (λ), and incident X ray angle with crystal plane (θ_B), that is,

$$T = \frac{0.9\lambda}{\beta \cos \theta_B}. \quad (4)$$

The average crystallite size for the (100), (002), and (101) XRD peaks was found to be between 35–105 nm and 35–141 nm for F1 and F2 films, respectively.

3.4. Surface Morphology of Nanostructures. Figures 5 and 6 shows the SEM micrographs of the samples F1 and F2, respectively. From Figures 5(a) and 5(b) one can see the growth of uniform and densely packed array of ZnO NRs with diameter 100–150 nm and length 0.5–1 μm . Figures 6(a)–6(c) show growth of ZnO NPPs over uniform and densely packed array of NRs which is shown in Figure 6(d). The NPPs are with pod diameter about 150–200 nm and pod length 1.5–2 μm . The formation of NPPs in sample F2 may be attributed to the addition of TEA as capping agent [31].

4. Gas Sensing

4.1. Effect of Temperature on Sensor Response for LPG and Oxygen. Figures 7(a), 7(b), 8(a), and 8(b) show the sensor

response (S) as a function of temperature for films F1 and F2 over the temperature range from ambient 25°C to about 425°C, at three different concentrations of 0.2 vol.%, 0.32 vol.%, and 0.4 vol.% of LPG and oxygen, respectively. The response to the LPG and oxygen is due to oxygen vacancies on metal-oxide (ZnO) surfaces, which are electrically and chemically active. These vacancies function as n-type donors and often significantly increase the conductivity of oxide. Initially, the sensor response (S) increases with the increase in temperature and reaches a maximum value for both samples with the gases. Observation of Figures 7(a) and 7(b) shows that for LPG the sensor response reaches the maximum value at 385°C temperature for film F1, while for F2 the maximum value lies in the range from 280°C to 345°C; similar behavior has been reported by Patil et al. [32], Shinde et al. [4], and Sun et al. [10]. Observation of Figures 8(a) and 8(b) shows that for oxygen the sensor response reaches the maximum value at temperatures of 405°C, 385°C, and 380°C for film F1, while for F2 the maximum response is at 195°C, 270°C, and 275°C. This temperature is called optimal temperature, and activation energy at this temperature may be enough to complete the chemical reaction, which results in the maximum adsorption of the concerned gas, and above the optimal temperature the sample temperature increases and it causes a decrease in the sensitivity (S), indicating the rate of

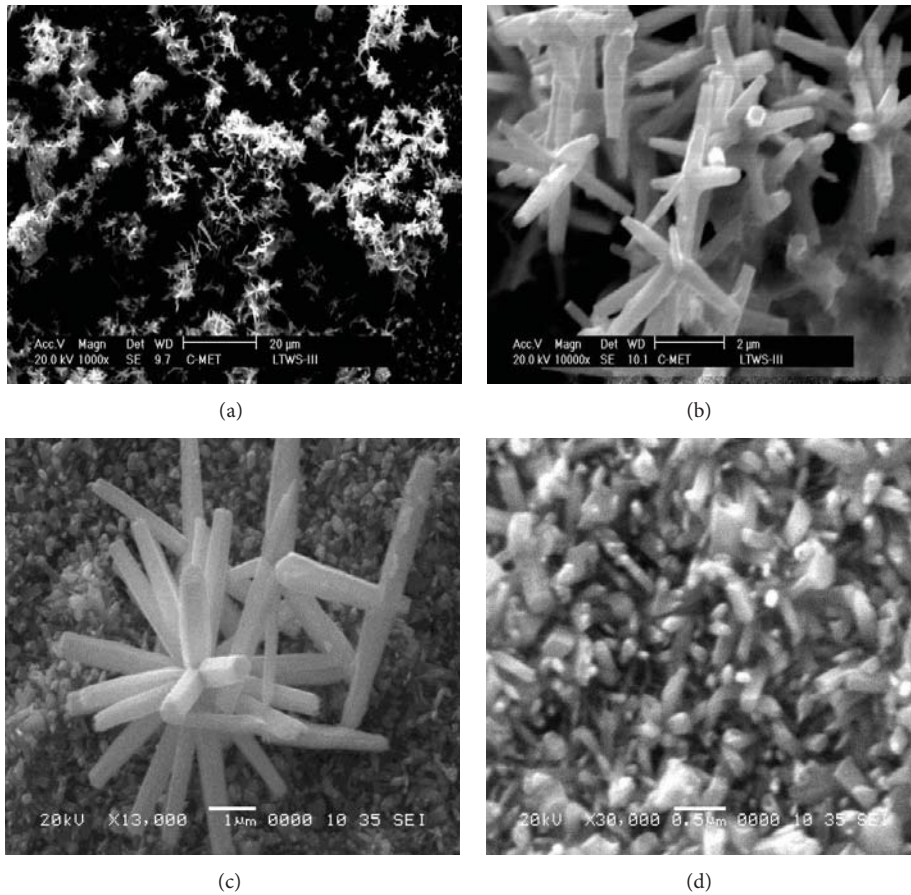


FIGURE 6: SEM images of ZnO of film F2: (a) ZnO nanopolypods (NPPs) with scale 20.0 μm, (b) enlarged view of nanopolypods (NPPs) with scale 2.0 μm, (c) nanopolypods (NPPs) with nanorods (NRs) in the background with scale 1.0 μm, and (d) enlarged view of ZnO nanorods (NRs) with scale 0.5 μm.

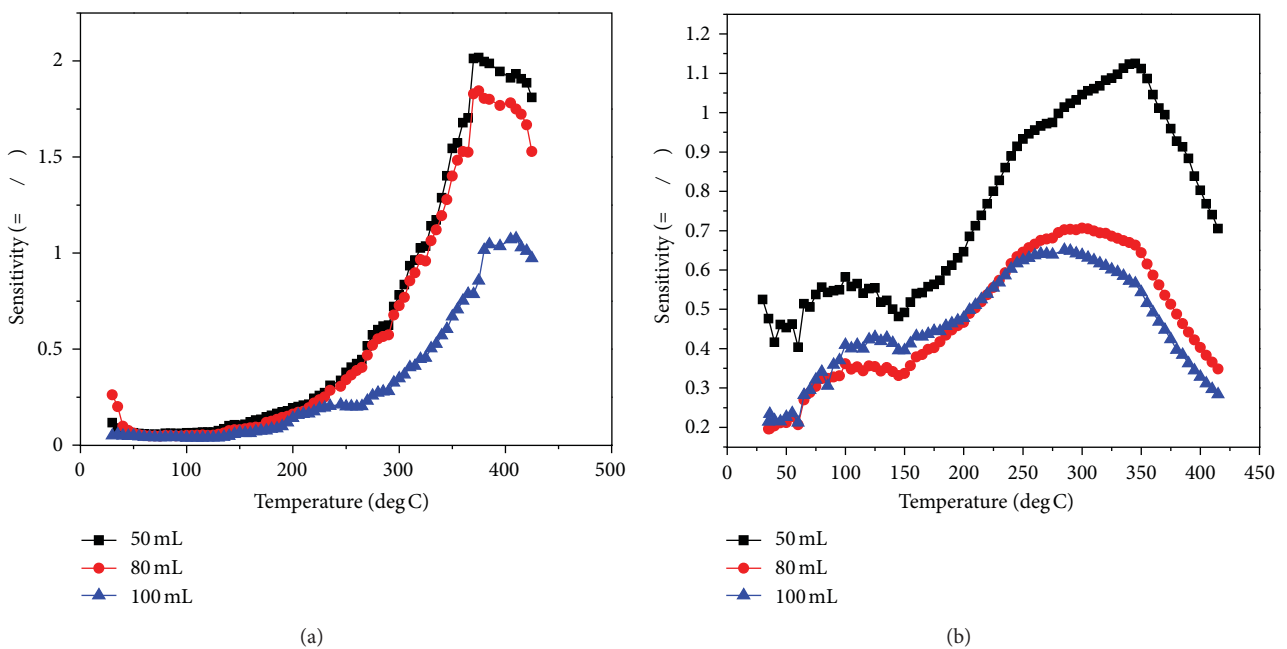
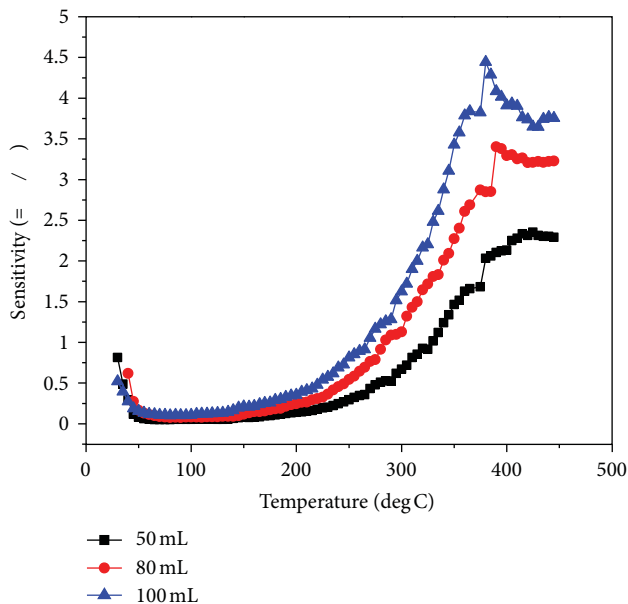
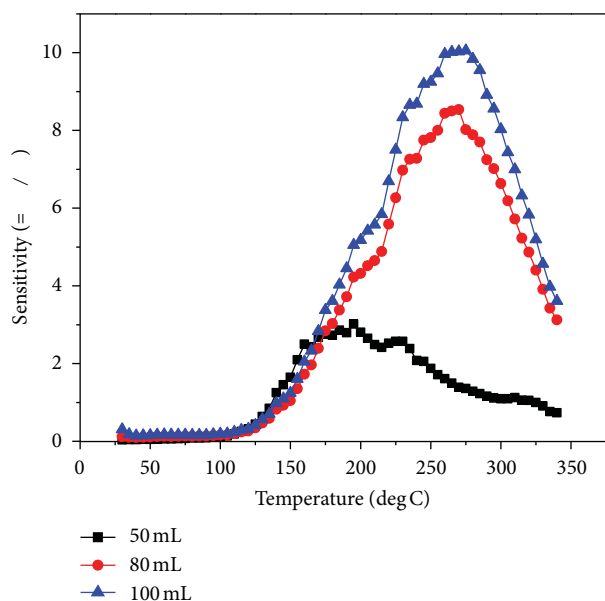


FIGURE 7: Sensor response (R_g/R_a) with temperature for LPG: (a) ZnO nanorods (NRs) film F1 and (b) ZnO nanopolypods (NPPs) film F2.



(a)



(b)

FIGURE 8: Sensor response (R_g/R_a) with temperature for oxygen gas: (a) ZnO nanorods (NRs) film F1 and (b) ZnO nanopolypods (NPPs) film F2.

desorption of the reducing gas. The increase and decrease in the sensitivity observed in the figures indicate the adsorption and desorption phenomenon of the gases. The change in resistance of a semiconductor oxide like ZnO sensors in the presence of target gas takes place according to two reactions [33]. In the first reaction, atmospheric or injected oxygen O_2 molecules are adsorbed onto the surface by taking electron from the conduction band and are thus chemisorbed on the surface as O_{ads}^- ; this leads to an increase in the resistance of

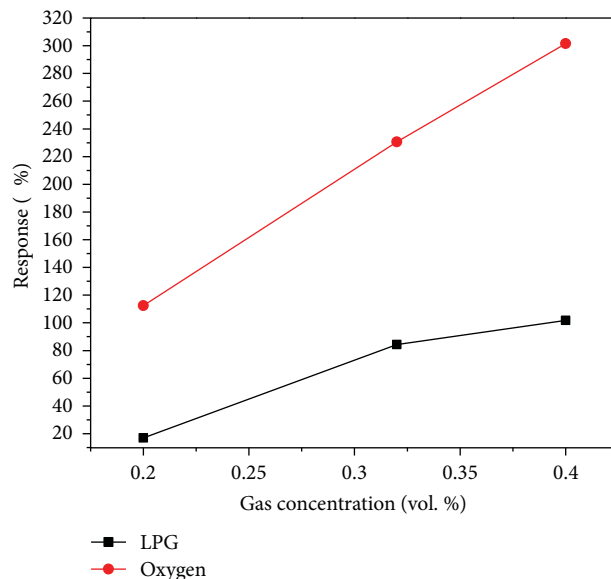
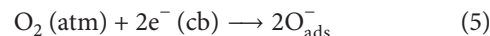
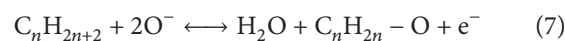
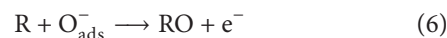


FIGURE 9: Percentage sensor sensitivity ($S\%$) with LPG and oxygen concentration (vol.%) at 385°C for ZnO nanorods (NRs) film F1.

the sensor material. The chemical reaction can be explained by the following equation:



In the second reaction, the reducing gases (R) present in the ambient air or injected into the reaction chamber react with the chemisorbed oxygen O_{ads}^- thereby releasing an electron back to the conduction band and decreasing the resistance of the sensor material given by the following equation:



As LPG consists of CH_4 , C_3H_8 , C_4H_{10} , and so forth, in these molecules the reducing hydrogen species are bound to carbon atoms. The overall reaction of LPG molecules with adsorbed oxygen can be explained in a similar way by the previous equation.

In case of oxygen, the maximum sensitivity value increases with the increase in gas concentration, whereas for LPG the maximum sensitivity value reduces with the increase in the concentration of gas. This opposite behavior is due to LPG and oxygen being reducing and oxidizing gases, respectively.

4.2. Effect of Gas Concentration on Sensor Response. Figure 9 shows the sensor response ($S\%$) of film F1 as a function of LPG/oxygen concentration at 385°C ; it reveals that the sensor percentage sensitivity ($S\%$) increases from nearly 17% to 102% for LPG and 106% to 329% for oxygen as the concentration of gas increased from 0.2 vol. % to 0.4 vol.%; similar increasing behavior has been reported for LPG by Shinde et al. [4]. As the LPG gas concentration increased from 0.2% to 0.32 vol.%, the response increased rapidly from 17% to 84%, but at a

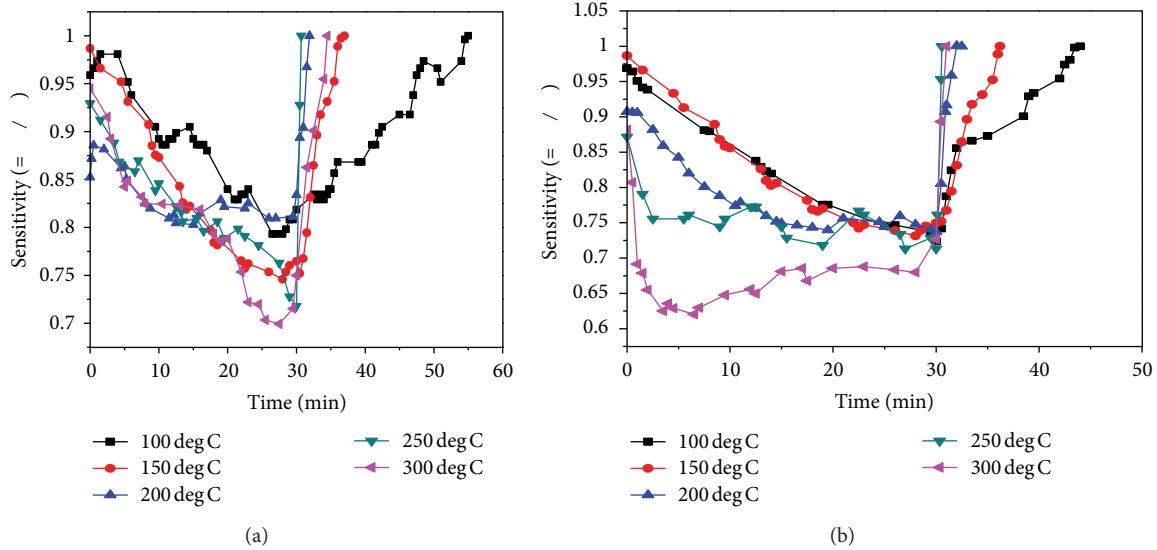


FIGURE 10: Sensing and recovery time for LPG: (a) ZnO nanorods (NRs) film F1 and (b) ZnO nanopolypods (NPPs) film F2.

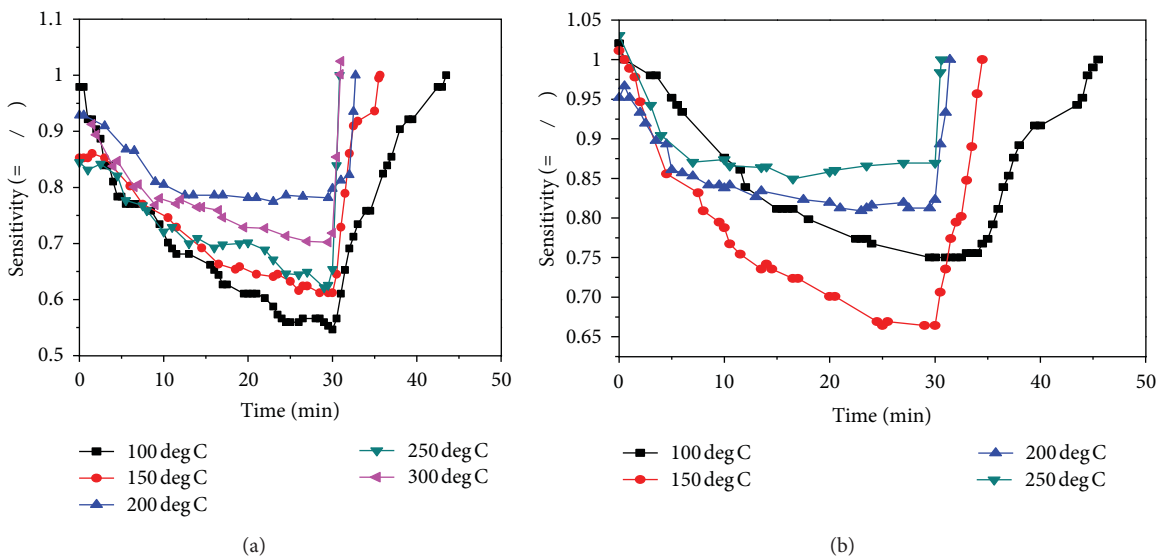


FIGURE 11: Sensing and recovery time for oxygen gas: (a) ZnO nanorods (NRs) film F1 and (b) ZnO nanopolypods (NPPs) film F2.

higher concentration the increase in gradual response has been observed and after which it gets saturated; however, a linear variation has been observed in the case of oxygen. The response can be explained on the basis of the removal of adsorbed oxygen molecules by reaction with the target gas and generation of electrons. For a small concentration of gas, exposed on a fixed surface area of a sample, there is a lower coverage of gas molecules on the surface and hence lower surface reaction, while for an increase in gas, concentration increases the surface reaction due to a larger surface coverage. A further increase in surface reaction will be gradual when the saturation point on the coverage of molecules is achieved [33].

4.3. Sensor Recovery Analysis for LPG and Oxygen. Figures 10(a), 10(b), 11(a), and 11(b) show the sensor sensitivity (S) to LPG and oxygen with time at fixed temperatures for films F1 and F2, respectively. The sensor sensitivity (S) for films F1 and F2, during exposure to 0.4 vol.% of LPG/oxygen in an airtight chamber for 30 min and thereafter recovery in air, was observed at fixed temperatures of 100°C, 150°C, 200°C, 250°C, and 300°C. The sensor sensitivity (S) for both samples decreases with time in the presence of LPG/oxygen due to the desorption process of reducing gas species present in the LPG and the ambient air [4, 7]. After 30 min, the recovery time was checked by the immediate exposure of sample to ambient air. It shows that the recovery time (t), defined by (3), reduces

TABLE 1: Comparison table of sensitivity ($S\%$) and recovery time (t) for films F1 and F2 for LPG.

Temperature ($^{\circ}\text{C}$)	ZnO nanorods (NRs) (F1)		ZnO nanopolygons (NPPs) (F2)	
	Percentage of sensor sensitivity ($S\%$)	Recovery time (min)	Percentage of sensor sensitivity ($S\%$)	Recovery time (min)
100	18.2	25	27.7	14
150	33.3	2.9	25	6.2
200	17	1.9	26.3	2.5
250	28.2	0.7	28.7	0.66
300	25	2.75	27.3	1.0

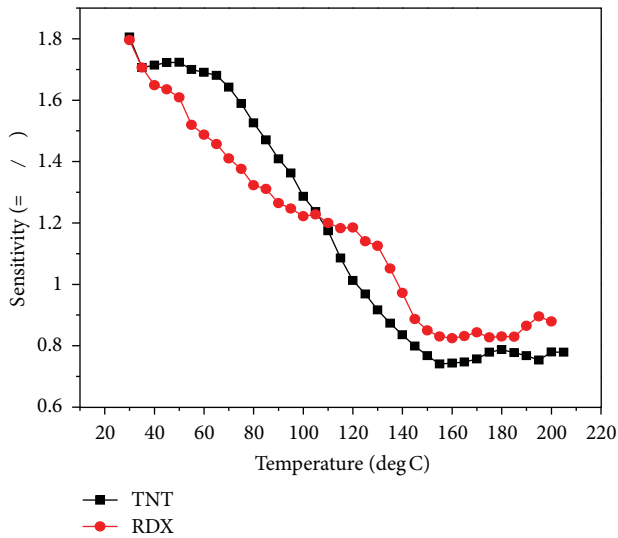
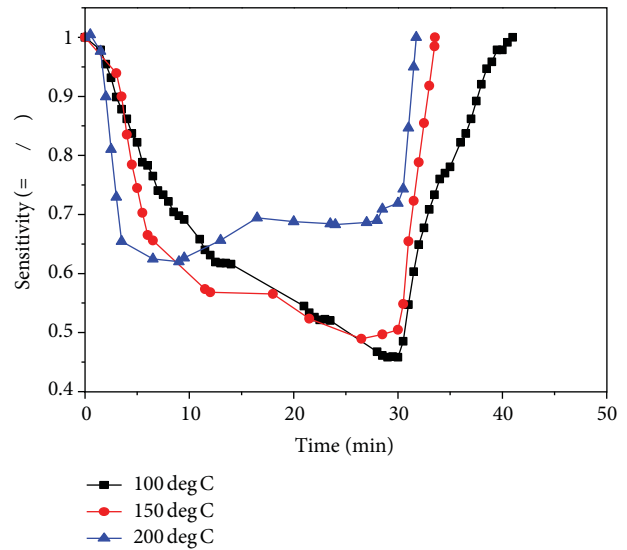


FIGURE 12: Sensitivity response with temperature in the presence of TNT/RDX, for film F1.

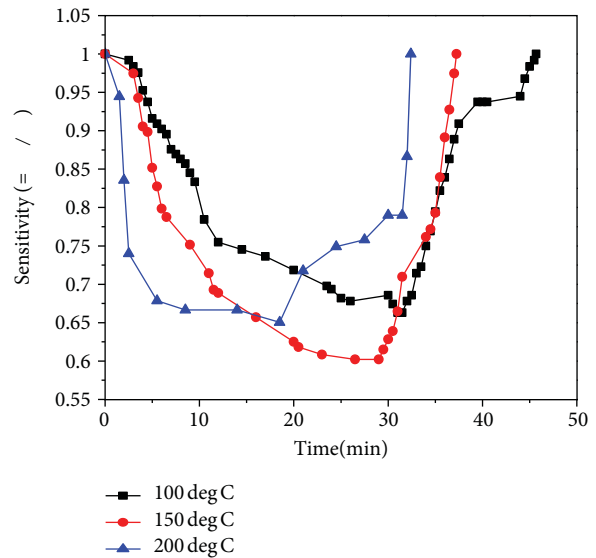
with an increase in operation temperature up to 250°C and thereafter increases for higher temperatures. The recovery of the resistance when target gas is removed is determined by both oxygen readsorption from the ambient on the surface and reoxidation of the oxide. The films F1 and F2 sensitivity (S) response and recovery patterns achieved for LPG are similar and with better recovery time, in comparison to those reported by Chatterjee et al. [7] for higher concentration (2 vol%) of LPG on ZnO thin film. Tables 1 and 2 show the comparison of percentage sensor sensitivity ($S\%$) and recovery time (t) of films F1 and F2 for both LPG and oxygen. At temperature 250°C both films have shown the least recovery time for both LPG and Oxygen. Also the LPG recovery time achieved at 150°C for both films is much lesser than that reported by Chatterjee et al. [7] using ZnO thin films.

5. Explosives Sensing

5.1. TNT and RDX Explosives Sensing. Explosives are chemical compounds that can be initiated to undergo self-propagating decomposition resulting in the sudden release of heat and pressure [34]. The TNT [$(\text{C}_6\text{H}_2(\text{NO}_2)_3\text{CH}_3)$] and RDX [$(\text{CH}_2\text{-N-NO}_2)_3$] belong to a class of nitroaromatic and nitramines compounds and have extremely low vapour pressure of 4.8×10^{-6} (Torr) and 8.3×10^{-10} (Torr) at 20°C , respectively. Nanostructures such as NRs and nanoparticles



(a)



(b)

FIGURE 13: Sensing and recovering response for RDX: (a) ZnO nanorods (NRs) film F1 and (b) ZnO nanopolygons (NPPs) film F2.

offer a highly sensitive platform for the detection of molecular adsorption on their surfaces [35–39]. The chemical reaction of reducing species CH_3/CH_2 present in the TNT/RDX molecule with the adsorbed oxygen (O_{ads}^-) at elevated temperature results in the release of free electrons (e^-),

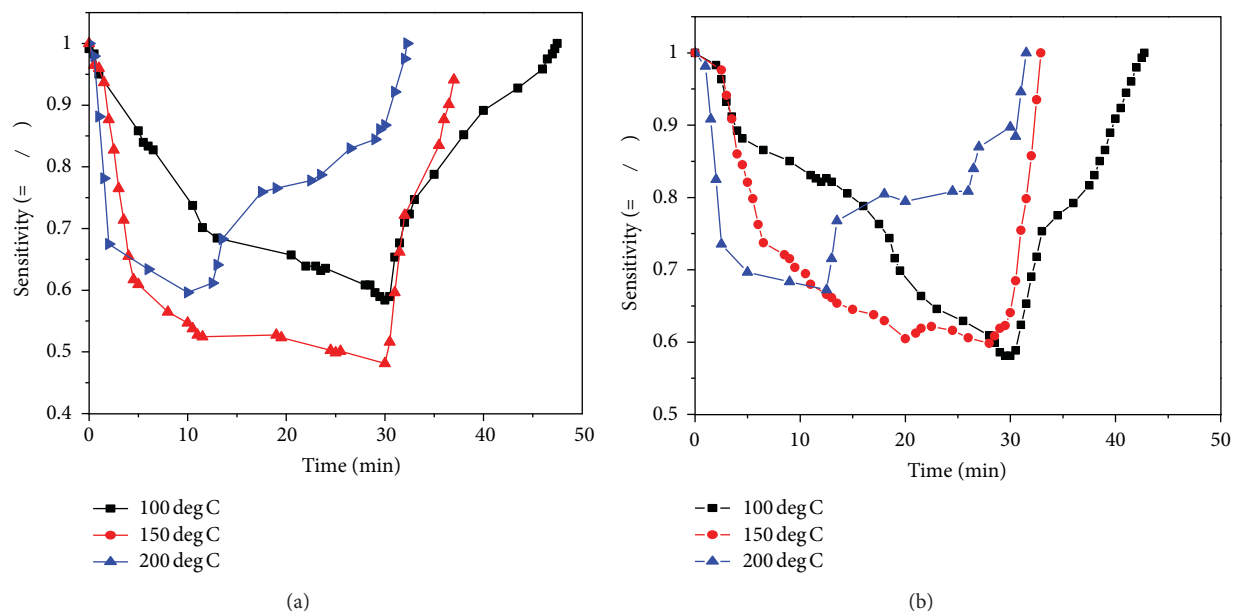


FIGURE 14: Sensing and recovering response for TNT: (a) ZnO nanorods (NRs) film F1 and (b) ZnO nanopolygons (NPPs) film F2.

TABLE 2: Comparison table of sensitivity (S%) and recovery time (t) for films F1 and F2 for oxygen.

Temperature (°C)	ZnO nanorods (NRs) (F1)		ZnO nanopolygons (NPPs) (F2)	
	Percentage of sensor sensitivity (S%)	Recovery time (min)	Percentage of sensor sensitivity (S%)	Recovery time (min)
100	45.4	13.5	25	15.5
150	38.8	5.65	33.5	4.5
200	20.2	2.75	17.7	1.4
250	34.6	0.85	14	0.6
300	28.2	0.95	—	—

therefore reducing the resistance of ZnO nanostructure film. For the experiment 0.2 mg quantity of TNT grains/RDX powder was used for explosive sensing using samples S1 and S2. Additionally, after placing TNT/RDX powder inside the airtight glass chamber, 0.2 BHP rotary suction pump connected to the chamber base was run for 10 min to drain out atmospheric air from the chamber to create vacuum of ~220 mm of Hg pressure below atmosphere. As the vapor pressure of target explosives is very low, the use of vacuum condition for the experiment might have been useful in improving sensor sensitivity to detect low vapour pressure TNT/RDX explosive molecules available inside the airtight chamber.

5.2. Effect of Temperature on Sensor Response for TNT and RDX. Figure 12 shows the sensor response of film F1 in the presence of TNT and RDX in the temperature range from 30°C to 210°C. The sensitivity (S) of sensor was found to decrease gradually with temperature from 30°C to 157°C in the presence of TNT and from 30°C to 172°C in the presence of RDX and then nearly stabilize with higher temperature.

The decrease in sensitivity response with the increase in temperature indicates the rate of desorption of reducing gas species present in TNT and RDX as per (6). This results in the increase of conductivity or the decrease of resistance, while in the stabilized region, the activation energy may be enough to complete the chemical reaction.

5.3. Sensor Recovery Analysis for TNT/RDX. The response of films F1 and F2 to a quantity of 0.2 mg of RDX/TNT as explosive source placed for 30 min inside an airtight chamber and thereafter recovery in air were measured at different temperatures of 100°C, 150°C, and 200°C. Figures 13(a), 13(b), 14(a), and 14(b) show the sensing and recovery time plots for films F1 and F2 in the presence of RDX and TNT, respectively. The sensitivity (S) for both samples decreased during exposure to RDX/TNT over a period of 30 min at different temperatures due to desorption process of the reducing gas species present in RDX/TNT. After 30 min, the recovery time was found to decrease with the increase in operation temperature. Tables 3 and 4 show the comparison

TABLE 3: Comparison table of sensitivity (S%) and recovery time (t) for films F1 and F2 for RDX.

Temperature (°C)	ZnO nanorods (NRs) (F1)		ZnO nanopolygons (NPPs) (F2)	
	Percentage of sensor sensitivity (S%)	Recovery time (min)	Percentage of sensor sensitivity (S%)	Recovery time (min)
100	54.16	11	31.42	15.7
150	49.54	3.55	37.2	7.25
200	28	1.75	21	2.4

TABLE 4: Comparison table of sensitivity (S%) and recovery time (t) for films F1 and F2 for TNT.

Temperature (°C)	ZnO nanorods (NRs) (F1)		ZnO nanopolygons (NPPs) (F2)	
	Percentage of sensor sensitivity (S%)	Recovery time (min)	Percentage of sensor sensitivity (S%)	Recovery time (min)
100	41.62	17.5	42	12.75
150	51.9	7.5	36	2.9
200	13.4	2.25	10.3	1.5

of sensitivity (S%) and recovery time (t) of films F1 and F2 for both RDX and TNT explosives.

6. Conclusions

Uniform array of aligned ZnO NRs with diameter of about 3100–150 nm and length of 0.5–1 μm and ZnO NRs/NPPs with pod diameter of about 150–200 nm and length of about 1.5–2 μm were grown on glass substrates with microwave-assisted wet chemical synthesis (with capping and without capping agents). Use of triethanolamine as capping agent has resulted in the additional growth of ZnO NPPs. The structural analysis showed hexagonal wurtzite structure of ZnO nanostructure with planes highly oriented along (002) direction. The sensing study of ZnO NRs and ZnO NRs/NPPs samples showed that the sensor response (S) increases with temperature for both LPG and oxygen, while with the increase in gas concentration from 0.2 to 0.4 vol%, the sensor response increases gradually and attains saturation for LPG, while for oxygen, the response was found to be linear with the increase in gas concentration. The sensor sensing and the recovery time analysis showed that the recovery time reduces with the increase in operation temperature for both gas and explosives. The recovery time of both samples has been found to be the least at the operation temperature of 250°C for LPG/oxygen and 200°C for TNT/RDX. Additionally the recovery time achieved for LPG at 0.4 vol% concentration in this study is much lesser than that previously reported for ZnO thin film with much higher LPG concentration. The present work shows that both ZnO NRs and ZnO NRs/NPPs have excellent potential for both gas and explosive sensing applications.

Acknowledgments

The author is thankful to the Vice-Chancellor, DIAT(DU), Pune and Director of ARDE, Pune, for granting permission to publish this work. The author would like to acknowledge Department of Physics, University of Pune, and C-MET,

Pune, for providing SEM facilities and HEMRL, Pune, for providing XRD facilities.

References

- [1] C. R. Gorla, N. W. Emanetoglu, S. Liang et al., "Structural, optical, and surface acoustic wave properties of epitaxial ZnO films grown on (0112) sapphire by metalorganic chemical vapor deposition," *Journal of Applied Physics*, vol. 85, no. 5, pp. 2595–2602, 1999.
- [2] X. D. Wang, C. J. Summers, and Z. L. Wang, "Large-scale hexagonal-patterned growth of aligned ZnO nanorods for nano-optoelectronics and nanosensor arrays," *Nano Letters*, vol. 4, no. 3, pp. 423–426, 2004.
- [3] S. B. Patil and A. K. Singh, "Solution grown nanocrystalline ZnO thin films for UV emission and LPG sensing," *Journal of Materials Science*, vol. 45, no. 19, pp. 5204–5210, 2010.
- [4] V. R. Shinde, T. P. Gujar, and C. D. Lokhande, "LPG sensing properties of ZnO films prepared by spray pyrolysis method: effect of molarity of precursor solution," *Sensors and Actuators B*, vol. 120, no. 2, pp. 551–559, 2007.
- [5] B. Ismail, M. Abaab, and B. Rezig, "Structural and electrical properties of ZnO films prepared by screen printing technique," *Thin Solid Films*, vol. 383, no. 1-2, pp. 92–94, 2001.
- [6] X. Q. Liu, S. W. Tao, and Y. S. Shen, "Preparation and characterization of nanocrystalline α by sol-gel process," *Sensors and Actuators B*, vol. 40, no. 2-3, pp. 161–165, 1997.
- [7] A. P. Chatterjee, P. Mitra, and A. K. Mukhopadhyay, "Chemically deposited zinc oxide thin film gas sensor," *Journal of Materials Science*, vol. 34, no. 17, pp. 4225–4231, 1999.
- [8] W. Y. Feng, N. Chiu, H. Lu, H. Shih, D. Yang, and C. Lin, "Surface plasmon resonance biochip based on ZnO thin film for nitric oxide sensing," in *Proceedings of the 30th Annual International Conference of the IEEE Engineering in Medicine and Biology Society (EMBS'08)*, Vancouver, Canada, August 2008.
- [9] L. Satyanarayana, K. M. Reddy, and S. V. Manorama, "Nano-sized spinel NiFe_2O_4 : a novel material for the detection of liquefied petroleum gas in air," *Materials Chemistry and Physics*, vol. 82, no. 1, pp. 21–26, 2003.

- [10] Z. P. Sun, L. Liu, L. Zhang, and D. Z. Jia, "Rapid synthesis of ZnO nanorods by one step-room temperature solid state reaction and their gas sensing properties," *Nanotechnology*, vol. 17, no. 9, pp. 2266–2270, 2006.
- [11] Z. R. Dai, Z. W. Pan, and Z. L. Wang, "Novel nanostructures of functional oxides synthesized by thermal evaporation," *Advanced Functional Materials*, vol. 13, no. 1, pp. 9–24, 2003.
- [12] Z. Q. Liu, D. H. Zhang, S. Han et al., "Laser ablation synthesis and electron transport studies of tin oxide nanowires," *Advanced Materials*, vol. 15, no. 20, pp. 1754–1757, 2003.
- [13] W. I. Park, D. H. Kim, S. W. Jung, and G. C. Yi, "Metalorganic vapor-phase epitaxial growth of vertically well-aligned ZnO nanorods," *Applied Physics Letters*, vol. 80, no. 22, pp. 4232–4236, 2002.
- [14] S. Y. Bae, H. W. Seo, and J. Park, "Vertically aligned sulfur-doped ZnO nanowires synthesized via chemical vapor deposition," *Journal of Physical Chemistry B*, vol. 108, no. 17, pp. 5206–5210, 2004.
- [15] B. Liu and H. C. Zeng, "Hydrothermal synthesis of ZnO nanorods in the diameter regime of 50 nm," *Journal of the American Chemical Society*, vol. 125, no. 15, pp. 4430–4431, 2003.
- [16] J. M. Wang and L. Gao, "Wet chemical synthesis of ultralong and straight single-crystalline ZnO nanowires and their excellent UV emission properties," *Journal of Materials Chemistry*, vol. 13, no. 10, pp. 2551–2554, 2003.
- [17] M. K. Hossain, S. C. Ghosh, Y. Boontongkong, C. Thanachayanont, and J. Dutta, "Growth of zinc oxide nanowires and nanobelts for gas sensing applications," *Journal of Metastable and Nanocrystalline Materials*, vol. 23, pp. 27–30, 2005.
- [18] A. K. Singh and V. S. Raykar, "Microwave synthesis of silver nanofluids with polyvinylpyrrolidone (PVP) and their transport properties," *Colloid and Polymer Science*, vol. 286, no. 14–15, pp. 1667–1673, 2008.
- [19] C. C. Li, Z. F. Du, L. M. Li, H. C. Yu, Q. Wan, and T. H. Wang, "Surface-depletion controlled gas sensing of ZnO nanorods grown at room temperature," *Applied Physics Letters*, vol. 91, no. 3, Article ID 032101, 3 pages, 2007.
- [20] J. X. Wang, X. W. Sun, Y. Yang et al., "Hydrothermally grown oriented ZnO nanorod arrays for gas sensing applications," *Nanotechnology*, vol. 17, no. 19, pp. 4995–4998, 2006.
- [21] Y. Lv, L. Guo, H. Xu, and X. Chu, "Gas-sensing properties of well-crystalline ZnO nanorods grown by a simple route," *Physica E*, vol. 36, no. 1, pp. 102–105, 2007.
- [22] H. Zhang, J. Wu, C. Zhai, N. Du, X. Ma, and D. Yang, "From ZnO nanorods to 3D hollow microhemispheres: solvothermal synthesis, photoluminescence and gas sensor properties," *Nanotechnology*, vol. 18, no. 45, Article ID 455604, 2007.
- [23] C. Baratto, G. Sberveglieri, A. Onischuk, B. Caruso, and S. Di Stasio, "Low temperature selective NO₂ sensors by nanostructured fibres of ZnO," *Sensors and Actuators B*, vol. 100, no. 1–2, pp. 261–265, 2004.
- [24] G. Kenanakis, D. Vernardou, E. Koudoumas, G. Kiriakidis, and N. Katsarakis, "Ozone sensing properties of ZnO nanostructures grown by the aqueous chemical growth technique," *Sensors and Actuators B*, vol. 124, no. 1, pp. 187–191, 2007.
- [25] K. J. Choi and H. W. Jang, "One-dimensional oxide nanostructures as gas-sensing materials: review and issues," *Sensors*, vol. 10, no. 4, pp. 4083–4099, 2010.
- [26] W. T. Wu, L. Shi, Q. Zhu, Y. Wang, G. Xu, and W. Pang, "Rapid synthesis of ZnO micro/nanostructures in large scale," *Materials Letters*, vol. 62, no. 1, pp. 159–162, 2008.
- [27] H. Gong, J. Q. Hu, J. H. Wang, C. H. Ong, and F. R. Zhu, "Nanocrystalline Cu-doped ZnO thin film gas sensor for CO," *Sensors and Actuators B*, vol. 115, no. 1, pp. 247–251, 2006.
- [28] A. K. Singh, V. Viswanath, and V. C. Janu, "Synthesis, effect of capping agents, structural, optical and photoluminescence properties of ZnO nanoparticles," *Journal of Luminescence*, vol. 129, no. 8, pp. 874–878, 2009.
- [29] Y. L. Wu, A. I. Y. Tok, F. Y. C. Boey, X. T. Zeng, and X. H. Zhang, "Chemical synthesis of ZnO nanocrystals," *IEEE Transactions on Nanotechnology*, vol. 6, no. 5, pp. 497–503, 2006.
- [30] A. Ghosh, N. G. Deshpande, Y. G. Gudage et al., "Effect of annealing on structural and optical properties of zinc oxide thin film deposited by successive ionic layer adsorption and reaction technique," *Journal of Alloys and Compounds*, vol. 469, no. 1–2, pp. 56–60, 2009.
- [31] K. Thongsuriwong, P. Amornpitoksuk, and S. Suwanboon, "The effect of aminoalcohols (MEA, DEA and TEA) on morphological control of nanocrystalline ZnO powders and its optical properties," *Journal of Physics and Chemistry of Solids*, vol. 71, no. 5, pp. 730–734, 2010.
- [32] D. R. Patil, L. A. Patil, G. H. Jain, M. S. Wagh, and S. A. Patil, "Surface activated ZnO thick film resistor for LPG gas sensing," *Sensor and Transducer Journal*, vol. 74, no. 12, pp. 874–883, 2006.
- [33] A. D. Garje and R. C. Aiyer, "Electrical and gas-sensing properties of a thick film resistor of nanosized SnO₂ with variable percentage of permanent binder," *International Journal of Applied Ceramic Technology*, vol. 3, no. 6, pp. 477–484, 2006.
- [34] L. Senesac and T. G. Thundat, "Nanosensors for trace explosive detection," *Materials Today*, vol. 11, no. 3, pp. 28–36, 2008.
- [35] F. Patolsky and C. M. Lieber, "Nanowire nanosensors," *Materials Today*, vol. 8, no. 4, pp. 20–28, 2005.
- [36] N. Grobert, "Carbon nanotubes—becoming clean," *Materials Today*, vol. 10, no. 1–2, pp. 28–35, 2007.
- [37] B. L. Allen, P. D. Kichambare, and A. Star, "Carbon nanotubes FET based biosensors," *Advanced Materials*, vol. 19, no. 11, pp. 1439–1451, 2007.
- [38] Y. Cui, X. Duan, Y. Huang, and C. M. Lieber, *Nanowires and Nanobelts—Materials, Properties and Devices*, edited by Z. L. Wang, Kluwer Academic/Plenum, Dordrecht, The Netherlands, 2003.
- [39] Z. L. Wang, "Nanostructures of ZnO," *Materials Today*, vol. 7, no. 6, pp. 26–33, 2004.

Research Article

Green Chemistry Approach for Efficient Synthesis of Schiff Bases of Isatin Derivatives and Evaluation of Their Antibacterial Activities

Jnyanaranjan Panda,¹ V. Jagannath Patro,¹ Biswa Mohan Sahoo,¹ and Jitendriya Mishra²

¹ Department of Pharmaceutical Chemistry, Roland Institute of Pharmaceutical Sciences and Berhampur, Odisha 760010, India

² University Institute of Pharmaceutical Sciences, UGC Centre of Advanced Study (CAS), Panjab University, Chandigarh 160014, India

Correspondence should be addressed to Jnyanaranjan Panda; jnyana@rediffmail.com

Received 31 December 2012; Accepted 12 January 2013

Academic Editor: Amir Kajbafvala

Copyright © 2013 Jnyanaranjan Panda et al. This is an open access article distributed under the Creative Commons Attribution License, which permits unrestricted use, distribution, and reproduction in any medium, provided the original work is properly cited.

Microwave-assisted organic synthesis, a green chemistry approach, is nowadays widely used in the drug synthesis. Microwave-assisted synthesis improves both throughput and turnaround time for medicinal chemists by offering the benefits of drastically reduced reaction times, increased yields, and pure products. Schiff bases are the important class of organic compounds due to their flexibility, and structural diversities due to the presence of azomethine group which is helpful for elucidating the mechanism of transformation and rasemination reaction in biological system. This novel compound could also act as valuable ligands for the development of new chemical entities. In the present work, some Schiff bases of Isatin derivatives was synthesized using microwave heating method. Schiff base of Isatin were synthesized by condensation of the keto group of Isatin with different aromatic primary amines. They were characterized by means of spectral data and subsequently subjected to the *in vitro* antibacterial activities against gram positive and gram negative strains of microbes. It was observed that the compound with electron withdrawing substituents exhibited good antibacterial activities against almost all the micro organisms.

1. Introduction

Microwave-assisted organic synthesis is widely used as a source of heating in drug synthesis. Drug molecules can be built in a fraction of the time by this method. As a result, this technique has rapidly gained acceptance as a valuable tool for accelerating drug discovery and development processes. A microwave is a form of electromagnetic energy, which falls at the lower end of the electromagnetic spectrum and is defined in a measurement of frequency as 300 to 300,000 Megahertz. The microwave region of the electromagnetic spectrum lies between infrared and radio frequencies. The basic mechanism of microwave assisted synthesis involves agitation of polar molecules or ions that oscillate under the effect of an oscillating electric or magnetic field. In the presence of an oscillating field, particles try to orient themselves or be in phase with the field. Only materials that absorb

microwave radiation are relevant to microwave chemistry. These materials can be categorized according to the three main mechanisms of heating such as dipolar polarization, conduction mechanism, and interfacial polarization. The technique offers simple, clean, fast, efficient, and economical for the synthesis of a large number of drug molecules, having provided the momentum for many medicinal chemists to switch from traditional heating method to microwave heating method [1, 2]. Thus it follows green chemistry approach. The role of green chemistry is essential in ensuring that the next generation of chemicals, materials, and energy is more sustainable than the current generation. Worldwide demand for environmentally friendly chemical processes and products requires the development of novel and cost-effective approaches to prevent pollution of the environment [3]. The important area of green chemistry is the elimination of solvents during chemical processes or the replacement

TABLE 1: Comparative study on yield and reaction time of the synthesized compounds 2(a-j) by conventional and microwave assisted method.

Compound code	Conventional method			Microwave assisted method		
	Time (h)	Energy (Temp. °C)	Yield (%)	Time (min.)	Energy (power. watt)	Yield (%)
2a	3	98-100	64	5	210	84
2b	3	98-100	62	7	210	82
2c	3	98-100	56	6	210	85
2d	2	98-100	58	10	210	75
2e	2	98-100	66	7	210	85
2f	2	98-100	53	9	210	74
2g	2	98-100	57	8	210	77
2h	3	98-100	53	10	210	76
2i	3	98-100	56	10	210	72
2j	3	98-100	60	8	210	84

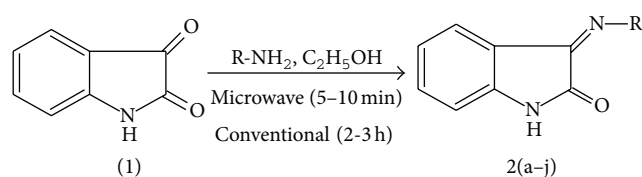
TABLE 2: TLC report and melting point data of the synthesized compounds 2(a-j).

Compound code	R	Tm (°C)	R _f
2a	phenyl	144-145	0.56
2b	2-nitrophenyl	120-121	0.67
2c	3-nitrophenyl	140-141	0.62
2d	4-nitrophenyl	150-151	0.68
2e	3-chlorophenyl	135-136	0.66
2f	4-chlorophenyl	140-141	0.67
2g	4-bromophenyl	230-231	0.62
2h	4-fluorophenyl	141-142	0.56
2i	3-Cl-4-F-phenyl	129-130	0.54
2j	2,6-dichlorophenyl	241-142	0.55

of hazardous solvents with environmental friendly solvents. Heterocyclic compounds are the most commonly used pharmacophore in the development of drugs and pharmaceutical substances. Due to their drug-likeness and structural diversity, these are routinely employed in high-throughput screening at early stages of drug discovery processes. Therefore, the goal of the present study is to carry out the synthesis of some heterocyclic compounds under green chemistry approach [4]. The above facts prompted us to synthesize some Schiff base of Isatin derivatives by using microwave heating method [5-7]. Azomethine group (-C=N-) containing compounds typically known as Schiff bases has been synthesized by the condensation of primary amines with active carbonyls [8]. Schiff bases form a significant class of compounds in medicinal chemistry due to various biological activities such as antibacterial [9], antifungal [10], antiviral [11], anti-HIV [12], and anticonvulsant [13] activities. The structures of the synthesized compounds were confirmed by means of their physical and spectral data. The synthesized compounds were evaluated for their possible antibacterial activities by cup plate method.

2. Experimental Method

2.1. Materials. The chemicals and solvents used for the experimental work were of commercial grade. All the melting



SCHEME 1

points were taken in open capillaries and are uncorrected (Table 2). Followup of the reactions and checking the purity of the compounds were made by TLC on precoated Silica gel-aluminum plates (Type 60 F254, Merck, Darmstadt, Germany) and were visualized by exposure to UV-light (254 nm) or iodine vapor for few seconds. The IR spectra of the compounds were recorded on FT-IR Spectrophotometer, model IR Affinity-1 (SHIMADZU), using KBr powder and the values are expressed in cm^{-1} . ^1H NMR spectra of selected compounds were recorded on multinuclear FT NMR Spectrometer, model Advance-II (Bruker), (at 400 MHz) using tetramethylsilane as an internal standard. The multiplicities of the signals are denoted with the symbols s, d, t, and m for singlet, doublet, triplet, and multiplet, respectively. The microwave irradiated synthesis was performed in scientific microwave oven, Catalyst System (operating between 140-700 W). All the reactions were carried out at power level-1, which corresponds to 140 W.

2.2. Conventional Synthesis of Schiff Bases of Isatin. Equimolar (0.01 mol) quantity of Isatin and substituted anilines were dissolved in ethanol (10 mL) and refluxed for 3 h in presence of glacial acetic acid. In between TLC was checked to confirm the completion of reaction. After completion of reaction, the reaction mixture was kept overnight to get the solid product. The product was filtered, dried, and recrystallized from ethanol (Scheme 1).

2.3. Microwave Synthesis of Schiff Bases of Isatin. The required quantities of above reactants are subjected to microwave irradiation for 5-10 min at power level 1 (140 watts). In between TLC was checked to confirm the completion of

TABLE 3: Antibacterial activities of the synthesized compounds 2(a–j).

Compounds	Diameter of zone of inhibition (millimeters)				
	<i>P. vulgaris</i>	<i>P. aeruginosa</i>	<i>E. coli</i>	<i>S. aureus</i>	<i>S. epidermidis</i>
2a	12.23 ± 0.57	15.02 ± 1.00	12.00 ± 1.00	13.32 ± 0.57	12.56 ± 0.57
2b	16.33 ± 0.55	17.10 ± 1.00	22.00 ± 1.00	23.00 ± 1.00	15.33 ± 0.57
2c	18.33 ± 0.55	18.11 ± 1.00	21.00 ± 1.00	19.00 ± 1.00	14.00 ± 1.00
2d	18.66 ± 0.52	16.00 ± 1.00	18.66 ± 0.57	19.34 ± 0.57	17.00 ± 1.00
2e	15.33 ± 0.57	17.00 ± 1.00	16.33 ± 0.57	16.32 ± 0.57	14.33 ± 0.57
2f	21.32 ± 0.53	21.00 ± 1.00	21.00 ± 1.00	19.34 ± 0.57	15.33 ± 0.57
2g	17.33 ± 0.57	18.00 ± 1.00	20.00 ± 1.00	19.23 ± 0.57	12.33 ± 0.57
2h	16.33 ± 0.56	20.10 ± 1.00	20.00 ± 1.00	22.20 ± 1.00	16.33 ± 0.57
2i	12.33 ± 0.57	14.10 ± 1.00	12.33 ± 0.57	16.32 ± 0.57	11.66 ± 0.57
2j	14.34 ± 0.53	14.10 ± 1.00	14.33 ± 0.57	17.35 ± 0.57	16.00 ± 1.00
Control	—	—	—	—	—
Standard	23.33 ± 0.57	20.33 ± 0.57	31.33 ± 0.57	21.66 ± 0.57	23.33 ± 0.57

Results were expressed as mean ± S.D. ($n = 3$); “—” indicates no zone of inhibition.

reaction. After completion of reaction, the reaction mixture was kept overnight to get the solid product. The product was filtered, dried, and recrystallized from ethanol (Scheme 1).

3. Results and Discussion

The synthetic protocol followed was outlined in Scheme 1. The synthesized compounds were characterized by their physical and spectral studies. As compared to conventional heating, microwave heating provides high yield with pure product in less reaction time (Table 1). The IR spectra of all the synthesized compounds were recorded using KBr (Merck). All the compounds have exhibited -NH stretching in the region of 3400–3200 cm^{-1} . IR spectra of synthesized compounds showed the presence of characteristic absorption peaks around 3000–3100 cm^{-1} (C–H, Ar), 2800–2780 cm^{-1} (–C=N–), 1640–1602 cm^{-1} (C=N), 1580–1520 cm^{-1} (C=C Ar), and 1346–1330 cm^{-1} (C–N). The halogenated derivatives showed the IR absorption bands in the regions and 1400–1000 cm^{-1} , 800–600 cm^{-1} , and 600–500 cm^{-1} which correspond to (C–F str.), (C–Cl str.), (C–Br str.), respectively. The N–O stretching vibrations in nitro group occur near 1550–1475 cm^{-1} (asymmetrical) and 1365–1290 cm^{-1} (symmetrical), with the band at 1550 cm^{-1} being the stronger. The ^1H NMR spectra above synthesized compounds have shown singlet in the region of δ 9.35 to 9.98 corresponding to secondary amino group (–NH). The aromatic protons resonate as multiplet in the region of δ 7.03 to 7.90. The synthesized compounds were evaluated for their *in-vitro* antibacterial activities by cup plate method against both gram positive and gram negative bacteria. The results of the study were summarized in Table 3 including the activity of standard. The compound 2f showed most promising effect whereas compound 2a and 2i were found to be least effective against *P. vulgaris*. Similarly the compound 2f was found to have maximum zone of inhibition and compounds 2i and 2j were found to have minimum zone of inhibition against *P. aeruginosa*. The compound 2b exhibited most

promising effect whereas compound 2a was found to have mild effect against *E. coli* and *S. aureus*. The compound 2d showed maximum effect against *S. epidermidis* whereas compound 2i was found to have mild effect against this species. Most of the tested compounds exhibited antibacterial activities against all the test organisms but the activity was less than that of the standard drug tetracycline in this test concentration. Thus taking into account the antibacterial activities of the tested compounds most of the compounds displayed poor activities against *S. epidermidis* and promising activities against *P. vulgaris*, *P. aeruginosa*, *E. coli*, and *S. aureus*.

The photographs of zone of inhibition of standard, control, and some of the tested compounds were given in Figure 1. Figure 1(a) showed the zone of inhibition of the standard drug against *E. coli* whereas there is no zone of inhibition in case of control. Similarly Figure 1(b) displayed the zone of inhibition of the standard drug against *S. aureus* whereas there is no zone of inhibition in case of control. Figure 1(c) showed the zone of inhibition of test compound 2h (L) which was more than that of 2a (R) against *S. aureus*. Figure 1(d) showed the zone of inhibition of test compounds 2i (L) and 2f (R) against *P. vulgaris*. In case of Figure 1(e) it was clearly visible that the diameter of zone of inhibition of compound 2c was more than that of compound 2d against *E. coli*. Figure 1(f) showed the diameter of zone of inhibition of compounds 2c and 2d against *P. aeruginosa*.

4. Biological Evaluation

4.1. Antibacterial Study. The synthesized compounds were screened *in-vitro* for their antibacterial activities against *Staphylococcus aureus* (MTCC-87), *Escherichia coli* (MTCC-40), *Staphylococcus epidermidis* (MTCC-2639), *Pseudomonas aeruginosa* (MTCC-424), and *Proteus vulgaris* (MTCC 426) using cup plate method [14, 15]. The compounds were tested at 500 μg concentration in dimethyl sulphoxide (DMSO), using nutrient agar as the medium. After 24 h of incubation

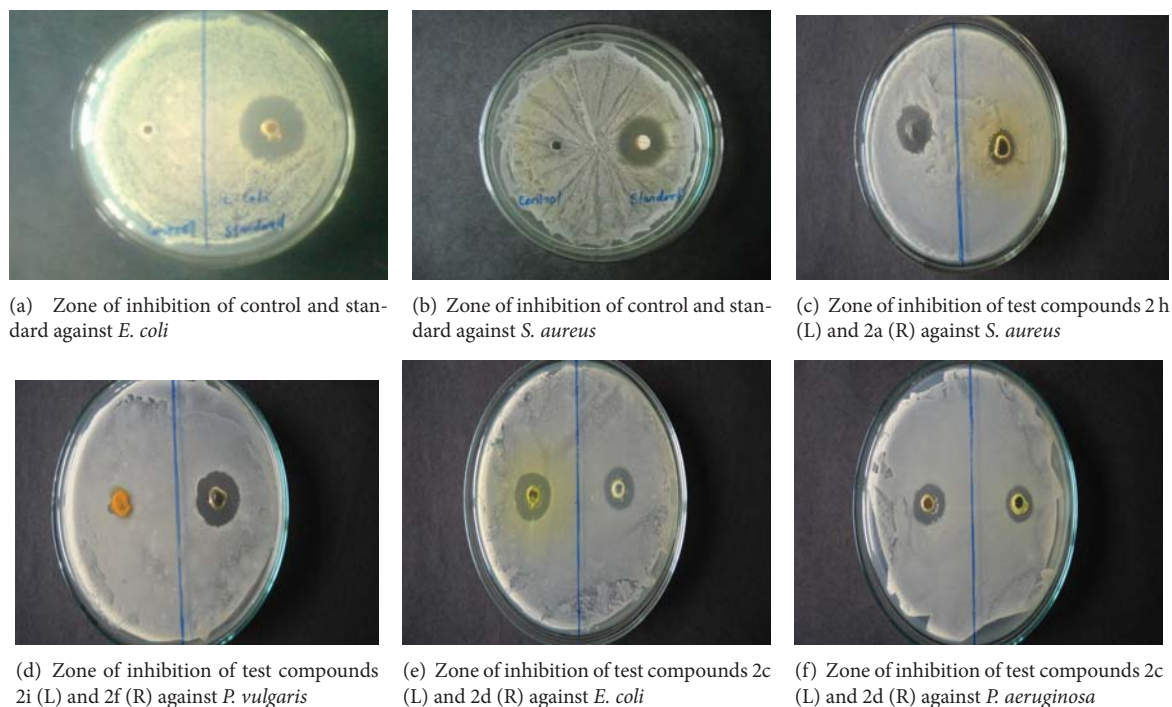


FIGURE 1: Photographs displaying zone of inhibition of control, standard, and various test compounds against different test organisms (R: right, L: left).

at 37°C, the zone of inhibition formed were measured in millimeters against standard drug tetracycline and the data were presented in Table 3.

5. Conclusion

We have synthesized some Schiff base of Isatin derivatives by conventional and microwave irradiation method. With the help of microwave synthesis, the yield of product was increased from 60% upto 85% as compared to conventional method. By microwave irradiation the reactions were completed within 5–10 minutes and the products were obtained in good to high yields, which reduced the time, waste, and formation of byproduct. The microwave assisted synthesis is simple ecofriendly and can be used as an alternative to the existing conventional heating method. From the results of antibacterial studies it was concluded that the tested compounds exhibited significant antibacterial activities against both gram positive and gram negative organisms. Among the tested compounds, compound substituted with electron withdrawing group in Isatin residue preferably at paraposition showed promising antibacterial activities; this may be attributed to their enhanced electronic character which favors greater penetration through microbial membrane.

Acknowledgments

The authors are very much thankful to Roland Institute of Pharmaceutical Sciences, Berhampur, Odisha, India, for providing necessary facilities to carry out the research work.

The authors are also thankful to SAIF, Panjab University, Chandigarh, for spectral analysis of synthesized compounds.

References

- [1] M. Charde, A. Shukla, V. Bukhariya, J. Mehta, and R. Chakole, "A review on: a significance of microwave assist technique in green chemistry," *International Journal of Phytopharmacy*, vol. 2, no. 2, pp. 39–50, 2012.
- [2] S. Ravichandran and E. Karthikeyan, "Microwave synthesis—a potential tool for green chemistry," *International Journal of ChemTech Research*, vol. 3, no. 1, pp. 466–470, 2011.
- [3] S. Sharma, S. Gangal, and A. Rauf, "Green chemistry approach to the sustainable advancement to the synthesis of heterocyclic chemistry," *Rasayan Journal of Chemistry*, vol. 1, no. 4, pp. 693–717, 2008.
- [4] M. Kidwai, "Green chemistry trends toward sustainability," *Pure and Applied Chemistry*, vol. 78, no. 11, pp. 1983–1992, 2006.
- [5] H. M. Mamun, M. A. Foysal, and M. Mahabub, "Microwave-assisted efficient synthesis of isatins and spiro-thiadiazolines under green chemistry protocol," *Journal of Scientific Research*, vol. 2, no. 2, pp. 322–329, 2010.
- [6] A. Kulshrestha and S. Baluja, "Microwave promoted synthesis of some Schiff bases," *Archives of Applied Science Research*, vol. 2, no. 3, pp. 221–224, 2010.
- [7] R. Somani, S. Pawar, S. Nikam, P. Shirodkar, and V. Kadam, "Microwave assisted synthesis and antimicrobial activity of some Schiff's bases," *International Journal of ChemTech Research*, vol. 2, no. 2, p. 860, 2010.
- [8] S. K. Sridhar, S. N. Pandeya, J. P. Stables, and A. Ramesh, "Anticonvulsant activity of hydrazones, Schiff and Mannich

- bases of isatin derivatives," *European Journal of Pharmaceutical Sciences*, vol. 16, no. 3, pp. 129–132, 2002.
- [9] S. N. Pandeya, D. Sriram, G. Nath, and E. De Clercq, "Synthesis and antimicrobial activity of Schiff and Mannich bases of isatin and its derivatives with pyrimidine," *Farmaco*, vol. 54, no. 9, pp. 624–628, 1999.
- [10] A. Jarrahpour, D. Khalili, E. De Clercq, C. Salmi, and J. M. Brunel, "Synthesis, antibacterial, antifungal and antiviral activity evaluation of some new bis-Schiff bases of isatin and their derivatives," *Molecules*, vol. 12, no. 8, pp. 1720–1730, 2007.
- [11] S. S. Chhajed and M. S. Padwal, "Antimicrobial evaluation of some novel Schiff and Mannich bases of isatin and its derivatives with quinolin," *International Journal of ChemTech Research*, vol. 2, no. 1, pp. 209–213, 2010.
- [12] T. R. Bal, B. Anand, P. Yogeewari, and D. Sriram, "Synthesis and evaluation of anti-HIV activity of isatin β -thiosemicarbazone derivatives," *Bioorganic and Medicinal Chemistry Letters*, vol. 15, no. 20, pp. 4451–4455, 2005.
- [13] M. Verma, S. N. Pandeya, K. N. Singh, and J. P. Stables, "Anticonvulsant activity of Schiff bases of isatin derivatives," *Acta Pharmaceutica*, vol. 54, no. 1, pp. 49–56, 2004.
- [14] S. H. Gillespie, *Medical Microbiology-Illustrated*, Butterworth Heinemann, London, UK, 1994.
- [15] U. K. Singh, S. N. Pandeya, A. Singh, B. K. Srivastava, and M. Pandey, "Synthesis and antimicrobial activity of Schiff's and N-Mannich bases of isatin and its derivatives with 4-Amino-N-carbamimidoyl benzene sulfonamide," *International Journal of Pharmaceutical Sciences and Drug Research*, vol. 2, no. 2, pp. 151–154, 2010.

Research Article

Studying the Effects of Adding Silica Sand Nanoparticles on Epoxy Based Composites

Tahir Ahmad,¹ Othman Mamat,² and Rafiq Ahmad¹

¹Department of Metallurgy and Materials Engineering, College of Engineering and Emerging Technologies, University of the Punjab, Lahore, Pakistan

²Mechanical Engineering Department, Universiti Teknologi PETRONAS, Bandar Seri Iskandar, 31750 Tronoh, Perak, Malaysia

Correspondence should be addressed to Tahir Ahmad; tahirengg4051@yahoo.com

Received 10 December 2012; Accepted 24 December 2012

Academic Editor: Amir Kajbafvala

Copyright © 2013 Tahir Ahmad et al. This is an open access article distributed under the Creative Commons Attribution License, which permits unrestricted use, distribution, and reproduction in any medium, provided the original work is properly cited.

The research about the preparation of submicron inorganic particles, once conducted in the past decade, is now leading to prepare polymer matrix composite (PMC) reinforced with nanofillers. The objective of present research is to study the modified effects of reinforcement dispersion of nanoparticle silica in epoxy resin on the physical properties, mechanical and thermal behaviour, and the microstructure of resultant composites. Stirrer mixing associated with manual mixing of silica sand nanoparticles (developed in our earlier research) (Ahmad and Mamat, 2012) into epoxy was followed by curing being the adopted technique to develop the subject nanocomposites. Experimental values showed that 15 wt.% addition of silica sand nanoparticles improves Young's modulus of the composites; however, a reduction in tensile strength was also observed. Number of holes and cavities produced due to improper mixing turn out to be the main cause of effected mechanical properties. Addition of silica sand nanoparticles causes a reduction in degree of crystallinity of the nanocomposites as being observed in differential scanning calorimetry (DSC) analysis.

1. Introduction

Nowadays industrial and academic research laboratories are focusing much of their efforts to develop and improve physical, mechanical, and electrical properties of polymer nanocomposites. Their interest to develop such composites is mainly because of the fact that nanoparticles present a high surface-to-volume ratio which may induct unique properties to these nanocomposites as compared to macro-scale composites [1]. Andritsch et al. [2] prepared nanocomposites filled with SiO₂, Al₂O₃, and AlN with an average particles size from 22 nm to 10 nm and studied the nanoparticles dispersion and DC breakdown strength. They observed the highest DC breakdown strength for 0.5 wt.% for two component system. It was also noticed that the DC breakdown strength increased with 10 wt.% as compared to 2 and 5 wt.% and again decreased with 15 wt.% nano-fillers. Yasmin et al. [3] studied the dispersion of clay nanoparticles in epoxy-based composites using a three roll mill with the concentration of 1–10 wt.%. This technique was found highly efficient

and environmentally friendly due to excellent dispersion of nanoparticles within a short time. Elastic modulus was improved up to 80% with 10 wt.% addition of clay nanoparticles in epoxy. Absence of any improvement in tensile strength of the nanocomposites over pure epoxy was due to the clustering of nanoparticles and/or to the occasional occurrence of nano- to microsize voids in the microstructure. Li et al. [4] prepared the Epoxy nanocomposites with exfoliated nanoclay and a novel ultrafine full-vulcanized powdered rubber. The morphology of the epoxy/rubber/clay nanocomposites has been studied using X-ray diffraction (XRD) and transmission electron microscopy (TEM). Their study showed that the unmodified clay was fully exfoliated and uniformly dispersed in the resulting nanocomposite and found that the impact strength of this special epoxy/rubber/clay nanocomposite increased up 107% over the neat epoxy resin. Thermal analyses showed that thermal stability of the nanocomposite was much better than that of epoxy nanocomposite based on organically modified clay. Damian et al. [5] synthesized epoxy-based nanocomposites reinforced with multiwalled

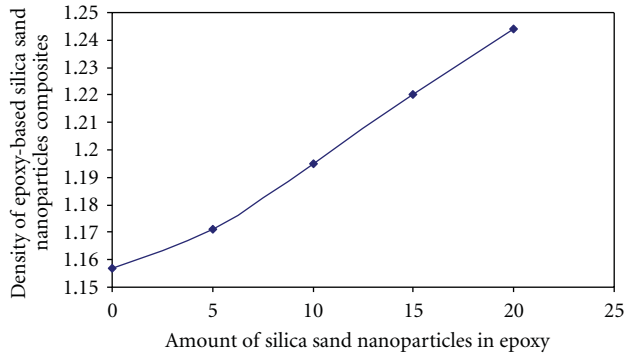


FIGURE 1: Density analyses of epoxy-SiO₂ composites.

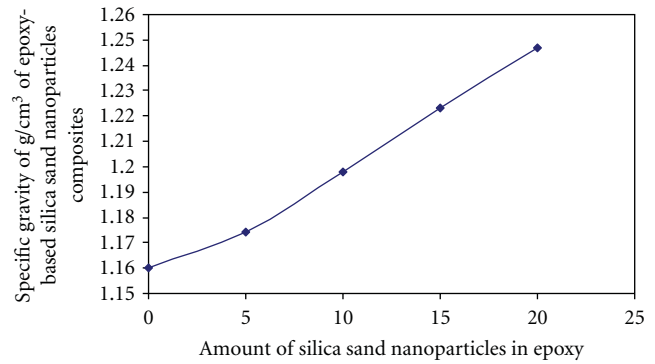


FIGURE 2: Specific gravity analyses of epoxy-SiO₂ composites.

carbon nano-tubes (MWNT). They functionalized MWNTs in order to increase the dispersion in the polymer matrix and thus to ensure good adhesion between the two components. Their study showed that the structure of amine MWNT-B100 exhibit compatibility with the epoxy matrix. However, the higher thermostability was achieved by the composite based on MWNTCOOH as observed from TGA. Frache et al. [6] prepared the epoxy based nanocomposites reinforced with home-made hydrotalcites (HTlc) and montmorillonite-(MMT)-type layered silicates and studied the morphology, dispersion and thermal analysis of the nanocomposites. Their research showed possibility to obtain nano-structured materials, characterized by the resin intercalation into HTlc galleries, by using a proper exchange of the pristine hydrotalcite with stearate anions. The thermal analysis indicated that nanocomposites based on HTlc were prone to decompose, both in air and nitrogen, while in the case of the nanocomposite based on the organophilic MMT a slight improvement was found in air. Jordan et al. [7] studied the effect of addition of micron and nanosized silica inclusions on polyurethane matrix and found it as an increment in density as the filler content increased. He investigated that the composite density further can be increased with micron-sized inclusions as compared to the density for the nanosized inclusions. In above studies, no body tried to utilize silica sand nanoparticles as reinforcement agents in epoxy based composites. Exclusively, the objective of present research is to fill this gap and study the effect of addition of silica sand nanoparticles on epoxy based composites.

2. Experimental Work

The processing and characterization of silica sand nanoparticles have already been discussed in our earlier papers [8]. Before mixing with epoxy resin (E-51), silica sand nanoparticles were dried at 120°C to remove any moisture for 5 hours. The silica sand nanoparticles were mixed with epoxy using stirrer and manual mixing for several hours. The resultant mixture was degassed and cured in steel mould at 120°C to form dog-bone-shaped samples (ASTM D638-97). ASTM D790-03 standard was used to develop flexural test specimens. The Universal Tensile Testing machine (5 KN) LLOYD Instruments, LR 5 K was engaged to determine the

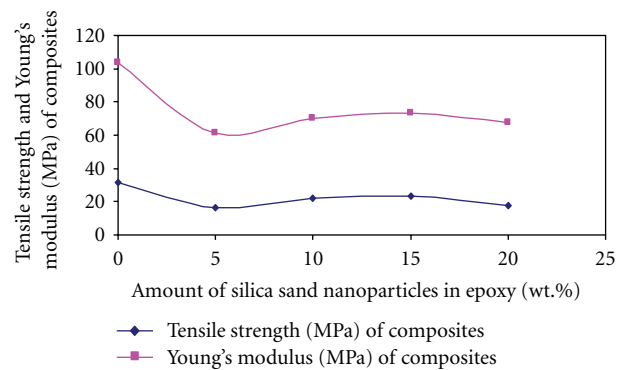


FIGURE 3: Tensile strength and Young's modulus of epoxy-SiO₂ composites.

tensile and flexural properties of the composites with a cross-head speed of 50 mm/min. ASTM D 792-08 standard was used to determine the densities of epoxy based composites. Differential scanning calorimeter (DSC) in nitrogen atmosphere was incorporated to analyse the thermal properties of the epoxy based composites. A 5 mg weight sample was prepared to obtain the scans between 40 to 210°C with a heating rate of 10°C/min.

3. Results and Discussion

3.1. Processing of Tronoh Silica Sand. The silica sand originated naturally from Tronoh Perak, Malaysia was washed with water to remove any clay particles followed by drying it in an oven at 120°C. The dried silica sand was meshed about <600 μm using sieve analysis. The <600 μm size of natural silica sand was ground to nanoparticles using dry ball milling with zirconia balls as grinding media with different steps of sieve analysis. This high-energy milling was known as one of the "top-down" nanoparticles type approach, which generally relies on physical methods for their production. Different particles sizes went through a precise sieve analysis (Sieve Shaker (EFL2000)). The analysis of silica sand nanoparticles had been verified using the ZetaSizer, Nano ZS (ZEN 3600) (MALVERN) analyzer. The nanoparticles results were also checked microscopically through FESEM.

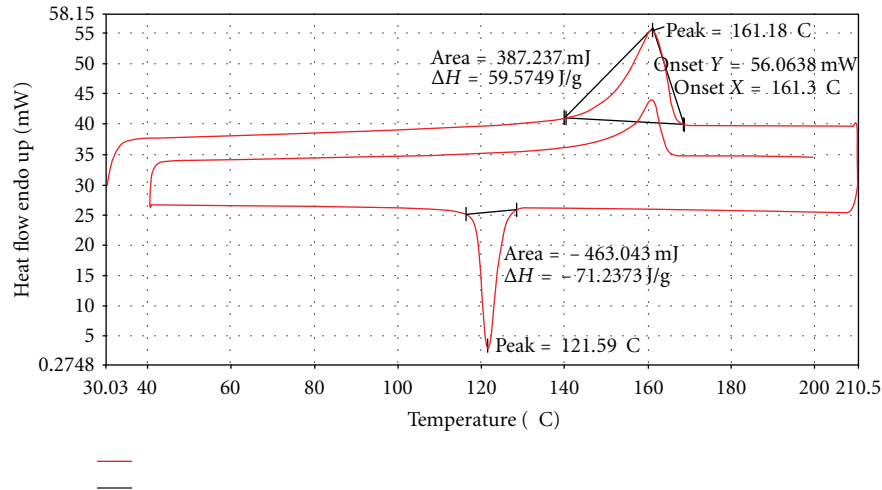


FIGURE 4: DSC curves of crystallization of epoxy-SiO₂ composites.

The chemical composition of silica sand nanoparticles was analyzed adopting XRF technique [8].

3.2. Characterization of the Epoxy-Silica Sand Nanoparticles Composites

3.2.1. Density and Specific Gravity Determination of Epoxy-Silica Nanoparticles Composites. The silica sand being denser as compared to epoxy may cause an enhancement in density of epoxy when added as reinforcement as shown in Figure 1. For every 5 wt.% increase in weight of silica sand nanoparticles, the density of epoxy raised with an average incremental value of 1.8%. Temperature recorded during testing procedure remained as 22.6°C. The inclusions of silica nanoparticles when added to polymer tended to create a linkage of bonding between SiO₂ and polymer which some time results in higher density of the composites.

Results obtained above may actually be expanded to get specific gravity values for each sample. The density and specific gravity were determined using D 792-08 ASTM standard. Specific gravity, or relative density, increases in accordance to sample density as well as wt% increment of silica sand nanoparticles. An increase between 2%–6% can be seen by comparing silica sand nanoparticles added epoxy with its pure form as control element. For every 5% increase in weight of silica sand nanoparticles, it can be found that specific gravity increased by an average value of 1.8%, which is the same compared to density measurement. The results of specific gravities are shown in Figure 2.

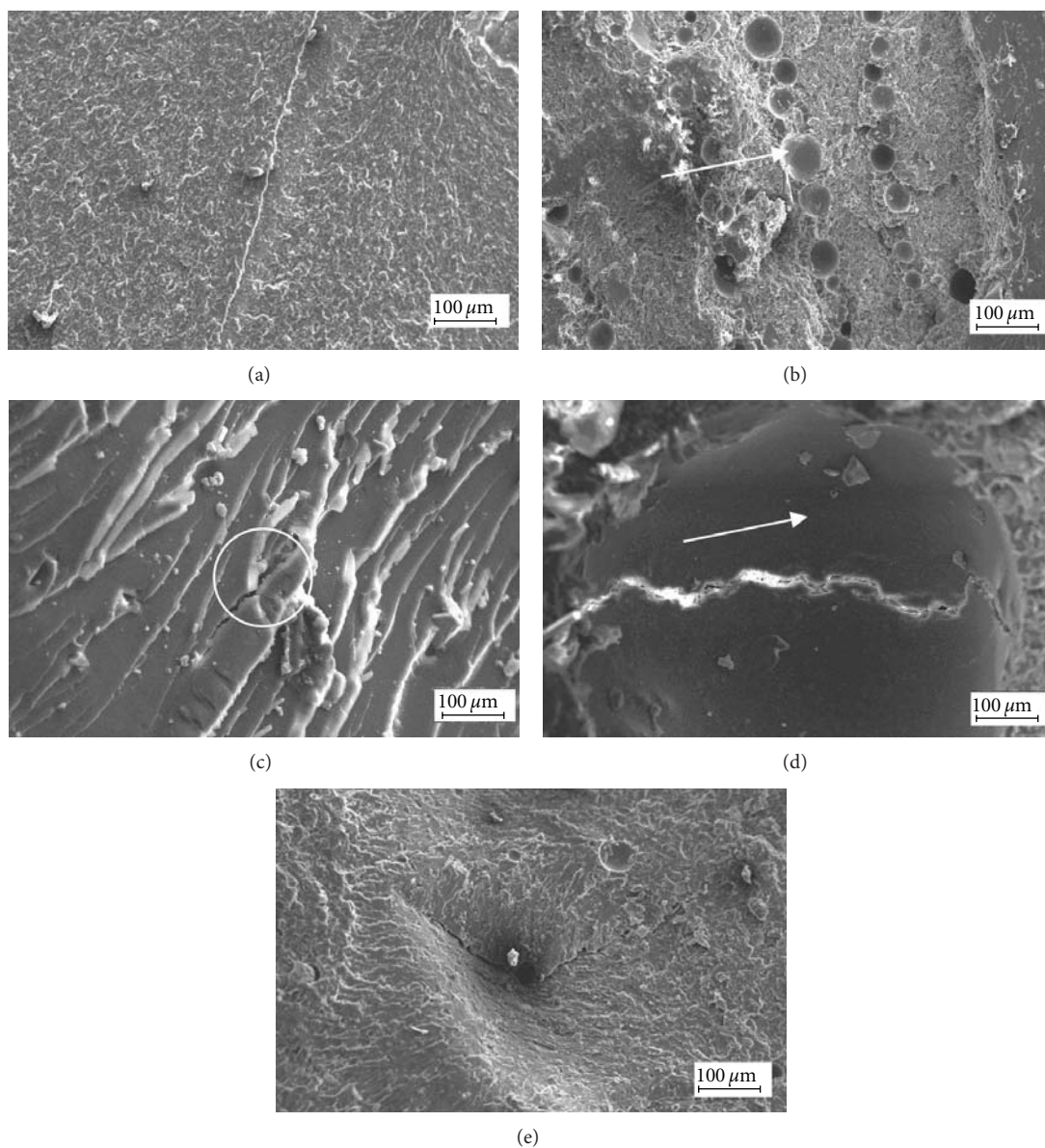
3.2.2. Mechanical Properties of the Epoxy-Silica Sand Nanoparticles Composites. The properties of the composites depend upon the method of dispersion of particles, aggregation of particles, and interaction between particles and polymers. The thickness and density of the interphase developed between two constituents depend on the interaction between particles and polymer [7]. Interparticle distance also plays an important role in the interphase

behaviour and properties of the composites. Tensile properties of the composites are mostly affected by the materials, method, specimen condition and preparation, and also by percentage of the reinforcement [9]. For the comparative testing of materials, the preparation of samples and adopted method are very important to get relatively same properties of the composites. Silica nanoparticles, if not properly mixed with the epoxy, cause voids and increase level of porosity inside the system. This is the reason why pure epoxy exhibited highest value of tensile strength and Young's modulus, and why this strength got reduced when silica nanoparticles between 15 wt.% and 20 wt.% dispersed in it. The mechanical properties of the epoxy-silica sand nanoparticles composites are shown in Figure 3. As wt.% of silica sand nanoparticles increases, tensile strength as well as Young's modulus also rises. These numbers conversely drop when 20 wt% of silica sand nanoparticles is introduced to system. Nature of interface is important in producing high-performance epoxy-nanosilica composites [10]. Better tensile properties are achieved when the samples have good interface between matrix and filler because the applied load mostly transferred through the filler via interface.

3.2.3. Thermal Analysis of the Epoxy-Silica Sand Nanoparticles Composites. The thermal analysis of epoxy-SiO₂ nanocomposites was performed using DSC technique as shown in Table 1. Neat epoxy showed the values of crystallization temperature between 111.12 and 110.32°C; however, for 20 wt.% of silica sand nanoparticles addition to epoxy, the values remain between 121.59 and 119.97. The increase in weight percentage of silica sand nanoparticles to epoxy increases the crystallization temperature; however, it reduces the percentage crystallinity of the nanocomposites as shown in Figure 4 DSC curves. Melting endotherms showed a slight difference for all samples as observed in DSC thermograms and the same results were also found by other researcher using different kinds of nanoparticles [10]. Built-in software

TABLE 1: DSC analysis of epoxy-silica sand nanoparticles composites.

Composites	Crystallization T_c . (onset) (°C)	Crystallization T_c . (peak) (°C)	Melting T_m .(onset) (°C)	Melting T_m .(peak) (°C)	ΔH (J/g)	Crystallinity (%)
Pure epoxy	110.32	111.12	160.20	161.14	250.774	86.8
5 wt.% silica sand + epoxy	112.34	113.40	160.33	161.40	240.523	83.5
10 wt.% silica sand + epoxy	115.44	160.45	161.21	239.804	80.3	
15 wt.% silica sand + epoxy	117.95	118.60	179.64	161.46	237.495	79.5
20 wt.% silica sand + epoxy	119.97	121.59	138.30	145.55	230.444	77.6

FIGURE 5: Fracture surface analysis of pure epoxy, epoxy-SiO₂ nanoparticles composites with (a) pure, (b) 5 wt.% SiO₂, (c) 10 wt.% SiO₂, (d) 15 wt.% SiO₂, (e) 20 wt.% SiO₂.

as shown in (1) below was used to determine the heat of fusion (ΔH) from the scans as follows:

$$X_{\text{DSC}} = \frac{\Delta H_{\text{sample}}}{293}. \quad (1)$$

The reduction in degree of crystallinity was mainly due to reducing trend of heat of fusion from 5 wt.% to 20 wt.% of silica sand nanoparticles in epoxy. The same results were also discussed by some other researchers [11, 12].

3.2.4. Fracture Surfaces SEM Analysis of Tensile Samples of Epoxy-SiO₂ Composites. For pure epoxy, Figure 5(a) shows a brittle fracture which is due to quite surface roughness, and river line pattern in fracture surface [10]. A lot of holes and cavities can be seen in Figure 5(b), which could be due to other small molecular chemical compounds adhered to the silica nanoparticles. This behaviour confirms the reason, as discussed earlier, why tensile strength drops drastically between pure epoxy and 5% silica nanoparticles added to it. In Figure 5(c), tiny crack lines are visible and the arrow indicates the slow propagating crack area. Circled crack propagation in Figure 5(c) justifies that the crack direction is from top to bottom in the micrograph. Figures 5(d) and 5(e) signify crack propagation as a result from cavities and holes formed, due to improper mixture process. The white zones in SEM analysis show that the deformation and cohesive failure of the composites is because of the silica sand nanoparticles surrounds a large part of the polymer matrix. Decreasing trend of mechanical properties is due to agglomeration of silica sand nanoparticles in epoxy as shown in SEM results images.

4. Conclusion

Epoxy-SiO₂ nanocomposites were successfully produced using Tronoh silica sand nanoparticles as reinforcement. The density of the epoxy-SiO₂ nanocomposites was increased from 1.157 g/cm³ to 1.244 g/cm³ with an average increment of 1.796%. The mechanical properties of the nanocomposites decrease with the addition of silica sand nanoparticles due to improper mixing of the nanoparticles. SEM micrograph showed white and agglomerate zones on fracture surfaces which indicate that silica sand nanoparticles are not homogeneously dispersed in epoxy. A reduction in degree of crystallinity in epoxy based nanocomposites was observed with increasing trend of silica sand nanoparticles addition in epoxy as shown by DSC analysis.

Acknowledgments

The authors would like to thank the Universiti Teknologi PETRONAS Perak, Malaysia and University of the Punjab Lahore Pakistan for providing the necessary support to complete this research.

References

- [1] J. Gonzalez-Benito and D. Olmos, "Efficient dispersion of nanoparticles in the thermoplastic polymers," *Society of Plastics Engineers, Plastics Research Online*, 2010.
- [2] T. Andritsch, R. Kochetov, Y. T. Gebrekiros, U. Lafont, P. H. F. Morshuis, and J. J. Smit, "Synthesis and dielectric properties of epoxy based nanocomposites," in *Proceedings of the Annual Report Conference on Electrical Insulation and Dielectric Phenomena (CEIDP '09)*, pp. 523–526, October 2009.
- [3] A. Yasmin, J. L. Abot, and I. M. Daniel, "Processing of clay/epoxy nanocomposites by shear mixing," *Scripta Materialia*, vol. 49, no. 1, pp. 81–86, 2003.
- [4] B. Li, X. Zhang, J. Gao et al., "Epoxy based nanocomposites with fully exfoliated unmodified clay: mechanical and thermal properties," *Journal of Nanoscience and Nanotechnology*, vol. 10, no. 9, pp. 5864–5868, 2010.
- [5] C. M. Damian, A. M. Pande, C. Andronescu, A. Ghebaour, S. A. Garea, and H. Iovu, "Epoxy-based nanocomposites reinforced with new amino functionalized multi-walled carbon nanotubes," *Fullerenes Nanotubes and Carbon Nanostructures*, vol. 19, no. 3, pp. 197–209, 2011.
- [6] A. Frache, O. Monticelli, M. Nocchetti, G. Tartaglione, and U. Costantino, "Thermal properties of epoxy resin nanocomposites based on hydrotalcites," *Polymer Degradation and Stability*, vol. 96, no. 1, pp. 164–169, 2011.
- [7] J. Jordan, K. I. Jacob, R. Tannenbaum, M. A. Sharaf, and I. Jasiuk, "Experimental trends in polymer nanocomposites—a review," *Materials Science and Engineering A*, vol. 393, no. 1–2, pp. 1–11, 2005.
- [8] T. Ahmad and O. Mamat, "Tronoh silica sand nanoparticle production and applications design for composites," *Defect and Diffusion Forum*, vol. 330, pp. 39–47, 2012.
- [9] American Standard of Testing Material (ASTM), *Standard Test Method for Tensile Properties of Reinforced Thermosetting Plastics Using Straight Sided Specimens*, ASTM International, West Conshohocken, Pa, USA, 2004.
- [10] Y. Zheng, K. Chonung, G. Wang, P. Wei, and P. Jiang, "Epoxy/nano-silica composites: curing kinetics, glass transition temperatures, dielectric, and thermal-mechanical performances," *Journal of Applied Polymer Science*, vol. 111, no. 2, pp. 917–927, 2009.
- [11] K. Chrissafis, K. M. Paraskevopoulos, E. Pavlidou, and D. Bikiaris, "Thermal degradation mechanism of HDPE nanocomposites containing fumed silica nanoparticles," *Thermochimica Acta*, vol. 485, no. 1–2, pp. 65–71, 2009.
- [12] M. Joshi and B. S. Butola, "Studies on nonisothermal crystallization of HDPE/POSS nanocomposites," *Polymer*, vol. 45, no. 14, pp. 4953–4968, 2004.